Particle production in proton proton and heavy ion collisions

By

Priyanka Sett

PHYS01200904017

Bhabha Atomic Research Center, Mumbai

A thesis submitted to the

Board of Studies in Physical Sciences

In partial fulfillment of requirements

for the Degree of

DOCTOR OF PHILOSOPHY

of

HOMI BHABHA NATIONAL INSTITUTE

September, 2015

Homi Bhabha National Institute[1]

Recommendations of the Viva Voce Committee

As members of the Viva Voce Committee, we certify that we have read the dissertation prepared by Priyanka Sett entitled "Particle Production in proton proton and heavy ion collisions" and recommend that it may be accepted as fulfilling the thesis requirement for the award of Degree of Doctor of Philosophy.

Chairman - Dr. V. M. Datar		**Date:** 21-9-2015
Guide / Convener - Dr. P. Shukla	Prashant	**Date:** 21-9-15
Member 1 - Dr. A. K. Mohanty		**Date:** 21-9-15
Member 2 - Dr. R. S. Bhalerao		**Date:** 21-9-15
Member N - <Name> ABHIJIT BHATTACHARYYA		**Date:** 21/9/2015

(Examiner). Abhijit Bhattacharyya

Final approval and acceptance of this thesis is contingent upon the candidate's submission of the final copies of the thesis to HBNI.

I/We hereby certify that I/we have read this thesis prepared under my/our direction and recommend that it may be accepted as fulfilling the thesis requirement.

Date: 21-9-15

Place: Mumbai

Prashant

<Signature> **<Signature>**

Co-guide (if applicable) **Guide**

[1] This page is to be included only for final submission after successful completion of viva voce.

STATEMENT BY AUTHOR

This dissertation has been submitted in partial fulfillment of requirements for an advanced degree at Homi Bhabha National Institute (HBNI) and is deposited in the Library to be made available to borrowers under rules of the HBNI.

Brief quotations from this dissertation are allowable without special permission, provided that accurate acknowledgement of source is made. Requests for permission for extended quotation from or reproduction of this manuscript in whole or in part may be granted by the Competent Authority of HBNI when in his or her judgment the proposed use of the material is in the interests of scholarship. In all other instances, however, permission must be obtained from the author.

Priyanka Sett

DECLARATION

I, hereby declare that the investigation presented in the thesis has been carried out by me. The work is original and has not been submitted earlier as a whole or in part for a degree / diploma at this or any other Institution / University.

Priyanka Sett

List of Publications

Journals

1. *Measurement of K_S^0 and K^{*0} in p+p, d+Au and Cu+Cu collisions at $\sqrt{s_{NN}} = 200$ GeV, A. Adare *et.al* (PHENIX Collaboration), Phys. Rev. C**90** (2014) 054905; arXiv:1405.3628[hep-ex].

   PHENIX Publication Group : **Priyanka Sett (chair)**, Prashant Shukla, Dipak Kumar Mishra, Rajnikant Choudhury, Deepali Sharma, Alexander Milov, Itzkak Tserruya, Victor Ryabov, Dmitry Ivanischev, Dmitry Kotov and Yuri Riabov.

2. *Pion p_T spectra in p+p collisions as a function of $\sqrt{s}$ and event multiplicity, **P. Sett** and P. Shukla, Adv. High Energy Phys.**2014** (2014) 896037; arXiv:1408.1034[hep-ph].

3. *Inferring freeze-out parameters from pion measurements at RHIC and LHC, **P. Sett** and P. Shukla, Int. J. Mod. Phys. E**24** (2015) 06, 1550046 (2015); arXiv: 1505.05258[hep-ph].

4. System size dependence of hadron p_T spectra in p+p and Au+Au collisions at $\sqrt{s_{NN}} = 200$ GeV, P. K. Khandai, **P. Sett**, P. Shukla and V. Singh, J. Phys. G**41** (2014) 025105; arXiv:1310.4022[hep-ex].

5. Hadron spectra in p+p collisions at RHIC and LHC energies, P. K. Khandai, **P. Sett**, P. Shukla and V. Singh, Int. J. Mod. Phys. A**28** (2013) 1350066; arXiv:1304.6224[hep-ex].

6. Transverse Mass Spectra and Scaling of Hadrons at RHIC and LHC Energies, P. K. Khandai, **P. Sett**, P. Shukla and V. Singh, 1205.0648[hep-ex].

7. *Study of strange mesons in $p + p$, d+Au and Cu+Cu collisions at $\sqrt{s_{NN}} = 200$ GeV , P. Sett for PHENIX Collaboration, J. Phys. Conf. Ser. **612** (2015) 1, 012063.

8. *PHENIX measurements of nuclear modification factor of hadrons in d+Au and A+A collisions, P. Sett for PHENIX Collaboration, Proceedings of Science (to appear).

9. Measurements of elliptic and triangular flow in high-multiplicity ^{3}He+Au collisions at $\sqrt{s_{NN}} = 200\,\text{GeV}$, A. Adare *et.al* (PHENIX Collaboration), arXiv:1507.06273[hep-ex].

10. ϕ meson production in d+Au collisions at $\sqrt{s_{NN}} = 200\,\text{GeV}$, A. Adare *et.al* (PHENIX Collaboration), arXiv:1506.08181[hep-ex].

11. Measurement of higher cummulants of net-charge multiplicity distributions in Au+Au collisions at $\sqrt{s_{NN}} = 7.7$ - 200 GeV, A. Adare *et.al* (PHENIX Collaboration), arXiv:1506.07834[hep-ex].

12. Measurement of parity-violating spin asymmetries in W$^{\pm}$ production at midrapidity in longitudinally polarized $p + p$ collisions, A. Adare *et.al* (PHENIX Collaboration), arXiv:1504.07451 [hep-ex].

13. Systematic study of charged-pion and kaon femtoscopy in Au+Au collisions at $\sqrt{s_{NN}} = 200\,\text{GeV}$, A. Adare *et.al* (PHENIX Collaboration), arXiv:1504.05168[hep-ex].

14. Beam-energy dependence and system-size dependence of the space-time extent of the pion emission source producuced in heavy ion collisions, A. Adare *et.al* (PHENIX Collaboration), arXiv:1410.2559[hep-ex].

15. Search for dark photons from neutral meson decays in $p + p$ and d+Au collisions at $\sqrt{s_{NN}} = 200\,\text{GeV}$, A. Adare *et.al* (PHENIX Collaboration), Phys. Rev. C**91** (2015) 3, 031901; arXiv:1409.0851[hep-ex].

16. Cross section and transverse single-spin asymmetry of η mesons in p+p collisions at $\sqrt{s} = 200$ GeV at forward rapidity, A. Adare *et.al* (PHENIX Collaboration), Phys. Rev. D**90** (2014) 7, 072008; arXiv:1406.3541[hep-ex].

17. Low mass vector-meson production at forward rapidity in p+p collisions at $\sqrt{s} = 200$ GeV, A. Adare *et.al* (PHENIX Collaboration), Phys. Rev. D**90** (2014) 5, 052002; arXiv:1405.4260[hep-ex].

18. Comparison of space-time extent of the emission source in d+Au and Au+Au collisions at $\sqrt{s_{NN}} = 200$ GeV, A. Adare *et.al* (PHENIX Collaboration), Nucl. Phys. A**931** (2014) 1082-1087; arXiv:1404.5291[hep-ex].

19. Nuclear matter effects on J/ψ production in asymmetric Cu+Au collisions at $\sqrt{s_{NN}}$ = 200 GeV, C. Aidala *et.al* (PHENIX Collaboration), Phys. Rev. C**90** (2014) 6, 064908 arXiv:1404.1873[hep-ex].

Conferences

1. Estimation of fractional energy loss of light and heavy flavor mesons in heavy ion collision, **P. Sett** and P. Shukla, Proc. DAE Symp. on Nucl. Phys. **59**, 708 (2014).

2. Strange meson measurement in Cu+Cu system at $\sqrt{s_{NN}} = 200$ GeV in PHENIX, **P. Sett** and P. Shukla, Proc. DAE Symp. on Nucl. Phys. **58**, 720 (2013).

3. Description of hadron p_T spectra with modified Tsallis function, P. K. Khandai, **P. Sett** and P. Shukla, Proc. DAE Symp. on Nucl. Phys. **58**, 718 (2013).

4. Thermal model description of hadronic ratios in p+p collision at RHIC and LHC energies, **P. Sett**, P. K. Khandai and P. Shukla, Proc. DAE Symp. on Nucl. Phys. **57**, 828 (2012).

5. K^{*0} meson production in Cu+Cu collisions at $\sqrt{s_{NN}} = 200$ GeV, **P. Sett** and P. Shukla, Proc. DAE Symp. on Nucl. Phys. **57**, 826 (2012).

6. Hadronic spectra in p+p collisions at RHIC and LHC energies, P. K. Khandai, **P. Sett** and P. Shukla, Proc. DAE Symp. on Nucl. Phys. **57**, 768 (2012).

7. Study of K^{*0} meson production in d+Au and Cu+Cu systems at $\sqrt{s_{NN}} = 200$ GeV, **P. Sett**, D. K. Mishra, P. Shukla and R. K. Choudhury, Proc. DAE Symp. on Nucl. Phys. **56**, 952 (2011).

8. Freeze out conditions in Au+Au collisions at $\sqrt{s_{NN}} = 200$ GeV, **P. Sett**, P. K. Khandai and P. Shukla, Proc. DAE Symp. on Nucl. Phys. **56**, 954 (2011).

9. J/ψ-μ correlation as a probe for b-bbar production and interaction mechanism at LHC, A. Abdulsalam, **P. Sett**, P. Shukla, R. K. Choudhury, Proc. DAE Symp. on Nucl. Phys. **55**, 600 (2010).

(*) indicate papers on which this thesis is based.

Priyanka Sett

DEDICATIONS

I would like to dedicate this thesis to my parents, for supporting me throughout my ups and downs. Also my husband for tolerating me in my blues and ever-ready to help me out no matter what.

—— Thank you.

ACKNOWLEDGEMENTS

I take the opportunity to thank all people without whom, I would have probably couldn't make this journey through Ph.D.

First of all, I would like to thank my supervisor Dr. Prashant Shukla for his constant support during these tough years of Ph.D. His encouragement and personal guidance has helped me a lot during the critical times. This thesis would not have been possible without his patience and guidance.

I would like to thank my Doctoral Committee members - Dr. Datar, Prof. Bhalerao, Prof. Mohanty and Dr. Shukla, for their valuable suggestions during my Ph.D. I would also like to thank Dr. Choudhury and Dr. Chatterjee.

I would like to thank the whole High Energy Physics group. I take the opportunity to thank Dr. Mohanty to be there whenever I was in trouble. I personally thank Dr. Mishra for helping me always and specially helping me while writing the collaboration paper. I thank Dr. Netrakanti for being there. The lively discussions with him has helped me a lot to learn many things. I thank Raman Sehgal for helping me with various computer related stuffs throughout my Ph.D life. I thank Dr. Salar for the technical and scientific supports. I also thank Dr. Dutta for discussions. I would like to thank my fellow researchers Abdulla and Ruchi for being with me always.

I would take this platform to thank the entire PHENIX collaboration for giving me the opportunity to work in such a great field. I thank my PHENIX publication group without whom the paper wouldn't have been possible. I personally thank Victor, Sasha, Itzhak, Deepali for guiding me throughout the paper. I also thank Kenta, Julia and Ron for providing important inputs.

I would also like to thank my friends who were there whenever I needed them. They have being a constant support system for me and have made my life cheerful. To name a few Semanti, Susmita, Nitya, Mitali, Sriloy, Sohini and many more. The girly chats, shopping, outings are the days which used to keep me off from the blues. I would also like to give my sincere gratitude to Deepali, who is not only a collaborator but also like my elder sister. Thank you D (Deepali) for all those evenings and times we spend together. The lengthy video chats were really cool and also inspiring. These are one of the best times I have ever had. Hope to see you soon.

Finally, I would like to thank my parents for encouraging me to go ahead in my academic career. I am grateful and happy to have you Ma-Papa. Thank you for believing me and taking stand for me whenever needed. I also thank my in-laws for backing me. Thank you Chinmay for being such a supportive and loving husband.

SYNOPSIS

At very high energy densities, exceeding approximately $1\,\mathrm{GeV/fm^3}$, quantum chromodynamics predicts a phase transition from ordinary hadronic nuclear matter to a new state of matter where the degrees of freedom are quarks and gluons. Matter at such high energy density can be produced in laboratory conditions by colliding heavy nuclei at relativistic energies at the Relativistic Heavy Ion Collider (RHIC) and recently at the Large Hadron Collider (LHC). This state of matter exhibits very strong coupling between its constituents and is thus called the strongly coupled Quark-Gluon Plasma (sQGP).

The quark gluon matter presumably with local thermal equilibrium expands hydrodynamically and undergoes a phase transition to hadronic matter which further cools till the multiple scatterings among particles are sufficient to keep them as one system. The hadrons then decouple from the system and their spectra would reflect the condition of the system at the time of freeze-out. Hadrons (pions, kaons and protons) form the bulk of particles produced and are usually the first and easiest to be measured in a heavy ion collision experiment. Traditionally, statistical model has been used at SPS and RHIC energies to infer the conditions at freezeout using measured hadron ratios as input. Alternatively one can consider full transverse momentum (p_T) spectra of hadrons in heavy ion collisions. The bulk and collective effects show up in the low and intermediate p_T regions of hadron spectra while the high p_T region above 5 GeV/c consists of particles from jets which are produced in hard interactions.

Experimental measurement of strange meson

The particle spectra in heavy-ion collisions are modified due to presence of the medium and are quantified by the "nuclear modification factor" (R_{AB}) defined as:

$$R_{\mathrm{AB}} = \frac{d^2N_{AB}/p_T\,dydp_T}{N_{\mathrm{coll}} \times d^2N_{pp}/p_T\,dydp_T}, \tag{1}$$

where the numerator is the of particle production in A+B (heavy ion) collisions, measured as a function of p_T and rapidity (y), $d^2N_{pp}/p_T\, dydp_T$ is the yield of the same process in $p+p$ collisions and $N_{\rm coll}$ is the number of nucleon-nucleon collisions in the A+B system. $R_{\rm AB}$ different from unity is a manifestation of medium effects.

In central Au+Au collisions at RHIC, $R_{\rm AB}$ of hadrons reaches a maximum suppression of a factor of ~ 5 at $p_T \sim 5\,{\rm GeV}/c$. The high p_T suppression is found to be independent of the particle type, mesons or baryons, and their quark flavor content. In the intermediate p_T range ($2 < p_T < 5\,{\rm GeV}/c$), mesons containing light quarks (π, η) exhibit suppression, whereas protons show very little or no suppression. Measurements of particles with different quark content provide additional constraints on the models of collective behavior, parton energy loss and parton recombination. Experimental measurements of particles containing strange quarks are important to find out whether flow or recombination mechanisms boost strange hadron production at intermediate p_T and to understand their suppression at high p_T. In heavy ion collisions, the ϕ meson shows at high p_T the same suppression as particles containing only u and d quarks, however at intermediate p_T it is less suppressed than the π meson. On the other hand, the η meson, which has a significant strange quark content, is suppressed at the same level as π meson in the p_T range from 2–10 GeV/c.

The main part of this thesis concentrates on the measurements of the nuclear modification factor of strange meson K^{*0} at PHENIX experiment. The K^{*0} meson spectra for different centralities are measured in the p_T range from 1.1 GeV/c up to 8 GeV/c in Cu+Cu collisions via $K^{*0} \rightarrow K^+\pi^-$. The measurements extend the momentum coverage of the previously published results by the STAR collaboration. These measurements are further combined with the K^0_S meson ($K^0_S \rightarrow \pi^0(\rightarrow \gamma\gamma)\pi^0(\rightarrow \gamma\gamma)$) measurements over the p_T range of 3–12 GeV/c. This gives strange meson $R_{\rm AB}$ over a wider p_T range.

The PHENIX detector consists of global, tracking and PID detectors. The event information is obtained from the Beam Beam Counters (BBC), located at $|\eta| < 0.35$ and covering 2π in azimuth. The track reconstruction and momentum determination are done with the help of the Drift Chambers (DC) and first layer of the Pad Chambers (PC). The second and third layers of PC help to suppress contribution of the secondary tracks originating from the decay of long-lived particles or from the interaction of tracks with the detector material. The Time of Flight (TOF) detector identifies charged hadrons.

The K^{*0} meson invariant mass is reconstructed via $K^{*0} \rightarrow K^{\pm}\pi^{\mp}$ which has a branching ratio of $\sim 67\%$. The Minimum Bias triggered samples are used for the K^{*0} meson study. The charged kaons and pions are identified by the TOF in PHENIX. The TOF detector has a small acceptance and has limitation in identification of particles. This limitation leads to the measurement of K^{*0} in low p_T region. To increase the extent of measurement up to high p_T, unidentified tracks with opposite charge are also included in the analysis. The unidentified tracks are required to have associated hits in PC3 and EMCal to do away the contribution originating from secondary tracks. Depending on the track selection criteria, three different techniques are used to reconstruct the K^{*0} invariant mass distribution.

1. *Fully Identified*, where both the tracks are identified as kaons and pions via the TOF.

2. *Kaon Identified*, where one of the tracks is identified as kaon via the TOF and the other PC3-matched track is given the mass of pion.

3. *Unidentified*, where both the tracks are PC3-matched tracks. The invariant mass spectra is obtained by the combinatorial method. The total invariant mass distribution for charged kaon-pion consists of the both signal and background. The uncorrelated background is removed by the event-mixing technique. The correlated part of the background is mainly dominated by the mis-identified track pairs. Two of the most dominating processes are : $\phi \rightarrow K^+K^-$ and $K_S^0 \rightarrow \pi^+\pi^-$. These are estimated and removed from the obtained invariant mass spectra. The contribution of residual background is also removed and the raw yield for K^{*0} is obtained by bin-counting. The raw yield is then divided by acceptance to get the corrected yield.

The invariant transverse momentum spectra and nuclear modification factors of K^{*0} are obtained for different centralities in the Cu+Cu system and are combined with the

K_S^0 meson results. In the Cu+Cu collisions system, no nuclear modification is observed in peripheral collisions within the uncertainties of the measurement. In central Cu+Cu collisions both mesons show suppression. In the range p_T = 2-5 GeV/c, the strange mesons show an intermediate suppression between the more suppressed π^0 and the nonsuppressed baryons. This behavior provides a particle species dependence of the suppression mechanism and provides additional constraints to the models attempting to quantitatively reproduce nuclear modification factors. At higher p_T, all particles, π^0, strange mesons and baryons, show a similar level of suppression.

Systematics of hadron spectra in $p + p$ and heavy-ion collisions

Phenomenological studies are done for the charged pion transverse momentum spectra for different collisional energies and also for different event-multiplicities (at LHC energies) in p+p collisions using Tsallis distribution. The Tsallis distribution describes a system in terms of two parameters; temperature and q which measures deviation from thermal distribution. It has been shown that the functional form of the Tsallis distribution in terms of parameter q is the same as the QCD-inspired Hagedorn formula in terms of power n. Both n and q are related and describe the power law tail of the hadron spectra coming from QCD hard scatterings.

The Tsallis parameter n decreases with increasing $\sqrt{s}$ and starts saturating at LHC energies. The value of T also reduces slowly from SPS energies to LHC energies. It means that the spectra at SPS energies have large softer contribution and as the collision energy increases more and more contribution from hard processes are added. The p_T integrated pion yield increases with increasing $\sqrt{s}$ and becomes 10 times when going from SPS to highest LHC energy. The Tsallis parameters are also obtained as a function of event multiplicity for all three LHC energies which can be described by the same curve. The variation of n and T as a function of multiplicity is very similar to the variation which we find as a function of $\sqrt{s}$. It means that events with higher multiplicity have larger contribution from hard processes.

The value of n for high multiplicity events at 7 TeV is ~ 4 which is depictive of production from point quark-quark scattering. The p_T integrated pion yield distribution for the three LHC energies shows that as the energy increases, more and more high mutliplicity events are added in the sample with mean of the distribution shifting towards higher multiplicity.

The transverse momentum spectra of charged pions measured in Au+Au collisions at $\sqrt{s_{NN}} = 200$ GeV and Pb+Pb collisions at $\sqrt{s_{NN}} = 2.76$ TeV are analysed using the modified Tsallis distribution. All the spectra used in this analysis are well described by this distribution. The parameter q of the modified Tsallis distribution suggests similar thermalization characteristics for systems at RHIC and LHC energies. The kinetic freeze-out temperature and transverse flow velocity are extracted from pion p_T spectra. The kinetic freeze-out temperature is also obtained from a model independent method using the measurement of HBT radii and particle multiplicity.

Contents

List of Figures

List of Tables

CHAPTER 1

INTRODUCTION

These days, the theoretical and experimental study of high-energy nuclear physics is one of the most active fields of research. The aim of this program is to study the nuclear matter under extreme conditions. Theoretically, lattice Quantum Chromodynamics (lQCD) predicts a phase transition from hadrons to a new phase [1, 2, 3] known as Quark Gluon Plasma (QGP), where the degrees of freedom are quarks and gluons. The high energy nuclear collisions provide unique opportunity to create this new phase in laboratory and perform detailed study. One can perform systematic study of QGP properties by colliding various nuclei at different energies. The advances in accelerator and detector technologies have made it possible to build very high energy collider facilities, RHIC at BNL (2000 - present) and LHC at CERN (2010 - present). These facilities have taken the study of high-energy nuclear physics to a new dimension.

In this introductory chapter, the fundamental particles, interactions, the concepts of QCD and heavy ion collisions are briefly discussed. At the end of this chapter, the organization and contents of this thesis are outlined.

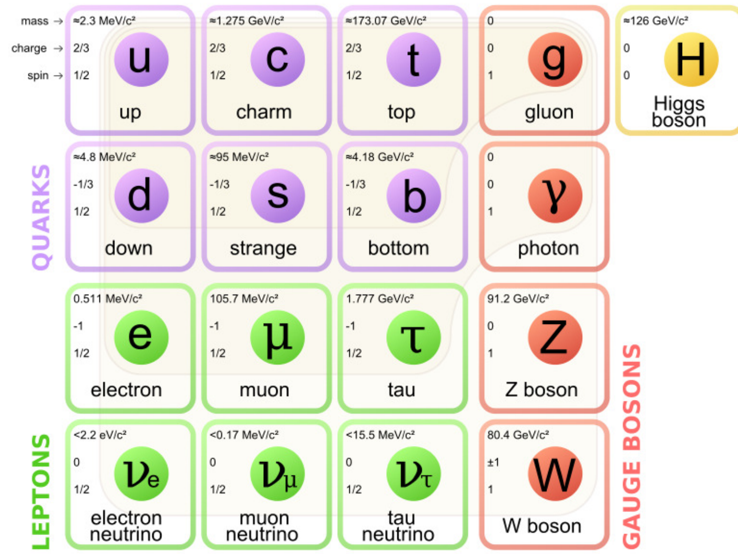

Figure 1.1: Constituents of Standard Model

1.1 Fundamental particles and interactions

1.1.1 Quarks and leptons

The theoretical and experimental understanding about the particle kinematics and interactions are encapsulated in the 'Standard Model' of particle physics, which comprises of fundamental particles (quarks and leptons) and fundamental forces. This model unifies the Strong, Weak and Electromagnetic interactions but does not include the Gravitational interactions. The basic building blocks of 'Standard Model' are shown in Fig. 1.1. The mass and charge for different quarks and leptons are listed in Table 1.1.

<u>Flavors and colors:</u>

Gell-Mann introduced the 'Eight-fold way' [6] method in early 60's to explain the decay kinematics and the interactions of the elementary particles (proton [4], neutron [5]), the mesons (neutral and charged pions, kaons etc.) and the baryons (Λ, Ξ, Ω, etc.) Later in 1964, both Gell-Mann [7] and Zweig [8] independently proposed the 'Quark-Model', in which 'quark' (name proposed by Gell-Mann) plays the role of fundamental entity. In this

Table 1.1: Physical properties of quarks and leptons [9].

Quarks			Leptons		
Flavour	Charge (e)	Mass (MeV/c^2)	Flavour	Charge (e)	Mass (MeV/c^2)
u	$+\frac{2}{3}$	1.5 - 3.3	e	-1.0	0.511
d	$-\frac{1}{3}$	3.5 - 6.0	ν_e	0	$<$ 0.003
s	$-\frac{1}{3}$	104^{+26}_{-34}	μ	-1	105.6
c	$+\frac{2}{3}$	1270^{+70}_{-110}	ν_μ	0	$<$ 0.19
b	$-\frac{1}{3}$	4200^{+170}_{-70}	τ	-1	1776.8
t	$+\frac{2}{3}$	171200$\pm$2100	ν_τ	0	$<$ 18.2

model, quarks didn't have any physical existence, they were just mathematical concept. In later times, quarks were discovered in deep inelastic scatterings (DIS).

In 'Quark-Model', the quarks are the fundamental blocks which build up hadrons. Similar to the particle-antiparticle concept, every quark has its own anti-quark. In early days, there were three different types or 'flavors' of quarks (anti-quarks) : $u(\bar{u})$, $d(\bar{d})$ and $s(\bar{s})$ known as *up*, *down* and *strange*, respectively. Theoretical prediction [10] for another quark named as *charm* represented by c, was proposed by Bjorken and Glashow in 1970. The bound state of $c\bar{c}$ [11] was found experimentally simultaneously by two different groups, one at BNL and the other one at SLAC, hence confirming the existence of c. The other two flavors *bottom* (b) [12] and *top* (t) [13] were discovered in the late 1977 and 1995 respectively. This completes the three generations of quarks.

The 'flavor' symmetry can be described in mathematical form using the $SU(3)$ group theory. Each quark is a half-spin (spin = $\pm 1/2$) particle with fractional charge. The anti-quark has the same magnitude of spin and charge but with opposite sign. According to this model, mesons consist of $q\bar{q}$ and baryons consist of combination of 3 quark or antiquarks of different flavors. The 'Quark-Model' approach worked well in explaining the mass and spin of the particles, except for Δ^{++}, Δ^{-} and Ω^{-}, whose constituent quarks are uuu, ddd and sss respectively. This violates Pauli exclusion principle. This condition required additional quantum number known as 'color charge' or 'color'. There are three types of colors, *red*

(r), *blue* (b) and *green* (g) and anti-colors $anti - red$ ($\bar{r}$), $anti - blue$ ($\bar{b}$) and $anti - green$ ($\bar{g}$). Anti-quark posses anti-color. While forming hadrons (mesons or baryons), the quarks combine among themselves in such a way that the final state is colorless. The color charges bind the quarks inside hadron via strong interaction. The strong interaction (Section 1.1.2) is mediated by 'gluons'. The quarks and gluons are collectively known as 'partons'.

Leptons:

Unlike the quarks, leptons were not a mathematical concept, they existed since beginning. In fact, electron (e) is the first fundamental particle to be observed. Muon (μ) was discovered from the analysis of cosmic-rays. Later, electron-neutrino (ν_e) was proposed by Pauli in order to preserve the energy conservation in β decay. Initially, e, μ and ν_e were grouped as 'leptons'. Later muon-neutrino (ν_μ), tau (τ) and tau-neutrino (ν_τ) were discovered. The e and ν_e forms isospin doublet. Also, the μ and ν_μ pair and the τ and ν_τ pair form the isospin doublets. The quantum number associated with electron family is known as electronic leptonic number L_e and has the value 1. The muon and tau family also have muonic and tauonic lepton numbers $L_\mu = 1$ and $L_\tau = 1$ respectively. The e, μ and τ carry negative charges. Their anti-particles carry positive charges and negative lepton number. The neutrinos are 1/2 spin charge-less particles. Leptons undergo both electromagnetic and weak interactions.

1.1.2 Interactions

Interaction is simply described as the force acting between particles. The first well understood interaction was the Electromagnetic interaction, which takes place between two charge particles via an exchange quanta known as *photons* (γ). The range of this interaction is very large, theoretically ∞. Next comes the Gravitation, which plays role for massive bodies. The exchange particle is known as *graviton*. The gravitational effects are significant for the masses of order $mc^2 = 10^{19}$ GeV, hence not a significant interaction for the subatomic

Table 1.2: Fundamental forces and their relative strength

Force	Relative Strength	Range (m)	Mediator	Mass of Mediator (GeV/c^2)	Spin
Strong	1	10^{-15}	gluon	0	1
Electromagnetic	10^{-2}	∞	photon	0	1
Weak	10^{-4}	10^{-18}	W$^\pm$, Z^0	80, 91	1
Gravitation	10^{-38}	∞	graviton	0	2

particles. The Weak interaction was first observed in β decay. This interaction is mediated by the massive $W^\pm$ and Z^0 vector mesons having integral spin. The extent of this interaction is within a distance $< fm$. The Strong interaction helps in binding the quarks inside the hadrons. The *gluons* (g) are the mediators of strong interaction having integral spin and zero mass. The theory of strong interaction is explained by the 'Quantum Chromodynamics (QCD)', as the *gluons* carry 'color-charge'. The main aspects of QCD will be discussed in the next section (Section 1.2). The relative strength, range and the mediators for different interactions are listed in Table 1.2. The quarks participate in Strong and Weak interactions whereas, the leptons experience Weak and Electromagnetic interactions.

1.2 Quantum chromodynamics

The strong interaction is formulated and understood by the Quantum Chromodynamics (QCD), which gives the interaction among the colored charges. QCD is a non-abelian gauge theory. This theory exhibits two remarkable features, namely $Asymptotic\ freedom$ and $Confinement$. This can be understood from the expression of the strong interaction coupling constant, α_s which is given by;

$$\alpha_s(Q^2) = \frac{12\,\pi}{(33 - 2\,n_f)\,log(Q^2/\Lambda^2)} \tag{1.1}$$

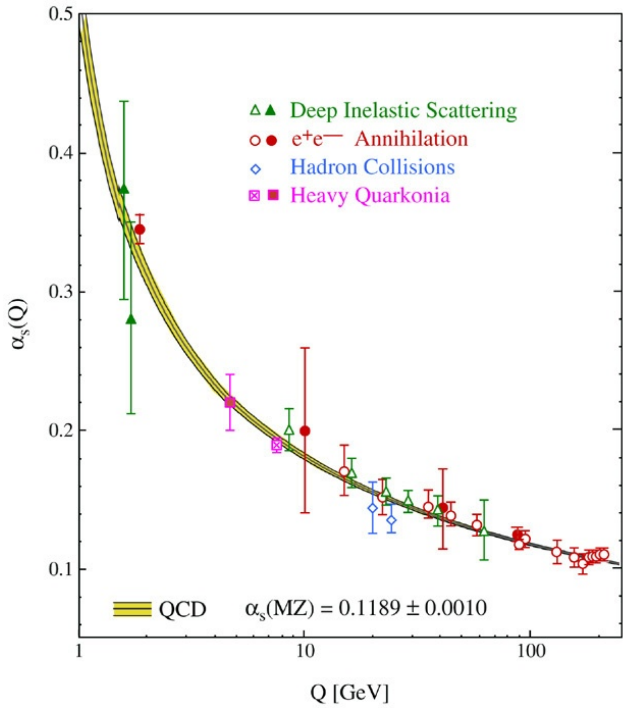

Figure 1.2: The strong interaction coupling constant α_s as a function of momentum transfer (Q), measured in different experiments and obtained from different calculations [14].

where, Q^2 is the momentum transfer, n_f is the number of quark flavors and Λ is the QCD scaling parameter. The coupling constant is a function of momentum transfer and hence known as 'running coupling constant'. The expression in Eq. 1.1 shows that at large Q (i.e at small distance), the coupling α_s decreases and for $Q^2 \to \infty$ the $\alpha_s \to 0$ which implies that the quarks behave as $free$ at this energy-regime. This phenomenon is known as $Asymptotic\ freedom$. This was discovered by Gross and Wilczek [15] and Politzer [16]. At high momentum transfer, the coupling constant is small enough which allows perturbative treatment for QCD problems.

For small Q (i.e large distance), $\alpha_s(Q^2)$ increases significantly. This shows that the coupling increases if the partons are tried to pull apart at large distances. This signifies why the quarks are not observed free and are found only inside hadrons. This is known as $Confinement$ or sometimes $Quark\ Confinement$. The strong coupling constant is shown as a function of momentum transfer in Fig. 1.2 from a recent review [14].

One can also understand these features considering the phenomenological potential between a $q\bar{q}$ pair, given as;

$$V(r) = -\frac{K_1}{r} + K_2 r \tag{1.2}$$

where, at small distances the potential behaves like Coulomb interaction and at large distances the potential increases linearly with distance.

QCD calculations for small momentum transfer cannot be done using perturbation theory. In this case one uses 'Lattice QCD' where the discrete lattice points are treated as space-time points and then numerical methods are applied to predict the thermodynamical quantities.

1.3 QCD phase transition and QGP

QCD phase transition can be perceived from the outcomes of two very different features of QCD theory. One is the 'Deconfinement' which results due to the *asymptotic freedom* and the other is the 'Chirality Restoration' which comes directly from *QCD Lagrangian*. Both of these phenomena take place for high energy density and are discussed in detail.

1.3.1 Deconfinement

The discovery of asymptotic freedom led to the predictions [17, 18] of the existence of a deconfined state of quarks and gluons at high temperature and/or high pressures. At very high temperatures, the partons (quarks and gluons) will interact weakly among themselves and the system will replicate an ideal ultra-relativistic gas, where the degrees of freedom will be determined by the number of flavors, colors, charge and spin states of partons. This deconfined state can be described as "soup of quarks and gluons", later named as "Quark Gluon Plasma" by Shuryak [3, 19]. Along with the predictions from Cabibo *et.*

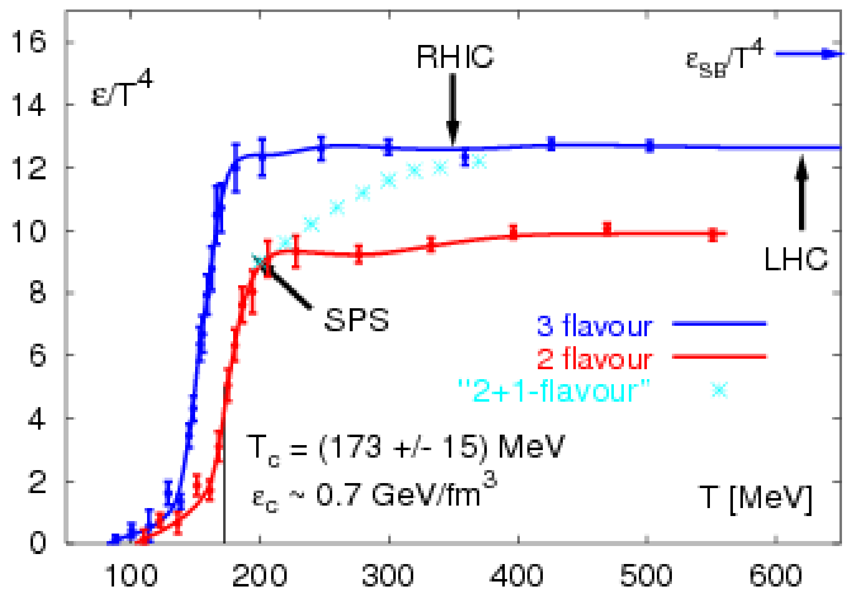

Figure 1.3: The energy density of bulk hadronic matter as a function of temperature from lattice QCD calculations [20]. T denotes the temperature and T_C the critical temperature for QGP. Different colored lines shows the results corresponding to different number of flavors taken in lattice calculations.

al. [18], lattice QCD also shows a sharp change in energy density (ϵ) and pressure (p) around temperature (T) $\approx$ 170 MeV, known as critical temperature (T_C). The results from Lattice QCD [20] are shown in Fig. 1.3 where ϵ is plotted as a function of T. The results are shown for different number of active quarks. For 2 flavored system the T_C is 173 $\pm$ 15 MeV and ϵ_C is 0.7 $\pm$ 0.3 GeV/fm^3 [20]. It is also seen that, above T_C, ϵ is proportional to T^4, but the proportionality constant is smaller than the value expected for the ideal gas of gluons and massless quarks.

1.3.2 Chirality restoration

The QCD Lagrangian is chirally symmetric for massless quarks. The foremost consequence of this symmetry should be the zero value of the quark condensate ($\langle q\bar{q}\rangle$). But the existence of pion, rules out the possibility of $\langle q\bar{q}\rangle = 0$. This is called as *spontaneous* symmetry breaking of QCD. The spontaneous breaking of symmetry is one of the predictions

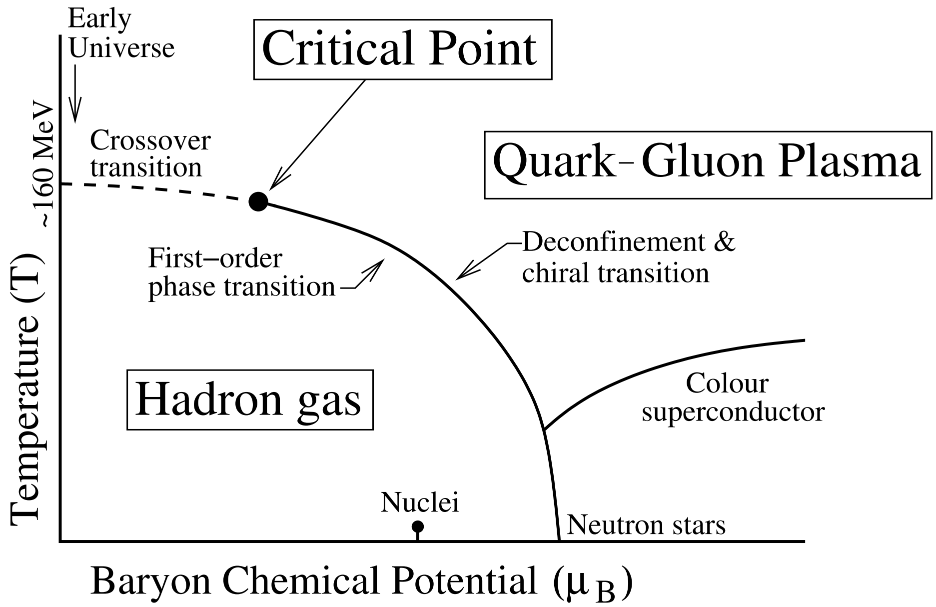

Figure 1.4: A schematic phase-diagram [21] of QGP in terms of the temperature (T) and baryo-chemical potential (μ_B).

of QCD, which leads to the prediction of the existence of the Goldstone bosons. Physically, any kind of phase transition involves the spontaneous breaking of symmetry at ground state. Lattice QCD predicts the restoration of chiral symmetry at high temperatures or densities which is spontaneously broken at low temperatures by $\langle q\bar{q}\rangle$ condensate.

1.3.3 QGP phase diagram

The schematic phase diagram of QGP phase transition is shown in Fig. 1.4. The Y-axis is the temperature (T) and the X-axis is the baryon-chemical potential (μ_B) which determines the energy required to add or remove a baryon at fixed pressure and temperature. This quantity reflects the net baryon density of the matter. For normal nuclear matter the value of μ_B is $\sim$ 1 GeV.

The black curve (dashed and solid) defines the boundary of the QGP phase and hadron gas. From lattice QCD calculations [22, 23], for higher μ_B value, the phase transition is found to be *1*st *order* (shown by solid line in Fig. 1.4), which ends in the critical point. For small μ_B and $m_s >> m_u$, m_d, [24] the transition is of the crossover type. For vanishing μ_B, the transition temperature is ~ 170 MeV. From lattice QCD calculations it has been confirmed that the chiral transition and deconfinement occurs at same critical temperature.

1.3.4 Bag model

Apart from perturbative and non-perturbative QCD calculations, the thermodynamical parameters for the confined state can be estimated by phenomenological models. *MIT Bag Model* [25] is the most popular of all models as it contains the characteristics of the phenomenology of the quark confinement and can be used for understanding the circumstances beyond the phase transition.

This model assumes that, the quarks are massless particles and are confined inside a *bag* of finite dimension, but are infinitely massive outside the bag. A parameter B is introduced, known as 'bag-pressure', which takes into account the non-perturbative QCD effects. The 'bag-pressure' is the difference of the energy density in the vacuum and that of inside the bag. This pressure works inwards to balance the outward kinetic pressure of the quarks and gluons inside the bag.

One can estimate the energy of the bag consisting of N quarks in a bag of radius R. The energy density shows an inverse relation with the bag radius R. Phenomenologically one can have the energy E in terms of bag-radius and bag-pressure as;

$$E = \frac{2.04N}{R} + \frac{4\pi}{3}R^3 B \tag{1.3}$$

In equilibrium condition, $dE/dR = 0$, which gives the bag-pressure;

$$B = \left(\frac{2.04N}{4\pi}\right)^{1/4} \frac{1}{R} \tag{1.4}$$

For $R = 0.8$ fm and $N = 3$, $B = 206$ MeV.

Now considering the system of quark and gluons as a non-interacting mass-less particles, from standard statistical physics, the pressure for quarks and gluons can be given as (Appendix A.2);

$$P = g\frac{\pi^2}{90}T^4 \tag{1.5}$$

where, $P = P_q + P_g$, i.e. the total pressure due to both quarks-antiquarks and gluons. The factor g, is known as the degeneracy factor which consists of the factors both for gluons and quarks-antiquarks, $g = g_g + \frac{7}{8} \times (g_q + g_{\bar{q}})$. Considering the spin, flavor and color degrees of freedom,

$g_q = N_{color} \times N_{flavor} \times N_{spin}$, $g_g = N_{gluons} \times N_{spin}$.

N_{color} is $= 3$, N_{flavor} can be 2 or 3, $N_{spin} = 2$ and $N_{gluons} = 8$. This gives, for $N_f = 2$,

$$P = 37\frac{\pi^2}{90}T^4 \tag{1.6}$$

The energy density is given by,

$$\epsilon = 37\frac{\pi^2}{30}T^4 \tag{1.7}$$

At a certain temperature (critical temperature T_C), the inward and outward pressure of bag will be equal and beyond which, the quarks and gluons will be no longer confined inside bag. This T_C can be estimated by equating the expression for the P and B. This leads to,

$$T_C = \left(\frac{90}{37}\right)^{1/4} B^{1/4} \tag{1.8}$$

For $B = 206$ MeV, $T_C = 144$ MeV.

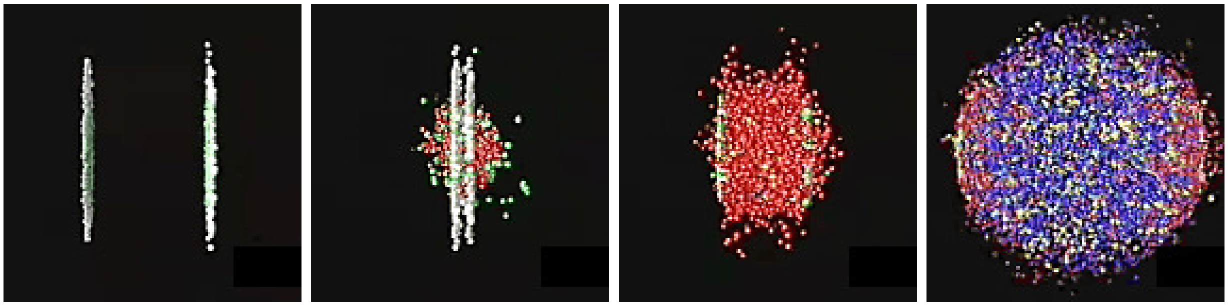

Figure 1.5: This sketch depicts the stages of high energy heavy-ion collisions. The nuclei approach each other with almost the speed of light c. The lorentz contracted nuclei collide and form QGP, which expands, hadronizes, rescatters and finally freezes-out.

1.4 Relativistic heavy ion collisions

It is believed that the QGP phase existed for a few micro-seconds ($\sim 10\ \mu$s) after the Big-Bang occurred. The initial stages of Big-Bang are not well understood till now. Some models are there which try to explain the phenomena during the early time. Relativistic heavy ion collisions (RHIC) or Ultra-Relativistic heavy ion collisions (URHIC) are the means to recreate the Big-Bang scenario in laboratory. RHIC also allow to study the phase-space evolution of the system created.

In relativistic heavy ion collisions (Fig. 1.5), two nuclei travel with 99.95% of speed of light (and hence appear as Lorentz contracted discs) and collide with each other. Upon collisions large amount of energy is deposited in a small region of space, resulting in high energy density. Depending on the amount of energy-density created in collisions, deconfined state of quarks and gluons may be produced or medium of hot/dense hadronic gas will be formed. The medium starts expanding and temperature drops down leading to hadronization and finally kinetic freeze-out of particles. The space-time evolution of such a system is shown in Fig 1.6.

The evolution is described in terms of the proper time τ and it consists of different phases :

1. Pre-equilibrium stage ($\tau = 0 \rightarrow \tau_0$) : This is the initial stage, where the nuclei collide

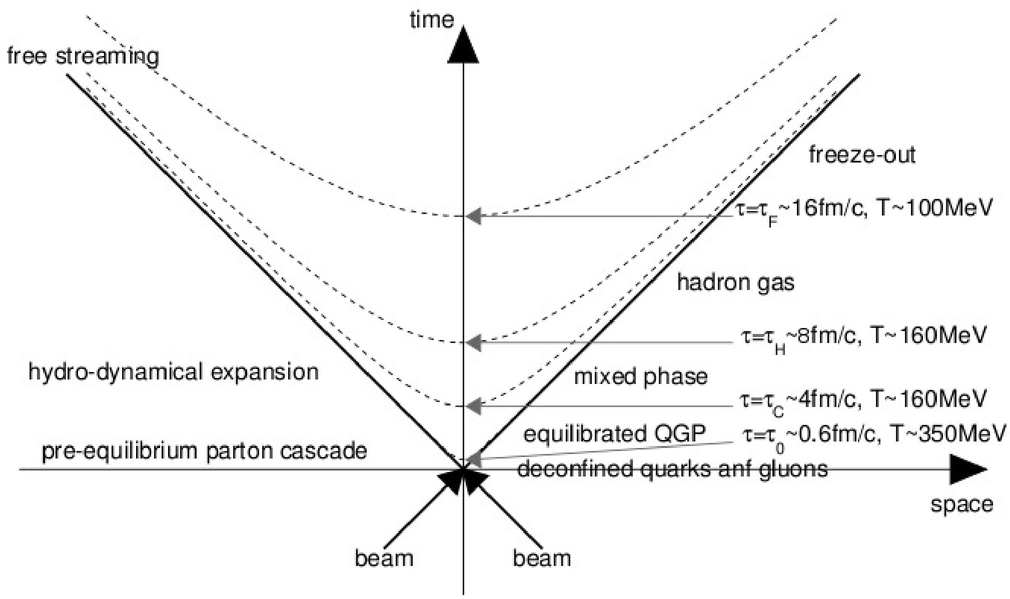

Figure 1.6: Space time evolution of heavy-ion collisions [26].

each other and the energy density at the colliding region becomes very high, which leads to particle production. The produced particles interact with each other and a local equilibrium sets in the medium.

2. Deconfined stage ($\tau = \tau_0 \rightarrow \tau_C$) : If the energy density is high enough ($\epsilon \geq 1$ GeV/fm^3), QGP phase can be formed.

3. Mixed stage ($\tau = \tau_C \rightarrow \tau_H$) : The dense/hot medium starts expanding due to the difference in pressure created in the collision zone. When the temperature of the medium goes below the transition temperature ($T_C \sim$ 160-170 MeV), hadronization starts. The mixed phase of hadrons and partons will exist if 1$^{\text{st}}$ order phase transition occurs.

4. Hadron gas ($\tau = \tau_H \rightarrow \tau_F$) : After τ_H, the hadronization process ceases. This is known as *Chemical Freeze-out* ($T_{chem} \sim$ 100 MeV), as the particle composition of the medium gets fixed. From τ_H to τ_F, the hadrons keep interacting with each other till the *Kinetic Freeze-out*. After this, the momentum distributions of the particles do not

change. Experimentally, one can have an estimate of the temperature corresponding to the *Chemical Freeze-out* and *Kinetic Freeze-out* from the ratio of the particles and spectra of the particles, respectively.

The system formed in URHIC has a very short lifetime ($\sim$ 5 - 10 fm/c). During this small time-span, numerous physical phenomena take place which make this medium interesting. The particles detected in the detectors are 'traced back' to study the properties of the hot/dense medium.

Estimation of initial energy density:

In order to infer the hot/dense medium as QGP or hot/dense matter in the heavy ion collisions, the estimation of the initial energy density is very crucial measurement in high energy heavy ion experiments. From experimental quantities, one can estimate the initial energy density using Bjorken's prescription [1]. This prescription gives the energy density (ϵ_0) as :

$$\epsilon_0 = \frac{1}{A_T}\frac{dE_T}{dz} \tag{1.9}$$

$$\epsilon_0 = \frac{1}{\tau_0\, A_T}\frac{dE_T}{dy} \tag{1.10}$$

Here, one considers that the nuclei are traveling along the Z axis, and collide at origin of the assumed co-ordinate system (space) at time $t = 0$. The equilibration volume is $A_T\, dz$, where A_T is the overlapping transverse area around mid-rapidity (i.e $y \sim 0$) region, dz is the longitudinal slice of the medium. One can use the relation $dz = \tau_0\, dy$, where τ_0 is the proper time for formation of QGP and is normally taken as 1 fm/c in Ref. [1]. The numerator dE_T is the total transverse energy, defined as $dE_T = \langle m_T\rangle\, dN$, where m_T is the mean transverse mass, $\langle m_T\rangle = \sqrt{\langle p_T\rangle^2 + m^2}$, m is the particle mass. In terms of particles per unit rapidity

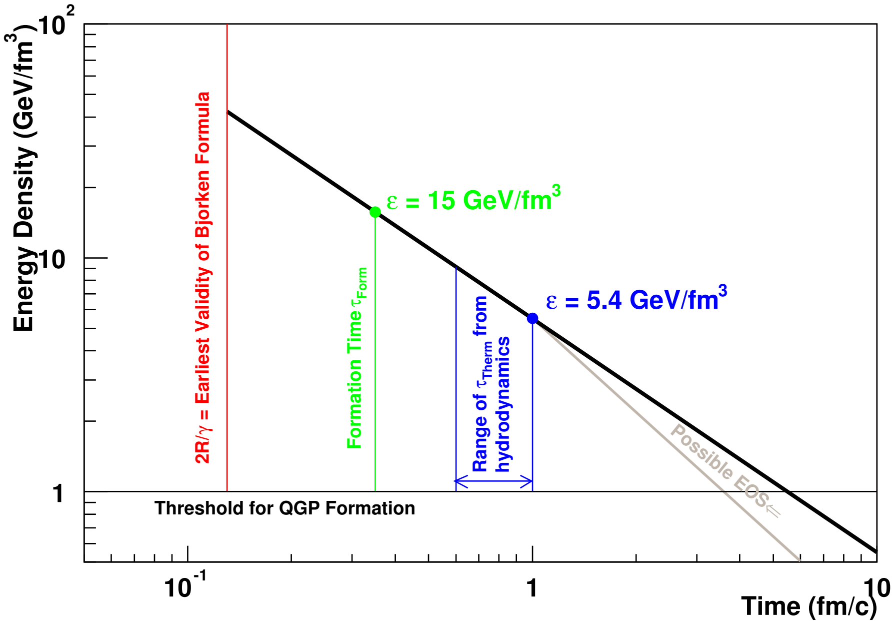

Figure 1.7: ϵ_0 as a function of proper time τ obtained with various assumptions [30].

(dN/dy) , the above expression takes the form

$$\epsilon_0 = m_T \frac{1}{\tau_0\, A_T} \frac{dN}{dy}\Big|_{y=0} \tag{1.11}$$

Usually, dE_T/dy is obtained experimentally, A_T is calculated from nuclear geometry (πR^2).

Using Bjorken's prescription, the energy density measured [28, 29] experimentally by PHENIX experiment (See Chapter 2) for different collision energies, comes out around 4.5 - 5.5 GeV/fm^3 in Au+Au collisions for $\tau_0 = 1$ fm/c. The ϵ_0 obtained from experiment is well above the critical energy density ($\sim$ 1 GeV/fm^3 [2, 27]). The confirmation of the QGP formation cannot be inferred only from the initial energy density measurement. To have a robust conclusion, several other physical observables are required to be studied prior to confirming the formation of QGP.

Other than the experimentally measured value of dE_T/dy, the value of τ_0 will also effect the value of ϵ_0. In an earlier Ref. [1], τ_0 was taken as 1 fm/c. One can have a logical estimation for this. One can refer to the Ref. [30] for some simple approaches. The proper time τ_0 can be estimated as the crossing time τ_{cross}, which the two nuclei take to cross each other. Crossing time can be given as, $\tau_{cross} = 2R/\gamma$, where, R is the radius of the pancakes and γ is the Lorentz factor (See Appendix A.1). This approach leads to a very small time duration (0.13 fm/c [30] at RHIC with $R = 7$ fm for Au) in QCD scale. However, a more realistic τ_0 can be obtained using Heisenberg uncertainty principle : We have, $\Delta E\ \Delta t \geq 1 \implies \langle m_T \rangle\ \tau_{form} \geq 1$, where τ_{form} is the time needed for the production of particles. This assumption yields a formation time of $\tau_{form} = 0.35$ fm/c [30] for $\langle m_T \rangle \approx 0.57$ GeV, which further gives $\epsilon_0 = 15$ GeV/fm^3 [30] for 0 - 5% central Au+Au collisions at RHIC. One can also estimate this τ_0 from the thermalization time, which comes around 0.6 - 1 fm/c, resulting in $\epsilon_0 = 5.4$ - 9.0 GeV/fm^3 [30]. Figure 1.7 shows the different energy density estimates using different τ_0 values discussed.

1.5 Experimental observables

The formation of QGP is studied through different observables. Some of them give the properties of bulk whereas the others help to study the medium modification due to the interaction among the partons in the dense matter. Among the various observables/probes, few of them, which are relevant to this thesis work, are discussed in detail.

1.5.1 $dN_{ch}/d\eta$ measurements

In heavy-ion collisions, $dN_{ch}/d\eta$ per participant pair measurement is of primary importance as this quantity helps to estimate the initial energy density. Also, the dependence of $dN_{ch}/d\eta$ per participant pair with centrality or center of mass energy, reveals the interplay of hard and soft processes. The left plot of Fig. 1.8, shows the dependence of $dN_{ch}/d\eta$ per participant pair measurement on center of mass energy both for $p+p$ and heavy-ion collision systems. It is observed that the energy dependence is steeper for the heavy-ion

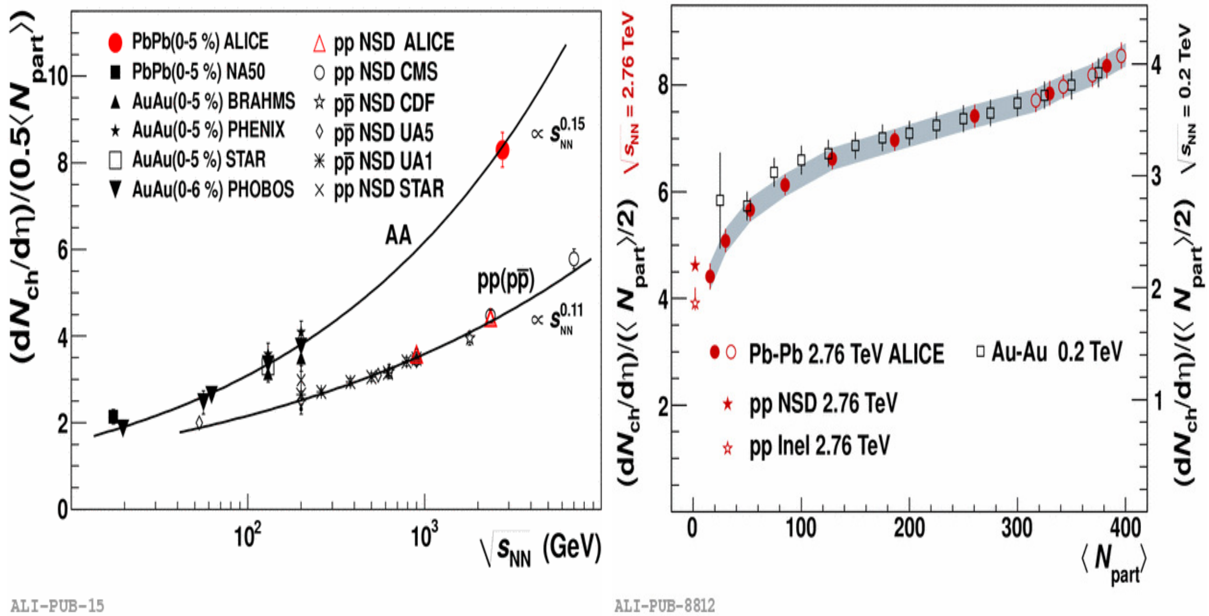

Figure 1.8: $(dN_{ch}/d\eta)/(0.5\langle N_{part}\rangle)$ as a function of center of mass energy (left panel) [31] both for $p+p$ and heavy ion collisions and as a function of number of participants (right panel) [32] in central heavy ion collisions at RHIC and LHC energies.

collisions than for pp, $p\bar{p}$ collisions. Instead of the logarithmic dependence of $dN_{ch}/d\eta$ per participant pair with $\sqrt{s_{NN}}$ as seen upto RHIC, a power law dependence is seen. The two unscalable different curves are needed to describe the data for heavy-ion and $p+p$ which points to the fact that, the heavy-ion collisions can not be recognized as superposition of several $p+p$ collisions.

The dependence of $dN_{ch}/d\eta$ per participant pair with centrality is shown in the right panel of Fig. 1.8. It shows the results from both RHIC and LHC energies. The $dN_{ch}/d\eta$ per participant pair for LHC is higher by a factor of 2.1 than that of at RHIC. Apart from the most central and the most peripheral collisions, the variable in Y-axis has a weak dependence on $\langle N_{part}\rangle$. For Pb+Pb data, the uncorrelated uncertainties are shown by error bars, whereas, correlated uncertainties are shown by the grey band.

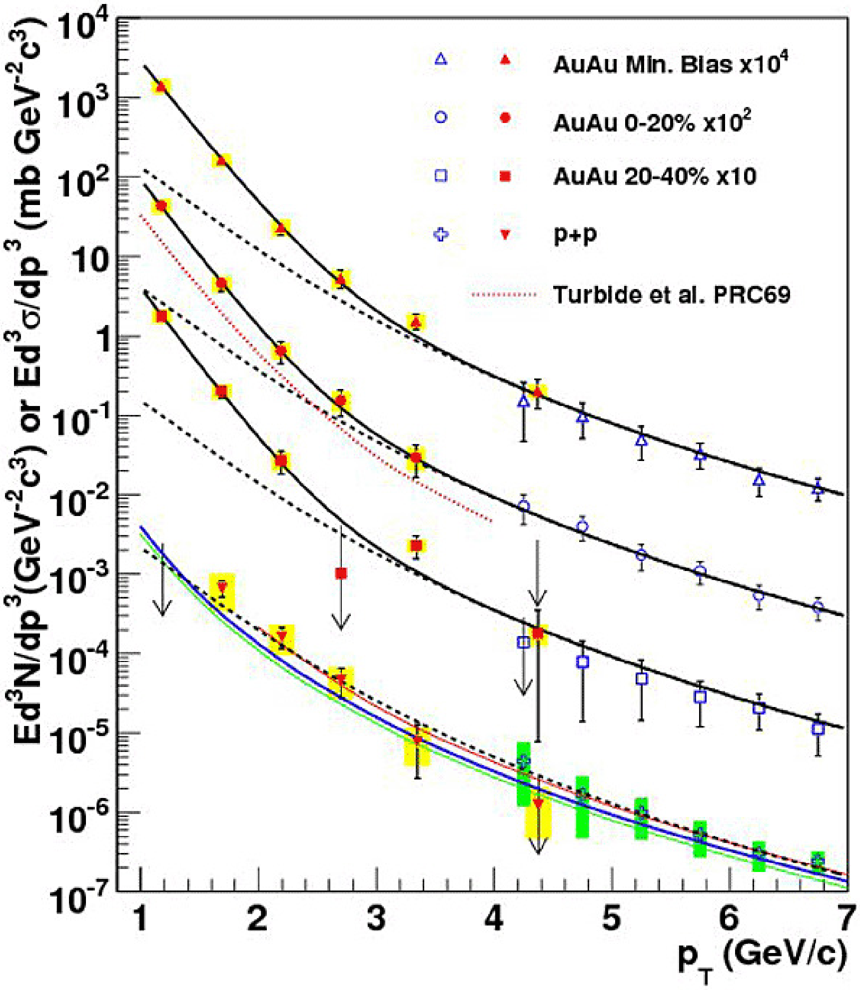

Figure 1.9: The invariant cross-section ($p + p$) and invariant yield (Au+Au) p_T spectra for photons at center of mass energy 200 GeV. measured by PHENIX [33]. The three curves on $p + p$ data represent NLO calculations (See Ref. [33] for details), the dashed curves show a modified power-law fit to the $p + p$ data, scaled by T_{AA}. The solid black curves are the exponential plus the T_{AA} scaled $p + p$ fit. The red dotted curve near the 0-20% centrality data is a theory calculation.

1.5.2 Photon spectra and temperature

Temperature is one of the most important observables in high energy collisions, as it gives an insight of the initial energy density of the system. For the measurement of the medium temperature, one relies on direct photons, because they do not interact with the colored medium and come out as soon as they are created. The recent direct photon measurement [33] by PHENIX in $p+p$ and Au+Au at $\sqrt{s_{NN}} = 200\,\text{GeV}$ is shown in Fig. 1.9. Usually, the spectra are described by an exponential function: $Ae^{-B\,x/T}$. The inverse slope parameter (T) in the function is physically interpreted as temperature. In this case, for central collisions, the inverse slope parameter $T = 221 \pm 19^{stat} \pm 19^{sys}$ MeV for the central (0-20%) collisions. Recently similar study was done by ALICE experiment in Pb+Pb collisions, which gives $T = 305 \pm 51^{stat+\text{sys}}$ MeV [34] for the most central collisions. The slope of the spectra at LHC energy is higher due to the availability of higher collisional energy at LHC than that at RHIC.

1.5.3 Hadron spectra

In relativistic high energy nuclear collisions, hadrons are abundantly produced and are the final product which reach the detector. Hence, the invariant yield p_T spectra of particles are the most common measurement done in the high energy experiment. Thermally originated particles constitute the low p_T region of the particle spectra. The high p_T region of the particle spectrum is governed by the particles coming from hard-scatterings. The slope of particle spectra gives an estimate of the kinetic freeze-out temperature of that particle. Also the total yields obtained from spectra help to find out the particle ratios which inturn are used to estimate chemical freeze-out temperature of the system formed. The spectral shape are different for different particles. Due to the presence of medium effects, the spectral shape of particles in heavy-ion collisions are significantly different than that of in $p+p$ collisions. Figure 1.10 shows the spectra for $\pi^{\pm}$, $K^{\pm}$, p and $\bar{p}$ in d+Au and Au+Au collisions for the

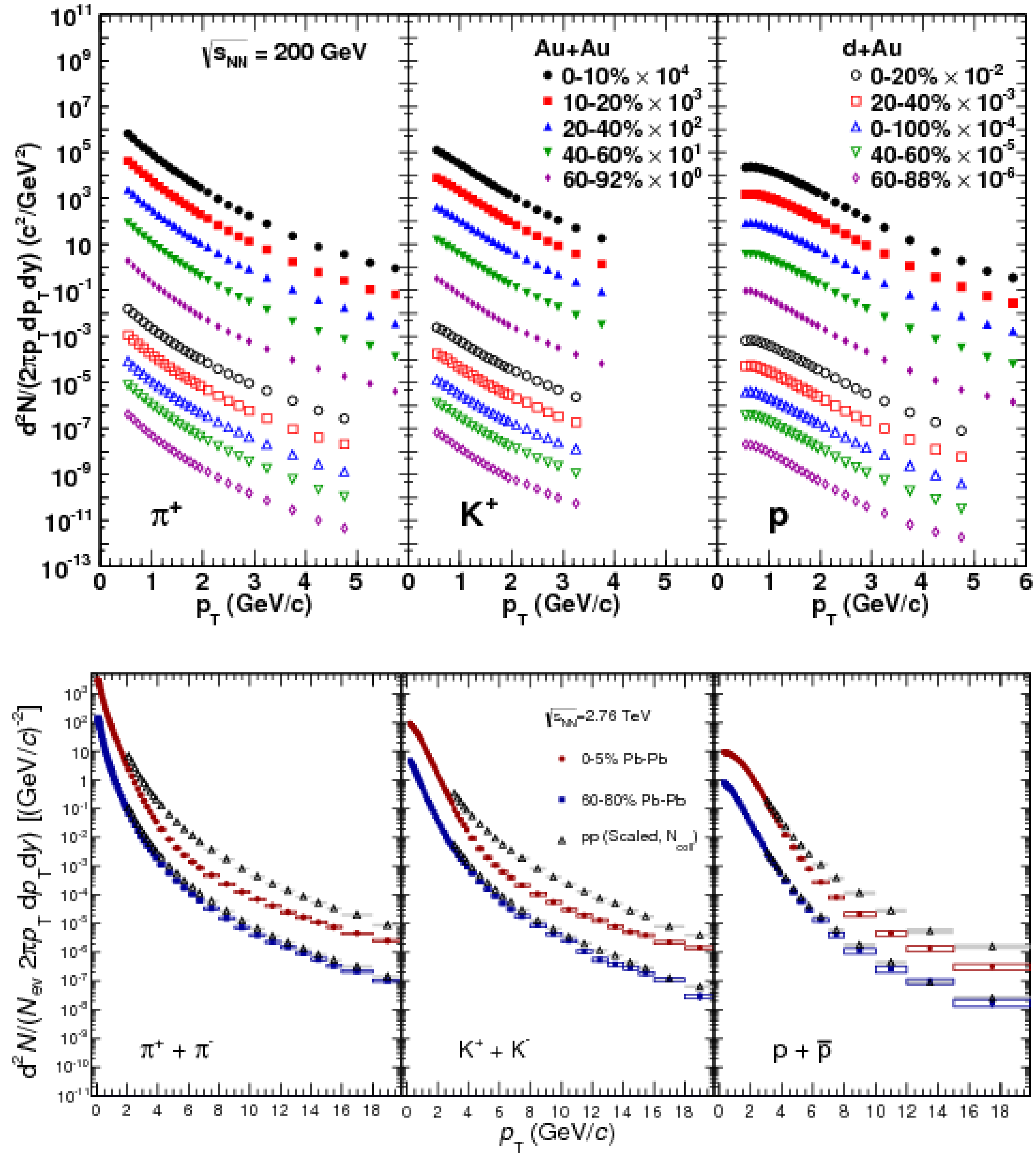

Figure 1.10: Top panel : The invariant yield p_T spectra for π^+, K^+ and p [35] as a function of p_T in Au+Au and d+Au collisions at $\sqrt{s_{NN}} = 200\,\text{GeV}$ for different centralities. The p_T spectra corresponding to different centralities are scaled up for visual clarity. Bottom panel : The invariant yield p_T spectra for charged pions, kaons and protons [36] as a function of p_T in Pb+Pb collisions for 0-5%, 60-80% centralities. The $p + p$ yield scaled by proper N_{coll} is also shown.

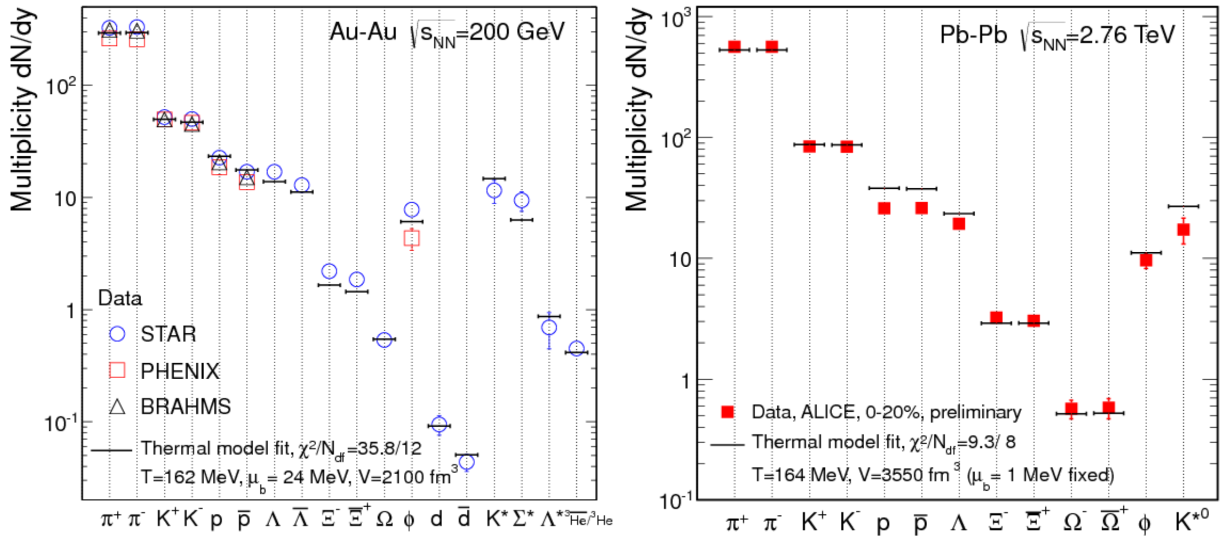

Figure 1.11: Left Panel : Comparison of the thermal model results with RHIC data. Right Panel : Comparison of the thermal model results with central LHC data [37].

top RHIC energy (top panel) for different centralities. The bottom panel shows the spectra for the same particles at center of mass energy 2.76 TeV for the most central and the most peripheral Pb+Pb collisions along with the $p+p$ data scaled by the number of binary collisions. One can easily notice the differences in the spectral shape among the particle species and also among the collision systems. Phenomenological functions (e.g. Tsallis, Hadron Resonance Gas Model, Blastwave, Tsallis Blastwave etc.) are used to describe the spectra and also used to estimate the kinetic freeze-out temperature for different particles, $\sqrt{s_{NN}}$ etc. Some of these phenomenological functions are described in Chapter 5 and Chapter 6.

1.5.4 Particle yields and equilibration

The integrated yields of particles and their ratio help to extract the chemical freeze-out temperature (See Section 1.4). Statistical model [38] describes the hadron ratios very well. This model assumes the statistical evolution of the hot matter to freeze-out. Hence, the hadron yields can be expressed by Bose and Fermi Statistics as,

$$n_i = \frac{N_i}{V} = \frac{g_i}{2\,\pi^2} \int_0^\infty \frac{p^2\,dp}{\exp[(\mathrm{E_i} - \mu_\mathrm{i})/\mathrm{T}]\,\pm\,1} \tag{1.12}$$

where, n_i is the particle number density, E_i is the particle energy, T is the system temperature, g_i is the degeneracy factor and μ_i is the chemical potential of the particle concerned. Mostly $\mu_i = \mu_B$, where μ_B is the baryon chemical potential. Hence, one is left with only two parameters, T and μ_B, which can be obtained from hadron ratios. Hadron yield study (Fig. 1.11) by Andronic *et. al* shows [37] that, the chemical freeze-out temperature at RHIC and LHC are very similar and $\sim$ 160 MeV. The baryon chemical potential has a non-zero ($\sim$ 20 MeV) value at RHIC energy and it reduces to $\sim$ 0 at LHC energy. It should be noted that at LHC p and $\bar{p}$ yield does not follow the thermal model and is a matter of investigation.

1.5.5 Strangeness enhancement

Enhancement in strangeness production was proposed as one of the possible signatures of the QGP formation [40]. This can be understood by comparing the energy threshold (E_{thres}) required to produce a $s\,\bar{s}$ pair in hadronic interactions and colored interactions. In hadronic interaction, $E_{thres} \sim$ 540 MeV, whereas, in QGP, due to the chirality restoration $E_{thres} \sim 2$ $m_s \sim$ 300 MeV. Apart from the lowering of the strange quark mass (m_s) inside QGP, the availability of bigger system size (phase space) in heavy ion collisions and the high density of gluons and quarks leads to the formation of $s\,\bar{s}$ pairs via QCD interactions. Also, the interaction cross-sections in colored interactions are higher than the hadronic interactions, which result in enhancement in strangeness production rates in colored medium.

The rise in strange particle yields has been observed earlier in SPS and RHIC with the increase of system size and now, also has been observed in LHC. The enhancement is studied as the ratio of the yields of strange hadrons per number of participants ($\langle N_{\mathrm{part}} \rangle$)

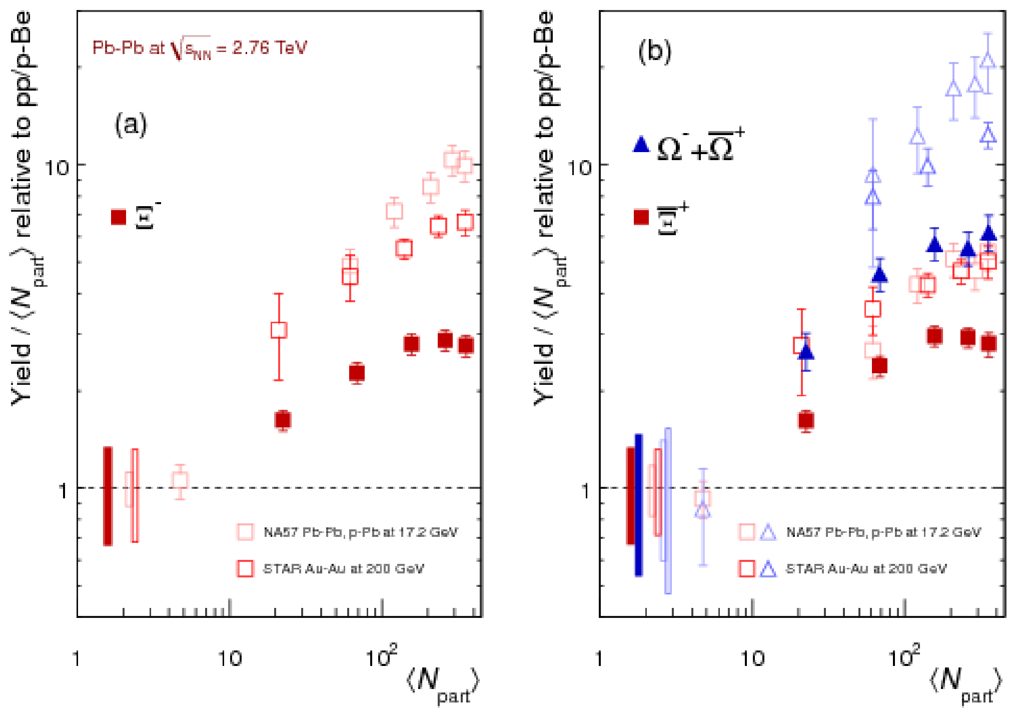

Figure 1.12: Strangeness enhancement measured by ALICE collaboration [39] ($|y| < 0.5$) as a function of number of participants ($\langle N_{part} \rangle$). The closed symbols are for the ALICE data and the open symbols are the results from RHIC and SPS energies. The error bars on the data represent the measurement uncertainties. The systematic and statistical uncertainties on the $p + p$ and p+Be reference are shown by the boxes at Y = 1.

(See Section 2.2.5) in nucleus-nucleus collisions to that in the $p+p$ or p+A collisions as a function of $\langle N_{\text{part}}\rangle$. In Fig. 1.12, the measurements from ALICE Collaboration [39] shows the enhancement of multi-strange baryons ($\Xi^{\pm}$ and $\Omega^{\pm}$). The plot also shows the comparison among the SPS, RHIC and LHC energy data. It is seen that as a function of $\langle N_{\text{part}}\rangle$, strangeness is enhanced and then saturates. However, the enhancement is more for the lower energy data. It should be noted that with the increase in collisional energy the strange hadron yield increases both in $p+p$ and heavy-ion collisions, resulting in a less pronounced enhancement of relative yield than at lower energies.

1.5.6 Nuclear modification factor

To verify the existence of the hot and dense color medium in nucleus-nucleus collisions *Nuclear modification factor* is one of the most handy observable widely used. If a highly dense hot medium is produced in nucleus-nucleus collisions, the partons travelling inside it will loose sufficient energy [41, 42] resulting in the modification of fragmentation functions [43] and softening of the measured p_T spectra. The softening of spectrum is quantified by the *Nuclear modification factor*, which is defined as the ratio,

$$R_{AB} = \frac{d^2N_{AB}/(2\pi\, p_T\, dy\, dp_T)}{N_{coll}\ \times\ d^2N_{pp}/(2\pi\, p_T\, dy\, dp_T)} \tag{1.13}$$

where, $d^2N_{AB}/(2\pi\, p_T\, dy\, dp_t)$ is the yield of particle in A+B (nucleus-nucleus) collisions for a particular centrality class, $d^2N_{pp}/(2\pi\, p_T\, dy\, dp_t)$ is the yield of particle in $p+p$ collisions at the same collisional energy. N_{coll} is known as the number of binary collisions (See Section 2.2.5) for the same centrality class. The yield in $p+p$ collisions is used as a baseline measurement.

R_{AB} can have three possible values,

- $R_{AB} = 1$: Particle yields in A+B collisions scale with the number of binary collisions, which further implies that nucleus is simply an incoherent superposition of nucleons,

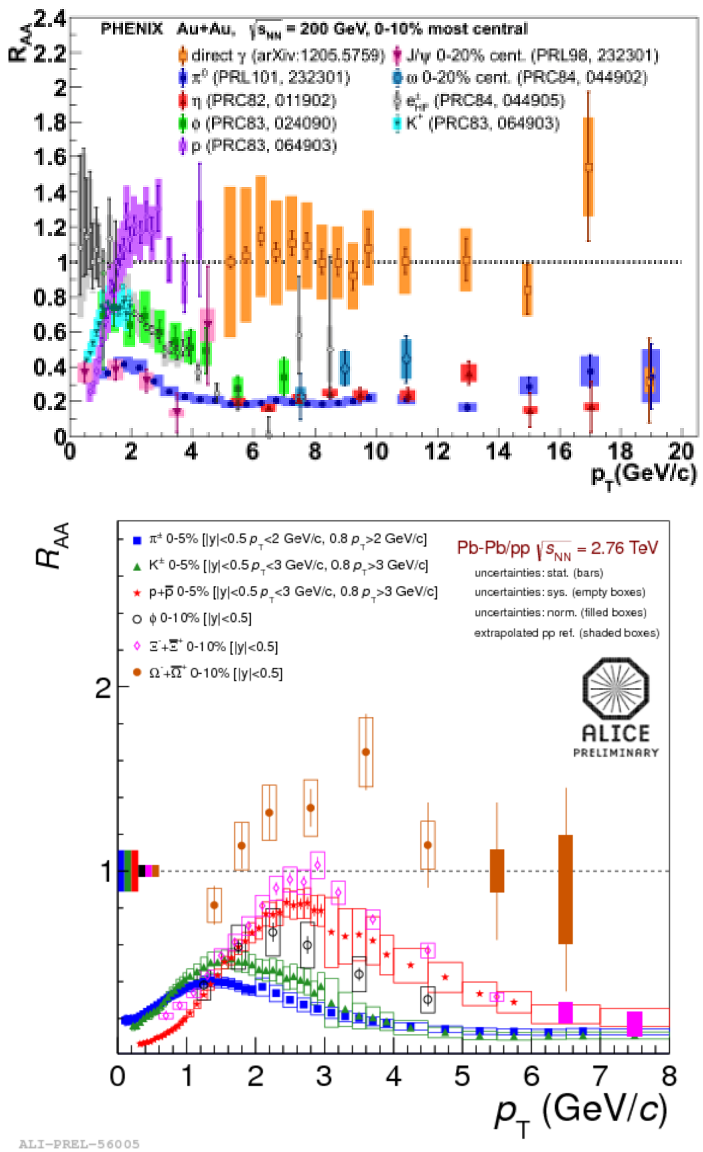

Figure 1.13: Top Panel : R_{AA} [46] as a function of p_T for π^0, η, ω, direct γ, p, $K^{\pm}$, ϕ, J/ψ and single electrons from heavy flavor for most central Au+Au collisions at $\sqrt{s_{NN}} = 200\,\mathrm{GeV}$. Bottom Panel : Recent LHC measurement [47] of R_{AA} as a function of p_T for $\pi^{\pm}$, $K^{\pm}$, p+$\bar{p}$, ϕ, $\Xi^+ + \Xi^-$, Ω^++Ω^- for the most central Pb+Pb collisions at $\sqrt{s_{NN}} = 2.76$ TeV.

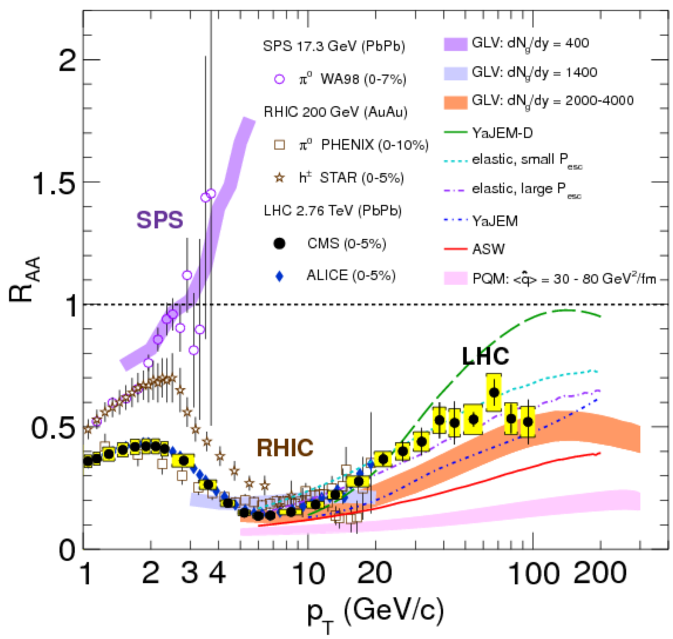

Figure 1.14: This compilation [48] shows the R_{AA} for neutral pions, charged hadrons for the most central collisions at different collisions (SPS, RHIC and LHC.) The theoretical comparisons are also shown. The error bars on the data points are the statistical errors. The yellow band on the black circles are the systematic errors for CMS measurement. The different colored bands corresponds to the systematic uncertainties of different theoretical approaches.

hence no medium effects are observed. It should be noted that this N_{coll} scaling is valid for high p_T region. In case of low p_T region one expects this scaling to be true with respect to N_{part}.

- $R_{AB} < 1$: At high p_T this is the manifestation of parton energy loss due to the medium. In case of low p_T, this result can point to various effects, e.g. shadowing [44], rescattering of particles etc.

- $R_{AB} > 1$: Usually this enhancement behavior is seen at the intermediate p_T ($2 < p_T$ GeV/$c < 5$) and corresponds to the Cronin effect [45] (For details see Section 1.5.7).

One can also try to investigate the modifications in the central collisions in compare to the peripheral collisions. This is quantified by R_{CP} which is the ratio of yields in central to peripheral collisions, scaled by the corresponding numbers of binary nucleon-nucleon collisions,

$$R_{CP} = \frac{d^2 N_{AB}^{central}/(2\pi\, p_T\, dy\, dp_T)}{d^2 N_{AB}^{peripheral}/(2\pi\, p_T\, dy\, dp_T)} \, \frac{N_{coll}^{peripheral}}{N_{coll}^{central}} \tag{1.14}$$

This measurement does not require the knowledge of $p+p$ measurement. The values of R_{CP} can be equal to, greater than or lesser than 1. The physical significances of these values hold same as discussed for R_{AB}.

The nuclear modification factor as a function of p_T is shown in Fig. 1.13, for both RHIC [46] (top panel) and LHC energies [47] (bottom panel). In the upper plot it is seen that, direct photons, being an electromagnetic probe, do not interact with color medium and hence do not loose energy, resulting in $R_{AA} = 1$ within uncertainties. At high p_T, the light mesons (π^0, η and ω) are the most suppressed species with $R_{\text{AA}} \sim 0.2$. The protons do not show any kind of suppression in the intermediate p_T range (2–5 GeV/c) at RHIC energy. The particles with strange quark content (ϕ and charged kaon) are suppressed more than protons but less than light mesons in the intermediate p_T. The bottom panel of

Fig. 1.13 shows that the suppression for light quark mesons are more at LHC than that of at RHIC energy. The results from LHC also include the multi-strange baryons which seem to follow mass hierarchy. The trend for strange mesons are similar to what is observed at RHIC energy. The R_{AA} measurements in broader p_T range ($\approx$ 100 GeV/c) at LHC energies gives the opportunity to do a comprehensive study of the medium effects up to high p_T. Figure 1.14 shows the result from CMS experiment [48] for the central Pb+Pb collisions. In the most central collisions, the suppression reaches to a factor of $\sim$ 7 at $p_T \sim$6–7 GeV/c. At higher p_T, the R_{AB} starts to increase reaching a value of 0.5 at $p_T > 40\,\mathrm{GeV}/c$. In RHIC energy also we find a similar trend of increasing R_{AA} for π^0 (Fig. 1.14), but due to systematic uncertainties, no firm conclusion can be drawn.

1.5.7 Cold nuclear matter effects

The intrinsic nuclear effects present in high energy p+A (d+Au or p+Pb) and A+B (Au+Au or Pb+Pb) collisions are termed collectively as *Cold Nuclear Matter* (CNM) effects. Due to the presence of medium in A+B collisions, it is difficult to extract any information related to the CNM effects. In order to have a good understanding of CNM effects and distinguish these effects from the hot/dense medium effects, control experiment of p+A are performed. In this kind of collision, as the number of participants are much lesser than in A+B collisions, no hot/dense matter is expected to form. The matter formed in p+A collisions is usually termed as 'cold nuclear matter'. This goal is accomplished by the d+Au collisions at RHIC and p+Pb collisions at LHC.

The modifications of parton distribution functions (PDF) inside nucleus were obtained from the Deep Inelastic Scattering (DIS) experiments [49] and are given as,

$$R_i^A(x, Q^2) = \frac{f_i^A(x, Q^2)}{f_i(x, Q^2)} \tag{1.15}$$

Here, x is the Bjorken x, Q^2 is the momentum transfer, $f_i(x, Q^2)$ is the PDF of parton

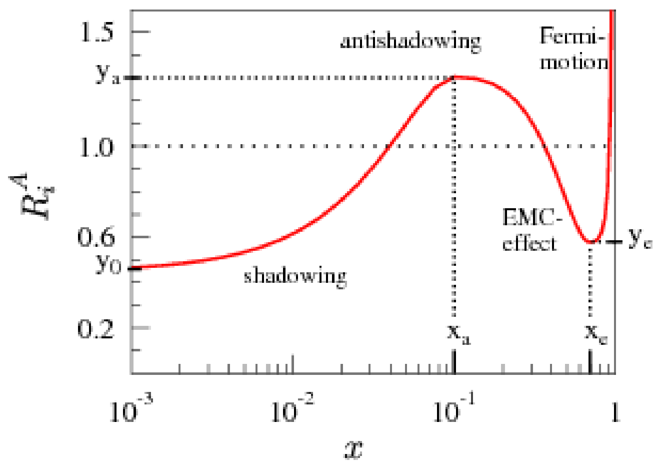

Figure 1.15: Schematic example of the modification of the parton distribution function inside nuclei. The plot is taken from the Ref. [50]

flavor i inside a free proton, $f_i^A(x, Q^2)$ is the PDF of parton flavor i inside a nucleus A. The CNM effects can be understand for different values of R_i^A as a function of x or Cronin enhancement [45], discussed below in detail.

- Depending on the value of $R_i^A(x, Q^2)$ and x (Fig. 1.15) the CNM effects are classified as,
  - Shadowing : For low x region ($x < 0.03$), $R_i^A < 1$. This effect can be understood from the overlapping of the nuclear PDFs. This effect is largest for the gluons, as they populate mostly the low x region. The gluons in low x region fuse into a single, higher x gluon which lead to the depletion of gluons at lower x.
  - Anti-Shadowing : Due to the above mentioned gluon-fusion, the value of $R_i^A(x, Q^2)$ is above 1 for the $0.03 < x < 0.3$ region. The phenomenon of gluon-fusion of low x gluons creates an excess in this region and a deficit in the lower x region.
  - EMC effect : For $0.3 < x < 0.7$ region, $R_i^A < 1$. This effect is named as EMC

effect after the name of the experiment which discovered this phenomenon.

  - Fermi Motion : Above $x > 0.7$, the ratio R_i^A again rises above unity due to Fermi motion of the nucleons.

- Cronin effect : The enhancement in the nuclear modification factor in d+Au collisions at the intermediate p_T is generally termed as *Cronin Effect*. This 'enhancement' was first observed in 1974 by Cronin and his collaborators [45] and hence the name of the phenomenon. This effect arises due to the multiple soft scatterings of the incoming partons while propagating through the target nucleus. Figure 1.16 shows the R_{dAu} for charged pions, kaons and protons along with ϕ. It is observed that for pions, kaons and ϕ mesons, $R_{dAu} = 1$ within uncertainties. The protons show enhancement in the intermediate p_T range. This can be explained by flow and recombination effects.

1.5.8 Jets

Usually, *jet*s are perceived as the collimated stream of hadrons from the end stage of a parton shower. In a simple picture, *jet*s are the fragmenting partons. Jets are the basic QCD objects which sustain as the final state object in hadronic collisions. Hence, *jet*s are one of the important observables in high energy heavy ion collisions and help to understand the medium modifications. Figure 1.17 shows a schematic sketch of the *jet* production in $p + p$ and heavy ion collisions. In heavy ion collisions, the jets get modified and lose energy due to the medium which is manifested by the changes in the jet-yield, jet-shape, jet-fragmentation function etc. One can perform various studies with jets, depending on the physics processes one wants to look into.

At RHIC, due to the smaller jet-production cross-section, the energy of the reconstructed jets can have the maximum value of 30-50 GeV. Hence, most of the jet study at RHIC are performed by particle correlations. Whereas, at LHC, the jets can be fully reconstructed and the jet study are done above 25 GeV. The jets are largely produced at LHC because of

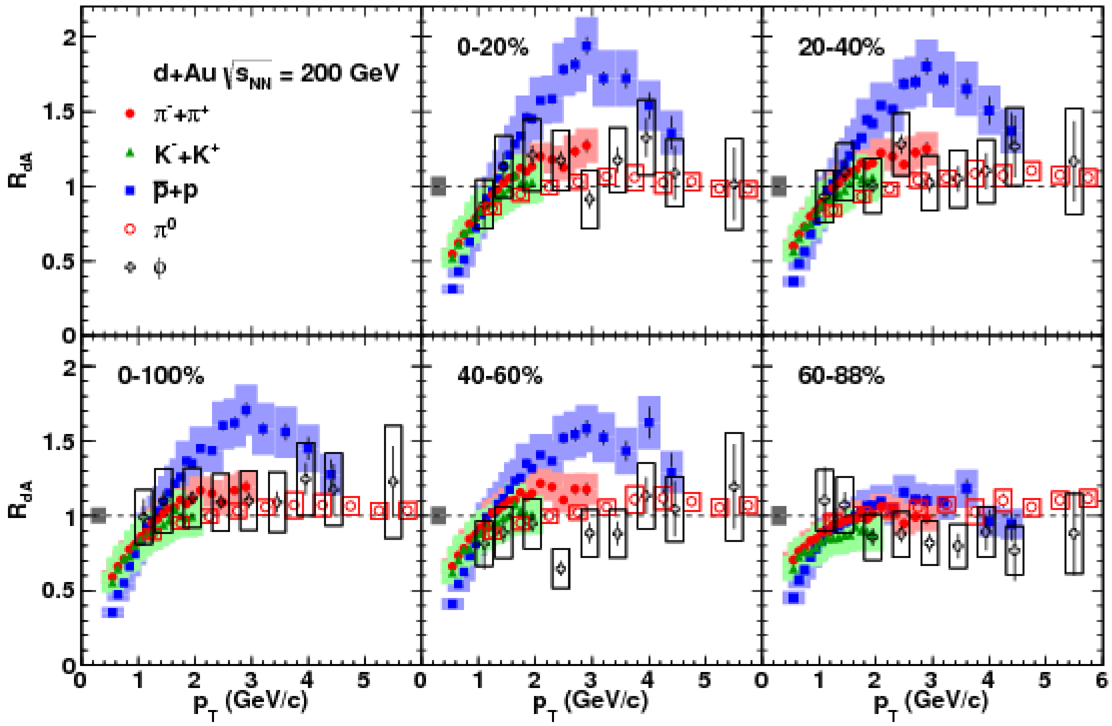

Figure 1.16: The nuclear modification factor for charged pions, kaons, protons, ϕ and π^0 [35] as a function of p_T in d+Au collisions at $\sqrt{s_{NN}} = 200\,\text{GeV}$ for different centralities. The statistical errors are shown with vertical bars and the systematic errors are shown with boxes.

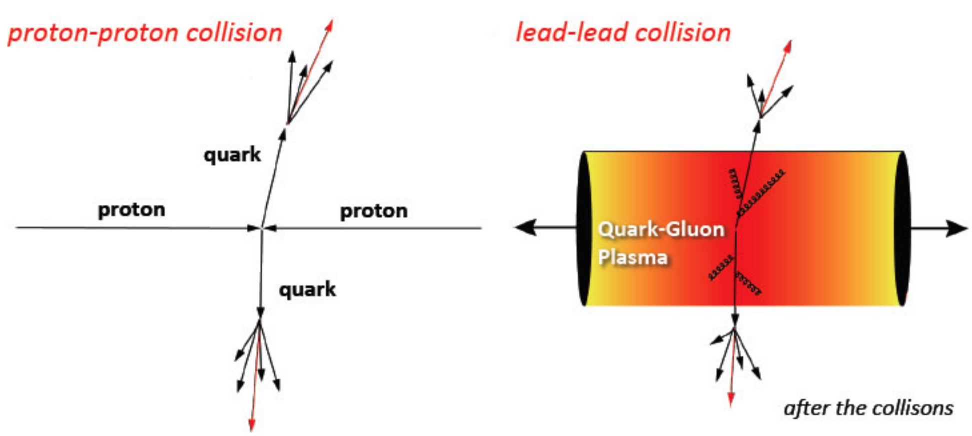

Figure 1.17: A schematic sketch of jet production by hard scattering in $p + p$ collision. Jets are also called as back-to-back oriented sprays of particles. The presence of medium in Pb+Pb collisions results in loss of energy of jets, commonly termed as jet-quenching.

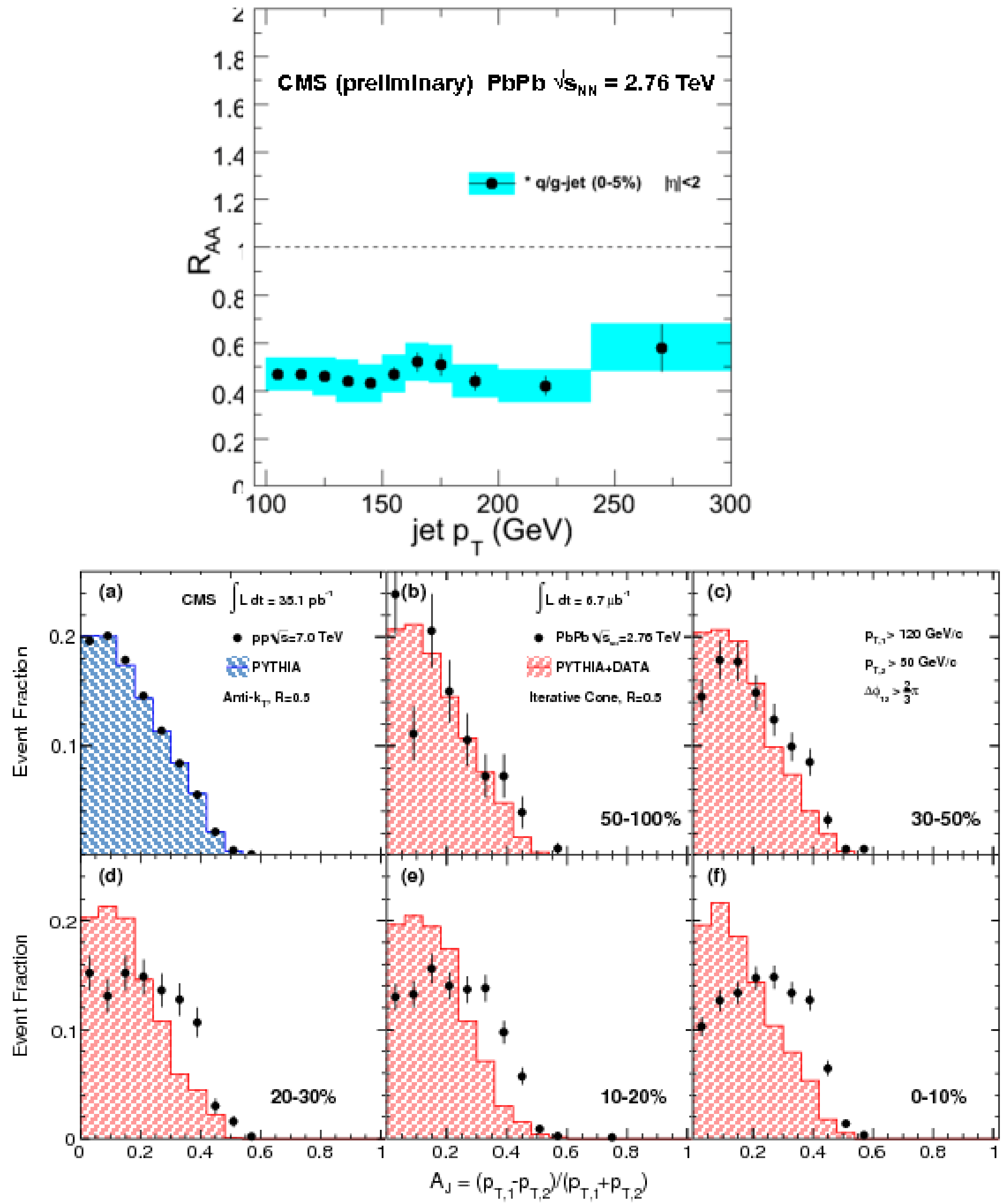

Figure 1.18: Suppression of jets [51] (top panel) and di-jet imbalance [52] (bottom panel) measurements in central Pb+Pb collisions at $\sqrt{s_{NN}} = 2.76$ TeV from CMS experiment.

the larger jet-production cross-section. Jet reconstruction is done by jet algorithm, in which the momenta (energy) of the fragmented particles are summed-up to that of the original parton. In practice, the particles present inside the jet-cone region are summed up. The jet-cone is realized in an indirect way by considering the annular ring of the cone, usually denoted by $R = \sqrt{(\Delta\eta)^2 + (\Delta\phi)^2}$. The value of R is taken as 0.2 for ATLAS and 0.5 for CMS experiment.

Some of the widely studied jet-physics observables are discussed below.

- Jet-R_{AA}: Similar to particle R_{AA}, *jet* R_{AA} are also studied to have a comparison in the jet-yield in $p+p$ and heavy ion collisions. It is found that in heavy-ion collisions the jet yields are suppressed in compare to the $p+p$ yield (Fig. 1.18 (top panel)). Experimentally the level of suppression is found to be around a factor of 2 and surprisingly, for the central collisions, the level of suppression for low p_T jets at RHIC is similar to the jet suppression at high p_T ($>$ 100 GeV) at LHC.

- Di-jets correlation: The *di-jet angular correlations* are studied to understand the effect of the medium on the near side ($\Delta\phi = 0°$) and the away side ($\Delta\phi = 180°$) jets. In heavy ion collisions, both at LHC and RHIC energies, it is observed that, the away side jet yield is suppressed. However, in $p+p$ collisions, no suppression in the away side jet yield has been observed.

- Di-jet energy imbalance : *Di-jet* energy imbalance results due to the incomplete accounting of the particle momentum of jet. This effect arises as the energy of the soft particles (originating from jets) are not taken in to account as they fall out of the jet-cone considered. The energy imbalance is defined by the quantity, $A_j = (E_{T1}$ - $E_{T2})/(E_{T1} + E_{T2})$, where E_{Ti} is the transverse energy of the jet i. The energy imbalance measurement from CMS experiment [52] in Pb+Pb and $p+p$ collisions at center of mass energy 2.76 TeV is shown in the bottom panel of Fig. 1.18. It is seen that for central collisions, the experimental data deviate from the monte carlo results.

1.6 Organization of thesis

This thesis mainly deals with the hadron p_T spectra in both $p + p$ and heavy ion collisions. The major work of this thesis is done for the K^{*0} measurement in Cu+Cu collisions at $\sqrt{s_{NN}} = 200\,\mathrm{GeV}$, with PHENIX data. The later half of this thesis consists of the studies involving hadron spectra analyzed with phenomenological functions in $p + p$ and heavy ion collisions. The experimental set-up - RHIC and PHENIX are discussed in Chapter 2. Chapter 3 gives the details of the K^{*0} measurements. The measured spectra and the nuclear modification factors are presented in Chapter 4. The phenomenological studies are discussed in Chapter 5 and in Chapter 6. Finally the conclusions of this thesis is given in Chapter 7.

Part I - PHENIX data analysis

CHAPTER 2

PHENIX EXPERIMENTAL SETUP

This chapter is devoted to describe the experimental facility RHIC and the PHENIX detector.

2.1 Relativistic heavy ion collider

The Relativistic Heavy Ion Collider (RHIC) [53, 54] is one of the oldest and versatile experimental facility to study the heavy ion collisions. It is situated at the Brookhaven National Laboratory (BNL) in Long Island in United States. It is the first collider facility (circumference of 3.8 kms) which is capable of colliding heavy ions accelerated to $\sqrt{s_{NN}}$ = 200 GeV. RHIC can collide various ion species at various energies. The designed luminosity is $2{\times}10^{26}$ cm^{-2} s^{-2} for Au ions and $2{\times}10^{32}$ cm^{-2} s^{-2} for protons. The collider facility is shown in Fig. 2.1 . RHIC also serves as a polarized proton collider.

In RHIC, the ions are accelerated gradually in few successive steps. Initially, the electrons from the atoms are removed by Tandem Van de Graff, leaving the nuclei only. Nuclei are accelerated to 1 MeV energy by Tandem. Then these are send to Booster by Tandem–to–Booster line where they travel with 5% of speed of light. Booster is a Synchrotron which boosts up the ion energy to 95 MeV/nucleon. Then the ions are send to Alternating Gradient

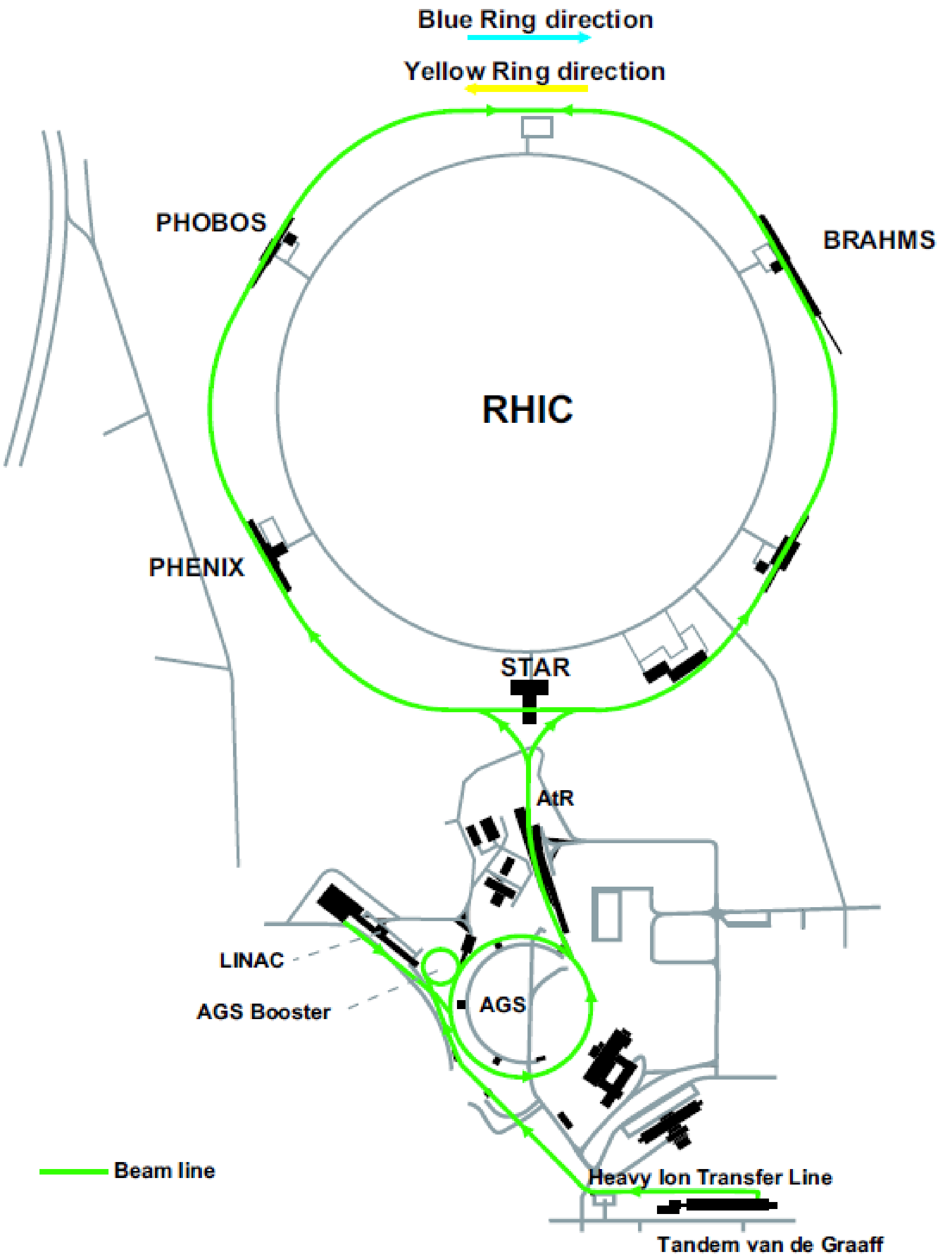

Figure 2.1: RHIC accelerator facility and arrangements of detectors.

Table 2.1: Some RHIC parameters for heavy ions.

Injection energy	9.5 GeV/nucleon
Average Luminosity	8×10^{26} cm^{-2} s^{-1}
Storage energy	100.0 GeV/nucleon
Bunch Intensity	1.0×10^{9} Au ions/bunch
Bunch Crossing Frequency	78 kHz
Number of bunches	56 filled bunches
Interaction diamond length	20 cm
Bunch Length	15 cm

Synchrotron (AGS), where the ions get more energy and they travel with almost light speed. Beams of accelerated nuclei are then send to RHIC by AGS–to–RHIC (ATR) beam transfer line. RHIC consists of two concentric quasi–circular rings of super conducting magnets ($\sim$ 400 dipoles and $\sim$ 500 quadrupoles). One of the ring is known as the Blue ring, accelerates the ions in clockwise direction and the other is known as Yellow ring which accelerates the ions in anticlockwise direction. These rings are continuous except for 6 intersection points, where the ion beams are allowed to collide with each other.

Beam injection is done in box car fashion, one bunch at a time. The AGS cycle is repeated 14 times to establish the 41 bunches for nucleons and 56 bunches for heavy ions. Acceleration and storage of beam bunches at RHIC use two RF systems. One of them operates at 28 MHz, used to capture the AGS bunches and accelerates to top energy. Another RF operates at 197 MHz is used to limit the bunch length growth due to intra–beam scattering due to Coulomb interaction, which scales with Z^4/A^2 (which limits the collision diamond RMS length to 20 cm). Some figure of merits are given in Table 2.1.

At the beginning of RHIC, there were four experiments (Fig 2.1), BRAHMS [55], PHOBOS [56], STAR [57] and PHENIX [58]. Of these BRAHMS and PHOBOS were smaller experiments and were decommissioned in 2005 and 2006 respectively after their physics goals were achieved. At present STAR and PHENIX are the two important experiments going on.

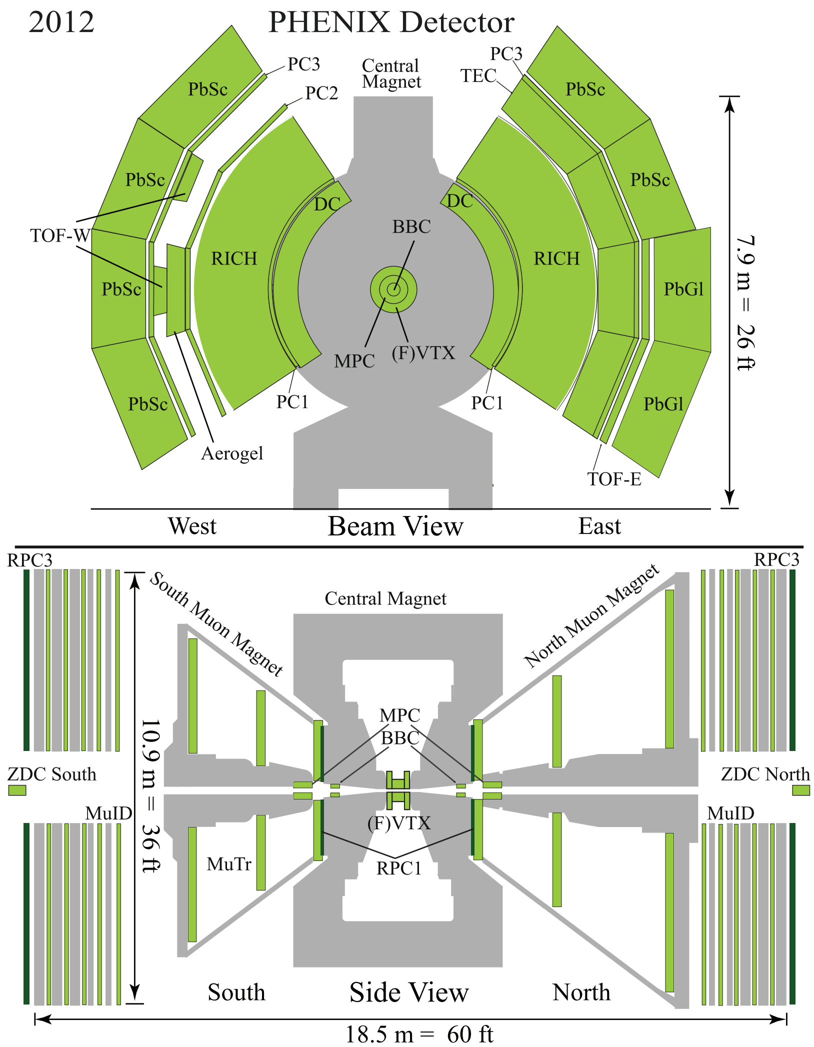

Figure 2.2: Configuration of the PHENIX detector in Run12.

The collision species, energy, luminosity for various PHENIX runs are listed in Table 2.2.

2.2 PHENIX

The PHENIX [58] (Pioneering High Energy Nuclear Interaction eXperiment), is one of the major experiments in RHIC. The detector subsystems are designed to measure different QGP probes. Different subsystems are specialized to measure particular probes like

Table 2.2: RHIC run summary with collision species, collision energy, integrated luminosity and samples events.

Run	Year	Species	$\sqrt{s_{NN}}$ (GeV)	$\int$ L dt	N_{tot}
1	2000	Au+Au	130	1 μb^{-1}	10 M
2	2001/2002	Au+Au	200	24 μb^{-1}	170 M
		p+p	200	0.15 pb^{-1}	3.7 G
3	2002/2003	d+Au	200	2.74 nb^{-1}	5.5 G
		p+p	200	0.35 pb^{-1}	606 G
4	2003/2004	Au+Au	200	241 μb^{-1}	1.5 G
		Au+Au	62.4	9 μb^{-1}	58 M
5	2004/2005	Cu+Cu	200	3 nb^{-1}	8.6 G
		Cu+Cu	62.4	0.19 pb^{-1}	0.4 G
		Cu+Cu	22.5	27 μb^{-1}	9 M
		p+p	200	3.8 pb^{-1}	85 G
6	2006	p+p	200	107 pb^{-1}	230 G
		p+p	62.4	0.1 pb^{-1}	28 G
7	2007	Au+Au	200	0.813 nb^{-1}	5.1 G
8	2008	d+Au	200	80 nb^{-1}	160 G
		p+p	200	5.2 pb^{-1}	115 G
9	2009	p+p	500	14 pb^{-1}	308 G
		p+p	200	16 pb^{-1}	936 G
10	2010	Au+Au	200	1.3 nb^{-1}	8.2 G
		Au+Au	62.4	0.11 nb^{-1}	700 M
		Au+Au	39	40 μb^{-1}	250 M
		Au+Au	7.7	0.26 μb^{-1}	1.6 M
11	2011	p+p	500	89.9 pb^{-1}	
		Au+Au	19.6	15.7 μb^{-1}	
		Au+Au	200	4.97 nb^{-1}	
		Au+Au	27	32.7 pb^{-1}	
12	2012	p+p	200	9.2 pb^{-1}	
		p+p	510	30 pb^{-1}	
		U+U	193	171 μb^{-1}	
		Cu+Au	200	4.96 nb^{-1}	
13	2013	p+p	510	156 pb^{-1}	
14	2014	Au+Au	15	44.2 μb^{-1}	
		Au+Au	200	2.56 nb^{-1}	

hadrons, electrons, muons and photons with good energy and momentum resolution. In a broad way PHENIX consists of Global Detectors, Central Arm Spectrometers and Muon Spectrometers. The work done in this thesis uses only Global Detectors (Section 2.2.1) and Central Arm Spectrometers (Section 2.2.2). Details about the Muon Spectrometer can be found in Ref [59]. PHENIX comprises of two central arm spectrometers (East and West) which detect hadrons, electrons and photons. Each arm covers $|\eta| < 0.35$ and $\phi = 90°$. Two forward spectrometers (North and South) are placed at the forward rapidity for muon detection. These cover $|\eta| = 1.15$–2.44 and $\delta\phi = 2\pi$. Global detectors are situated around the collision point covering 2π in azimuthal direction to characterize collision. The PHENIX detector with subsystems is shown in Fig. 2.2. The details of PHENIX detectors are given in next Section. The purpose of different detectors and their spatial coverage is listed in Table 2.3.

Table 2.3: Summary of PHENIX detector Subsystems.

SubSystem	$\Delta\eta$	$\Delta\phi$	Special Features
Central Magnet (CM)	± 0.35	2π	Upto 1.15 Tm
Muon Magnet South	-1.1–2.2	2π	0.72 Tm for $\eta = 2$
Muon Magnet South	1.1–2.4	2π	0.72 Tm for $\eta = 2$
Beam Beam Counters (BBC)	± 3.1–3.9	2π	Start timing for TOF, collision vertex, Minimum Bias Trigger and Centrality
Zero Degree Calorimeter (ZDC)	3 mrad	2π	Minimum Bias Trigger and Centrality
Drift Chambers (DC)	± 0.35	$2\times\pi/2$	Good Momentum and mass resolution Δm/m = 0.4% at m = 1 GeV
Pad Chambers (PC)	± 0.35	$2\times\pi/2$	Pattern recognition and tracking in non–bend direction
Ring Imaging Čerenkov (RICH)	± 0.35	$2\times\pi/2$	Identifies electron
Time of Flight (TOF)	± 0.35	$2\times\pi/2$	Identifies charged hadrons, resolution<100 ps
Electromagnetic Calorimeter (EMCal)			
EMCal (PbSc)	± 0.35	$\pi/2 + \pi/4$	Identifies electron and photon
EMCal (PbGl)	± 0.35	$\pi/4$	Identifies electron and photon Good $e^{\pm}/\pi^{\pm}$ separation at $p_T > 1$ GeV/c by EM shower and $p < 0.35$ GeV/c by ToF.

The coordinate system used in PHENIX is shown in Fig. 2.3. The co–ordinate system

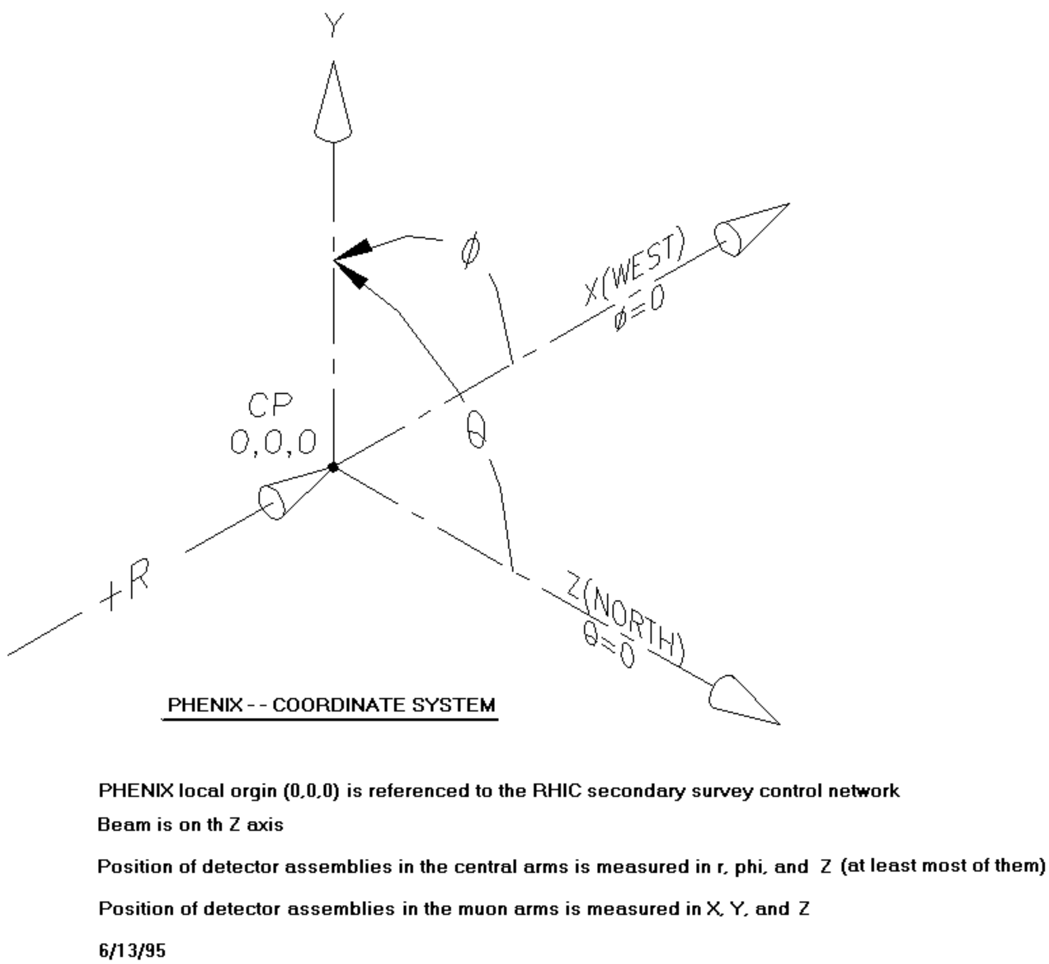

Figure 2.3: PHENIX co–ordinate system.

is defined relative to the beam axis with the origin at the center of interaction point. Beam direction is taken as the positive z axis pointing to North. The x axis is taken along the west direction and the y axis is taken perpendicular to both of these which point upwards. To describe any particle position usually Cylindrical Co–ordinate System (r, ϕ, θ) is used. The angle θ is defined w.r.t the z axis, ϕ is defined in the azimuthal plane. This co–ordinate system is chosen in such a way that, θ reaches 90° in y axis and ϕ is 0 at the x axis. We know that in high energy heavy ion collisions, particle properties like energy, mass, longitudinal momentum, transverse momentum etc. are related to rapidity y and pseudorapidity η. In an

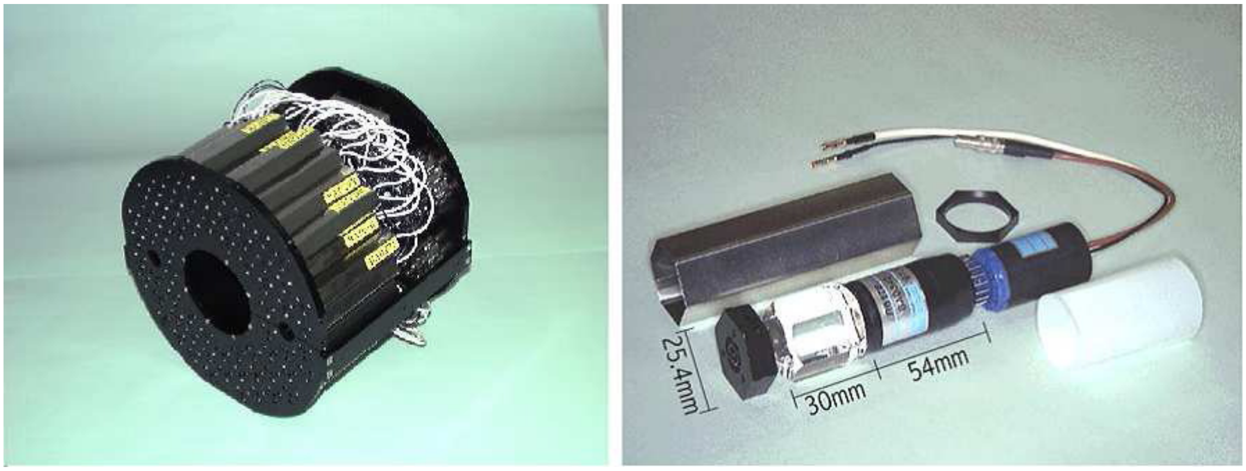

Figure 2.4: Beam Beam Counter (Left) and a single unit of BBC which consists of PMT mounted on Čerenkov radiators(Right).

experiment one cannot measure y and η directly. In an indirect way they can be measured using θ and ϕ.

2.2.1 Global detectors

In high energy collisions ($p+p$ or heavy ions), the collision time, collision vertex, impact parameter etc. are the main quantities which characterize a collision. The Global Detectors of PHENIX : Beam Beam Counter (BBC), Zero Degree Calorimeter (ZDC) and Forward Calorimeter (FCal) help to obtain these global information of an event.

2.2.1.1 Beam beam counters

The Beam Beam Counter (BBC) [60, 61] is located around the beam axis at a distance of 1.44 m from the collision vertex covering $3.1 < |\eta| < 3.9$. There are two BBC, one situated at North and the other situated at South. It has a inner radius of 5 cm and outer radius of 30 cm. Each BBC is made up of 64 hexagonal shaped PMTs mounted on quartz Čerenkov radiators (Fig. 2.4). The BBCs are designed to operate under various collision species (dynamic range 1–30 MIPs), high radiation and large magnetic field (0.3 T).

The main purpose of BBC is to provide the Minimum Bias Trigger, which signals the other electronics that an event has occurred. It also records the collision time (t^{BBC}) and position (z^{BBC}) along z axis. The BBC measures the time of collision with respect to the RHIC collider clock (synchronized with beam bunches). If the collision time is t_N^{BBC} measured by North BBC and collision time is t_S^{BBC} measured by South BBC and L is the distance between collision point and BBC (1.44 m), then collision time and collision vertex position is given by;

$$t_0^{BBC} = \frac{t_N^{BBC} + t_S^{BBC}}{2} - \frac{L}{c}, \tag{2.1}$$

$$z_0^{BBC} = c \times \frac{t_N^{BBC} + t_S^{BBC}}{2}, \tag{2.2}$$

where, c is the speed of light. An event is considered and acceptable if $|z_0^{BBC}| < 38$ cm and only then PHENIX Level–1 Trigger fires.

The time resolution of single BBC element is 52 ps. The Minimum Bias Trigger at PHENIX requires at least one PMT hit per BBC, to have an acceptable event, this leads to $|z_0^{BBC}|$ position resolution of ~ 1.1 cm for $p + p$ collisions. In heavy ion collisions, the PMTs tend to fire more and more due to high multiplicity which improves the time resolution to $\sim$ 14 ps for a typical Au+Au collision leading to position resolution of 3 mm. In case of d+Au collisions the position resolution is around 0.5 cm. BBC gives the start timing (t^{BBC}) for Time of Flight detector. BBCs are also used (along with ZDCs and FCals) to determine the centrality of collision.

2.2.1.2 Zero degree calorimeter

Zero Degree Calorimeter [62, 63] are the sampling type hadronic calorimeters situated 18 m away from the interaction point both in North and South direction. Each ZDC is made up of three Čerenkov sampling tungsten plate modules which are read out by a PMT. The thickness of plates corresponds to two hadronic interaction lengths.

ZDC measures the total energy of the spectator neutrons flying from the collision point.

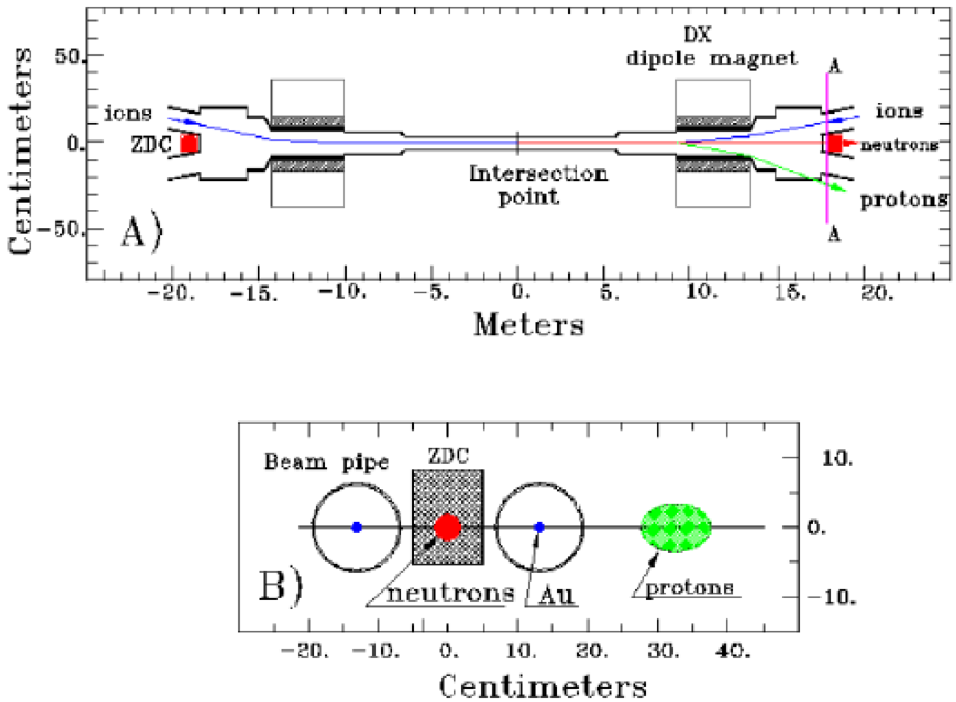

Figure 2.5: Zero Degree Calorimeters

The charged particles are deflected by the magnet situated before the ZDC. The total energy deposited by the spectator neutrons in ZDC is less if the participants are more (in case of central collisions) and vice verse. The energy deposited in ZDC along with the energy deposited by the participants in BBCs are used to determine the collision centrality in heavy ion collisions. In d+Au collisions only BBC is used to determine collision centrality. In heavy ion collisions, ZDC also plays the role to determine the Minimum Bias trigger along with the BBC and monitor the beam luminosity. Figure 2.5 shows the ZDC along with the beams.

2.2.2 Central arm spectrometers

The work done in this thesis is performed using the Central Arm detectors of PHENIX. The Central Arm detectors are placed in East–West direction. Most of the detectors covers $\Delta\phi = 2 \times 90^\circ$ (except ToF) and $\Delta\eta = \pm\, 0.35$. The Central Arm Spectrometers consists of particle tracking and particle identification detectors.

2.2.2.1 Central magnet

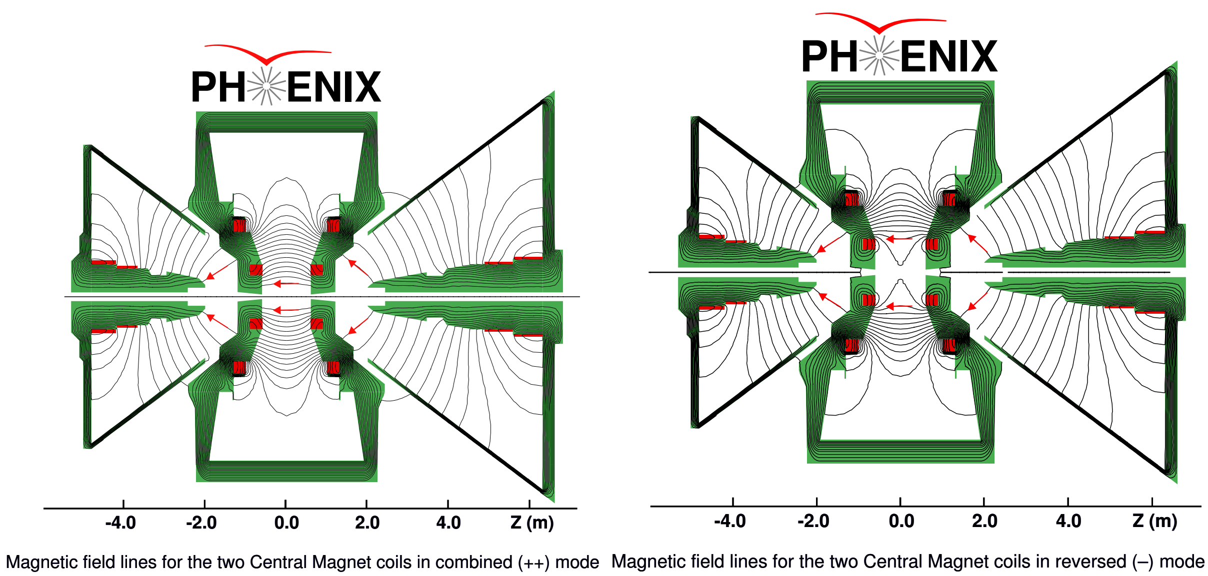

Figure 2.6: Magnetic field lines in the PHENIX detector, for the two central magnet coils operated in adding (++) and bucking (+-) mode.

The Central Magnet [64] is situated at the central part of the PHENIX detector (Fig. 2.2). The spectrometers are situated on either side of the magnet. It consists of two pairs of concentric coils. The outer coils have 120 turns and the inner coils have 144 turns each. The central magnet provides axially symmetric magnetic field parallel to beam axis and around the beam. The beam lines are shown in Fig. 2.6. This magnet works in both adding (++, --) and bucking (+-) modes giving the field integral of 1.15 T.m (z $\sim$ 0) and 0.43 T.m respectively. In bucking mode, a field free region is there upto a distance of 50–60 cm. Irrespective of modes the field dies off after a distance of 2 m from the z axis.

In the presence of the magnetic field, the charged particle suffers bending. The deflection angle of the particle due to the presence of magnetic field is accurately measured by the Drift chambers and are use to determine the particle momentum.

2.2.2.2 Drift chambers

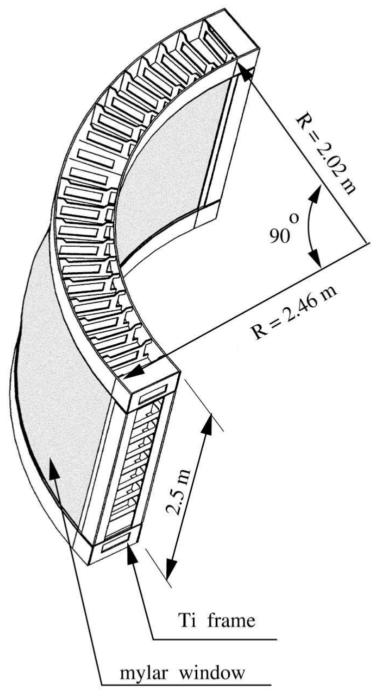

Figure 2.7: One section of Drift Chamber.

The tracking detector in PHENIX is the Drift Chamber [65], which is a multi–wire gaseous detector. It is located at a distance of 2–2.48 m in radial direction on both sides of beam axis, measures the track curvature of the charged particle in the r–ϕ plane, which is used to find the momentum of the particle. Each DC covers 90° in ϕ.

The frame of DC is made of titanium with 0.127 mm Al–mylar entrance and exit windows. The gaseous volume of DC is filled with 50% Argon and 50% Ethane. The main working principle of DC is based on the assumption that the drift time of electron is proportional to the distance traversed by electron from center of ionization. It follows a linear

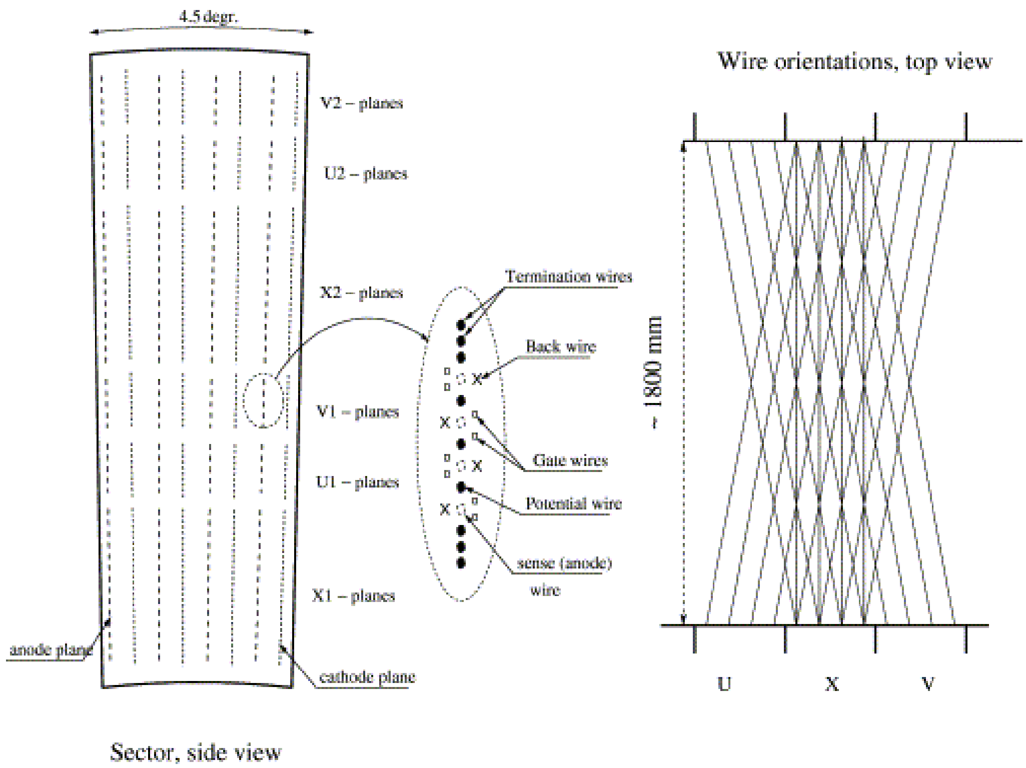

Figure 2.8: Wire arrangement in Drift Chamber.

relation $x = v_{drift} \times t$. This mixture ensures the stability of ionization drift velocity with low diffusion co–efficient and high gain.

Each of the DC is divided in 20 sectors, known as Keystones (Fig. 2.7), which are further segmented in 6 types of wire modules: X1, U1, V1, X2, U2 and V2. Each keystone covers 4.5° in azimuth and has 6400 anode wires. The X1 and X2 wires are placed parallel to beam pipe. The U and V wires are the stereo wires and are situated at an angle $\sim \pm$ 6° with X wires. The X wires measure the co–ordinate of the track and the U and V wires measure the z position of the track. The wire configuration is shown in Fig. 2.8. Each wire module consists of four anode and four cathode planes placed alternatingly. To have a clean reconstruction, there are also three kinds of wires, namely, "field wires", "anode wires" and "back wires". The "cathode wires" create uniform drift field between anode and cathode. The "field wires" create high electric field strength near the anode wire. The "gate wires" also create high field near the anode wire and localize the drift region width. The "back wires” stop drift from one side of the anode wire. By reducing the amount of ionization that reaches anode, the location of each track co–ordinate can be localized. In order to reconstruct the tracks in heavy ion collisions ($n_{tracks} \sim 500$), each anode is electrically insulated in the middle by a 100 μm thick kapton strip, which in turn increases the number of readouts by a factor of 2.

2.2.2.3 Pad chambers

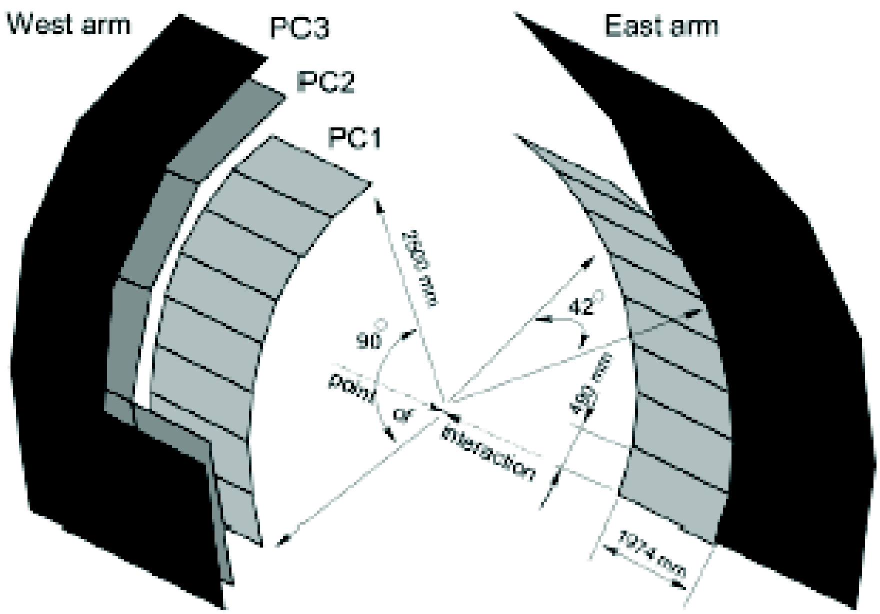

Figure 2.9: Three dimensional view of three layers of padchambers – both east and west arm.

The Pad Chambers (PC) [66] are the multi–wire proportional chambers with cathode read out, which give spatial positions of charged particles along their trajectories, to determine polar angle θ which in turn is used for momentum determination in z direction (p_z). In PHENIX there are three layers of PC. They are known as PC1, PC2 and PC3 situated at a radial distance of 2.47–2.52 m, 4.15–4.21 m and 4.91–4.98 m (Fig. 2.9), respectively from the interaction point. PC1 is situated in both arms between DC and RICH. PC2 is

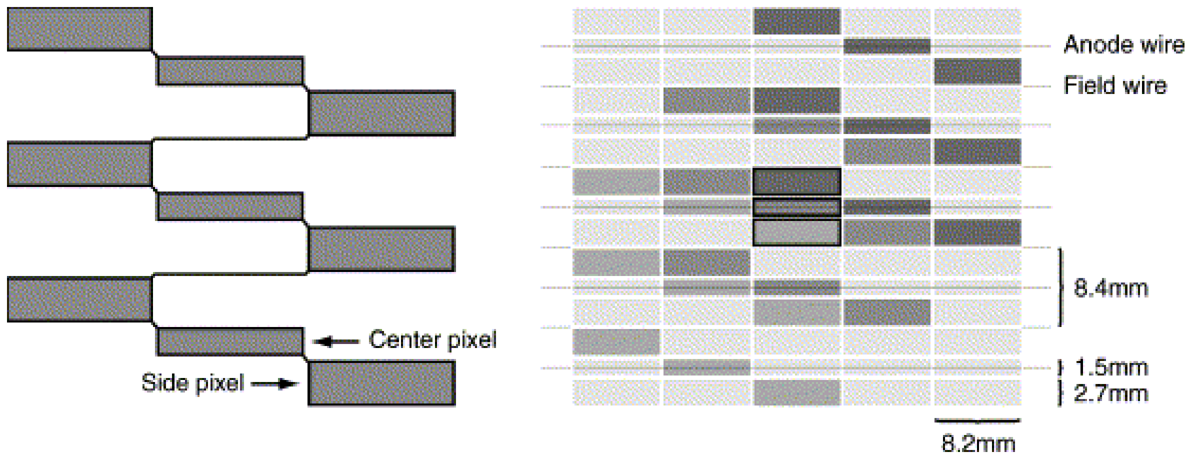

Figure 2.10: The pixel geometry. The nine pixels forming one pad (Left). The interleaved pad design (Right).

placed behind RICH in west arm. PC3 is there only in east arm, sandwiched between TEC and EMCal.

Each PC layer consists of two cathode planes. The gap between these planes consists of gas mixture (50% Argon and 50% Ethane) and a single plane of wires situated at equal distance from these cathode planes. Each cathode is finely segmented into an array of pixels. Three pixels from three neighbouring pads form a 'cell' in PC. To get a confirm and unambiguous signal, all three pixels in a cell must fire to constitute a hit. Nine pixels are connected to each other electronically to form a pad. This interleaved pad structure reduces the number of readouts by a factor of 9. The 'cell' and 'pad' structure is shown in Fig. 2.10. The pad size of PC1 is 0.84 cm x 0.845 cm which gives position resolution of 1.7 mm along z and 2.5 mm in r–ϕ. The pad size for PC2 and PC3 chosen such that they have similar angular resolution compared to PC1.

PC1 is essential to get the 3D momentum at the exit of the DC. The DC and PC1 information are combined to determine the straight line trajectories outside the magnetic field. PC2 and PC3 are used for matching those tracks far away (in EMCal, RICH etc) from collision points to resolve ambiguities. PC2 and PC3 are used to reject the particles produced from secondary interactions or particle decays and low momentum primary tracks that curve around PC1 in the magnetic field and PC2 and PC3.

2.2.2.4 Ring imaging Čerenkov

Ring Imaging Čerenkov [67, 68] is dedicated for electron identification. It is situated behind the PC1. The principle is to measure the Čerenkov radiation which is emitted by the particle travelling faster than the speed of light inside some medium. In Fig. 2.11, it is

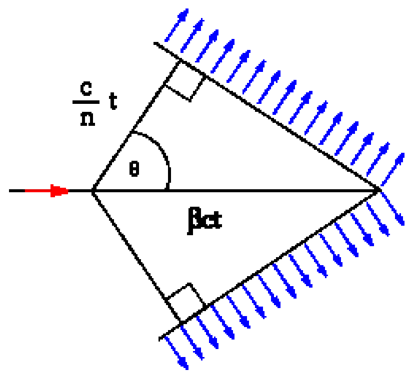

Figure 2.11: The Geometry of Čerenkov radiation. Red Arrow is the incoming particle and blue arrows are the radiated wave–fronts.

seen that,

$$cos\theta = \frac{1}{n\beta} \tag{2.3}$$

If the emission angle $\cos\theta < 1$, particle emits Čerenkov radiation. Now,

$$\gamma = \frac{1}{\sqrt{1-\beta^2}},\ p = m\gamma\beta. \tag{2.4}$$

So, this Čerenkov radiation is a strong function of mass. From the last relation, it is seen that Čerenkov threshold is lower for electrons than the other hadrons. RICH uses carbon di–oxide as radiator gas which has a refractive index (r. i) $\eta = 1.000045$. Using this r. i value, the threshold comes around $p_T = 18$ MeV/c for electrons and 4.87 Gev/c for pions.

Čerenkov radiation produced in the detector volume (40 m^3) is focused by the mirrors on an array of PMTs located on either side of the entrance window. The emitted photons are focused into a ring with an asymptotic diameter of $\sim$ 11.8 cm. A typical relativistic electron produces an average of 11 photo–electrons.

2.2.2.5 Time of flight

Charged hadron identification is done by Time of flight (TOF) detector. It is placed at a distance of $\sim$ 5 m from the event interaction point. Upto Run 6, the TOF was present only in east arm [69] covering only $\pi/8$ in ϕ. From Run 7 another TOF was added to the west arm [71] covering $\pi/4$ in ϕ.

1. TOF East: TOF East consists of 96 segments, each made up of plastic scintillator slat (Bicron Bc404) having 1.5 cm in width and depth. The PMTs are Hamamatsu R3478S with a diameter of 3/4 inch. It has a time resolution of $\sigma_t \sim$ 130 ps which enables TOF–E to separate kaons and pions upto p_T = 2.4 GeV/c and kaons and protons upto p_T = 4.0 GeV/c. The particle separation by TOF is shown in Fig. 2.12 for Au+Au collision system at $\sqrt{s_{NN}}$ = 200 GeV. Charged particles are identified by converting flight time into mass of particle by,

$$m^2 = \frac{p^2}{c^2}\left[\left(\frac{t_{tof}}{L/c}\right)^2 - 1\right], \tag{2.5}$$

   where, p is the particle momentum determined by DC, L is the flight length from the event vertex to TOF, t_{tof} is the time of flight of the particle measured by TOF (stop time) and BBC (start time). The charged particle identification is done using proper cuts in mass squared vs momentum space (left fig of Fig. 2.12). The width and mean of the m^2 distributions for each particle species are obtained for each p_T bin by fitting the vicinity of each peak in the distributions with a Gaussian functions. The momentum dependence of the width can be parametrized [70] as,

$$\sigma_{m^2}(p) = \frac{\sigma_\alpha^2}{K_1^2}(4m^4p^2) + \frac{\sigma_{ms}^2}{K_1^2}\left[4m^4\left(1+\frac{m^2}{p^2}\right)\right] + \frac{\sigma_t^2 c^2}{L^2}\left[4p^2(m^2+p^2)\right], \tag{2.6}$$

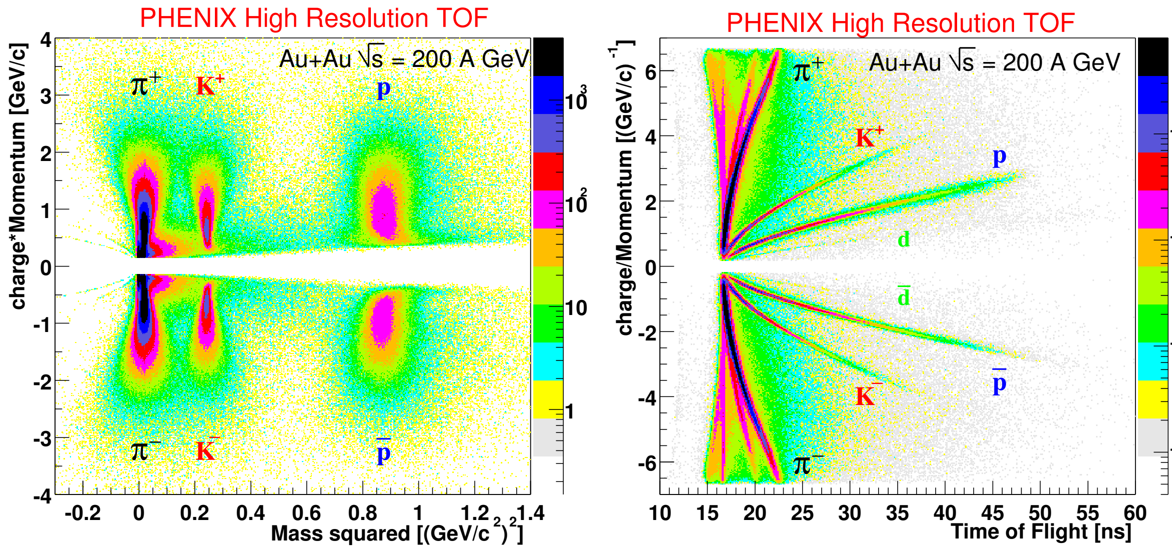

Figure 2.12: Particle Identification by TOF. Charge times momentum vs mass squared (on Left), charge times momentum vs time of flight (on Right).

where,

σ_α = angular resolution = 1.116 mrad (Run5 $p+p$),

σ_{ms} = multiple scattering term = 0.96 mrad (Run5 $p+p$),

σ_t = overall time of flight resolution $\sim$ 130 ps,

m^2 = centroid of the m^2 distribution for each particle species,

K_1 = magnetic field integral = 101.0 mrad GeV.

2. TOF West: TOF West uses the Multi–Gap Resistive Plate chamber technology which results in timing resolution of $\sim$ 75 ps. Using TOF West and applying advanced PID cuts (e.g. asymmetric cuts), kaons, pions and protons can be separated upto higher p_T. This improves the π and proton identification upto 5–6 GeV/c, and kaon identification upto 3.5–4 GeV/c. The pion, kaon and proton peaks are fitted independently with double Gaussian. Double Gaussian is used to minimize the uncertainties of the individual fits. The mean and widths of each particle are parametrized by a function

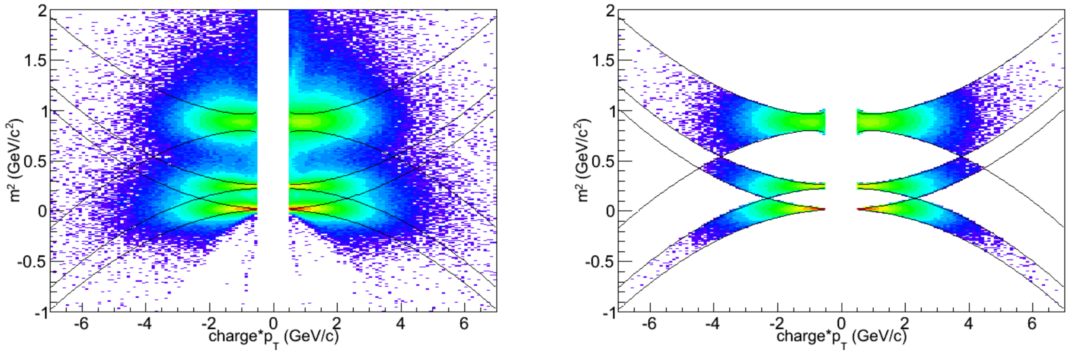

Figure 2.13: Particle Identification by Tof–W. Left: Charge times momentum vs mass squared time of flight. Right : Charge times momentum vs mass squared time of flight, after applying PID cuts.

like,

$$f(x) = p_0 + \frac{p_1}{x} + \frac{p_2}{x^2} + p_3 e^{\sqrt{x}} + p_4\sqrt{x}, \tag{2.7}$$

The charged hadron identification by Tof–W is shown in Fig. 2.13.

In this thesis work only TOF–East is used.

2.2.2.6 Electromagnetic calorimeter

Electromagnetic Calorimeter (EMCal) [72] is placed at the end of the central arms. The EMCal covers the full acceptance of the central spectrometers and is divided into eight sectors in azimuth. This uses lead–scintillator (PbSc) and lead–glass (PbGl) technologies, measures the position and energy of electrons and photons. PbSc is a shashlik type sampling calorimeter where as PbGl is a homogeneous Čerenkov calorimeter. Six of the EMCal sectors located at the radius of 5.0 m are built of PbSc and consist of 15552 individual towers with a granularity of 5.5×5.5 cm^2 and a depth of 18 X_0. The two other sectors located at the radius of 5.2 m are built of lead–glass (PbGl) and consist of 9216 lead–glass Čerenkov towers with a granularity of 4×4 cm^2 and a depth of 14.4 X_0. Due to the fine segmentation of the EMCal the electromagnetic showers typically spread over several towers. This spread provides the means to analyze the position and shape of the shower, and to reject hadrons

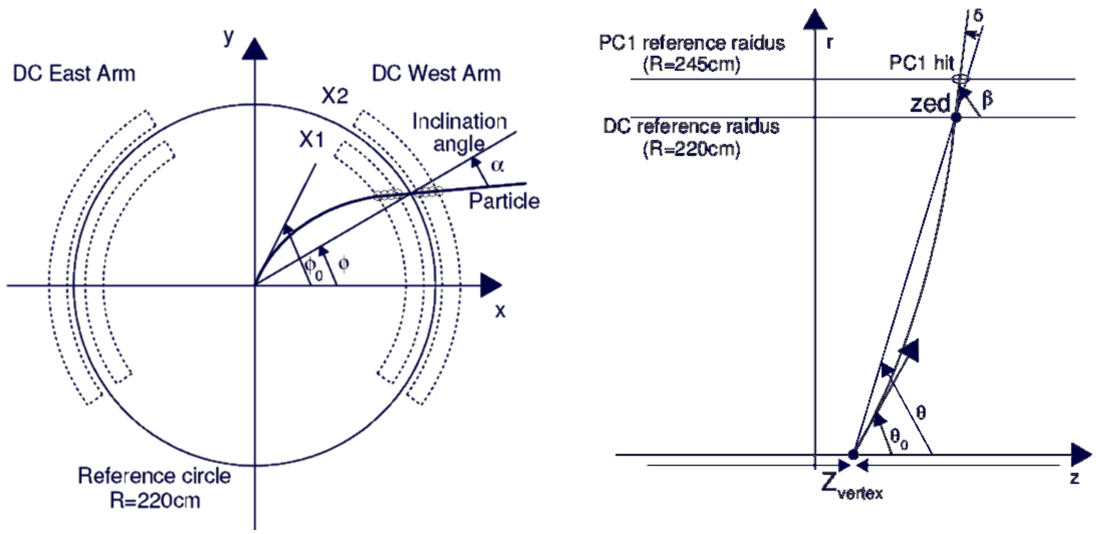

Figure 2.14: On Left, the view of a track is in the DC x–y plane. The X1 and X2 hits on the DC are shown as small circles. On Right the view of the track is in r–z plane, with various angles (discussed in text).

which produce showers of a different shape. The spatial resolution of the PbSc (PbGl) is $\sigma(E) = 1.55(0.2) \oplus 5.7(8.4)/\sqrt{E[\mathrm{GeV}]}$ mm for particles at normal incidence. The energy resolution of the PbSc (PbGl) calorimeter is $\delta E/E = 2.1(0.8)\% \oplus 8.1(5.9)/\sqrt{E[\mathrm{GeV}]}\%$. It also provides a trigger on rare events with high momentum photons.

2.2.3 Track reconstruction and momentum determination

2.2.3.0.1 Track reconstruction : Charged tracks are reconstructed by the DC and PC1 information. The combinatorial Hough transform technique [73] is used to reconstruct the tracks from the hits in DC and PC1. The tracking algorithm assumes that, the origin of all tracks is same as the event origin as measured by BBC. Another important assumption is, the tracks inside DC are taken as straight line tracks.

The path of charged particle is demonstrated in Fig. 2.14. On the left the track is shown in the r–ϕ plane. The hits are shown as small circles. On the right, the track is shown in r–z plane. The definitions of the different angles shown in Fig. 2.14 are :

1. ϕ : This is the azimuthal angle made by the particle track with reference circle located

at the radius of 2.2 m (inside DC), with respect to the vertex.

2. ϕ_0 : This is the azimuthal angle of the track at the event vertex.

3. α : This is the angle between the actual bend track and straight line track passing through same intersection point of particle with reference circle.

4. zed : This is the z co–ordinate of the track at the intersection point of particle with reference circle.

5. β : This is the angle of the track with respect to the z–axis at the intersection point in the r–z plane.

6. δ : This is the angle between the actual bend track and straight line track passing through same intersection point in the r–z plane.

7. θ : Polar angle of the straight line track at vertex.

8. θ_0 : Polar angle of the actual track at vertex.

An iterative procedure is used to associate the hits to tracks. Weightage is given to the hits according to their deviation from the straight line trajectory (initially guessed). More the deviation from the straight line track, lesser is the weightage. Each hit is associated to the closest track and simultaneously removed from the consideration of all other tracks. Only those tracks are considered as valid ones which have at least 8 hits in X1 and X2 layers. Then the tracks are reconstructed in r–z plane with the help of information of collision vertex from BBC, reconstructed clusters in the PC1 and hits in UV wires of the DC. The details of event reconstruction can be found in [74].

2.2.3.0.2 Track quality : In order to extract the best results from the analysis, track selection is a very important step. In PHENIX computing, the variable “quality” gives us the track quality, from which the best quality tracks can be chosen for analysis.

The reconstructed tracks are assigned a "quality", depending on the hit information of the DC (X, UV wires) and associated PC1 hit. The "quality" for each track is defined as a 6 bit variable as :

$$quality = A \times 2^0 + B \times 2^1 + C \times 2^2 + D \times 2^3 + E \times 2^4 + F \times 2^5 \tag{2.8}$$

where,

- $A = 1$ if there is a X1 plane hit.
- $B = 1$ if there is a X2 plane hit.
- $C = 1$ if there are UV plane hits.
- $D = 1$ if there are unique UV plane hits.
- $E = 1$ if there are PC1 hit.
- $F = 1$ if there are unique PC1 hits. If there are no hits, the bits are set to zero. To have a real track at least 8 hits are required in X1, X2 planes. The different combinations of A, B, C, D, E, F are shown in Table 2.4.

In the analysis presented in this thesis the tracks with quality either 63 or 51 or 31 are used.

2.2.3.0.3 Momentum determination : Theoretically one can measure the momentum of a charged particle in a known magnetic field. Considering only the Lorentz force (only magnetic part), the equation of motion looks like :

$$F_{centripetal} = F_{Lorentz} \tag{2.9}$$

$$\frac{mv^2}{r} = q\,v \times B \tag{2.10}$$

$$\tag{2.11}$$

Table 2.4: Track Quality

Nature of hits in PC1	Nature of hits in UV plane	A	B	C	D	E	F	Quality
Identified	Identified	1	0	1	1	1	1	61
		0	1	1	1	1	1	62
		1	1	1	1	1	1	63
Identified	No hit	1	0	0	0	1	1	49
		0	1	0	0	1	1	50
		1	1	0	0	1	1	51
Unidentified	Identified	1	0	1	1	1	0	29
		0	1	1	1	1	0	30
		1	1	1	1	1	0	31
Unidentified	Unidentified	1	0	1	0	1	0	21
		0	1	1	0	1	0	22
		1	1	1	0	1	0	23
Unidentified	No hit	1	0	0	0	1	0	17
		0	1	0	0	1	0	18
		1	1	0	0	1	0	19

assuming v and B are perpendicular the above reduces to,

$$m\,v = q\,B\,r \tag{2.12}$$

where B is the magnetic field, v is the velocity of the particle with charge q in the magnetic field and r is the radius of the track of the particle. The same principle is used in PHENIX to determine the momentum of the charged particles. But in PHENIX the magnetic field is complicated and has a non–uniform shape which makes this task complicated. In PHENIX, a four–dimensional field integral grid is constructed for momentum determination [75] using the magnetic field and the intersection of the charged track path with the DCs and PCs. The field integral $f(p, r, \theta_0, z)$ is a function of collision vertex z, initial polar angle θ_0, total momentum of particle p and the radius r from the beam axis. The field integral grid is generated by explicitly propagating particles through the measured magnetic field map and numerically integrating to obtain $f(p, r, \theta_0, z)$ for each grid point.

The track momentum is determined in an iterative process utilizing the fact that

$f(p, r, \theta_0, z)$ at a given radius r varies linearly with the angle ϕ,

$$\phi = \phi_0 + \frac{q}{p} f(p, r, \theta_0, z) \tag{2.13}$$

and assuming that all the tracks originate from the event vertex. An initial estimate of the track momentum and charge is made from the reconstructed bending angle α, of the track in the DC. The measured polar angle θ is used as an initial estimate for θ_0. Then using the radial position of each reconstructed track hit associated to the track, $f(p, r, \theta_0, z)$ is calculated. After this, fit is done in ϕ and $f(p, r, \theta_0, z)$ to extract the values for ϕ_0 and q/p. These extracted values are then fed back in the above equation and this process is repeated for a few times. Less than four iterations are necessary for convergence on the p and ϕ_0 values. A similar procedure is used in the r–z plane to find the value of θ_0.

The momentum resolution for reconstructed charged particles with the momentum above 200 MeV/c is $\sigma_p/p = 0.7\ \% \oplus 1\% p\ \ (\mathrm{GeV/c})$ where the first term is due to the multiple scattering and the second term is due to the intrinsic DC resolution.

2.2.4 Minimum bias trigger

Event Trigger is important to select the interesting events among all the events occurring in a collision. Beside, PHENIX has its own data recording capability and space to accommodate recorded data. So, the data which are recorded should be a good quality data.

The total $p+p$ inelastic cross section is $\sigma^{pp}_{inel} = 42 \pm 3$ mb at $\sqrt{s} = 200$ GeV. The BBC cross section in $p+p$ collisions was measured by Van der Meer [76] scan technique and is found to be $\sigma^{pp}_{BBC} = 23 \pm 2.2$ mb. This is $54.5 \pm 6\%$ of σ^{pp}_{inel}.

The Minimum Bias trigger in PHENIX is determined by at least 1 PMT firing in the BBC as well as the collision vertex within $\pm$ 38 cm (30 cm in case of $p+p$ or d+Au collisions). This condition of Minimum Bias introduces a bias that depends on the multiplicity of an event, i.e. in high multiplicity environment the number of PMTs that get fired in Cu+Cu or Au+Au collisions will be more than that in $p+p$ or d+Au collisions. Therefore, the BBC Minimum Bias trigger will bias the recorded sample to have a higher fraction of hard scattering events than would be recorded from the inclusive BBC trigger cross section. This bias is measured by using a random clock trigger, supplied by RHIC, which fires every time there is a bunch crossing. Upon the clock trigger firing, PHENIX looks in the central arms for any charged hadrons and can thereby determine the BBC trigger bias. In $p+p$ events, BBC fires on 79 ± 2 % of the events.

To take into account this bias errors (events missed by BBC and trigger bias), while calculating the invariant yield, a correction factor $C_{bias} = \epsilon_{BBC}/\epsilon_{bias} = 0.545/0.79 = 0.689$ is used for $p+p$ system.

2.2.5 Centrality measurement

In PHENIX, collision centrality is measured from BBC and ZDC information. BBC measures the charged particle multiplicity at the forward rapidity and ZDC measures the energy of spectator neutrons (Fig 2.14). The multiplicities in BBC and ZDC are correlated with collision geometry and hence can be used to measure the collision centrality (impact parameter 'b'). For central collisions (small b), participants are more hence the charged particle multiplicity measured in BBC is more and the energy deposited by spectators in ZDC is small. For peripheral collisions (large b), the spectators are more, hence energy deposited in ZDC is more and charge particle multiplicity measured in BBC is less. The two quantities, $N_{\rm coll}$ and $N_{\rm part}$ are used to describe collision centrality, $N_{\rm coll}$ is the number of the nucleon–nucleon binary collisions and $N_{\rm part}$ is the number of nucleons taking part in collisions.

In case of d+Au and Cu+Cu collisions only BBCs are used to determine the collision centrality. In case of Au+Au collisions both BBCs and ZDCs are used to determine the collision centrality.

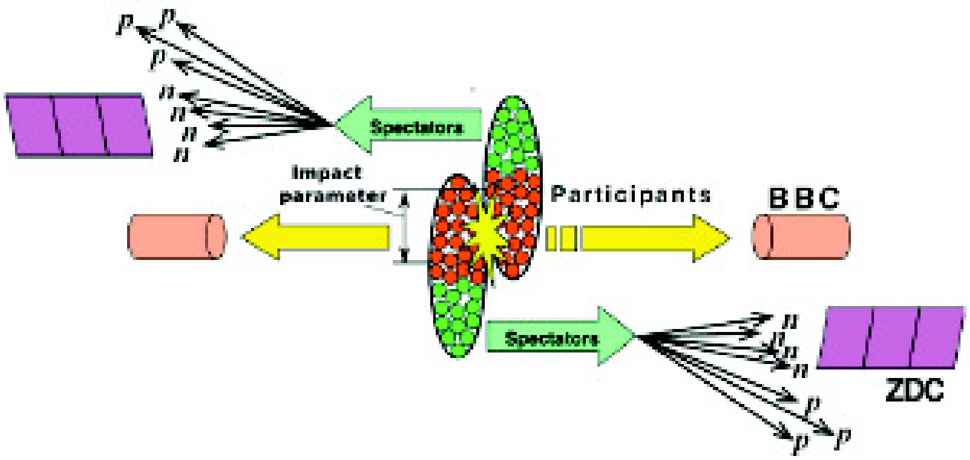

Figure 2.15: Participants and Spectators as seen by BBC and ZDC respectively.

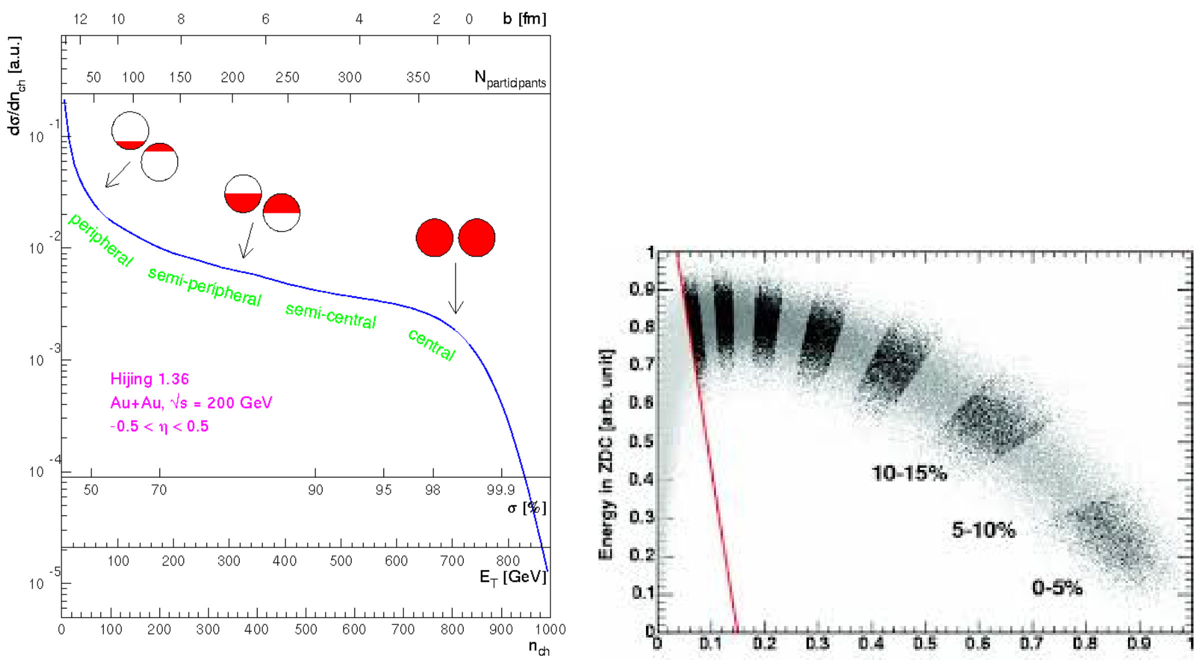

Figure 2.16: On top, an example of correlation between N_{ch}, N_{part} and b is shown. The scales are arbitrary and shown just for illustration. At bottom , energy deposition by spectators in ZDC and particle multiplicity in BBC is shown.

Table 2.5: $N_{\rm coll}$ for the centrality classes in Cu+Cu at $\sqrt{s_{NN}}$ = 200 GeV used in this work.

Centrality	$N_{\rm coll}$
Min Bias	51.8 ± 5.6
0–20%	151.8 ± 17.1
20–40%	61.6 ± 6.6
40–60%	22.3 ± 2.9
60–94%	5.1 ± 0.7

To evaluate the collision centrality, Glauber Monte Carlo (GMC) is used [77]. This model assumes that, at sufficiently high energies, the participant nucleons will carry sufficient momentum that they will travel in straight line trajectories. This hypothesis reduces the nucleus–nucleus interaction problem to nucleon–nucleon interaction.

Method:

Experimentally the per event charged particle multiplicity dN_{evt}/dN_{ch} is measured by BBC. Theoretically this distribution can be generated by GMC using different particle generators. Once this distribution is known, centrality classes are assigned by binning the distribution based upon the fraction of total integral. For each centrality class the mean value for $N_{\rm coll}$ and $N_{\rm part}$ is calculated by GMC. One can perform mapping to extract the $N_{\rm coll}$ and $N_{\rm part}$ mean values for experimental data. However the method of mapping differ for different experiments and collision systems. The values for $N_{\rm coll}$, for the centrality classes that has been used in this thesis work are listed in Table 2.5.

2.2.6 Data acquisition system

PHENIX is capable of handling high event rates, process them and store them. This is achieved by the Data Acquisition System (DAQ) [78]. PHENIX DAQ processes the signals from each detector subsystem, produces trigger decision and stores the triggered data. The typical data recording rates are 5 kHz and 3 kHz for $p + p$ and Cu+Cu collision system

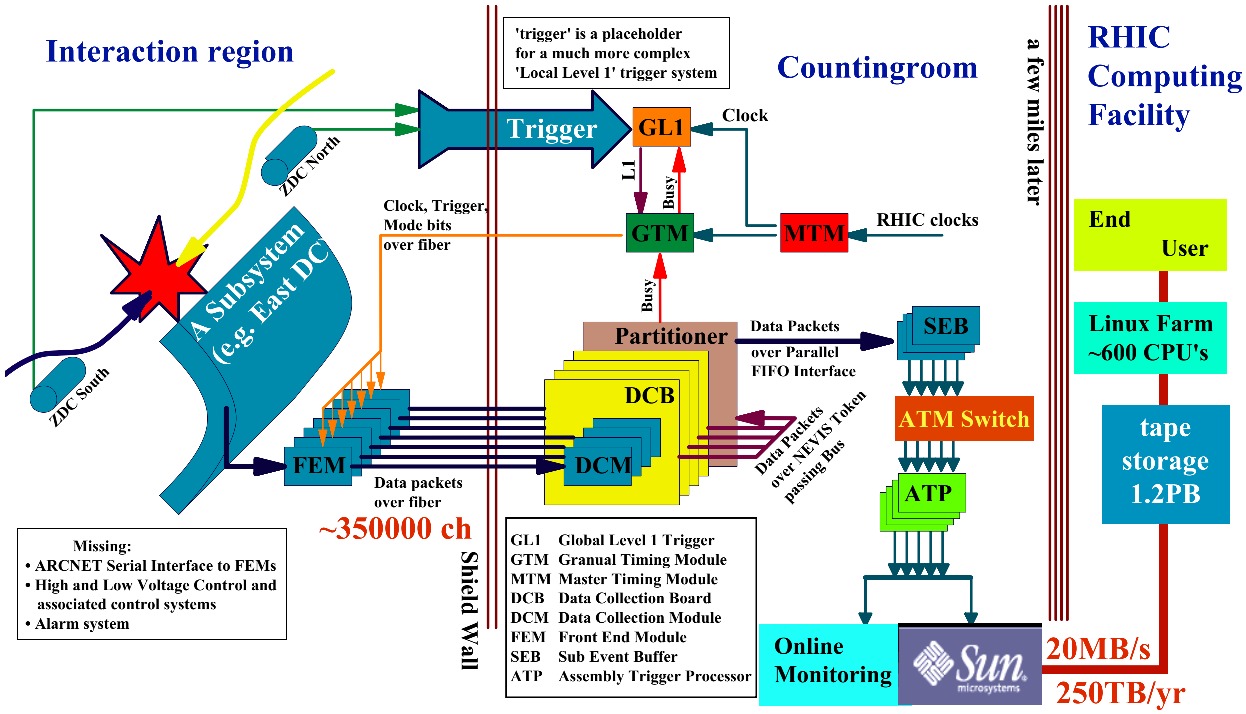

Figure 2.17: DAQ in PHENIX.

respectively in Run5. The zero suppressed events sizes are 160 kB for Au+Au, 110 kB for Cu+Cu and 40 kB for $p+p$ collisions. DAQ is shown in Fig 2.17.

DAQ is controlled by the Master Timing Module (MTM), the Granule Timing Module (GTM) and GL1. All these modules are synchronized by RHIC clock. The MTM receives 9.4 MHz RHIC clock and delivers it to the GTM and GL1. The Front End Module (FEM) of the detector subsystems are controlled by GTM. FEMs receive the event accept signal from GTM. GTM also provides the clock and the control commands (Mode Bits) to FEMs. GTM provides a fine delay of the clock with $\sim$ 50 ps step, to compensate the timing difference among the FEMs. The GL1 produces the first LVL1 trigger decision by combining LVL1 signals from detector components.

The main task of FEM is to convert the analog signal to digitized form. The LVL1 triggers are simultaneously generated. The generation of global decision that whether an event should be registered or not, takes $\sim$ 30 bunch crossings. In the mean time, the event data is stored in the FEM. When the FEM gets the accept signal, each FEM starts digitizing the data.

The data from FEM is collected by a Data Collection Module (DCM), via an optical fibre cable. The DCMs provide data buffering, zero suppression, error checking and data formatting. DCM sends the compressed data to Event Builder (EvB).

The Event Builder (EvB) consists of 39 Sub Event Buffers (SeBs), Asynchronous Transfer Module (ATM) switch and 52 Assembly Trigger Processors (ATPs). EvB communicates with each module via Sebs. The events are assembled in ATM. The SeBs transfer the data from granule to ATP with the help of ATM. The combined data are stored to the disk with maximum logging rate of 400 MB/s and are used for online monitoring.

CHAPTER 3

ANALYSIS METHODS FOR K^{*0} MEASUREMENTS

This chapter describes the analysis procedure for K^{*0} ($\bar{K^{*0}}$) meson measurement via its hadronic decay channel $K^{+}\pi^{-}$ ($K^{-}\pi^{+}$) in Cu+Cu collisions at $\sqrt{s_{NN}} = 200$ GeV using PHENIX detector at RHIC. The data used in this analysis was recorded during the year 2005 (Table 2.2) and commonly termed as *Run5 data*. This run has very good statistics $\sim$ 928 Million. For this analysis we choose two oppositely charged tracks and also require $|z_0^{BBC}| < 30$ cm, which reduces the analyzed events to 588 Million where approximately 337 Million events were with "++" magnetic field configuration and almost 251 Million events were with "- -" magnetic field configuration.

The data analysis procedure consists of - event selection (Section 3.1), data quality check (Section 3.2), invariant mass reconstruction (Section 3.3), corrections for detector geometry (acceptance) and reconstruction efficiency (Section 3.4) and then obtaining the invariant yield (Section 3.5). To extract the K^{*0} signal from the huge data set, three analysis techniques were implemented, which are discussed in Section 3.3.

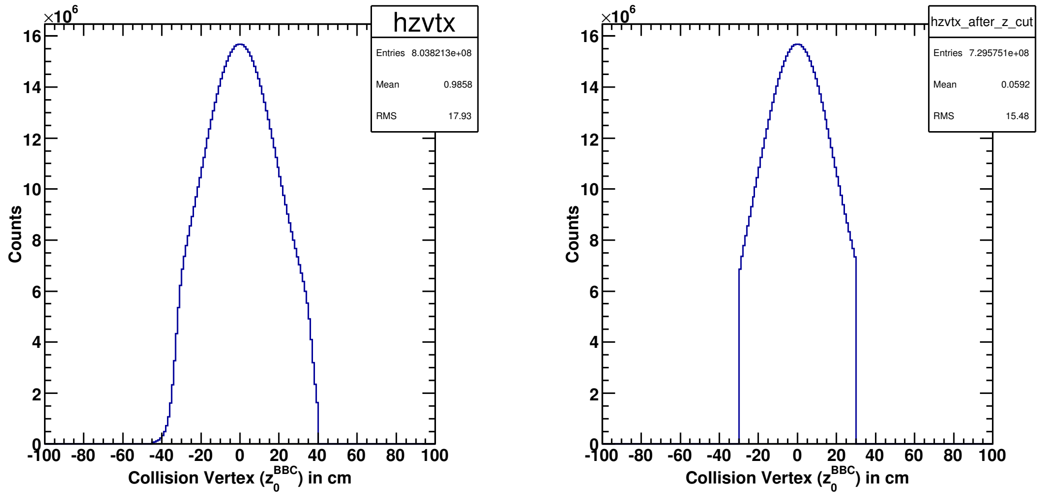

Figure 3.1: Left panel :Example of the collision vertex (z_0^{BBC}) distribution in Run5 Cu+Cu collisions at $\sqrt{s_{NN}} = 200\,\mathrm{GeV}$. Right panel : Distribution of (z_0^{BBC}) after(z_0^{BBC}) < 30 cm cut applied.

3.1 Event selection and track selection cuts

The left panel of Fig. 3.1 shows the distribution of collision vertex in Z direction (z_0^{BBC}). Events which have collision vertex away from $z_0^{BBC} = 0$ cm, have higher probability to interact with the central magnet. In order to reduce the probability for produced particles to interact with the central magnet, an offline analysis cut of $|z_0^{BBC}| < 30$ cm is applied for this analysis as shown in the right panel of Fig. 3.1. Also in order to reconstruct invariant mass, minimum two tracks with opposite charges were required in each event.

The details of track qualities are discussed in Section. 2.2. The best quality tracks were chosen by applying the track quality cut of the categories 31 or 51 or 63. The tracks within the p_T range of $0.3 < p_T$ (GeV/c) < 6 were chosen for this analysis. The tracking algorithm assumes that the tracks are originating from the collision vertex. This is not true for the tracks coming out from particle decay or shower particles or γ conversions. These lead to the reconstruction of tracks with wrong momentum. These tracks can be rejected by requiring a matching in the outer detector e.g. EMCal and PC3. This matching is done in ϕ and z direction. The variables $emcsd\phi$, $emcsdz$ in EMCal, $pc3sd\phi$, $pc3sdz$ in PC3,

Table 3.1: Track quality cuts used for K^{*0} analysis

Type of cuts	Value
PC3 matching	$\|pc3sd\phi\| < 3\sigma$ AND $\|pc3sdz\| < 3\sigma$
EMC matching	$\|emcsd\phi\| < 3\sigma$ AND $\|emcsdz\| < 3\sigma$
TOF matching	$\|tofsd\phi\| < 3\sigma$ AND $\|tofsdz\| < 3\sigma$
Kaon p_T	> 0.4 GeV/c
π p_T	> 0.3 GeV/c
Kaon PID	2.5 σ for $0.4 < p_T < 1.5$ GeV/c
	OR
	1.5 σ for $0.4 < p_T < 1.8$ GeV/c
Pion PID	2.5 σ for $0.3 < p_T < 6.0$ GeV/c
Ghost Rejection Cut	$\|\Delta zed\| > 2.0$ OR $\|\Delta\phi\| > 0.1$

$tofsd\phi$, $tofsdz$ in TOF are used for matching in terms of σ. It is convenient to express the matching cuts in terms of σ which is independent of p_T, charge of the particle and sectors of the detector. Before applying cuts in terms of σ, recalibration is done to have a symmetric shape of the above mentioned distributions (e.g. $emcsd\phi$, $emcsdz$, $pc3sd\phi$, etc.). The details of recalibration is discussed in Section 3.2. In this analysis EMCal or PC3 match cut is applied. The TOF variables IsK, IsPi, IsP are commonly used in PHENIX for kaon, pion and proton PIDs, respectively. The track cuts are listed in the Table 3.1.

3.2 Data quality check

The quality of the data depends on the detector performance. The tracking detectors (DC and PC) and the spectrometers (EMCal and TOF) may have some imperfections (e.g. dead chambers, bad wires etc.) during the data taking period. To take these things in account, it is important to check the detector performance and recalibrate data. Recalibration of data is done before applying the cuts mentioned in Table 3.1. The Drift Chamber recalibration was taken from PHENIX ananote AN486. In this analysis the recalibration of EMCal, PC3, TOF and IsK functions were done for both "++" and "--" field configurations.

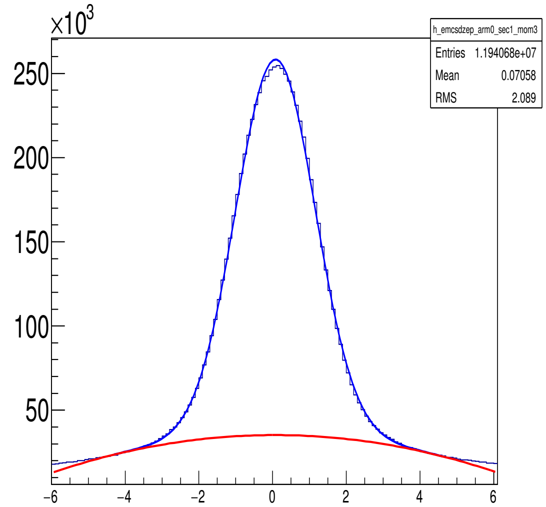

Figure 3.2: The 1D *emcsdz* distribution for p_T bin = 0.6 - 0.7 GeV/c, for the 1$^{\text{st}}$ sector of EMCal on east arm. The blue line represents the fit function gaussian plus second order polynomial. The red line represents the background shape fitted with second order ploynomial.

3.2.1 Method of recalibration

To calibrate any of the variables (e.g. $sd\phi$ and sdz for EMCal, PC3, TOF and isK), first a 2 D histogram is plotted for the variable say $sd\phi$ as a function of p_T. This 2 D histogram is then projected to $sd\phi$ axis, for different p_T bins. The resultant histogram looks like a gaussian with a sigma $\neq$ 1 and mean $\neq$ 0. In this analysis, these 1 D histograms are fitted with a gaussian and second order polynomial. The polynomial gives the shape of the background. The mean and the sigma are obtained from the gaussian. These sigma and mean values are used in the data as :

$$d\phi_{new} = (d\phi_{recorded} - mean)/sigma \tag{3.1}$$

which make the mean = 0 and sigma = 1 of sdϕ_{new} when plotted for different p_T bins. Figure 3.2 shows an example for the 1 D histogram for the *emcsdz* variable which corresponds to p_T bin = 0.6 - 0.7 GeV/c and the 1$^{\text{st}}$ sector of EMCal on east arm.

3.2.2 EMCal - $emcsd\phi$ and $emcsdz$ recalibration

The recalibration of EMCal is done by studying the parameters $emcsd\phi$ and $emcsdz$ as a function of p_T. The variables $emcsd\phi$ and $emcsdz$ are the standard deviations (expressed in terms of sigma (σ)) of $emcd\phi$ and $emcdz$, where,

$$emcd\phi = emc\phi_{projected} \text{ - } emc\phi_{hit} \quad \text{and} \quad emcdz = emcz_{projected} \text{ - } emcz_{hit}.$$

The variables $emcd\phi$ and $emcdz$ are the distances (in cm) between the projection point of a reconstructed track to the surface of the EMCal and closest hit position in ϕ and z direction respectively. These variables are not always zero because of the misalignment of detectors and also due to the momentum dependencies of these variables. The variables $emcsd\phi$ and $emcsdz$ are normalized with mean at zero and unit sigma. We recalibrate this variable for each EMCal sector for both positive and negative particle tracks. The method of recalibration is explained in Section 3.2.1. The mean and sigma of the uncalibrated distribution of $emcsd\phi$ as a function of p_T are shown in Fig. 3.3 for "++" field configuration. The calibrated distributions of the same are shown in Fig. 3.4. The eight figures for mean and sigma correspond to eight sectors of EMCal. The uncalibrated and calibrated distributions for $emcsdz$ as a function of p_T are shown in Appendix. C.1. Similarly, the calibration for the "- -" field are done.The figures are shown in Appendix. C.2.

3.2.3 PC3 - $pc3sd\phi$ and $pc3sdz$ recalibration

Similar to EMCal, recalibration is also done for PC3 by studying the $pc3sd\phi$ and $pc3sdz$ as a function of p_T. Each sector of the PC3 is recalibrated for positive and negative particles. The method of recalibration is stated in Section 3.2.1. The mean and sigma for uncalibrated and calibrated $pc3sd\phi$ and $pc3sdz$ distributions as a function of p_T are given in Appendix C.1 and Appendix C.2 for "++" and "- -" magnetic field configurations respectively.

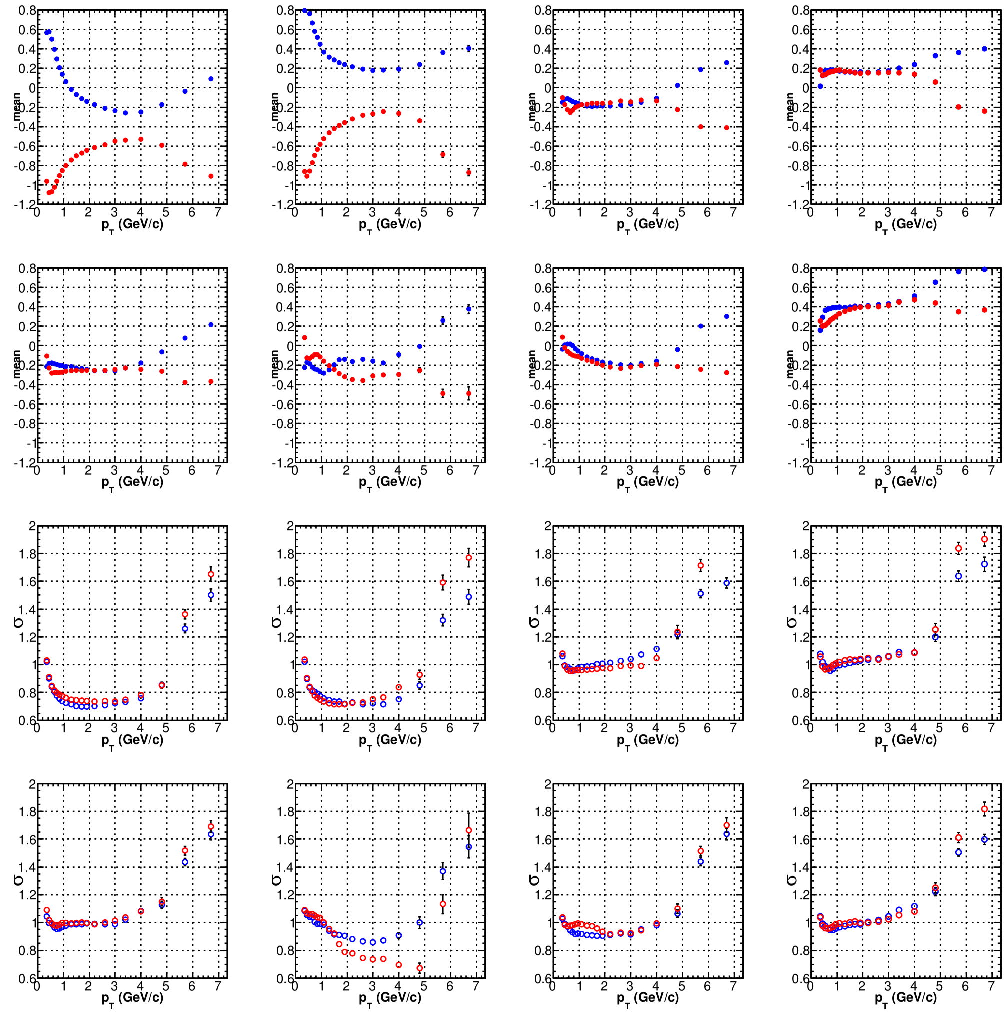

Figure 3.3: The $emcsd\phi$ distributions for eight sectors for normal field as a function of p_T without any calibration. The upper 8 plots are for the mean of $emcsd\phi$ and the lower 8 plots are the σ of $emcsd\phi$. The blue color markers are for the positive particle tracks and the red color markers are for the negative particle tracks.

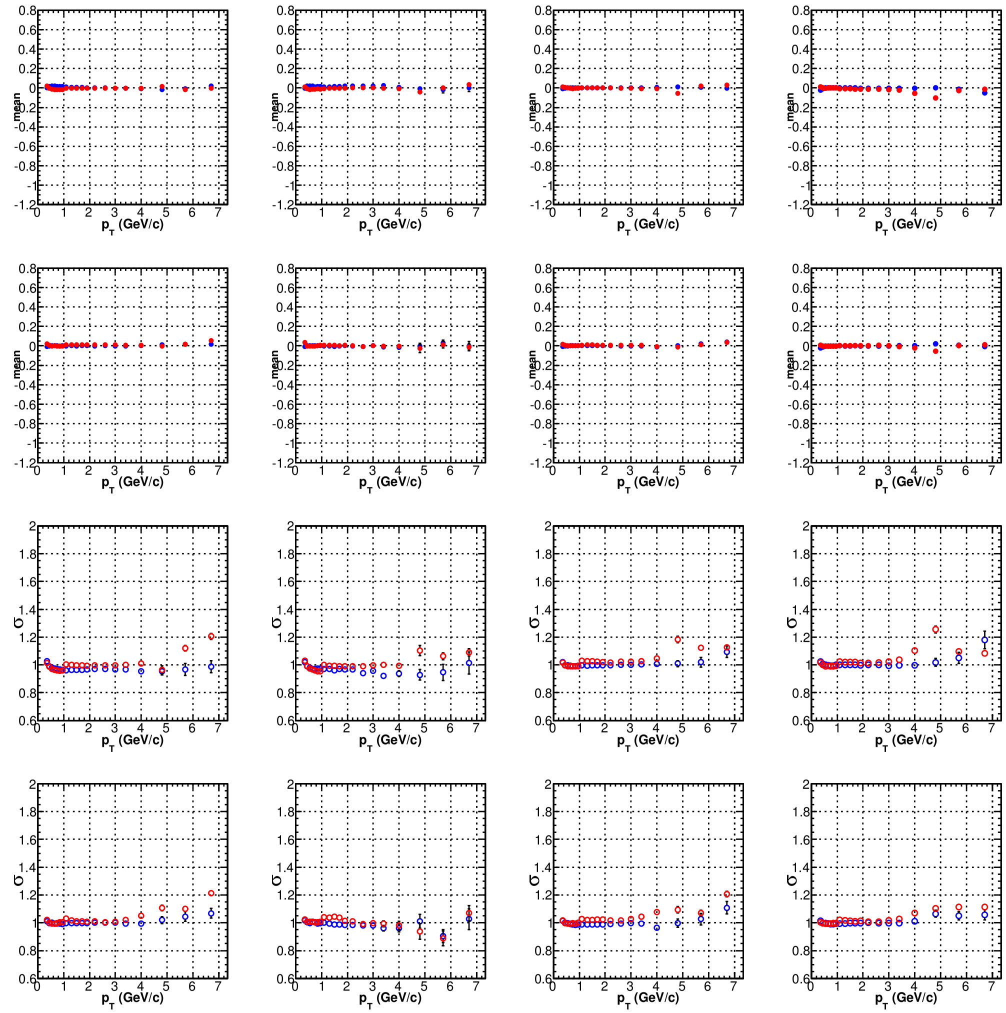

Figure 3.4: The $emcsd\phi$ distributions for eight sectors for normal field as a function of p_T after calibration. The upper 8 plots are for the mean of $emcsd\phi$ and the lower 8 plots are the σ of $emcsd\phi$. The blue color markers are for the positive particle tracks and the red color markers are for the negative particle tracks.

3.2.4 TOF - $tofsd\phi$ and $tofsdz$ recalibration

TOF is also recalibrated for the variables $tofsd\phi$ and $tofsdz$ in a similar manner as EMCal and PC3. The mean and sigma for uncalibrated and calibrated $tofsd\phi$ and $tofsdz$ distributions as a function of p_T are given in Appendix C.1 and Appendix C.2 for "++" and "- -" magnetic field configurations respectively.

3.2.5 IsK function recalibration

IsK function is defined as the relative deviation in sigmas of the mass squared measured using the high resolution TOF counter to that of kaon mass, taking into account the momentum dependent mass resolution. The mean and sigma for uncalibrated and calibrated isK distributions as a function of p_T are given in Appendix C.1 and Appendix C.2 for "++" and "- -" magnetic field configurations respectively.

3.3 Making pairs and extraction of raw yield

The K^{*0} meson is a resonance particle with mass 896 MeV/c^2 and lifetime of $\sim$ 4 fm/c. The K^{*0} ($\bar{K}^{*0}$) meson is reconstructed through its hadronic decay channel $K^+ \pi^-$ ($K^- \pi^+$) which has a branching ratio of $\sim$ 67%. These decay particles are identified in the Time of Flight Detector (Section 2.2). The track momentum is obtained from DC and PC1. Hence, the invariant mass spectrum of K^{*0} is reconstructed from these momenta and PID information.

When a particle decays to two or more daughter particles, the invariant mass of the parent particle can be reconstructed from the momentum and energy of the daughter particles. In case of two-body decay, the invariant mass of the parent particle is defined as,

$$m_{inv}^2 = (E_1 + E_2)^2 + (\vec{p_1} + \vec{p_2})^2. \quad (3.2)$$

$$(3.3)$$

The momentum ($|\vec{p}|$), the initial azimuthal angle ϕ_0 and polar angle θ_0 (Section 2.2.3) of the track are obtained experimentally. In PHENIX co-ordinate system, the Z axis is considered as the beam axis as shown in Fig. 2.3. Using the cylindrical polar co-ordinate system, the components of the momentum are given as;

$p_x = |\vec{p}|\ \sin\theta_0 \cos\phi_0 \quad p_y = |\vec{p}|\ \sin\theta_0 \sin\phi_0 \quad$ and $p_z = |\vec{p}|\ \cos\theta_0$.

As the Z axis is considered to be the beam axis, the colliding partons do not have significant transverse component of momentum. However, after collisions, all the effects take place in the transverse plane, i.e. X-Y plane. So instead of the longitudinal momentum (p_L), the transverse momentum (p_T) is of interest. In case of resonance particle, the transverse momentum of the parent particle is given as;

$$p^2_{T_{inv}} = (p_{x_1} + p_{x_2})^2 + (p_{y_1} + p_{y_2})^2 \tag{3.4}$$

In this analysis, m_{inv} is $M_{K^{*0}}$ and the daughter particles are the $K^+\pi^-$ for K^{*0} and $K^-\pi^+$ for $\bar{K}^{*0}$. The K^{*0} ($\bar{K}^{*0}$) invariant mass is reconstructed by combining the positive kaon and negative pion (negative kaon and positive pion) tracks in the same event. The aim of pair analysis is to extract the K^{*0} meson yield (Y) from the total signal (S) obtained from the combinations of the charged kaon and pion tracks. This procedure is described in the following subsections.

3.3.1 Total signal

The invariant mass distribution is obtained according to the Eq. 3.2, after applying the track cuts, kaon and pion PID cuts as listed in Table 3.1. Due to TOF's limited acceptance and to extend the K^{*0} measurement to higher p_T range, unidentified, oppositely charged tracks are included in this analysis. These tracks are required to have associated hits in PC3 or EMCal and are referred as PC3 matched tracks. Depending on track selection criteria, three different techniques are considered in this analysis.

1. Fully Identified : Both the tracks are identified as kaon and pion in TOF.

2. Kaon Identified : One of the track is identified in TOF as kaon and the other one is a PC3 - EMCal matched track to which pion mass is assigned.

3. Unidentified : Both tracks are PC3 matched tracks.

These three techniques are exclusive to each other and are statistically independent. The PC3 matched tracks are assigned a nominal mass of the pion or kaon depending on which technique is used. The p_T ranges accesible by different techniques in Cu+Cu system are : 1.4 - 4.0, 1.7 - 4.5 and 2.9 - 8.0 in "Fully Identified", "Kaon Identified" and "Unidentified" techniques respectively. The "Fully Identified" technique with both charged particles identified in the TOF has the highest signal-to-background ratio and provides access to K^{*0} meson measurement at low and intermediate p_T. The "Unidentified" technique has a poor signal-to-background ratio that prevents signal extraction at low p_T. Signal extraction at higher p_T (> 2.9 GeV/c) is possible because of the smaller combinatorial background. The p_T reach obtained by this technique is limited by the sampled luminosity i.e. statistics. The measurements performed with these three techniques have a wide overlap region that is used for evaluation of the systematic uncertainties.

The total signal is obtained by summing up the yield for each p_T bin within an invariant mass window of ± 75 MeV/c^2, which consists of both the signal and the background. In order to obtain the signal, the background is subtracted. The shape of invariant mass spectra are described by the Relativistic Breit Wigner distribution, discussed in detail in Section 3.3.3. The sources of background and its removal, the extraction of raw yield and the invariant yield after acceptance and efficiency correction are discussed the following subsections.

3.3.2 Background estimation and removal

The background in the invariant mass distribution comes due the combination of tracks in the same event. The sources of this background can be correlated or uncorrelated. The correlated background comes from different sources: e.g. elliptic flow in non - central nucleus - nucleus collisions, correlated real $K\pi$ pairs, correlated but mis-identified pairs etc. The detail of this can be found in Ref [79]. The uncorrelated background comes due the random combinations of tracks in the same event.

Removal of uncorrelated background :

The uncorrelated background can be estimated by the event mixing technique [80, 81, 82]. The event-mixing technique combines positive or negative charged tracks from one event with the opposite charged track from another event within the similar centrality class, which helps to generate the shape of the uncorrelated part of the combinatorial background. This technique is based on the fact that there are no physical correlations between oppositely signed tracks in artificially mixed events. In case of Cu+Cu data, tracks from a single event are mixed with tracks from 10 other events to generate the uncorrelated background. This mixed event background is subtracted from the total signal after proper normalization. There are certain methods for normalization. They are :

- The mixed event consisting of oppositely signed pairs can be normalised by the mass distribution of same signed pairs. Let N^{+-}_{mixed} be the integrated yield for oppositely signed mixed event pairs, N^{++} and N^{--} are the integrated yield of the same signed (++ and --) pairs in the same event. Then the normalization is given by,

$$N_{norm} = \frac{2 \times \sqrt{(N^{++} \times N^{--})}}{N^{+-}_{mixed}}, \tag{3.5}$$

  This method is valid if there is no correlation in the like-signed spectrum.

- The oppositely - signed mixed event distributions can be normalized to the measured oppositely - signed mass distribution above a certain mass $m > m_0$, only if there are no correlations in the measured oppositely - signed mass spectra above m_0.

- The mixed event distributions can be normalized by twice of the buffer size i.e $N_{norm} = 2N_{buff}$. This is valid if the particle multiplicity in the event follows a Poissonian Distribution.

In this analysis, the third method is used for mixed-event normalization.

Removal of mis-identified pairs :

The correlated part of the background comes from various sources. One of the sources of the background is due to mis-identified pairs. The ϕ meson decays to K^+K^- and the K^0_S meson decays to $\pi^+\pi^-$ channels. If the pion mass is assigned to one of these kaons from ϕ decay and kaon mass is assigned to one of these pions from K^0_S decay then these mis-identified pairs will create a smeared peak ($\sim$ 0.7 GeV/c^2) structures close to the K^{*0} mass peak. These contributions are estimated using the measured yields of ϕ meson and K^0_S meson. The location and shapes of these peaks are modeled by the PHENIX based simulations. The estimated contributions are then normalized by the number of events analyzed for K^{*0} meson and subtracted from the measured K^{*0} invariant mass distributions. Figure 3.5 shows the K^{*0} invariant mass distribution with all the background contributions for the "Kaon identified" technique for p_T = 2.3 - 2.6 GeV/c. The black histogram is the mixed event background after normalization, the magenta colored histogram is the mis-identified ϕ contributions and the green colored histogram is the mis-identified K^0_S contributions. The black line is the Relativistic Breit Wigner distribution (discussed in next Section) plus the third order polynomial. In order to get the signal, these backgrounds are subtracted.

The K^{*0} invariant mass distributions with the background contributions for all three analysis techniques and for all the measured p_T bins are given in Appendix C.3.1.

3.3.3 Raw yield extraction

Figure 3.6 shows the K^{*0} invariant mass distribution for different techniques for different p_T bins after removing the correlated background contributions from ϕ and K^0_S mesons. The

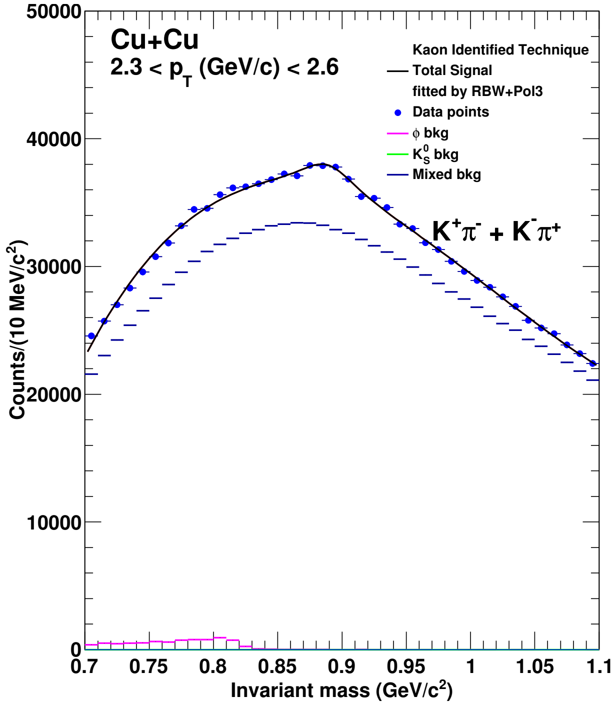

Figure 3.5: Invariant mass plots for Kaon Identified technique in Cu+Cu collisions for MB data. Blue symbols are the data points, black line is Relativistic Breit Wigner function plus third order polynomial fitted to the data points, red line is the third order polynomial as residual background, black histogram is the mixed event background. Magenta is the mis-identified pairs from ϕ and green one is the mis-identified pairs from K^0_S.

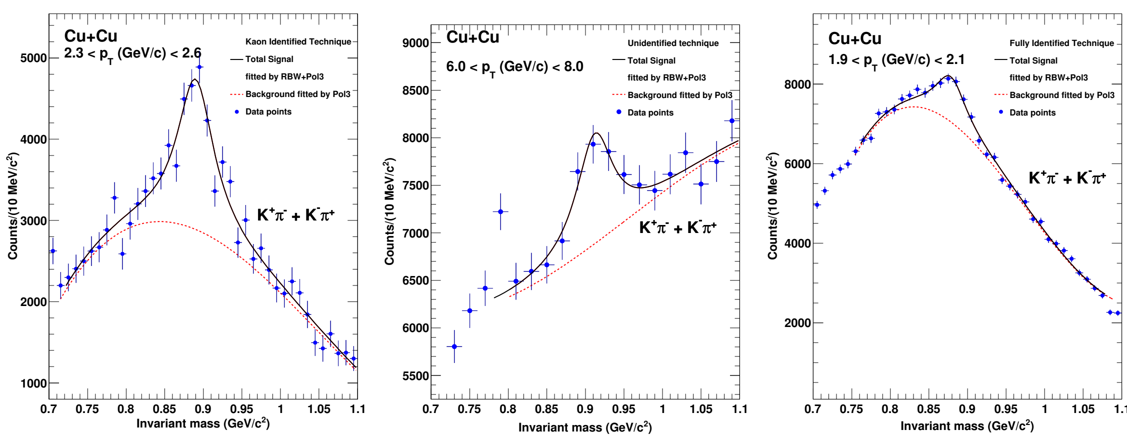

Figure 3.6: Invariant mass plots for K^{*0} meson in in Cu+Cu collisions for MB data. Blue symbols are the data points, black line is RBW function fitted to the data points, red line is the third order polynomial as residual background. The left most plot is for " Kaon Identified" technique, the middle plot is for "Unidentified" technique and the right most plots is for "Fully Identified" technique, plotted for different p_T bins.

residual background still exists. To extract the raw yield, the invariant mass spectra are fitted with a Relativistic Breit Wigner (RBW) and a 2^{nd} or 3^{rd} order polynomial depending on the shape of the residual background. The RBW is given as :

$$RBW = \frac{1}{2\pi} \frac{M_{K\pi} M_{K^{*0}} \Gamma}{(M_{K\pi}^2 - M_{K^{*0}}^2) + M_{K^{*0}}^2 \Gamma^2} \tag{3.6}$$

where, $M_{K\pi}$ is the reconstructed invariant mass, $M_{K^{*0}}$ is the fitted mass of K^{*0} meson and Γ is the width of K^{*0} meson fixed to the value obtained from simulation.

The raw yield in each p_T bin is summed up in the invariant mass window of $\pm$ 75 MeV/c^2 around the nominal mass of K^{*0} meson. The contribution from residual background is estimated by integrating the background component of the fit (second or third order polynomial) in the same mass window. The residual background contribution is subtracted from the total signal to obtain the raw yield for K^{*0} meson.

The K^{*0} invariant mass plots for all the measured p_T bins for all of the three techniques after removing contributions from mis-identified pairs are given in Appendix C.3.2.

3.4 Simulation

Simulation is an important part of data analysis. PHENIX Integrated Simulation Application (PISA) is used to correct the raw yields for detector acceptance and reconstruction efficiency. PISA is based on GEANT3 [83] code, which supports 24 different event generator interfaces. In PHENIX, EXODUS was developed as single particle event generator usually used for particle simulation. Other than EXODUS, one can use PYTHIA for single particle event generation in $p + p$ collisions. In heavy ion environment, for embedding correction, one can use embedding method (discussed later), or one can use the HIJING event generator for particle simulation.

3.4.1 EXODUS and PISA

EXODUS :

Exodus is the single particle generator developed within PHENIX. It works in an interactive way and also in batch mode. The Exodus package consists of several codes which are used to choose and specify the desired inputs, e.g. p_T distribution, p_T range, ϕ coverage, number of particles to be generated, particle to be generated, z_{vertex} range, rapidity range, type of generator one need to use etc. One can also decide if the generated particles should decay at the time of their generation or later. The outputs of Exodus are given in Oscar format, which looks like :

$ID \quad PID \quad p_x \quad p_y \quad p_z \quad E \quad M \quad x \quad y \quad z \quad 0.$

If some of the options are not there in the default settings of exodus, one can include them in the codes and run to get the desired output.

PISA :

PISA basically replicates the PHENIX detector volume and materials. The output of exodus are fed to PISA. The output of PISA is called "hits file", which is processed through the standard PHENIX reconstruction [74] software. In the detector response module software, information is obtained from the GEANT particle tracking through each detector subsystem and is converted into simulated detector signals. These simulated signals are very much like the real detector signals which appear on the real data obtained by the *online* system while taking data during experiment. Then these simulated detector signals are processed by the same software which reconstucts the real data files into useful physics information suitable for analysis. The reconstructed output is then treated in the same manner as the real data and is analyzed in the same way (codes, cuts etc.) that was done with data. For this analysis, the Run5 PISA environment is used.

Table 3.2: Inputs given to Exodus for the generation of K^{*0}

p_T	1 - 9 GeV/c
p_T distribution	Tsallis ($n = 9.75$, $T = 0.1128$ GeV)
particle generator type	single particle generator
no. of events	30 Million for K^{*0} and 30 Million for $\bar{K}^{*0}$.
rapidity range	$\pm$ 0.5
z_{vertex} range	$\pm$ 30 cm
ϕ coverage	$\pm$ 2π

3.4.2 K^{*0} simulation

3.4.2.1 Simulation inputs

The Exodus inputs for K^{*0} meson simulation are given in Table 3.2. The K^{*0} meson is simulated in the p_T range 1 - 9 GeV/c using the Tsallis distribution with parameters - $dN/dy = 1.0$, $n = 9.75$ and $T = 0.1128$ GeV.

For K^{*0} generation, some of the codes were modified. They are discussed below.

1. A new particle ID - 999 as well as particle properties were introduced for K^{*0} in `defined_particles.txt` as it is not there in default EXODUS.

2. A new option for the K^{*0} generation was added in `exodus_generate.cpp` and `InitializeSetup.cpp`.

3. The p_T spectrum shape for K^{*0} was generated using Tsallis distribution. For this, Tsallis distribution was added in `exodus_generate.cpp` and `GenerateSingleParticles.cpp`.

4. `event.par` - This is the PISA event generation configuration file. This is edited to make changes in vertex ditribution. The vertex distribution is set by ;
   `xyz0_input` = 0.0, 0.0, 0.0,
   `vrms` = 0.0, 0.0, 0.0,
   This `xyz0_input` corresponds to the mean vertex offset position along x, y and z

respectively, in cms. The term offset refers to the fact that the values assigned for `xyz0_input` (in this case, x = 0.0, y = 0.0, z = 0.0) are added to the vertex positions read from the exodus output files which are the input files to PISA. The `vrms` corresponds to the width of the generated distribution along x, y and z respectively, in cms. A positive value means that a Gaussian distribution is generated. A negative value means that a flat ditribution is generated. A zero value means that no distribution is generated and the vertex offset is added unchanged to the vertex read from the pisa input file. The default values should be all zero, which corresponds to no vertex generation, in which case the vertex read from the file used as an input to PISA is left unchanged.

5. `pisa.kumac` - This is the main PISA configuration file. This file contain several information related to detectors, magnetic field, GEANT commands etc. One can turn "off" and "on" the detectors as per requirements. The sign of magnetic field can also be chosen. By default the magnetic field is given as ;

   MAGF '3D+-' 1.00 0001 0.0 0.0

   "+-" corresponds to bulking field and "++" and "--" corresponds to normal and reverse field. One can change the field configuration according to the Run that one has used.

   To have "++" field one should use MAGF '3D++' 1.00 0001 0.0 0.0

   To have "--" field one should use MAGF '3D++' -1.00 0001 0.0 0.0

   To check the alignment, zero field is needed. For that one can put 0.

3.4.3 Acceptance correction

The simulated data files are analyzed in the same way, as the data. The correction factor (ϵ (p_T)) for a given p_T bin is defined as :

$$\epsilon\ (p_T) = N_{\text{reconstructed}}/N_{\text{generated}}.$$

where, $N_{\text{generated}}$ is the number of events generated and $N_{\text{reconstructed}}$ is the number of events reconstructed after passing the generated events through PISA. This correction ($\epsilon\ (p_T)$) includes both the geometrical acceptance correction and correction for reconstruction efficiency. This correction factor ($\epsilon\ (p_T)$) is further needed to be corrected for the difference in z_{vertex} distribution for data and simulation and also for the heavy ion environment. These corrections are incorporated as :

1. The z_{vertex} distribution for data is peaked around center (i.e. $z_0^{BBC} = 0$) as shown in Fig. 3.1. In case of simulation we had a flat z_{vertex} distribution. One need to correct this, as the number of events are more around $z_{vertex} = 0$ in data and falls off at $z_{vertex} > 0$. The z_{vertex} histogram for data is normalized by the same in simulation and as a function of vertex and the correction factors are obtained. The correction factors are used as weights and $\epsilon\ (p_T)$ is recalculated.

2. The embedding correction is done as follows :

We obtained the embedding correction for Cu+Cu system for different centrality classes using the correction factors in Au+Au from the ananote AN016. The embedding correction for a certain N_{part} value (for certain centrality bin) in Cu+Cu collision system is obtained from the embedding correction for similar N_{part} value in Au+Au collisions . In the ananote, AN016, the embedding correction was given for the single charged tracks as well as for the combined tracks. In this analysis, the embedding correction for the combined tracks are used. The embedding corrections are given in the Table. 3.3. The invariant mass plots for simulated data are shown in Figures 3.7, 3.8 and 3.9. The correction factor $\epsilon\ (p_T)$ for different analysis techniques are shown in Fig. 3.10.

Figure 3.11 shows the mass and width parameters for all three techniques, obtained from fitting of the K^{*0} invariant mass spectra for simulation. While fitting the invariant mass distributions for data, the widths were kept fixed to what was obtained from simulation. The mass parameter was kept free. The mass parameter as a function of p_T is shown in

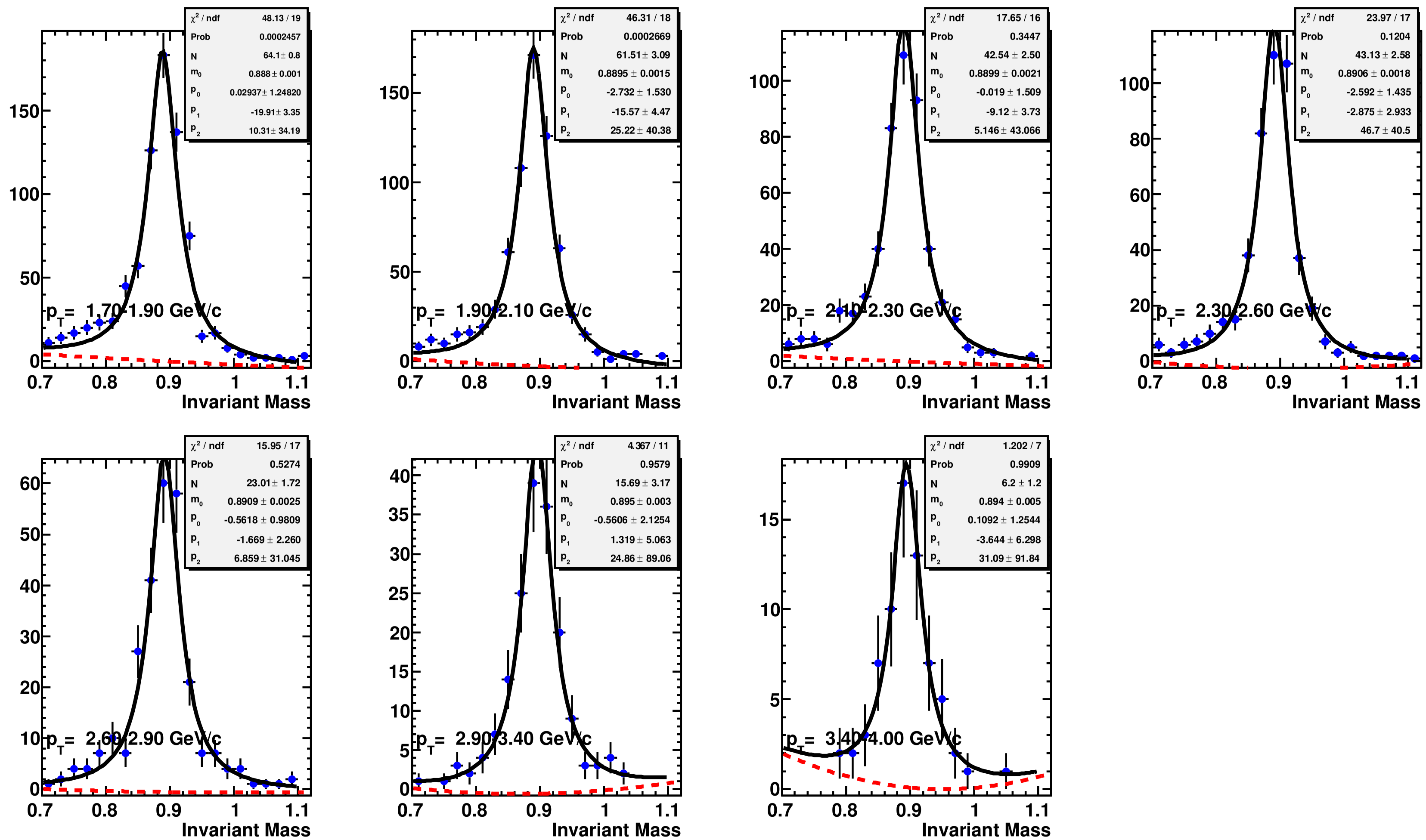

Figure 3.7: Invariant mass plots for Kaon Identified technique in Cu+Cu collisions for MB data. Blue symbols are the data points, black line is RBW function fitted to the data points, red line is the third order polynomial as residual background.

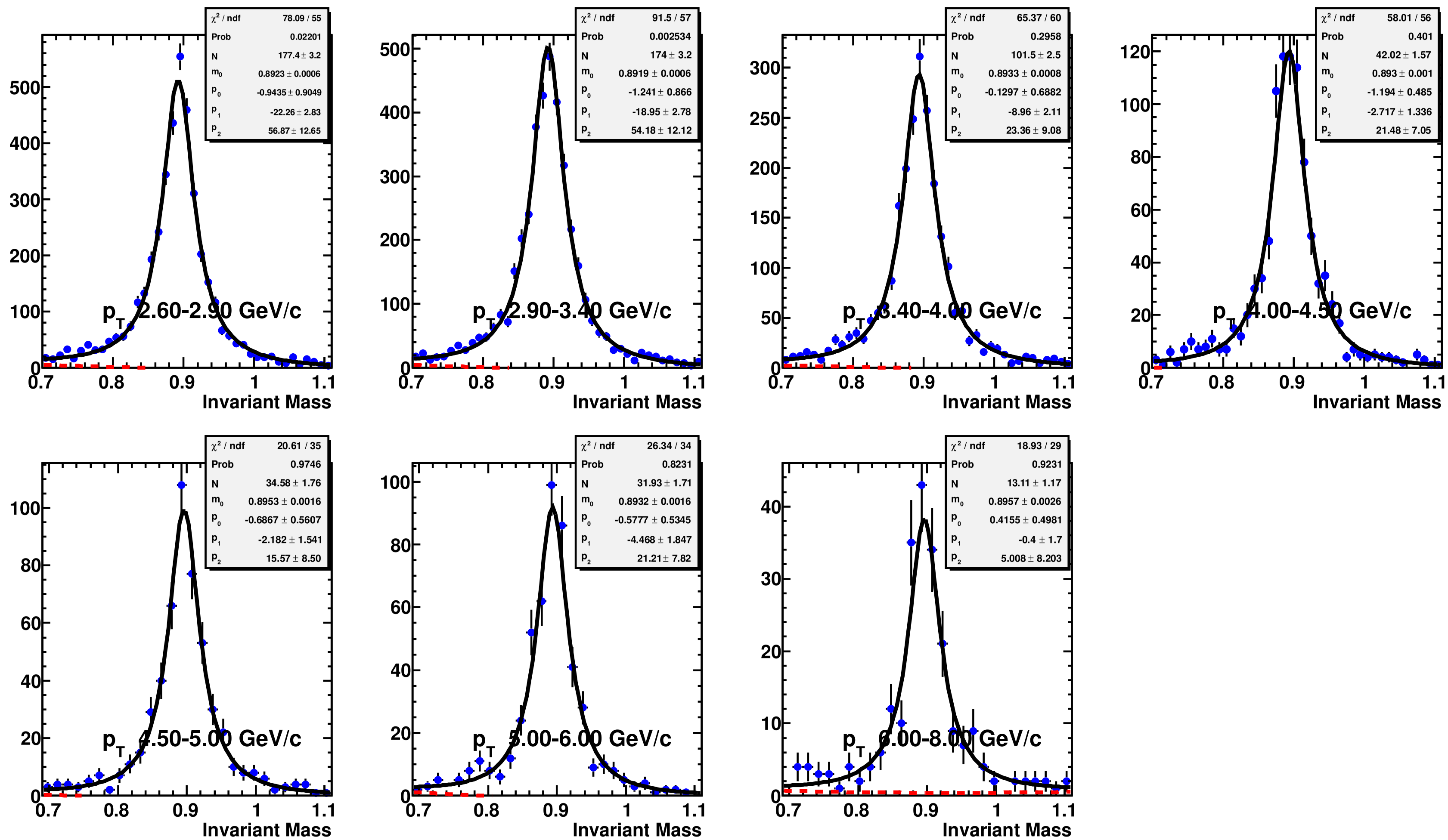

Figure 3.8: Invariant mass plots for Unidentified technique in Cu+Cu collisions for MB data. Blue symbols are the data points, black line is RBW function fitted to the data points, red line is the third order polynomial as residual background.

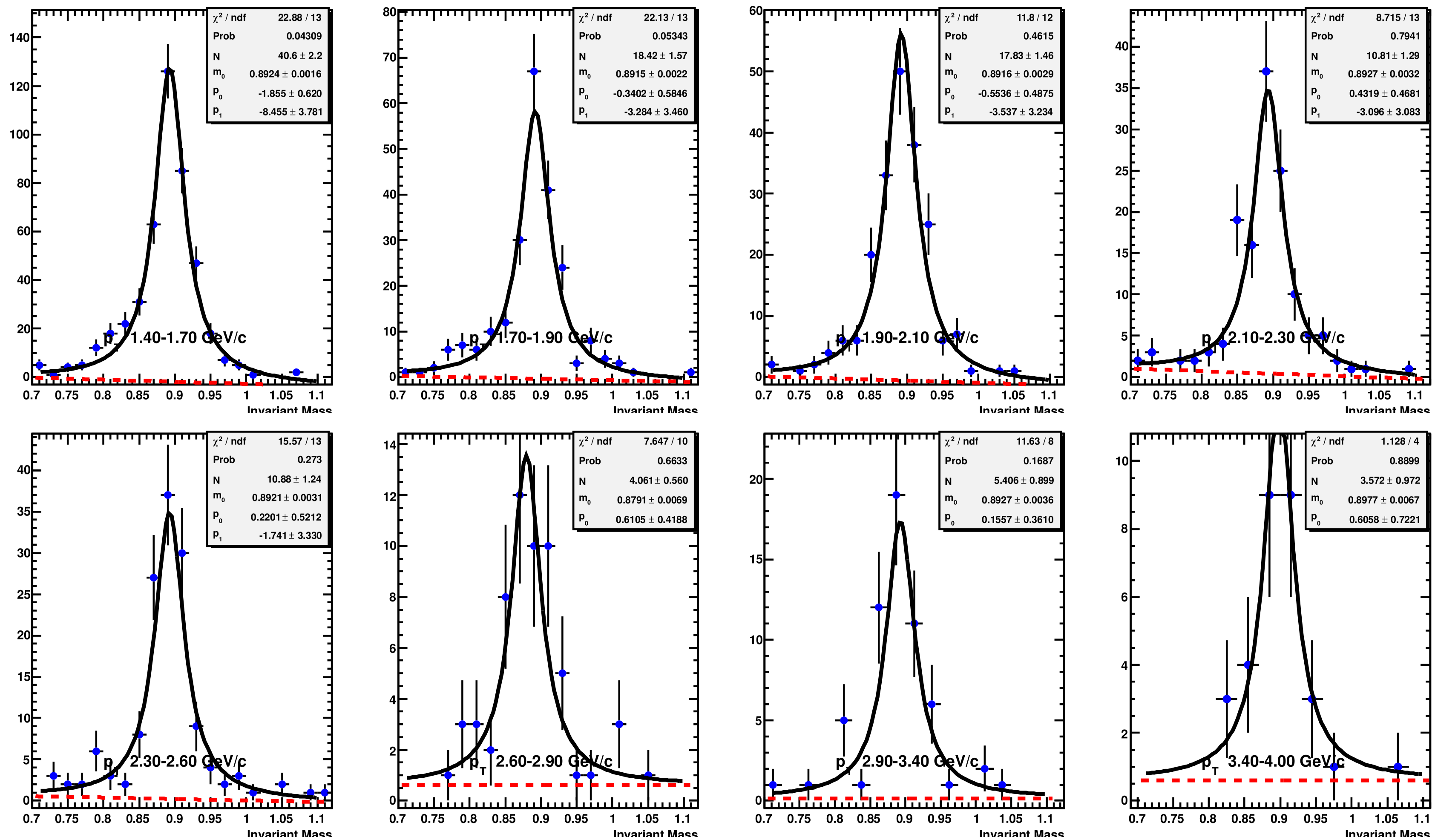

Figure 3.9: Invariant mass plots for Fully Identified technique in Cu+Cu collisions for MB data. Blue symbols are the data points, black line is RBW function fitted to the data points, red line is the third order polynomial as residual background.

Table 3.3: Emebedding corrections for different analysis techniques and for different centralities.

Cu - Cu centrality (%)	N_{part}	Au - Au centrality (%)	Embedding correction factor for Kaon Identified	Embedding correction factor for Unidentified	Embedding correction factor for Fully Idenified
Min Bias	34.6	55 - 60	0.9786	0.9582	0.9571
0 - 20	85.9	40 - 45	0.9534	0.9286	0.9675
20 - 40	45.2	50 - 60	0.9786	0.9582	0.9571
40 - 60	21.2	65 - 70	0.9815	0.9751	0.9956
60 - 94	6.4	80 - 92	0.9964	0.9876	1.0000

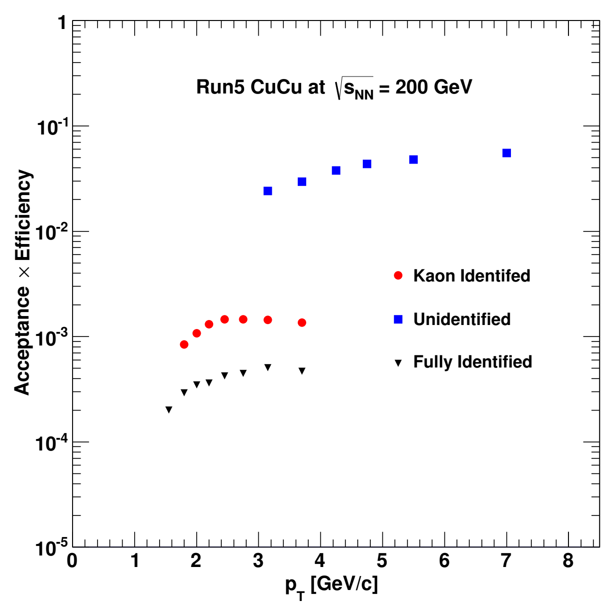

Figure 3.10: The acceptance×reconstruction efficiency for all three analysis techniques for K^{*0} analysis in Cu+Cu system.

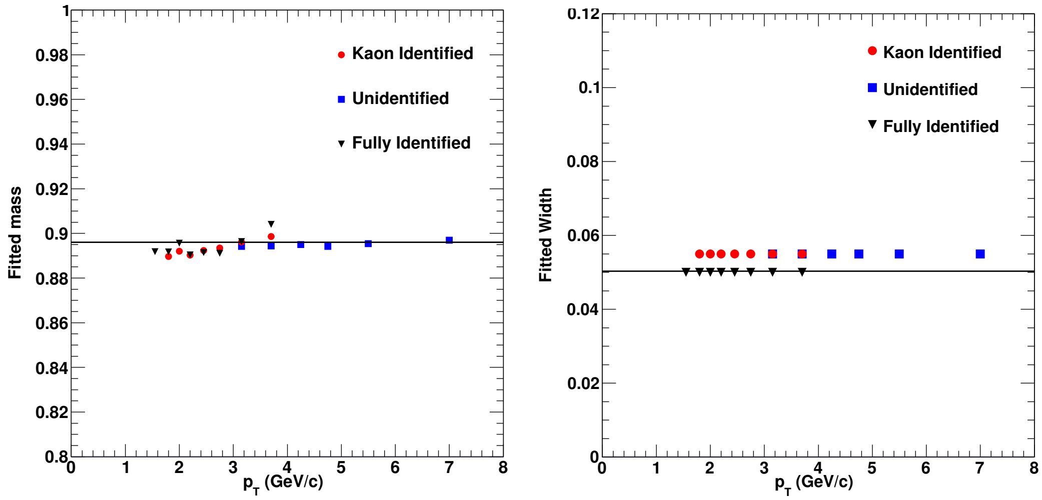

Figure 3.11: The mass and width parameter obtained from invariant mass spectra fitting for all three techniques in case of simulation.

Fig. 3.12 for data.

3.5 Invariant yield

The invariant yield is defined as :

$$E\frac{d^3N}{dp^3} = \frac{d^2N}{2\,\pi\,p_T\,dp_T\,dy} \tag{3.7}$$

In experiment the invariant yield is obtained from the raw yield (Section 3.3.3) as follows :

$$\frac{1}{2\pi p_T}\frac{d^2N}{dp_T dy} = \frac{1}{2\pi p_T \Delta p_T \Delta y} \times \frac{Y_{raw}}{N_{evt}\,\epsilon(p_T)\,BR} \times C_{bias}, \tag{3.8}$$

where,

- Y_{raw} is the K^{*0} raw yield. (Section 3.3.3).
- $N_{evt} = 5.886 \times 10^8$ is the total number of events analyzed.
- $\epsilon(p_T)$ is the reconstruction efficiency folded with detector acceptance and also includes

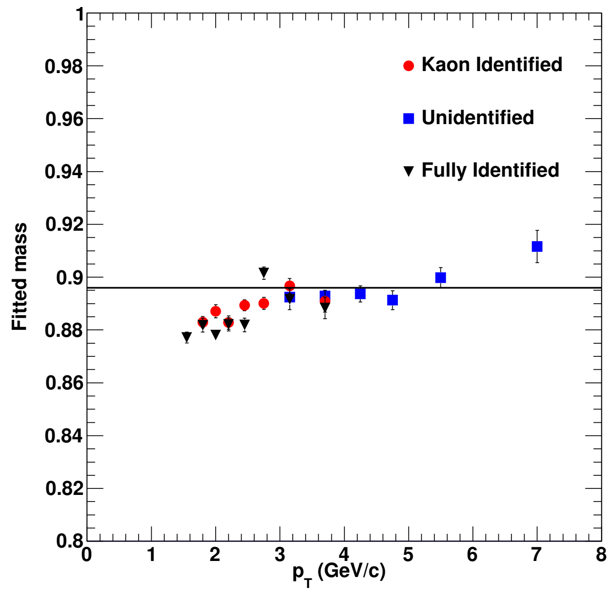

Figure 3.12: The mass parameter obtained from invariant mass spectra fitting for all three techniques in case of data.

the correction for the embedding in heavy ion collisions. (Section 3.4)

- BR is the branching ratio of $K^{*0} \rightarrow K^{\pm}\pi^{\mp} \sim 67\%$ (Ref [9]).
- $C_{bias} = \epsilon_{BBC}/\epsilon_{bias} = 1$ for Cu+Cu system. (For details See Chapter 2.)

3.6 Systematic uncertainties

The systematic errors arise due to various methods of extracting yield and also arise from the efficiency in momentum reconstruction. The systematic errors are calculated by the following method:

Syst error 1 (Peak extraction error): The peak extraction error is obtained as follows:
1. Bin counting range variation : By varying the mass window for bin counting. Two mass windows (0.80,0.99) and (0.83,0.96) are used for bin counting error estimation.
2. Fitting range variation: If the fitting range is (L, U) then it is changed to (L $\pm$ 0.02, U $\mp$ 0.02) GeV to extract the signals.

3. Varying mass, width parameters of the invariant mass peak : In course of obtaining the raw yield, the mass parameter was free but the width parameter was fixed to the width obtained from simulation. To estimate the systematic due to this, both mass and width were fixed to the simulated value and yield is obtained. Also, the variation of width by $\pm$ 2% is included to obtain the systematic errors.

4. The raw yield is obtained from the integral method along with bin counting method.

Syst error 2 (Matching error): The (PC3 OR EMC) matching used is 3 σ. Two more sets are generated with matchings 2.5 σ and 3.5 σ for both simulation and data. The standard deviation in yields with respect to yield using 3 σ gives error.

Syst error 3 (TOF PID error): Two intervals are used for kaon PID in TOF.

(2.3 σ for 1.5 $< p_T <$ 0.4 GeV/c OR 1.3 σ for 1.8 $< p_T <$ 0.4 GeV/c)

(2.7 σ for 1.5 $< p_T <$ 0.4 GeV/c OR 1.7 σ for 1.8 $< p_T <$ 0.4 GeV/c)

Sys error 4 (mom scale error): The momentum was changed by $\pm$ 0.5% in the simulation and the error in the reconstruction efficiency is obtained. The corresponding error in the yield gives the mom scale error.

Calculation of systematic error:

Each of the above error is obtained by calculating standard deviation in yield with respect to that for fit using standard procedure. The standard deviation is given by

$$\sigma = \sqrt{\frac{1}{N}\sum_{i}^{N}(x_i - \mu)^2} \tag{3.9}$$

In this case "i" is the number of sources in each method, e.g as in first case i.e. peak extraction case there are 7 sources namely increasing the fitting range, decreasing the fitting range, increasing and decreasing width of the peak, fixing mass and width of the peak, variation of width and peak extraction by integral method. Say if Y_1, Y_2, Y_3,Y_4, Y_5, Y_6 and Y_7 are the yield (for the same p_T bin) in the respective cases and Y is the yield without any correction. Then the systematic error is for this **Peak extraction Error** is given by:

$$\begin{aligned} e_{sys1} &= (\frac{1}{7}[(Y_1 - Y)^2 + (Y_2 - Y)^2 + (Y_3 - Y)^2 \\ &+ (Y_4 - Y)^2 + (Y_5 - Y)^2 + (Y_6 - Y)^2 + (Y_7 - Y)^2])^{1/2} \end{aligned} \tag{3.10}$$

Similarly e_{sys2}, e_{sys3}, e_{sys4} are calulated for the **Matching Error**, **Momentum scale Error** and **TOF PID Error**.

The total systematic error is then obtained by.

$$e_{sys} = \sqrt{e^2_{sys1} + e^2_{sys2} + e^2_{sys3} + e^2_{sys4}}. \tag{3.11}$$

This is done for all p_T bins and for all analysis techniques.

Averaging over all the analysis techniques is done as following. If the yields and errors in Technique1 for a particular p_T bin are Y_{tof} and e_{systof} and in Technique2 are Y_{pc3} and e_{syspc3} where e_{systof} and e_{syspc3} are taken as total errors excluding the momentum scale error, then the average yield is obtained as.

$$Y_{av} = \frac{(Y_{tof}/(e^2_{systof} + e^2_{stattof}) + Y_{pc3}/(e^2_{syspc3} + e^2_{statpc3}))}{(1/(e^2_{systof} + e^2_{stattof}) + 1/(e^2_{syspc3} + e^2_{statpc3})}. \tag{3.12}$$

Then each type of error on average is obtained in terms of corresponding type of errors in the techniques as

$$E_{av} = \frac{1}{\sqrt{(1/e^2_{systof} + 1/e^2_{syspc3})}}. \tag{3.13}$$

The errors due to differences between different techniques are obtained as follows:

$$e_{sysSets} = \sqrt{((Y_{tof} - Y_{av})^2 + (Y_{pc3} - Y_{av})^2)/2}. \tag{3.14}$$

The error due to the acceptance correction is also included while obtaining the average error.

After obtaining the systematic error in each case, we have fitted the errors (by second order polynomial) as a function of p_T and thereby the fluctuations in each of the systematic error is corrected by smoothening the error over p_T. The total error is obtained as described above.

It is seen that we do not have data in certain p_T bins in some techniques. This gives rise to large $e_{sysSets}$. For some p_T bins we have large error due to sets and for some other we have no error. This is fixed by averaging the systematic error over the sets $e_{sysSets}$ and applying the averaged value for all the p_T bins.

Bin Shift Correction

The bin shift correction is done as given in the ananote AN73 [84]. In the first step the yields are obtained at the center of the p_T bin. This spectrum is then fitted with Tsallis function (Eq. 3.16) f(p_T). The correction factor for each p_T bin is obtained as;
Correction Factor = f(Center of the p_T bin)/Mean.

$$Mean = \frac{1}{\Delta p_T} \int_{\text{binlow}}^{\text{binup}} f(p_T) dp_T, \tag{3.15}$$

where Δp_T is the binwidth, binlow and binup are the lower and upper edge of the bin. The fitting to the Tsallis function is done again after this correction.
The Tsallis funtion is given by:

$$\frac{1}{2\pi} \frac{d^2N}{dydp_T} = \frac{1}{2\pi} \frac{dN}{dy} \frac{(n-1)(n-2)}{(nT + m(n-1))(nT + m)} \times \left(\frac{nT + m_T}{nT + m} \right)^{-n} \tag{3.16}$$

CHAPTER 4
RESULTS FROM K^{*0} MEASUREMENTS

This chapter presents the result of K^{*0} meson in Cu+Cu collisions at $\sqrt{s_{NN}} = 200\,\mathrm{GeV}$. The nuclear modification factor of K^{*0} meson in the Cu+Cu collisions is compared to that of the strange mesons (ϕ and K^0_S), light quark mesons ($\pi^{\pm}$, π^0, η etc.) and baryons (e.g. p, $\bar{p}$). The comparison of the behavior of K^{*0} and ϕ mesons in the presence of the hot/dense medium is of importance as both of them are resonance particles with strange quark content. The ϕ meson is a hidden strange particle ($s\,\bar{s}$) with a lifetime of $\sim 46\ fm/c$, whereas, K^{*0} meson is an open strange particle ($d\,\bar{s}$) with a lifetime of $\sim 4\ fm/c$.

To have a detailed study, the invariant transverse momentum spectra have been obtained for MB and 0–20%, 20–40%, 40–60% and 60–94% centralities. The nuclear modification factor for these centralities have been obtained.

4.1 Invariant mass spectra

In Chapter 3, the analysis procedure has been discussed. The invariant yield as a function of p_T is obtained as described in Eq. 3.8. The fully corrected invariant K^{*0} p_T spectrum for minimum bias data is shown in Fig. 4.1. The different symbols in the Fig. 4.1 (a) correspond

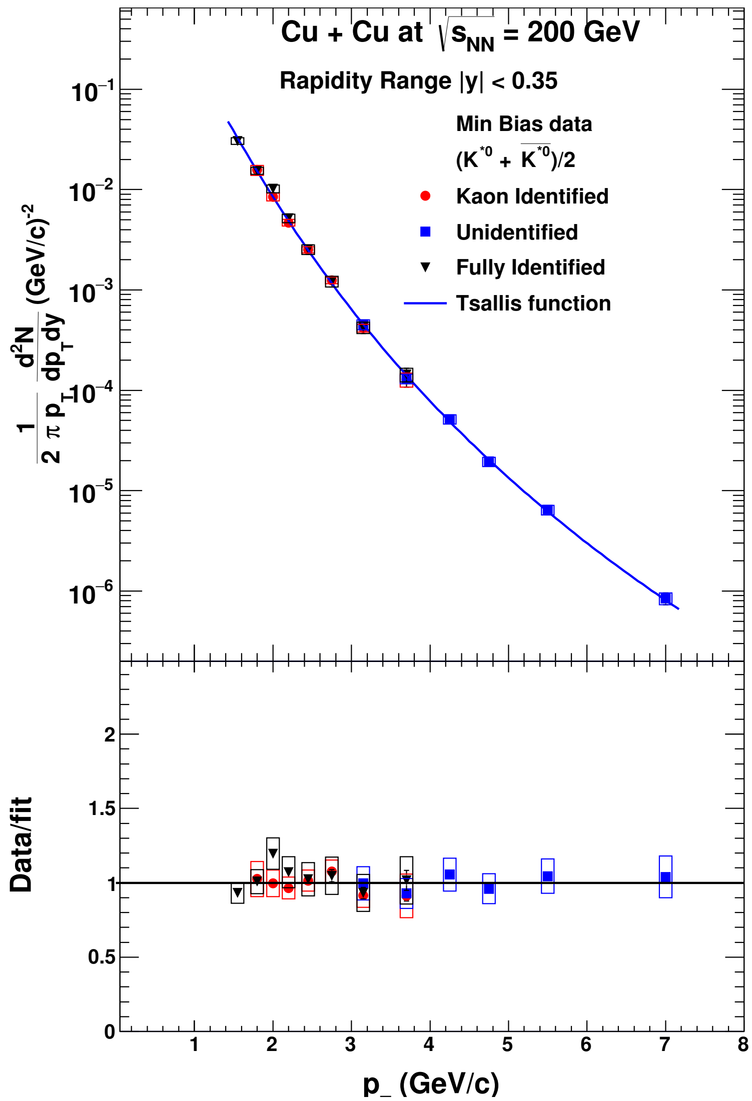

Figure 4.1: (a) Invariant yield of K^{*0} as a function of p_T obtained with the "Kaon identified", "Unidentified" and "Fully identified" analysis techniques in Cu+Cu collisions at $\sqrt{s_{NN}} = 200\,\text{GeV}$. The systematic uncetainties shown with the boxes are mostly uncorrelated between analysis techniques. The solid blue line is the Tsallis fit to the combined data points. (b) Ratio of the yields obtained with the three analysis techniques to the fit function. The scale of uncertainy of 10% is not shown.

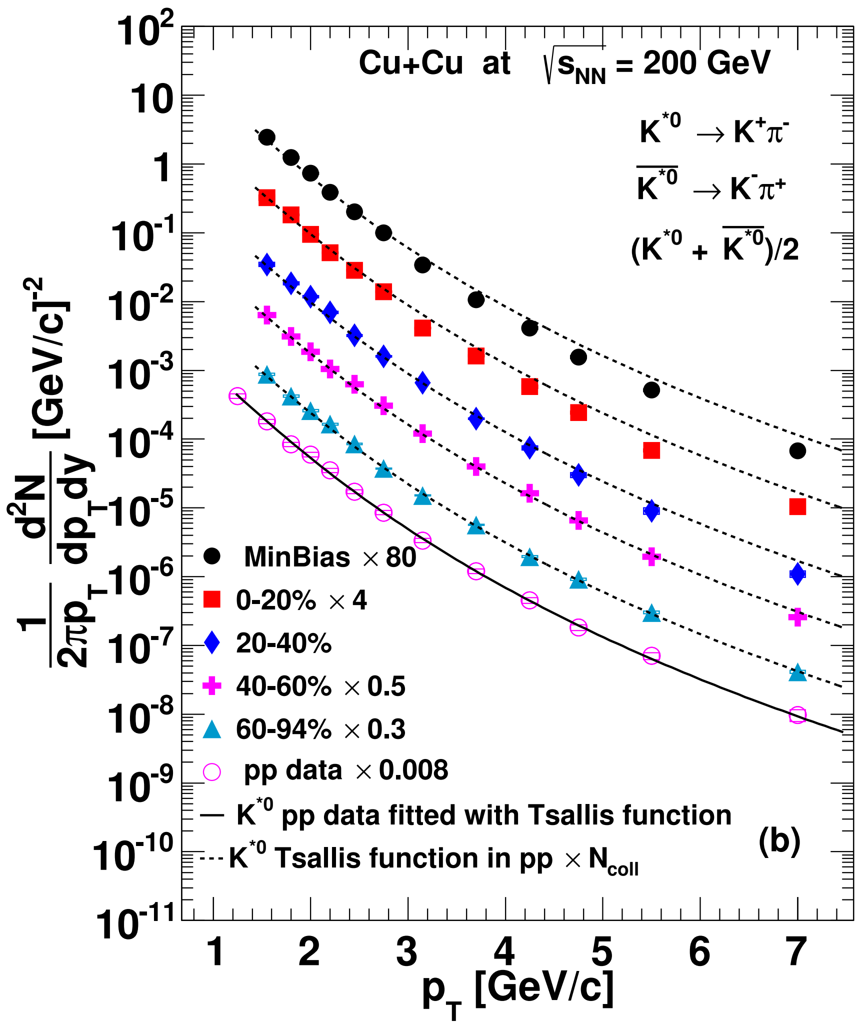

Figure 4.2: K^{*0} invariant p_T spectra for Cu+Cu collisions at $\sqrt{s_{NN}} = 200\,\mathrm{GeV}$ for different centrality bins. The systematic uncertainties are shown by boxes. The solid curve is a fit of the K^{*0} $p+p$ data by the Tsallis function. The dashed curves are the fit function scaled by N_{coll}. The global $p+p$ uncertainty of 10% is not shown.

to the invariant yield obtained from different analysis techniques (Section. 3.3.1) for MB data set. The systematic uncertainties are mostly uncorrelated for different techniques, shown by the boxes. The solid line in Fig. 4.1 (a) is the result of the common fit of the data with the Tsallis [85] function, given by;

$$\frac{1}{2\pi}\frac{d^2N}{dydp_T} = \frac{1}{2\pi}\frac{dN}{dy}\frac{(n-1)(n-2)}{(nT+m(n-1))(nT+m)} \times \left(\frac{nT+m_T}{nT+m}\right)^{-n} \tag{4.1}$$

where, dN/dy, n, T are the free parameters, $m_T = \sqrt{p_T^2 + m^2}$ and m is the K^{*0} mass. The parameter T determines the shape of the spectrum at low p_T where the particle production is dominated by soft processes. The parameter n governs the high p_T part of the spectrum where the particles are produced by the hard parton-parton scatterings. A good agreement is seen among the yields from different analysis techniques. Figure 4.1 (b) shows the ratio of the K^{*0} yields obtained with the three analysis techniques to the fit function. A good agreement is observed for the yields obtained with different analysis techniques which confirms the robustness of analysis. The final K^{*0} p_T spectrum is obtained by standard weighted averaging of the yield obtained from different techniques.

Figure 4.2 shows the invariant transverse momentum spectra of K^{*0} meson in Cu+Cu collisions for MB, 0–20%, 20–40%, 40–60% and 60–94% centrality bins. The results are scaled by arbitrary factors for clarity. The magenta colored open circles show the invariant transverse momentum spectrum for K^{*0} meson in $p+p$ collisions at $\sqrt{s} = 200$ GeV. The black solid line represents the Tsallis fit to the $p+p$ data. The dashed curves represent the same fit scaled by the number of binary collisions corresponding to the centrality bins concerned (Table 4.1). In central and semi-central Cu+Cu collisions, the production of K^{*0} is suppressed for $p_T > 2$–3 GeV/c, whereas, the peripheral spectrum follows binary scaling.

As the K^{*0} meson is a resonance state of kaon, it is interesting to find out the K^{*0}/π^0 ratio for different centralities in Cu+Cu collisions at $\sqrt{s_{NN}} = 200\,\mathrm{GeV}$. Figure 4.3 shows the K^{*0}/π^0 ratio for 0–20%, 20–40%, 40–60% and 60–94% centralities in Cu+Cu collisions.

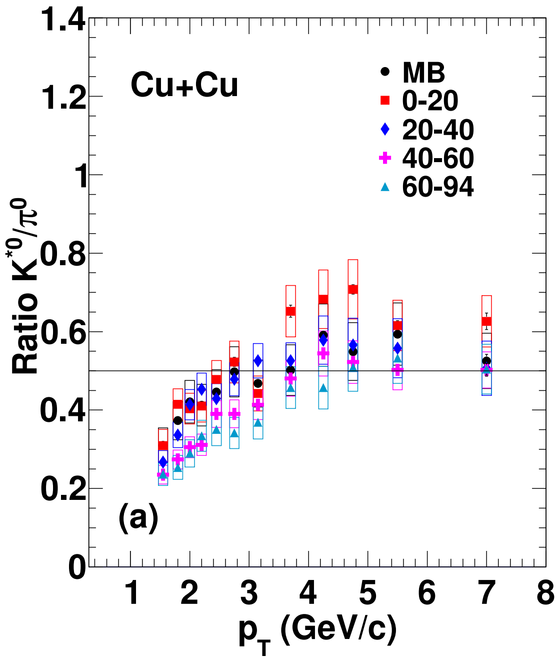

Figure 4.3: K^{*0}/π^0 ratio for 0–20%, 20–40%, 40–60% and 60–94% centralities in Cu+Cu collisions at $\sqrt{s_{NN}} = 200$ GeV. The statistical errors are shown by vertical bars and systematic errors are shown by boxes.

It is seen that, from low p_T to high p_T, this ratio increases and saturates to 0.5 for $p_T > 3$ GeV/c for all centralities within uncertainties.

4.2 Nuclear modification factor

The nuclear modification factor (R_{CuCu}) for K^{*0} meson is obtained from the ratio of the yield of K^{*0} in Cu+Cu collisions and the yield in $p + p$ collisions scaled by the nucleon-nucleon binary collisions ($\langle N_{\mathrm{coll}} \rangle$) for the corresponding centrality bin (Section 1.5.6). The values for $\langle N_{\mathrm{coll}} \rangle$ used in this analysis are listed in the Table. 4.1 for different centrality bins.

Figure 4.4, shows the nuclear modification factor for K^{*0} meson for different centrality bins in the measured p_T range (1.4–8.0 GeV/c). It is seen that the suppression decreases from central to peripheral collisions. For the most central collisions (0–20%), K^{*0} suffers

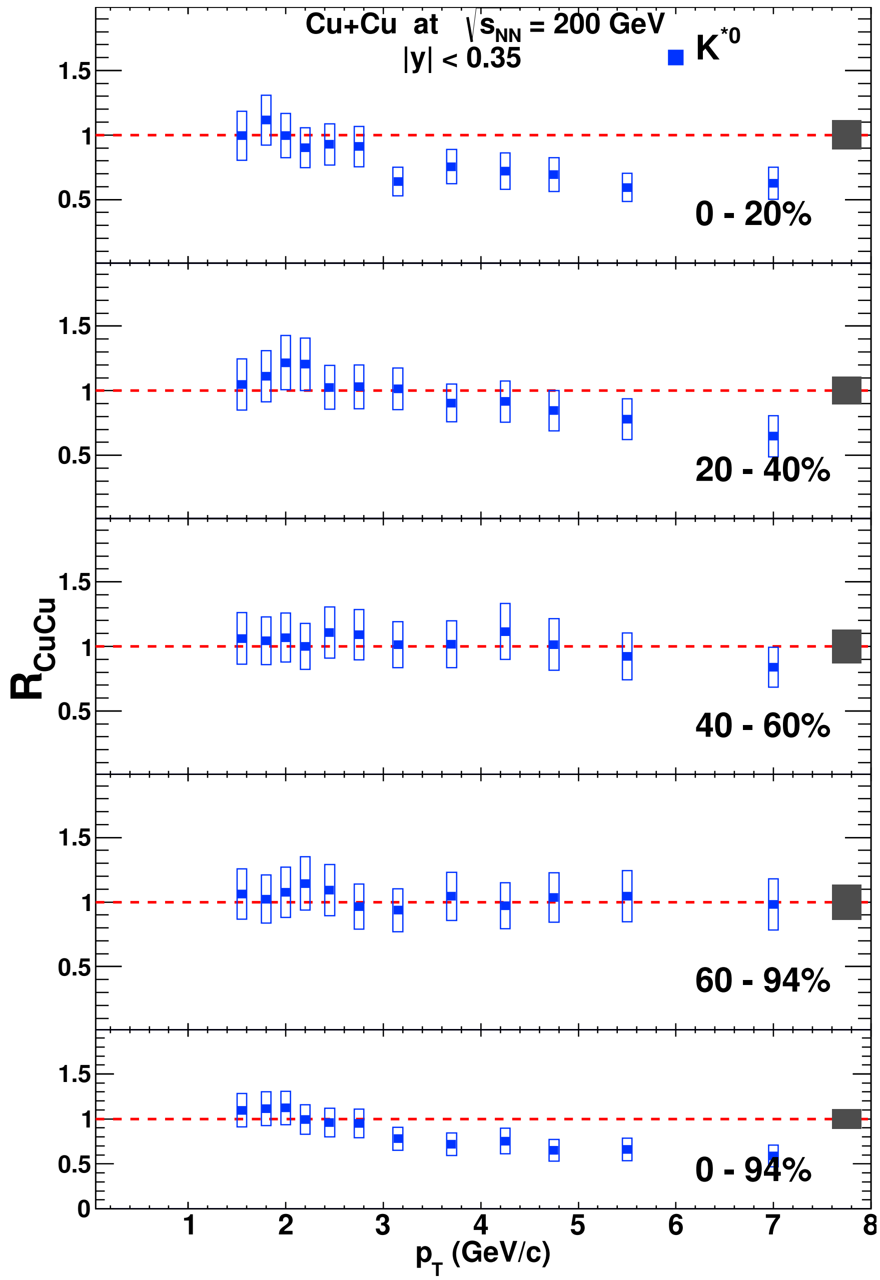

Figure 4.4: Nuclear modification factor for K^{*0} for 0–20%, 20–40%, 40–60% and 60–80% centrality bins in Cu+Cu collisions at $\sqrt{s_{NN}} = 200\,\text{GeV}$.

Table 4.1: The $\langle N_{\rm coll}\rangle$ and $\langle N_{\rm part}\rangle$ for different centralities used in this analysis

Centrality (%)	$\langle N_{\rm coll}\rangle$	$\langle N_{\rm part}\rangle$
0–20	151.8 ± 17.1	85.9 ± 2.3
20–40	61.6 ± 6.6	45.2 ± 1.7
40–60	22.3 ± 2.9	21.2 ± 1.4
60–94	5.1 ± 0.7	6.4 ± 0.4
0–94	51.8 ± 5.6	34.6 ± 1.2

significant suppression for $p_T > 3$ GeV/c. For the most peripheral centrality bin (60–94%), the nuclear modification factor is unity within uncertainties.

Figure 4.5, shows the comparison of nuclear modification factor between K^{*0} meson and ϕ [86] meson. It is seen that for the most peripheral bin, both the mesons follow binary scaling, hence the nuclear modification factor is consistent with unity within uncertainties. For the most central collisions, both the meson suffer suppression and for $p_T > 5$ GeV/c, the suppression is around 0.5. In the most central collisions, K^{*0} meson is more suppressed than that of ϕ meson. Below $p_T = 2$ GeV/c, none of the mesons are suppressed within uncertainties.

Figure 4.6 compares the $R_{\rm CuCu}$ results for K^0_S and K^{*0} mesons to the results obtained for the π^0 meson [87] and ϕ meson [86] in the most central, most peripheral, and MB Cu+Cu collisions. In peripheral collisions, the nuclear modification factors are consistent with unity for all measured mesons at all p_T. In central and MB collisions, for $p_T \geq 5\,$GeV/c, the $R_{\rm CuCu}$ of all mesons is below unity, and within the uncertainties the suppression is the same for all measured mesons, indicating that its mechanism does not depend on the particle species. However, at lower p_T between 1–5 GeV/c, there are differences among the suppression for different particles. The K^{*0} meson shows no suppression at $p_T \sim$ 1–2 GeV/c and then decreases with increasing p_T, as previously observed for the ϕ meson. The π^0 meson shows significantly stronger suppression and flat behavior over the same p_T range.

Figure 4.7 compares the suppression patterns of light-quark mesons, strange mesons, and baryons. The $R_{\rm AA}$ of π^0, K^{*0} and ϕ mesons measured in Cu+Cu at $\sqrt{s_{NN}} = 200\,$GeV are

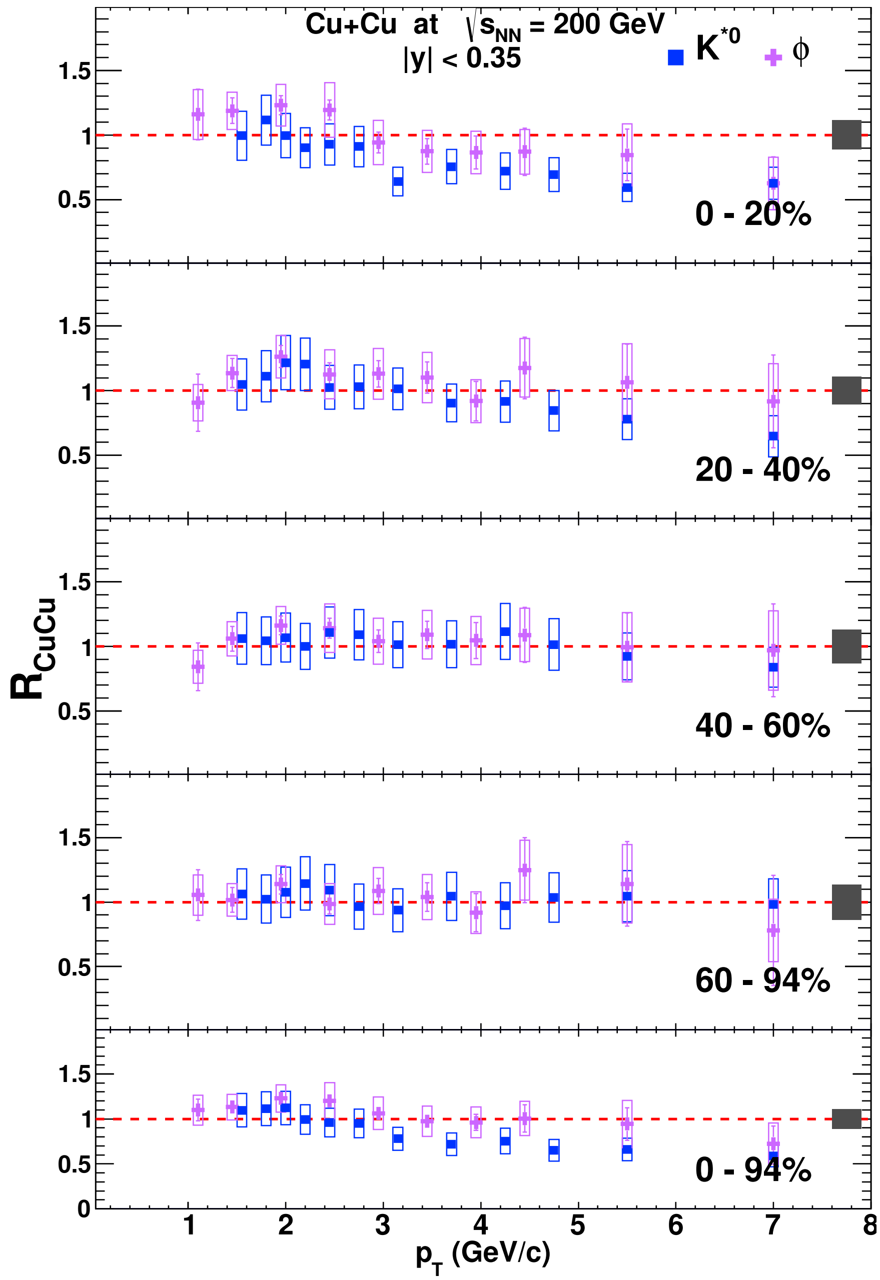

Figure 4.5: Comparison of the nuclear modification factor of K^{*0} and ϕ for 20–40%, 40–60% and 60–80% centrality bins in Cu+Cu collisions at $\sqrt{s_{NN}} = 200\,\mathrm{GeV}$.

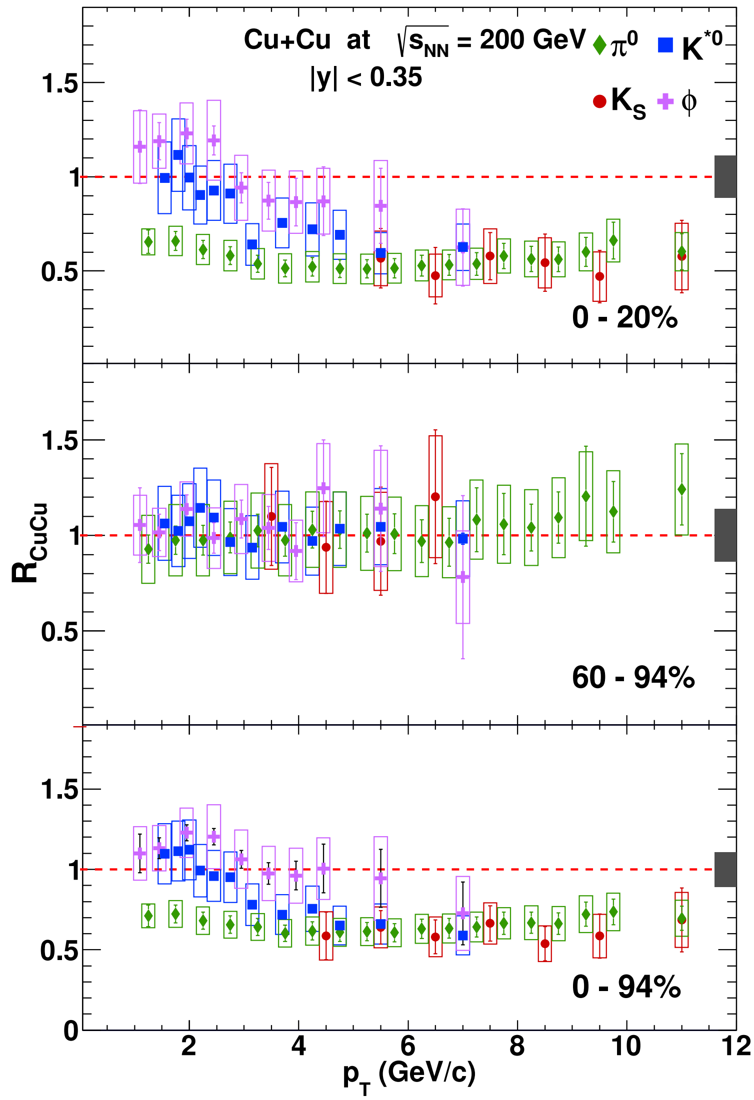

Figure 4.6: Nuclear modification factor as a function of p_T for K_S^0, K^{*0} for centralities (a) 0%–20%, (b) 0%–94% (MB) and (c) 60%–94% in Cu+Cu collisions at $\sqrt{s_{NN}} = 200\,\mathrm{GeV}$. Results from π^0 [87] and ϕ [86] are also shown. The statistical errors are shown by vertical bars. The systematic uncertainties are shown by boxes. The global $p+p$ uncertainty of $\sim$ 10% is not shown.

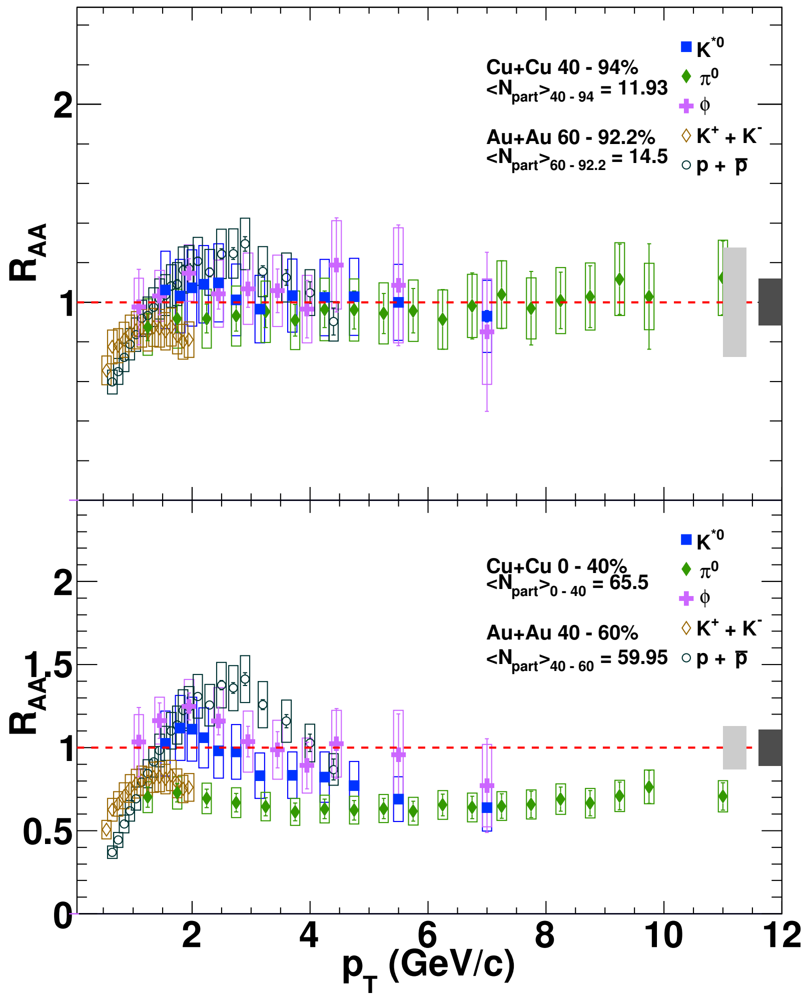

Figure 4.7: Comparison of the nuclear modification factor of π^0 [87], ϕ [86], and K^{*0} in Cu+Cu collisions and proton [35] and kaon [35] in Au+Au collisions at $\sqrt{s_{NN}} = 200\,\text{GeV}$. The comparisons are made for (a) 40%–60% and (b) 60%–92% in Au+Au system and 0%–40% and 40%–94% in the Cu+Cu system corresponding to similar N_{part} values in the two systems. The statistical errors are shown by vertical bars. The systematic uncertainties are shown by boxes. The global $p + p$ uncertainty of $\sim 10\%$ is not shown.

shown. As there are no measurements of R_{AA} for protons and charged kaons in the Cu+Cu system, we compare to proton and charged kaon measurements made in Au+Au collisions at the same energy [35]. The comparisons are made for centrality bins corresponding to similar number of participating nucleons (N_{part}), in the Cu+Cu and Au+Au systems: Cu+Cu 40%–94% ($\langle N_{\mathrm{part}}\rangle$ = 11.93 ± 0.63) and Au+Au 60%–92% ($\langle N_{\mathrm{part}}\rangle$ = 14.5 ± 2.5) in the bottom panel and Cu+Cu 0%–40% ($\langle N_{\mathrm{part}}\rangle$ = 65.5 ± 2.0) and Au+Au 40%–60% ($\langle N_{\mathrm{part}}\rangle$ = 59.95 ± 3.5) in the top panel. In peripheral collisions the R_{AA} factors for all mesons are consistent with unity for $p_T > 2\,\mathrm{GeV}/c$. A modest enhancement of $\approx$1.3 is observed for protons. In central collisions, all hadrons show suppression. In the intermediate p_T range (p_T = 2–5 GeV/c), there seems to be some hierarchy with baryons being enhanced, neutral pions being suppressed the most and K^{*0} and ϕ mesons showing an intermediate behavior. At higher p_T, all particles are suppressed and they seem to reach the same level of suppression, within uncertainties, irrespective of their mass or quark content. The fact that R_{AA} of all mesons becomes the same is consistent with the assumption that energy loss occurs at the parton level and the scattered partons fragment in the vacuum. We also note that the R_{AA} of the K^{*0} and ϕ mesons appear to be very similar to the R_{AA} of electrons from the semi-leptonic decay of heavy flavor mesons [88]. The present results provide additional constraints to the models attempting to quantitatively reproduce the nuclear modification factors in terms of energy loss of partons inside the medium.

4.3 Data tables for K^{*0} p_T spectra in different collision centralities

The values for the invariant yield as a function of p_T for the MB data and all other centralities (0–20%, 20–40%, 40–60% and 60–94%) are listed in Table 4.2 - Table 4.6. The statistical and systematic uncertainties are also mentioned. The systematic uncertainties are categorized in three types.

Table 4.2: The values of invariant yields in different p_T bins for minimum bias. The values for statistical and systematic errors are also given.

p_T	Inv yield	statistical error	Syst. A type error	Syst. B type error	Tot Syst. error
1.55	0.0305168	0.00049077	0.00203075	0.000954313	0.00231993
1.8	0.0154919	0.000191298	0.000520487	0.000405633	0.00105816
2	0.0091391	0.000138164	0.000265458	0.000303949	0.000604128
2.2	0.0048331	8.57134e-05	0.000133368	0.000193646	0.000303832
2.45	0.00252395	4.21907e-05	6.60754e-05	0.000116077	0.000157214
2.75	0.00124268	2.73352e-05	3.21042e-05	6.24212e-05	8.13819e-05
3.15	0.000427413	6.88639e-06	1.08165e-05	1.5012e-05	2.75463e-05
3.7	0.000132148	3.52135e-06	4.04458e-06	7.93052e-06	1.06186e-05
4.25	5.15824e-05	6.19508e-07	2.59513e-06	4.78206e-06	5.53131e-06
4.75	1.95254e-05	3.16065e-07	9.37048e-07	1.84023e-06	2.09923e-06
5.5	6.45646e-06	1.20697e-07	2.97516e-07	6.47772e-07	7.23655e-07
7	8.4271e-07	2.67955e-08	4.03688e-08	1.06515e-07	1.15065e-07

(a) Type A error - this error is uncorrelated between p_T bins.

(b) Type B error - this is p_T correlated error.

(c) Type C error - this is overall normalization uncertainty error and independent of p_T. This error is $\sim 10\%$ and not mentioned in these tables.

4.4 Data tables for K^{*0} nuclear modification factor in different collision centralities

The values for the R_{CuCu} as a function of p_T for the MB data and all other centralities (0–20%, 20–40%, 40–60% and 60–94%) are listed in Table 4.7 - Table 4.11. The statistical and systematic uncertainties are also mentioned.

Table 4.3: The values of invariant yields in different p_T bins for 0-20% centrality. The values for statistical and systematic errors are also given.

p_T	Inv yield	statistical error	Syst. A type error	Syst. B type error	Tot Syst. error
1.55	0.0797853	0.00129109	0.00769531	0.00292621	0.00882753
1.8	0.0457631	0.000575002	0.00107592	0.00100101	0.00325354
2	0.0233855	0.000378876	0.000664459	0.000676093	0.0017151
2.2	0.012755	0.000226008	0.000429287	0.000454692	0.000964147
2.45	0.00705331	0.000111452	0.000274586	0.000302774	0.000557261
2.75	0.0033182	7.35014e-05	0.000139115	0.000166081	0.000275931
3.15	0.000996124	1.88872e-05	3.87109e-05	5.63284e-05	8.52247e-05
3.7	0.00041305	9.91236e-06	1.57795e-05	2.64078e-05	3.76016e-05
4.25	0.000142703	1.78852e-06	8.14744e-06	1.57498e-05	1.8625e-05
4.75	6.08015e-05	1.01559e-06	3.17644e-06	5.83628e-06	7.07414e-06
5.5	1.65322e-05	3.27714e-07	7.85375e-07	1.46105e-06	1.78523e-06
7	2.54408e-06	8.53482e-08	1.20007e-07	3.12118e-07	3.49477e-07

Table 4.4: The values of invariant yields in different p_T bins for 20-40% centrality. The values for statistical and systematic errors are also given.

p_T	Inv yield	statistical error	Syst. A type error	Syst. B type error	Tot Syst. error
1.55	0.034647	0.000553112	0.0024099	0.0030283	0.00396263
1.8	0.0183915	0.00024181	0.000878754	0.000861241	0.00172428
2	0.0117911	0.000167634	0.000504504	0.00055563	0.000984829
2.2	0.00697775	0.000115983	0.000258264	0.000318872	0.000522368
2.45	0.00320998	5.36375e-05	9.87267e-05	0.000142156	0.000217001
2.75	0.00160184	3.48891e-05	4.60185e-05	7.29175e-05	0.000104165
3.15	0.000660416	1.05363e-05	1.16332e-06	2.21147e-05	3.25785e-05
3.7	0.000197886	4.51034e-06	4.82018e-06	8.1115e-06	1.14203e-05
4.25	7.44364e-05	8.93729e-07	4.91611e-06	3.68472e-06	6.40999e-06
4.75	3.01735e-05	4.88575e-07	2.60488e-06	1.69067e-06	3.19265e-06
5.5	9.05805e-06	1.69829e-07	9.6265e-07	6.85391e-07	1.20248e-06
7	1.09978e-06	3.55023e-08	1.1925e-07	1.71787e-07	2.10858e-07

Table 4.5: The values of invariant yields in different p_T bins for 40-60% centrality. The values for statistical and systematic errors are also given.

p_T	Inv yield	statistical error	Syst. A type error	Syst. B type error	Tot Syst. error
1.55	0.0125672	0.00019446	0.000744494	0.000822898	0.00113188
1.8	0.00626828	7.43893e-05	0.000192898	0.000162753	0.00036819
2	0.00369652	5.19825e-05	0.000109447	0.000108098	0.000207251
2.2	0.0020672	3.50404e-05	5.95172e-05	6.75597e-05	0.00011538
2.45	0.00127828	2.08426e-05	3.95913e-05	4.37564e-05	7.39061e-05
2.75	0.000581923	1.29361e-05	2.14165e-05	2.29752e-05	3.6885e-05
3.15	0.000235017	3.70637e-06	9.34666e-06	7.79046e-06	1.45838e-05
3.7	8.29358e-05	1.81776e-06	3.69839e-06	4.50132e-06	6.27149e-06
4.25	3.23818e-05	3.86055e-07	2.14575e-06	2.85411e-06	3.61667e-06
4.75	1.28931e-05	2.07985e-07	8.30312e-07	1.23656e-06	1.50693e-06
5.5	3.7758e-06	7.10854e-08	2.23877e-07	3.91447e-07	4.55895e-07
7	4.98204e-07	1.60837e-08	2.03057e-08	5.33509e-08	5.77649e-08

Table 4.6: The values of invariant yields in different p_T bins for 60-94% centrality. The values for statistical and systematic errors are also given.

p_T	Inv yield	statistical error	Syst. A type error	Syst. B type error	Tot Syst. error
1.55	0.00291113	4.45408e-05	0.000114782	9.92813e-05	0.000157676
1.8	0.00140081	1.66253e-05	5.222e-05	3.55276e-05	7.21738e-05
2	0.000862035	1.17754e-05	3.07022e-05	2.32845e-05	4.39974e-05
2.2	0.000548787	8.81736e-06	1.77036e-05	1.52141e-05	2.71215e-05
2.45	0.000283184	4.39416e-06	7.68128e-06	8.13716e-06	1.34635e-05
2.75	0.000124287	2.66048e-06	2.96552e-06	4.05078e-06	6.07014e-06
3.15	5.05256e-05	7.85715e-07	9.03952e-07	1.19982e-06	1.8503e-06
3.7	1.88898e-05	4.1226e-07	4.44577e-07	5.23909e-07	8.34312e-07
4.25	6.53122e-06	7.57972e-08	2.01156e-07	3.06377e-07	3.78868e-07
4.75	3.0583e-06	4.78733e-08	1.06492e-07	1.63332e-07	2.00094e-07
5.5	1.00662e-06	1.80775e-08	4.11631e-08	6.43253e-08	7.77878e-08
7	1.38265e-07	4.16358e-09	7.35243e-09	1.19337e-08	1.41633e-08

Table 4.7: The values of R_{CuCu} in different p_T bins for minimum bias. The values for statistical and systematic errors are also given.

p_T	R_{CuCu}	statistical error	Syst. A type error	Syst. B type error	Tot Syst. error
1.55	1.09694	0.0176409	0.182032	0.170247	0.186444
1.8	1.11431	0.0137599	0.173484	0.171891	0.18571
2	1.12172	0.016958	0.173607	0.174555	0.185946
2.2	0.992553	0.0176026	0.153353	0.15604	0.163279
2.45	0.959334	0.0160364	0.147984	0.152365	0.157604
2.75	0.950437	0.0209068	0.146556	0.152168	0.157321
3.15	0.780165	0.0125698	0.120232	0.121724	0.128818
3.7	0.719091	0.0191617	0.111509	0.117525	0.123647
4.25	0.754757	0.00906468	0.120857	0.13439	0.14041
4.75	0.650795	0.0105346	0.103746	0.116404	0.121175
5.5	0.660389	0.0123453	0.104902	0.120285	0.124728
7	0.589616	0.0187479	0.0939776	0.116568	0.12048

Table 4.8: The values of R_{CuCu} in different p_T bins for 0-20% centrality. The values for statistical and systematic errors are also given.

p_T	R_{CuCu}	statistical error	Syst. A type error	Syst. B type error	Tot Syst. error
1.55	0.978642	0.0158365	0.178893	0.156145	0.186593
1.8	1.12325	0.0141134	0.176407	0.176141	0.191831
2	0.979454	0.0158685	0.154615	0.154704	0.168201
2.2	0.893855	0.0158384	0.142021	0.142409	0.15437
2.45	0.914829	0.0144555	0.146451	0.147383	0.159385
2.75	0.866016	0.0191831	0.13929	0.141288	0.152544
3.15	0.620454	0.0117643	0.0993157	0.102534	0.110001
3.7	0.766982	0.018406	0.122649	0.128797	0.138055
4.25	0.712521	0.00893011	0.117882	0.13574	0.144532
4.75	0.691536	0.011551	0.113297	0.126243	0.134181
5.5	0.577025	0.0114382	0.0937001	0.103096	0.109137
7	0.607407	0.0203771	0.0985744	0.120204	0.125928

Table 4.9: The values of R_{CuCu} in different p_T bins for 20-40% centrality. The values for statistical and systematic errors are also given.

p_T	R_{CuCu}	statistical error	Syst. A type error	Syst. B type error	Tot Syst. error
1.55	1.05584	0.0168556	0.17645	0.185088	0.200807
1.8	1.12153	0.0147457	0.178649	0.178331	0.20025
2	1.22694	0.0174434	0.19369	0.195199	0.212748
2.2	1.21488	0.0201935	0.190005	0.192775	0.205795
2.45	1.03438	0.0172841	0.160368	0.163719	0.172033
2.75	1.03866	0.0226226	0.160626	0.16476	0.171675
3.15	1.02199	0.0163048	0.155307	0.159023	0.163275
3.7	0.912911	0.0208076	0.140493	0.143681	0.14839
4.25	0.923378	0.0110866	0.152993	0.14757	0.161277
4.75	0.852624	0.0138058	0.14901	0.138089	0.157877
5.5	0.785468	0.0147267	0.145651	0.133335	0.158489
7	0.652357	0.0210589	0.121779	0.142162	0.159595

Table 4.10: The values of R_{CuCu} in different p_T bins for 40-60% centrality. The values for statistical and systematic errors are also given.

p_T	R_{CuCu}	statistical error	Syst. A type error	Syst. B type error	Tot Syst. error
1.55	1.04931	0.0162367	0.187248	0.189522	0.200323
1.8	1.04731	0.0124291	0.179213	0.178376	0.186717
2	1.0539	0.0148205	0.180123	0.180057	0.186981
2.2	0.986131	0.0167156	0.168403	0.169092	0.17488
2.45	1.1286	0.0184021	0.193164	0.193863	0.200869
2.75	1.03384	0.0229822	0.178135	0.178747	0.185953
3.15	0.996465	0.0157149	0.17235	0.170954	0.178767
3.7	1.04831	0.0229766	0.182547	0.185406	0.193448
4.25	1.10061	0.0131214	0.1991	0.209123	0.222334
4.75	0.998214	0.0161028	0.179904	0.193387	0.20456
5.5	0.897096	0.0168893	0.1601	0.177349	0.185836
7	0.809698	0.0261398	0.140233	0.161537	0.165499

Table 4.11: The values of R_{CuCu} in different p_T bins for 60-94% centrality. The values for statistical and systematic errors are also given.

p_T	R_{CuCu}	statistical error	Syst. A type error	Syst. B type error	Tot Syst. error
1.55	1.06283	0.0162615	0.189577	0.188407	0.193642
1.8	1.02339	0.012146	0.182068	0.179909	0.185671
2	1.07464	0.0146796	0.19082	0.189183	0.194823
2.2	1.1447	0.0183919	0.202525	0.201642	0.207009
2.45	1.09324	0.0169638	0.192476	0.192755	0.197153
2.75	0.965495	0.0206673	0.169528	0.170878	0.174449
3.15	0.93672	0.0145668	0.163809	0.164461	0.166521
3.7	1.04403	0.0227853	0.183272	0.183911	0.187379
4.25	0.970643	0.0112647	0.171477	0.174882	0.177991
4.75	1.03534	0.0162067	0.183678	0.188402	0.192422
5.5	1.04576	0.0187803	0.186876	0.193803	0.199059
7	0.982566	0.0295881	0.178733	0.190807	0.198358

Part II - Phenomenological studies

CHAPTER 5

DESCRIPTION OF HADRON SPECTRA WITH TSALLIS DISTRIBUTION

5.1 Introduction

The particle spectra measured in hadronic collisions are of utmost interest because of their fundamental nature and simplicity, which allow to verify pQCD [89] calculations and also help to make comprehensive phenomenological studies. The ratios of the particle yields obtained from the measured spectra allow to get the chemical freeze-out conditions, whereas the spectra themselves reflect the conditions at the kinetic freeze-out. The particle spectra provide useful information about the collision dynamics. The low p_T region of the spectrum corresponds to the particles originating from low momentum transfer and multi-scattering processes (non-perturbative QCD), whereas, the high p_T region comes from the hard-parton-scattering (pQCD) among the initial partons. The transition of this non-perturbative to perturbative dynamics has no sharp boundary, though one can have an estimate from the '$x_T - scaling$' [90]. Extensive [91, 38] and non-extensive [92, 93, 94, 95, 96] statistical approaches have been used to characterize particle spectra in terms of thermodynamic variables. Extensive statistics assume thermal and chemical equilibrium of the system at hadronic phase which lead to an exponential distribution of the particle spectra. In experiments, the particle spectra show a power-law behavior at high p_T. This behavior is reproduced by the non-extensive approach with an additional parameter. In recent times, the Tsallis [92] statistical approach is widely used to describe the particle spectra obtained in high-energy collisions with only two parameters; the temperature T and q, known as non-extensivity parameter which is a measure of temperature fluctuations or degree of non-equilibrium in the system.

The Tsallis distribution gives an excellent description of p_T spectra of all identified mesons measured in $p + p$ collisions at $\sqrt{s} = 200\,\text{GeV}$ [85]. In a recent work [97, 98], the Tsallis distribution has been used to describe the p_T spectra of identified charged hadrons measured in $p + p$ collisions at RHIC and at LHC energies. Such an approach has also been applied to the inclusive charged hadron $p + p$ data in recent publications [99, 100]. It has been shown in Ref. [97, 101] that the functional form of the Tsallis distribution with thermodynamic origin is of the same form as the QCD-inspired Hagedorn formula [102, 103]. This could be the reason of success of Tsallis distribution in $p+p$ collisions which is a power law typical of QCD hard scatterings. The hardness of the spectrum is thus related to q and the parameter T governs the contribution from soft collisions.

Using the Tsallis phenomenological function, we review and study the charged pion spectra in $p + p$ collisions in a large energy regime, spanning from SPS [104] (6.27 GeV - 17.27 GeV), RHIC [70] (62.4 and 200 GeV) to LHC [105] (900 GeV, 2.76 TeV and 7 TeV) energies. The object of the present work is to study the behaviour of the Tsallis parameters as a function of collision energy. We also study the charged pion spectra for different event multiplicities in p+p collisions for LHC energies. Among all hadrons, pions are chosen because of their abundance in collisions, simple quark structure and availability of the data at different energies.

5.2 Formalism

The transverse momentum spectra of hadrons, obtained from different fixed and collider experiments have shown that, the high p_T region of the spectra can be described successfully by the power law,

$$E\frac{d^3N}{dp^3} = C_P p_T^{-n}, \tag{5.1}$$

where C_P is the normalization constant and n is the power which determines the shape of the spectra at high p_T. However, the low p_T region of the particle spectra shows an exponential shape and can be described by the Boltzmann-Gibbs [106, 107] statistical approach,

$$E\frac{d^3N}{dp^3} = C_B e^{-E/T}, \tag{5.2}$$

where C_B is the normalization constant, E is the particle energy and T is the temperature of the system.

In the early 80's, Hagedorn [102] proposed a phenomenological function which describes the particle spectra for both the higher and lower p_T regions:

$$E\frac{d^3N}{dp^3} = A\left(1 + \frac{p_T}{p_0}\right)^{-n}, \tag{5.3}$$

where A, p_0 and n are the fit parameters. The above equation describes an exponential behavior for low p_T and a power-law behavior for high p_T.

$$\begin{aligned}
\left(1 + \frac{p_T}{p_0}\right)^{-n} &\simeq \exp\left(\frac{-np_T}{p_0}\right), \quad \text{for } p_T \to 0 && (5.4)\\
&\simeq \left(\frac{p_0}{p_T}\right)^{n}, \quad \text{for } p_T \to \infty. && (5.5)
\end{aligned}$$

The parameter n in this equation is often related to the 'power' in the 'QCD-inspired' quark interchange model [103].

In the late 80's, Tsallis [92] introduced the idea of the non-extensive statistics in place of thermal Boltzmann-Gibbs statistics. This approach includes a parameter q, known as non-extensive parameter which quantifies the temperature fluctuation [108] in the system as : $q-1 = Var(1/T)/\langle T\rangle^2$. The non-extensive statistics assume Boltzmann-Gibbs form in the limit $q \to 1$. In Tsallis approach, the Boltzmann-Gibbs distribution takes the form

$$E\,\frac{d^3N}{dp^3} = C_q\left(1+(q-1)\frac{E}{T}\right)^{\frac{-1}{q-1}}, \tag{5.6}$$

where C_q is the normalization factor. One can use the relation $E = m_T$ at mid-rapidity and $n = 1/(q-1)$ in Eq. 5.6 to obtain :

$$E\,\frac{d^3N}{dp^3} = C_n\left(1+\frac{m_T}{nT}\right)^{-n}, \tag{5.7}$$

where, C_n is the normalization factor. Eq. 5.7 can be re-written as :

$$\frac{1}{2\pi p_T}\frac{d^2N}{dp_T dy} = C_n\left(1+\frac{m_T}{nT}\right)^{-n}, \tag{5.8}$$

The value of C_n can be obtained by integrating Eq. 5.8 over momentum space :

$$C_n = \frac{dN/dy}{\int_0^\infty \left(1+\frac{m_T}{nT}\right)^{-n} 2\pi p_T dp_T}, \tag{5.9}$$

Here the quantity dN/dy is the p_T integrated yield. Eq. 5.7 with the normalization constant takes the form [85] :

$$E\frac{d^3N}{dp^3} \;=\; \frac{1}{2\pi}\frac{dN}{dy}\frac{(n-1)(n-2)}{(nT+m(n-1))(nT+m)}\left(\frac{nT+m_T}{nT+m}\right)^{-n}, \tag{5.10}$$

Larger values of q correspond to smaller values of n which imply dominant hard QCD point-like scattering. Both n and q have been interchangeably used in Tsallis distribution [93, 85, 109, 110, 111]. The Tsallis interpretation of parameters T as temperature and q as non-extensivity parameter is more suited for heavy ion collisions while for $p+p$ collisions Hagedorn interpretation in terms of power n and a parameter $T = p_0/n$ which controls soft physics processes is more meaningful. Phenomenological studies suggest that, for quark-quark point scattering, $n \sim 4$ [112, 113] and when multiple scattering centers are involved n grows larger.

There are many other forms of Eq. 5.10, which are used often to describe particle spectra in literature, see e.g. Refs. [93, 111, 114, 115, 116, 117, 118].

5.3 Results and discussions

All the studies are performed with Eq. 5.10 and the fit parameters n, T and dN/dy are obtained. The different experiments, energies, rapidity ranges and particles used in the analysis are summarized in Table 5.1. For SPS energies only available data is for π^- measured by NA61 Collaboration [104], for RHIC and LHC energies we use $(\pi^+ + \pi^-)/2$. All the data used are measured in mid-rapidity and are given for unit rapidity. The difference in rapidity range is not expected to affect the behaviour of the spectra. CMS experiment presented [105] transverse momentum spectra for different events classified on the basis of number of true tracks referred here as track multiplicity of event or simply multiplicity. Each multiplicity class is represented by average number of tracks ($\langle N_{tracks} \rangle$).

5.3.1 Tsallis parameters as a function of $\sqrt{s}$ in $p+p$ system

In this analysis all the Tsallis parameters are obtained for charged pion spectra as a function of $\sqrt{s}$ in $p+p$ system for SPS [104], RHIC [70] and LHC [105] energies. Similar

Table 5.1: The center of mass energy and rapidity of the data used for the study.

Experiments	Center of mass energy (GeV)	Rapidity	Particles Studied
SPS	6.27, 7.74, 8.76, 12.32, 17.27	0.0–0.2	π^-
RHIC	62.4, 200	$\lvert y\rvert < 0.35$	π^+, π^-
LHC	900, 2760, 700	$\lvert y\rvert < 1.0$	π^+, π^-

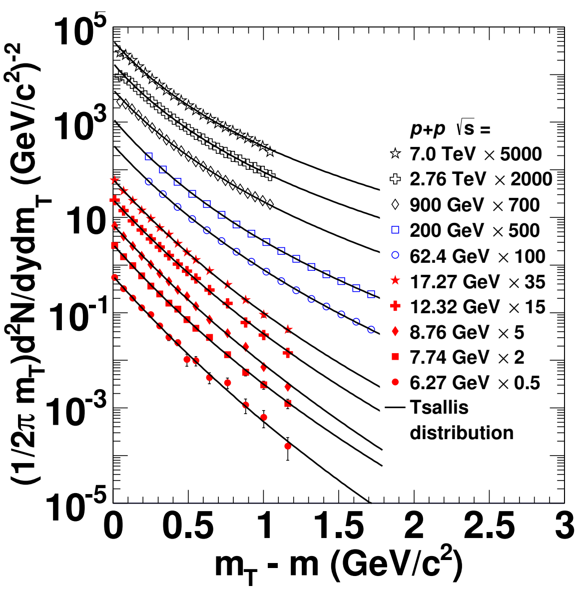

Figure 5.1: (Color online) The invariant yield spectra of charged pions as a function of $(m_T - m)$ for SPS [104] energies 6.27 GeV, 7.74 GeV, 8.76 GeV, 12.32 GeV and 17.27 GeV, RHIC [70] energies 62.4 GeV and 200 GeV and LHC [105] energies 900 GeV, 2.76 TeV and 7 TeV. The solid lines are the Tsallis function (Eq. 5.10). The negative pion yields are plotted for SPS energies and for all other energies, average yield for positive and negative pion are plotted.

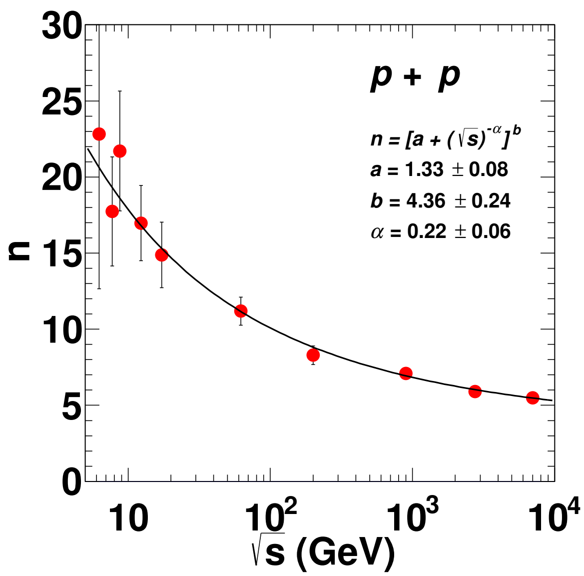

Figure 5.2: (Color online) The variation of the Tsallis parameter n for charged pions as a function of $\sqrt{s}$. The solid curve represents the parameterization $(a + (\sqrt{s})^{-\alpha})^b$.

study is available in Ref. [97] using RHIC and LHC data and in Ref. [98] for SPS and LHC data.

The pion p_T spectra measured in $p + p$ collisions at different $\sqrt{s}$ are shown in Fig. 5.1 along with with Tsallis fits (Eq. 5.10) shown by solid lines. The spectra are scaled by arbitrary factors (given in figure) for visual clarity. In case of RHIC data, we restrict the p_T range to 1.7 GeV/c^2 to have similar p_T range at all energies. It can be noticed that the spectra become harder with increase in $\sqrt{s}$ which is depictive of occurrence of harder scatterings at higher collision energy. The χ^2 per degree of freedom χ^2/NDF values for all the fits are given in Table 5.2. The χ^2/NDF values are $\lesssim 1$, which is indicative of good fit quality.

The parameters n and T obtained from this analysis are shown in Fig. 5.2 and Fig. 5.3, respectively, as a function of $\sqrt{s}$. The variation of dN/dy as a function of $\sqrt{s}$ is shown in Fig. 5.4. The parameter n decreases with increasing $\sqrt{s}$ and starts saturating at LHC energies. The value of T also reduces slowly from SPS energies to LHC energies. The integrated yield dN/dy increases 10 times when going from SPS to highest LHC energy.

Table 5.2: Values of the χ^2/NDF for Tsallis fits of pion spectra at different $\sqrt{s}$.

$\sqrt{s}$	χ^2/NDF
6.27 GeV	6.31/12
7.74 GeV	5.80/12
8.76 GeV	10.68/12
12.32 GeV	9.25/12
17.27 GeV	2.65/12
62 GeV	0.74/11
200 GeV	0.48/11
900 GeV	24.33/19
2.76 TeV	5.59/19
7.00 TeV	13.11/19

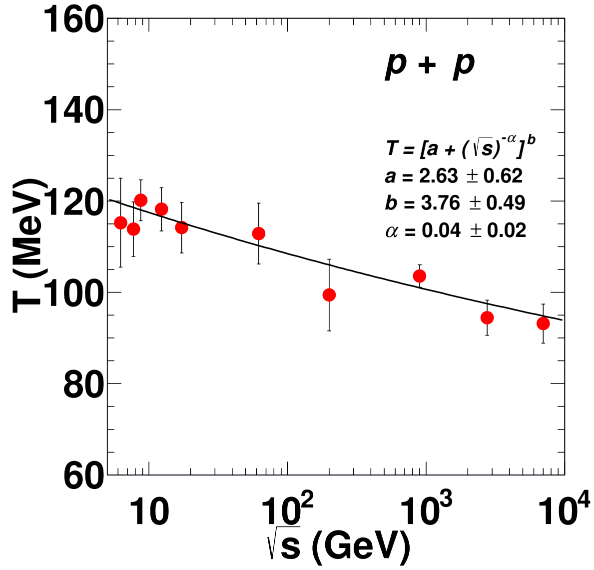

Figure 5.3: (Color online) The variation of the Tsallis parameter T for charged pions as a function of $\sqrt{s}$. The solid curve represents the parameterization $(a + (\sqrt{s})^{-\alpha})^b$.

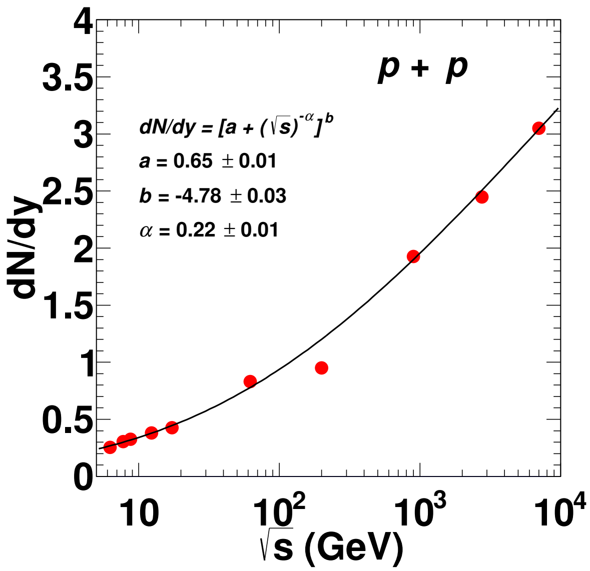

Figure 5.4: (Color online) The variation of the integrated yield dN/dy for charged pions as a function of $\sqrt{s}$. The solid curve represents the parameterization $(a+(\sqrt{s})^{-\alpha})^b$.

Larger value of n (also larger value of T) suggests that the spectra has contribution from processes involving small momentum transfer arising due to the re-scattering, recombination of partons, fragmentation from strings etc. Whereas, smaller values of n are indicative of harder processes are involved in particle-production. Thus the spectra at SPS energies have large softer contribution and as the collision energy increases more and more contribution from hard processes are added.

All the three parameters can be parametrized by a function of type

$$f(\sqrt{s}) = \left(a + (\sqrt{s})^{-\alpha}\right)^b \tag{5.11}$$

Here $a = 1.33 \pm 0.08$, $\alpha = 0.22 \pm 0.06$ and $b = 4.36 \pm 0.24$ for $n(\sqrt{s})$, $a = 2.63 \pm 0.62$, $\alpha = 0.04 \pm 0.02$ and $b = 3.76 \pm 0.49$ for $T(\sqrt{s})$ and $a = 0.65 \pm 0.01$, $\alpha = 0.22 \pm 0.01$ and $b = -4.78 \pm 0.03$ for $dN(\sqrt{s})/dy$. Using the parameterizations for n by Eq. 5.11 we get $n \sim 3.46$ in the limit $\sqrt{s} \to \infty$. The extrapolated values for n, T and dN/dy for $\sqrt{s} = 14$ TeV are, $n \sim 5.09$, $T \sim 90.33$ MeV and $dN/dy \sim 3.44$.

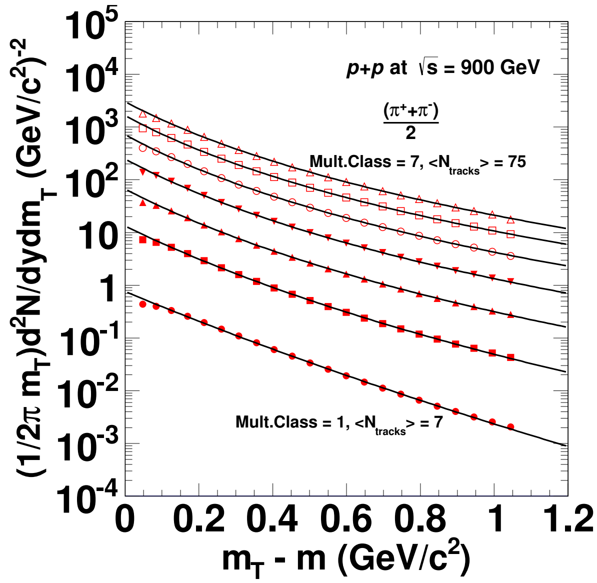

Figure 5.5: (Color online) The invariant yield spectra of $(\pi^+ + \pi^-)/2$ [105], as a function of $m_T - m$ for $p+p$ collisions at $\sqrt{s} = 900$ GeV. The yields are shown for $\langle N_{tracks}\rangle$ 7, 16, 28, 40, 52, 63 and 75. The spectra are scaled up for clarity by a factor of 6^i, where i = 0, 1, 2, 3, 4, 5 and 6. The solid lines show the Tsallis fits.

5.3.2 Tsallis parameters as a function of multiplicity ($\langle N_{tracks}\rangle$) for LHC energies

The Tsallis parameters for charged pion spectra are studied as a function of event multiplicity for different LHC energies 900 GeV, 2.76 and 7 TeV. The event multiplicity data was also studied in a recent work [96] but our analysis and interpretations are different.

The invariant yield spectra corresponding to different multiplicities are fitted with Eq. 5.10, are shown by the solid black lines in Fig. 5.5 for 900 GeV, in Fig. 5.6 for 2.76 TeV and in Fig. 5.7 for 7 TeV center of mass energy. The spectra are scaled up for distinctness. The Tsallis distribution describes all the spectra well, shown by the χ^2/NDF values given in Table 5.3. The χ^2/NDF values are little higher for some of the lower multiplicities due to the deviation of first data point in p_T spectra with the curve.

The parameters n and T obtained from the fits are shown in Fig. 5.8 and Fig. 5.9

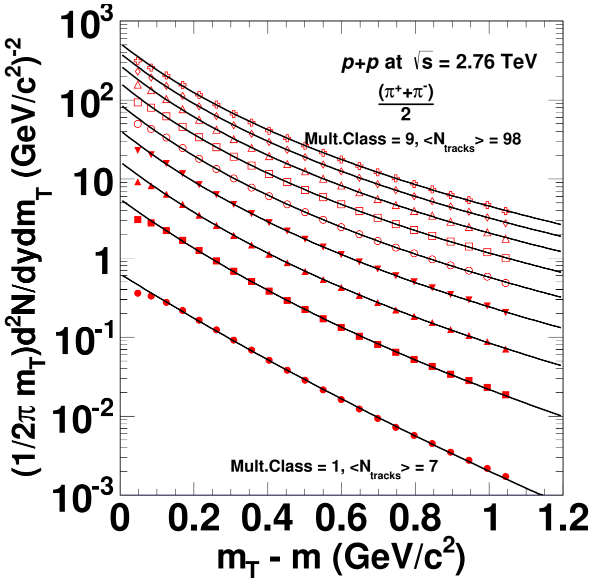

Figure 5.6: (Color online) The invariant yield spectra of $(\pi^+ + \pi^-)/2$ [105], as a function of $m_T - m$ for $p + p$ collisions at $\sqrt{s} = 2.76$ TeV. The yields are shown for $\langle N_{tracks} \rangle$ 7, 16, 28, 40, 52, 63, 75, 86 and 98. The spectra are scaled up for clarity by a factor of 3^i, where i = 0, 1, 2, 3, 4, 5, 6, 7 and 8. The solid lines show the Tsallis fits.

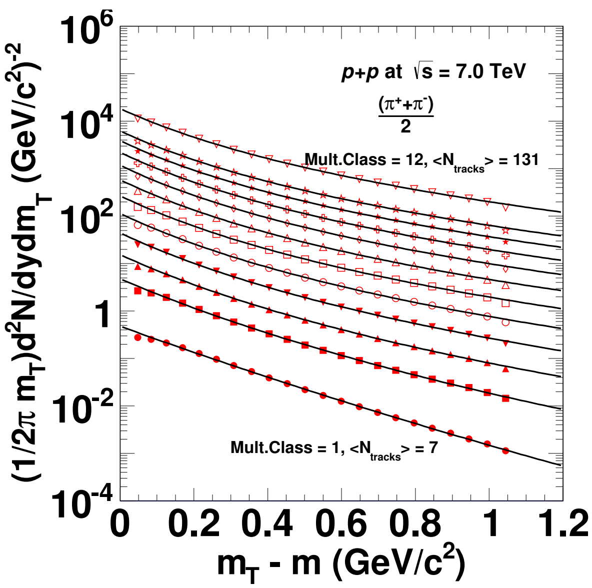

Figure 5.7: (Color online) The invariant yield spectra of $(\pi^+ + \pi^-)/2$ [105], as a function of $m_T - m$ for $p + p$ collisions at $\sqrt{s} = 7.00$ TeV. The yields are shown for $\langle N_{tracks} \rangle$ 7, 16, 28, 40, 52, 63, 75, 86, 98, 109, 120 and 131. The spectra are scaled up for clarity by a factor of 3^i, where i = 0, 1, 2, 3, 4, 5, 6, 7, 8, 9, 10 and 11. The solid lines show the Tsallis fits.

Table 5.3: Values of the χ^2/NDF for the Tsallis fits in different event multiplicities.

$\langle N_{tracks} \rangle$	χ^2/NDF values for		
	900 GeV	2.76 TeV	7.0 TeV
7	48.89/18	57.66/18	48.10/18
16	25.21/18	26.38/18	27.76/18
28	9.97/18	11.47/18	22.83/18
40	7.20/18	6.91/18	19.25/18
52	8.00/18	6.08/18	22.52/18
63	9.18/18	6.44/18	26.30/18
75	15.01/18	9.05/18	21.30/18
86		8.16/18	19.24/18
98		11.91/18	23.59/18
109			20.82/18
120			16.85/18
131			19.77/18

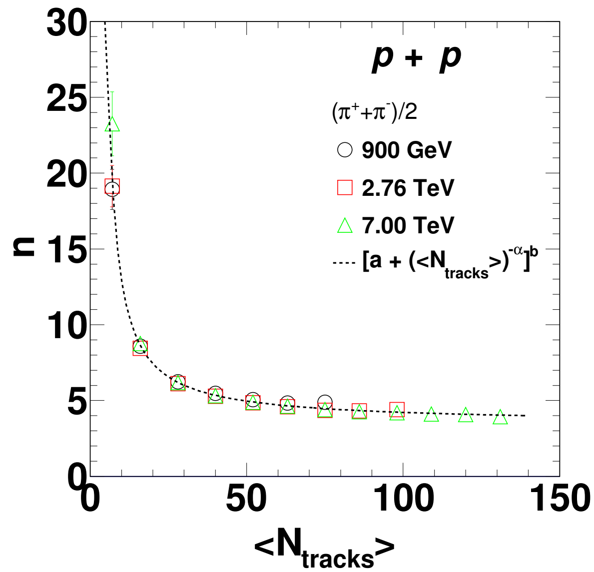

Figure 5.8: (Color online) The variation of the Tsallis parameter n for charged pions as a function of $\langle N_{tracks} \rangle$. The variation is shown for 900 GeV by black circles, 2.76 TeV by red squares and 7.00 TeV by green triangles. The dashed curve represents the parameterization $(a + (\langle N_{tracks} \rangle)^{-\alpha})^b$.

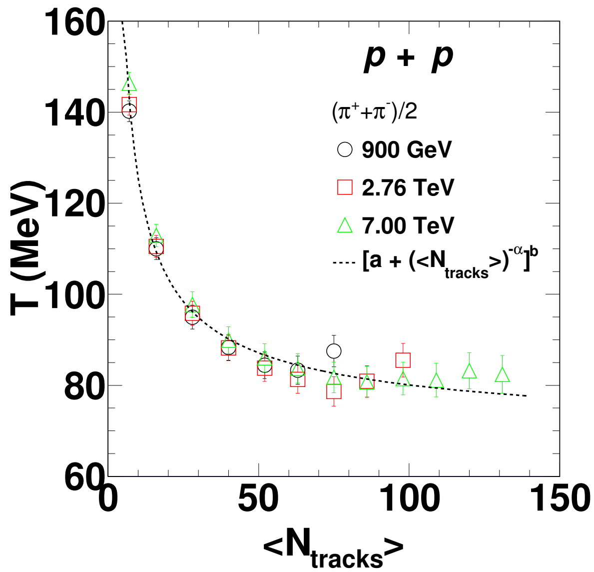

Figure 5.9: (Color online) The variation of the Tsallis parameter T for charged pions as a function of $\langle N_{tracks} \rangle$. The variation is shown for 900 GeV by black circles, 2.76 TeV by red squares and 7.00 TeV by green triangles. The dashed curve represents the parameterization $(a + (\langle N_{tracks} \rangle)^{-\alpha})^b$.

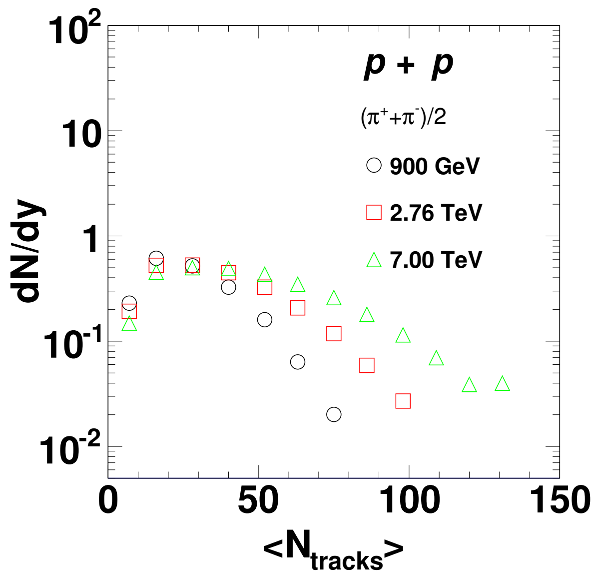

Figure 5.10: (Color online) The variation of the integrated yield dN/dy for charged pions as a function of $\langle N_{tracks} \rangle$. The variation is shown for 900 GeV by black circles, 2.76 TeV by red squares and 7.00 TeV by green triangles.

respectively, as a function of $\langle N_{tracks} \rangle$. The circles, squares and triangles correspond to the parameter values obtained from data at 900 GeV, 2.76 TeV and 7 TeV, respectively. It is seen that both the parameters n and T decrease rapidly and then start saturating with the increase of $\langle N_{tracks} \rangle$ for all three energies. This variation (of n and T) is very similar to the variation which we find as a function of $\sqrt{s}$. It means that events with higher multiplicity have larger contribution from hard processes. The value of n for high multiplicity events at 7 TeV is ~ 4 which is depictive of production from point quark-quark scattering. The variation of n and T as a function of $\langle N_{tracks} \rangle$ can be described by the same curve given in the figure for all three energies and are parameterized by,

$$f((< N_{tracks} >) = \left(a + (< N_{tracks} >)^{-\alpha}\right)^{b} \tag{5.12}$$

Here $a = 1.13 \pm 0.01$, $\alpha = 0.81 \pm 0.04$ and $b = 10.32 \pm 0.76$ for $n(\langle N_{tracks} \rangle)$ and $a = 2.20 \pm 0.06$, $\alpha = 0.56 \pm 0.08$ and $b = 5.33 \pm 0.23$ for $T(\langle N_{tracks} \rangle)$.

The p_T integrated pion yield distribution in different multiplicity classes is shown in Fig. 5.10 for the three LHC energies. The total p_T integrated pion yield for each energy can be obtained by integrating the above distributions over all multiplicity classes. It is noticed that as the energy increases more and more high mutliplicity events are added in the sample with mean of the distribution shifting towards higher $\langle N_{tracks} \rangle$.

5.4 Conclusion

This work presented the study of the transverse momentum spectra of the charged pions for different collisional energies and also for different event-multiplicities (at LHC energies) using Tsallis distribution. The Tsallis parameter n decreases with increasing $\sqrt{s}$ and starts saturating at LHC energies. The value of T also reduces slowly from SPS energies to LHC energies. It means that the spectra at SPS energies have large softer contribution and as the collision energy increases more and more contribution from hard processes are added. The p_T integrated pion yield increases with increasing $\sqrt{s}$ and becomes 10 times when going from SPS to highest LHC energy. The Tsallis parameters are also obtained as a function of event multiplicity for all three LHC energies which can be described by the same curve. The variation of n and T as a function of multiplicity is very similar to the variation which we find as a function of $\sqrt{s}$. It means that events with higher multiplicity have larger contribution from hard processes. The value of n for high multiplicity events at 7 TeV is ~ 4 which is depictive of production from point quark-quark scattering. The p_T integrated pion yield distribution for the three LHC energies shows that as the energy increases, more and more high mutliplicity events are added in the sample with mean of the distribution shifting towards higher multiplicity.

The calculation for the constant C_n is given in Appendix B.

CHAPTER 6

INFERRING FREEZE-OUT PARAMETERS FROM PION MEASUREMENTS AT RHIC AND LHC

6.1 Introduction

The Quantum Chromodynamics (QCD), the theory of strong interaction suggests that at energy density above ~ 1 GeV/fm^3 the hadronic matter undergoes a phase transition to Quark Gluon Plasma (QGP) [1], a phase where the relevant degrees of freedom are quarks and gluons. The heavy ion collisions at relativistic energy are the means to produce a large volume of hot/dense matter required to create and characterize such a phase [119, 120].

The quark gluon matter presumably with local thermal equilibrium expands hydrodynamically and undergoes a phase transition to hadronic matter which further cools till the multiple scatterings among particles are sufficient to keep them as one system. The hadrons then decouple from the system and their spectra would reflect the condition of the system at the time of freeze-out. Hadrons (pions, kaons and protons) form the bulk of particles produced and are usually the first and easiest to be measured in a heavy ion collision experiment. Traditionally, statistical model [38] has been used at SPS and RHIC energies to infer the conditions at freeze-out using measured hadron ratios as input. Alternatively one can consider full transverse momentum (p_T) spectra of hadrons in heavy ion collisions. The bulk and collective effects [121, 122] show up in the low and intermediate p_T regions of hadron spectra while the high p_T region above 5 GeV/c consists of particles from jets which are produced in hard interactions.

The Tsallis distribution [92, 93] describes a system in terms of two parameters; temperature and q which measures deviation from thermal distribution. It has been shown in Refs. [97, 101] that the functional form of the Tsallis distribution in terms of parameter q is the same as the QCD-inspired Hagedorn formula [102, 103] in terms of power n. Both n and q are related and describe the power law tail of the hadron spectra coming from QCD hard scatterings. The Tsallis distribution has been used extensively to describe the p_T spectra of identified charged hadrons measured in $p + p$ collisions at RHIC and at LHC energies [97, 124]. It does not always provide the best description of hadron p_T distributions in heavy ion collisions which are modified due to collective flow and thus Tsallis blast wave method is used as in Ref. [125]. The average transverse flow can be included in Tsallis distribution and keeping the functional form to be analytical as done in Refs. [126, 127]. The function presented in Ref. [126] can be used in a wider p_T range as was done for both meson and baryon spectra for Au+Au collisions at $\sqrt{s_{NN}}$ = 200 GeV.

We analyze the transverse momentum spectra of charged pions measured in heavy ion collisions. Recent measurements of identified charged particle spectra by PHENIX in different centralities of Au+Au collision at $\sqrt{s_{NN}}$ = 200 GeV [35] and by ALICE in the most central (0-5%) and the most peripheral (60-80%) Pb+Pb collisions at $\sqrt{s_{NN}}$ = 2.76 TeV [36] have been used in the study. The kinetic freeze-out temperature (T), average transverse flow (β) and degree of non thermalization (q) are obtained as a function of system size for both the energies. As an alternative the (kinetic) freeze-out temperature is also extracted using the measured charged particle multiplicity and HBT volume of the system.

6.2 Analysis of hadron spectra

The transverse momentum spectra of hadrons can be described using the modified Tsallis distribution including the transverse flow as proposed in Ref. [126] is given by :

$$E\frac{d^3N}{dp^3} = C_n \left(\exp\left(\frac{-\gamma\beta p_T}{nT}\right) + \frac{\gamma m_T}{nT}\right)^{-n}. \tag{6.1}$$

Here C_n is the normalization constant, $m_T = \sqrt{p_T^2 + m^2}$, $\gamma = 1/\sqrt{1-\beta^2}$, β is the average transverse velocity of the system and T is the temperature. The power n is related to the non-extensivity parameter q as $n = 1/(q-1)$. The parameter q gives temperature fluctuations [108] in the system as: $q - 1 = Var(T)/\langle T\rangle^2$. It can take a value between 1 and 4/3. Larger values of q correspond to smaller values of n which imply dominant hard QCD point-like scattering. Both n and q have been interchangeably used in Tsallis distribution [93, 85, 70, 110, 111]. In heavy ion collisions, the high p_T tail decides the value of n. Phenomenological studies suggest that, for quark-quark point scattering, $n \sim 4$ [112, 113], and when multiple scattering centers are involved n grows larger. When β is zero, Eq. 6.1 is the usual Tsallis equation which has been the most popular tool to characterize hadronic collisions [101, 108, 111, 128] in recent years. At low p_T, Eq. 6.1 represents a thermalized system with collective flow and at high p_T it becomes a power law as follows

$$\begin{aligned} E\frac{d^3N}{dp^3} &\simeq C_n \exp\left(\frac{-\gamma(m_T - \beta p_T)}{T}\right) \quad \text{for} \quad p_T \to 0, \\ &\simeq C_n \left(\frac{\gamma m_T}{nT}\right)^{-n} \quad \text{for} \;\; p_T \to \infty. \end{aligned} \tag{6.2}$$

In this work, we focus on the study of the charged pion spectra measured in heavy-ion collisions at RHIC and LHC energies. The errors on the data are taken as quadratic sums of statistical and uncorrelated systematic errors. The RHIC measurements are available in p_T range 0.5 - 6.0 GeV/c and we use the LHC measurements in the same range. The spectra are fitted with Eq. 6.1 and all the parameters are obtained as a function of system size (centrality) for both the energies.

The freeze-out temperature T can also be extracted from the measured multiplicity using following procedure. The particle number density n can be related to the measured particle multiplicity and HBT volume V as

$$n\,V = \frac{dN}{d\eta}, \tag{6.3}$$

where $dN/d\eta$ is 1.5 times the total measured charged particle multiplicty $(dN_{ch}/d\eta)$. The number density can also be expressed in terms of freeze-out temperature T

$$n = \frac{1.2}{\pi^2}\, a_n(T)\, T^3. \tag{6.4}$$

The parameter $a_n\,(T) = \sum_i g_i n_i(m_i/T)$ where g_i is the degeneracy factor and n_i for i^{th} meson species is given by

$$n_i(m_i/T) = \frac{1}{2\,\times\,1.2}\int_0^\infty \frac{x^2\,dx}{e^{(\sqrt{x^2+(m_i/T)^2}} - 1}. \tag{6.5}$$

The parameter $a_n\,(T) = 3$ for massless pion gas. In our study we assume that the system at freeze-out consists of pion ($g = 3$), kaon ($g = 4$), ρ ($g = 9$), ϕ ($g = 1$), η ($g = 1$), ω ($g = 3$) mesons and obtained n/T^3 as a function of temperature which is shown in Fig. 6.1 along with that for massless pion gas.

The freeze-out temperature T can be obtained by numerically solving the following equation

$$T^3 = \frac{1}{(1.2/\pi^2)\,a_n(T)}\,\frac{1}{V}\,\frac{dN}{d\eta}. \tag{6.6}$$

The HBT volume $V = (2\pi)^{3/2}\ R_{side}^2\, R_{long}$, where R_{side} and R_{long} are the measured HBT

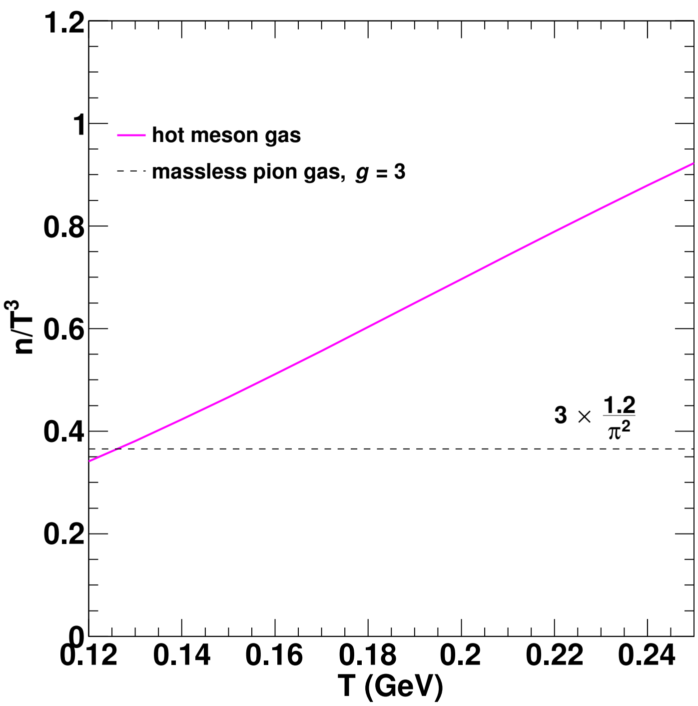

Figure 6.1: (Color online) The variation of n/T^3 as a function of temperature for both hot meson gas (solid line) and massless pion gas (dashed line).

radii [129, 130].

If transverse flow is present in the system, then the system volume obtained from measured HBT radii will be smaller than the fireball volume. To correct for this effect the HBT radii as a function of m_T are extrapolated to m_T = 0.140 GeV/c^2 which corresponds to p_T = 0 (Fig. 6.2).

6.3 Results and discussions

Figure 6.3 shows the charged pion invariant yield spectra in Au+Au collisions at $\sqrt{s_{NN}}$ = 200 GeV [35] as a function of (m_T - m), fitted with Eq. 6.1. The spectra in Au+Au collisions are given for 0-10%, 10-20%, 20-40%, 40-60% and 60-80% centralities, which are scaled up by factors given in the Fig. 6.3. Figure 6.4 shows the same for Pb+Pb collisions at $\sqrt{s_{NN}}$ = 2.76 [36] TeV fitted with Eq. 6.1. It is seen that Eq. 6.1 describes the data in

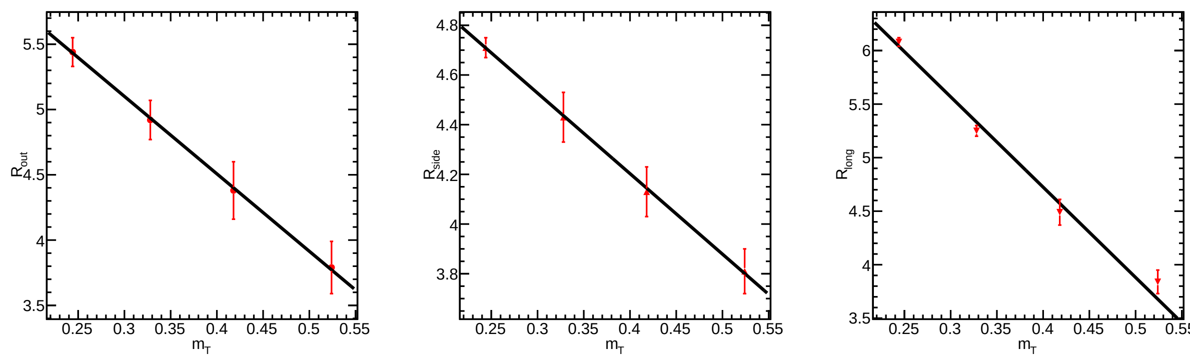

Figure 6.2: HBT radii R_{out}, R_{side} and R_{long} are plotted as a function of m_T for 10 - 20% centrality bin [129]. The data points are fitted with a straight line and extrapolated to m_T = 0.140 GeV/c^2.

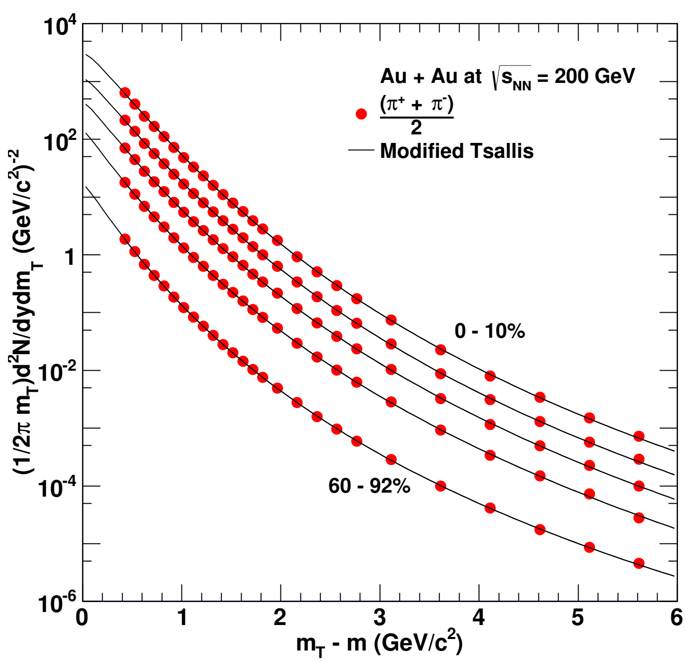

Figure 6.3: (Color online) Invariant yield for charged pions [35] as a function of (m_T - m) measured in Au+Au collisions at $\sqrt{s_{NN}}$ = 200 GeV for 0-10%, 10-20%, 20-40%, 40-60% and 60-92% centrality bins. The spectra are scaled up by a factor of 10, 5, 3, 2 and 1 for the respective centrality bins. The fitted Modified Tsallis function is shown by the black curve.

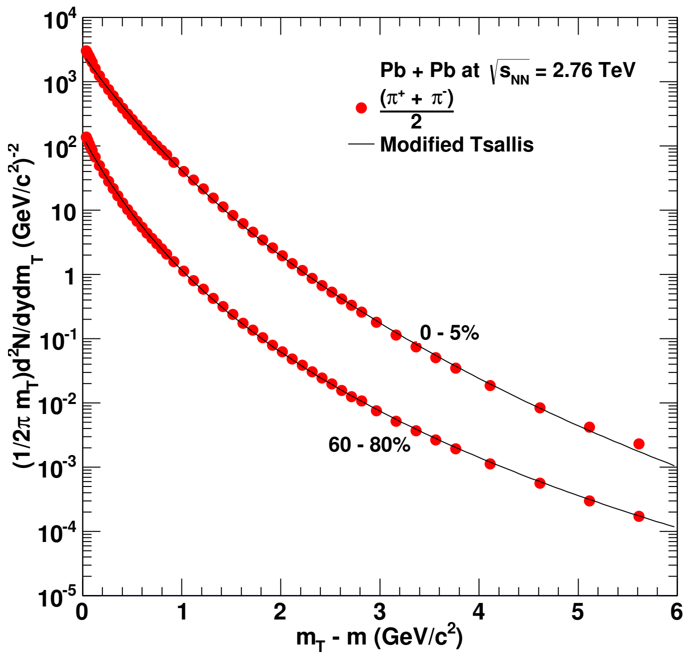

Figure 6.4: (Color online) Invariant yield for charged pions [36] as a function of (m_T - m) measured in Pb+Pb collisions at $\sqrt{s_{NN}}$ = 2.76 TeV for 0-5% and 60-80% centrality bins. The Modified Tsallis fitted function is shown by the black curve.

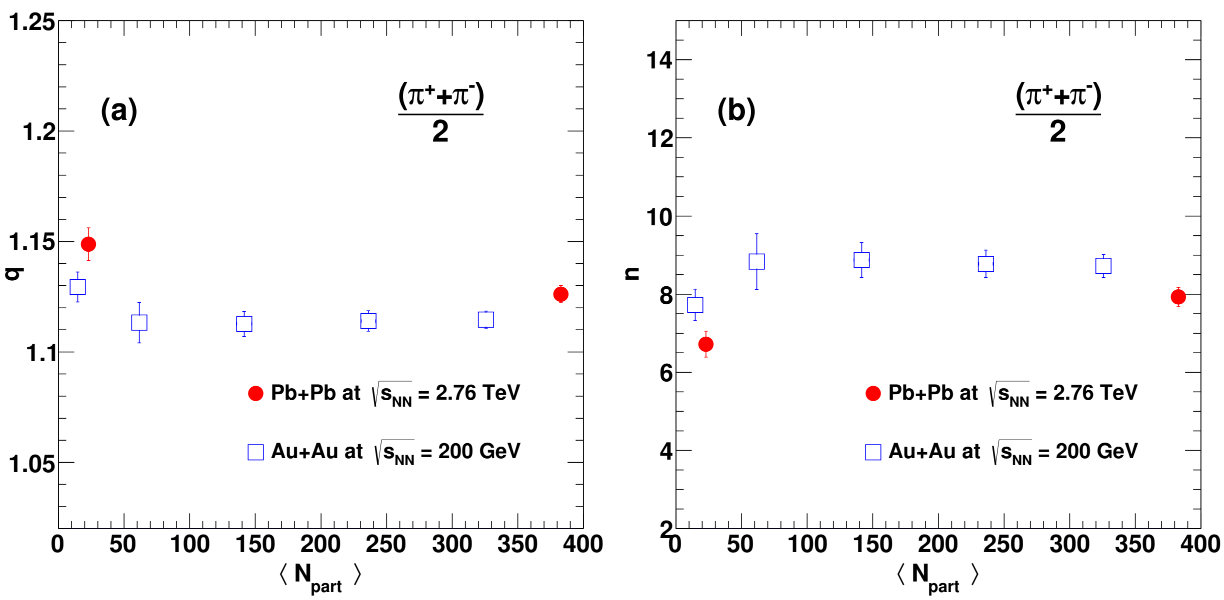

Figure 6.5: (Color online) Parameters (a) q and (b) n obtained from Eq. 6.1 for charged pions measured in Au+Au (open squares) collisions at $\sqrt{s_{NN}}$ = 200 GeV and in Pb+Pb (filled circles) collisions at $\sqrt{s_{NN}}$ = 2.76 TeV as a function of $\langle N_{part} \rangle$.

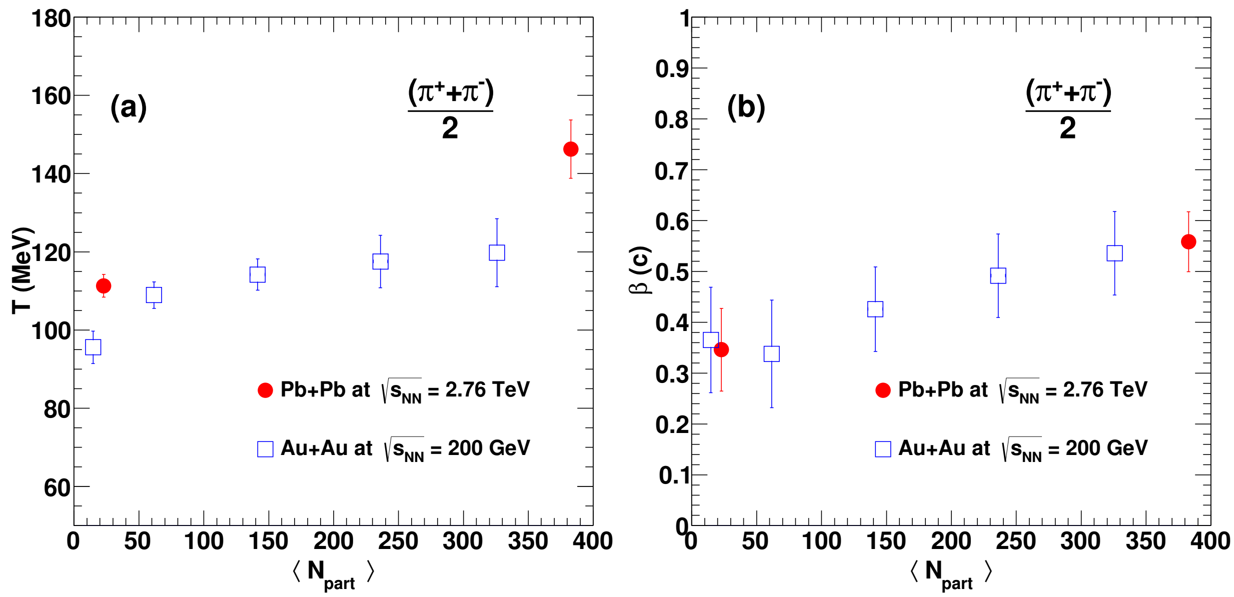

Figure 6.6: (Color online) Parameters (a) T and (b) β obtained from Eq. 6.1 for charged pions measured in Au+Au (open squares) collisions at $\sqrt{s_{NN}} = 200$ GeV and Pb+Pb (filled circles) collisions at $\sqrt{s_{NN}} = 2.76$ TeV as a function of $\langle N_{part} \rangle$.

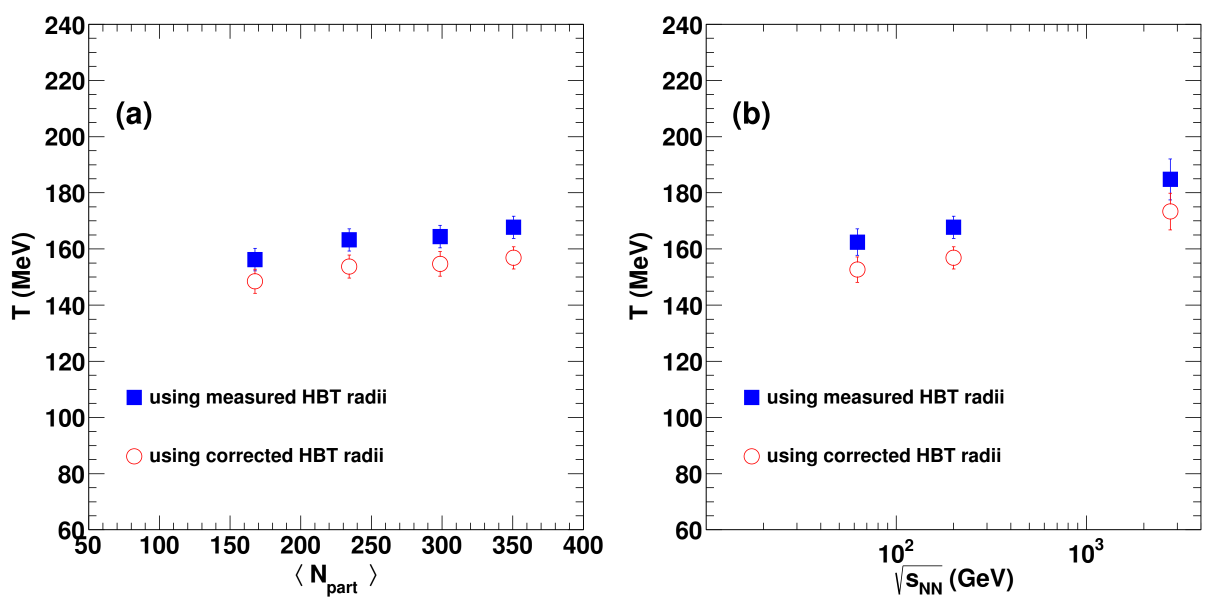

Figure 6.7: (Color online) Kinetic freeze-out temperature obtained using Eq. 6.6 (a) as a function of $\langle N_{part} \rangle$ and (b) as a function of $\sqrt{s_{NN}}$ (0-5% centrality) for RHIC and LHC energies.

full p_T range for all collision centralities, both at RHIC and LHC energies. The collision centralities can be converted to average number of participants $\langle N_{part} \rangle$ using Glauber model which is proportional to initial system size.

The parameter q as a function of $\langle N_{part} \rangle$ is shown in Fig. 6.5 (a). The value of q is higher for the peripheral collisions in comparision to other centralities, for both RHIC and LHC energies. The corresponding value for power n is shown in Fig. 6.5 (b). The values of q (or n) are similar for RHIC and LHC which show similar degrees of thermalization at the two energy regimes.

Figure 6.6 (a) and 6.6 (b) respectively show the kinetic freeze-out temperature (T) and the average transverse flow (β) as a function of $\langle N_{part} \rangle$. At RHIC energy, except for peripheral bin, the value of temperature remains constant for all centrality bins within uncertainties. For the most central collisions (0-5%), T has a higher value at LHC energy than that at RHIC. The transverse flow velocity β increases with the system size for both RHIC and LHC collisions and has almost same behavior in the two energy regimes.

The freeze-out temperature is obtained from Eq. 6.6 using the measured particle multiplicity and HBT volume. Figure 6.7 (a) shows the freeze-out temperature as a function of system size and Fig. 6.7 (b) shows the same as a function of collision energy. The solid squares show the result obtained from the measured HBT radii. The open circles show the result obtained using the corrected HBT radii (at $p_T = 0$) as explained before. This correction makes the values of T slightly smaller. It is seen that the freeze-out temperature increases while going from RHIC energy to LHC energy.

A comparison of Figs. 6.6 (a) and 6.7 (a) shows that the freeze-out temperature obtained from the two different methods follow similar trend as a function of system size. The temperature shows almost flat behavior with system size. Figures 6.6 (a) and 6.7 (b) show that the freeze-out temperature is more for LHC energy. The temperature obtained from two measurements namely the p_T spectra and the HBT measurements have same dependence on system size and energy. There is upto 20% difference in the magnitudes which might arise due to the experimental error and different p_T range of the measurements affected by transverse flow differently.

6.4 Conclusion

The transverse momentum spectra of charged pions measured in Au+Au collisions at $\sqrt{s_{NN}}$ = 200 GeV and Pb+Pb collisions at $\sqrt{s_{NN}}$ = 2.76 TeV are analysed using the modified Tsallis distribution. All the spectra used in this analysis are well described by this distribution. The parameter q of the modified Tsallis distribution suggests similar thermalization characteristics for systems at RHIC and LHC energies. The kinetic freeze-out temperature extracted from pion p_T spectra remains flat for all centrality bins except for the peripheral bin at RHIC energy. The freeze-out temperature is higher at LHC energy than that at RHIC energy for the most central collisions. The transverse flow velocity increases with system size for both of these energies. The kinetic freeze-out temperature is obtained as a function of system size and collision energy, from the measurement of HBT radii and particle multiplicity. The measured HBT radii are extrapolated to $m_T = 0.140$ GeV/c^2 to correct for the effect of transverse flow. The freeze-out temperature obtained from particle spectra and HBT measurements show similar trend as a function of system size as well as a function of collision energies. However, the kinetic freeze-out temperature obtained using HBT radii remains larger than that obtained from the particle spectra.

6.5 Data tables

The values for the measured HBT radii and the corrected HBT radii (by the extrapolation to $m_T = 0.140$ GeV) are given in the Table 6.1 for different centrality bins and in Table 6.3 as a function of collision energies. The values for the volumes and temperatures are given in Table 6.2 and Table 6.4.

Table 6.1: Measured and Corrected HBT radii for different centrality bins.

N_{part}	Measured HBT radii (fm)			Corrected HBT radii (fm)		
	R_{side}	R_{out}	R_{long}	R_{side}	R_{out}	R_{long}
167.6±5.4	4.42±0.09	5.04±0.09	5.72±0.07	4.68±0.15	5.52±0.20	6.39±0.16
234.3±4.6	4.71±0.04	5.44±0.11	6.08±0.04	5.04±0.11	6.05±0.28	6.92±0.13
298.6±4.1	5.13±0.05	5.99±0.17	6.59±0.06	5.50±0.15	6.68±0.36	7.49±0.19
350.6±2.4	5.41±0.02	6.2±0.17	6.72±0.03	5.87±0.08	6.79±0.33	7.67±0.12

Table 6.2: The values for volume and temperature obtained from the measured HBT radii and corrected HBT radii for different centrality bins.

N_{part}	Measured HBT radii (fm)		Corrected HBT radii (fm)	
	Volume (fm^3)	T (MeV)	Volume (fm^3)	T (MeV)
167.6±5.4	1759.99±55.07	156.23±3.98	2205.23±112.57	148.5±4.28
234.3±4.6	2124.3±29.09	163.23±3.95	2773.24±102.017	153.72±4.11
298.6±4.1	2731.43±45.12	164.43±4.03	3572.97±160.60	154.67±4.36
350.6±2.4	3097.66±21.29	167.71±3.98	4160.9±105.78	156.85±3.94

Table 6.3: Measured and Corrected HBT radii for different collision energies - 62.4 GeV, 200 GeV and 2.76 TeV.

N_{part}	Measured HBT radii (fm)			Corrected HBT radii (fm)		
	R_{side}	R_{out}	R_{long}	R_{side}	R_{out}	R_{long}
708±61.5	5.01±0.02	6.01±0.06	6.16±0.03	5.39±0.053	6.63±0.11	6.98±0.07
1036.5±73.5	5.41±0.02	6.2±0.17	6.72±0.03	5.87±0.08	6.78±0.33	7.66±0.12
2401.5±90	6.25±0.44	6.4±0.52	7.62±0.39	6.79±0.42	6.57±0.49	8.53±0.52

Table 6.4: The values for volume and temperature obtained from the measured HBT radii and corrected HBT radii for different collision energies - 62.4 GeV, 200 GeV and 2.76 TeV.

N_{part}	Measured HBT radii (fm)		Corrected HBT radii (fm)	
	Volume (fm^3)	T (MeV)	Volume (fm^3)	T (MeV)
708±61.5	2435.15±18.16	162.43±4.72	3200.69±55.23	152.67±4.51
1036.5±73.5	3097.66±21.29	167.71±3.98	4160.9±105.78	156.85±3.94
2401.5±90	4687.97±524.79	184.79±7.27	6206.44±662.37	173.32±6.53

CHAPTER 7 SUMMARY AND OUTLOOK

This thesis work presents experimental and theoretical studies of transverse momentum spectra of particles both in $p+p$ and heavy-ion collisions. The transverse momentum spectra (p_T) give an insight of particle production and also properties of hot/dense medium. The experimental study has been done to measure the K^{*0} meson in Cu+Cu collisions at $\sqrt{s_{NN}} = 200\,\text{GeV}$ with PHENIX detector. The theoretical works give an understanding of particle production in $p+p$ collisions and collective effects in heavy-ion collisions.

7.1 Measurement of K^{*0} meson

The K^{*0} meson is measured through the hadron decay channel $K^{*0} \to K^{+}\pi^{-}(\sim 67\%)$. The Drift Chambers and the Pad Chambers were used for tracking and momentum determination. These selected tracks were required to have associated hits in the third layer of Pad Chambers (PC3) or Electro-Magnetic Calorimeter (EMCal) referred as 'PC3 or EMCal matched tracks'. This was done to reject the contributions from secondary tracks. The time of flight detector was used to identify the charged hadrons. Two oppositely charged tracks were chosen in an event with $p_T > 0.3$ GeV/c for this study. In order to have good signal to background ratio, detector quality checks and optimized track selection cuts were implemented. Due to the limitation in PID of TOF detector, three different techniques were used to obtain the K^{*0} meson invariant mass spectra. In one of the methods, both the kaons and pions were identified in TOF. The K^{*0} measurement with this technique can be done upto $\sim$ 4 GeV/c. In the second method, kaon was identified but the other track was PC3 matched track and was given the mass of pion. This method extends the measurement towards the lower p_T region. In the third method, both the tracks were PC3 matched tracks and given the mass of kaon and pion as per combinatorial requirements. This technique extends the measurement in the higher p_T region upto $\sim$ 8.5 GeV/c. These three techniques are exclusive to each other and are statistically independent. The contributions from the uncorrelated background were estimated by the event-mixing method and then subtracted. The correlated background contributions from mis-identified pairs (arising from K_S^0 and ϕ decays) were also estimated and subtracted. The invariant mass spectra are fitted by the Relativistic Breit Wigner and a third order polynomial. The yield is obtained by the bin-counting method for each technique. The final invariant yield spectra are obtained by the standard weighted averaging method. It is seen that the yields obtained from different techniques are in good agreement with each other within systematic uncertainties. This also supports the robustness of the results.

The invariant mass transverse momentum spectra are obtained for MB, 0-20%, 20-40%, 40-60% and 60-94% centrality bins. In Cu+Cu collisions, the p_T spectra spans from 1.4-8.0 GeV/c. The nuclear modification factors (R_{CuCu}) are also obtained for these centrality bins. The study of the R_{CuCu} for K^{*0} meson as a function of different centralities shows that, there is no suppression in the peripheral collisions (60-94%). Suppression increases for p_T above 5 GeV/c with the increase in central collision. Also, a comparative study (Fig. 7.1) among the strange mesons (K^{*0}, K_S^0, ϕ) and π^0s are done for the most central (0-20%), most peripheral (60-94%) and MB data. It has been observed that, in peripheral collisions, none of the mesons are suppressed. Except for the peripheral collisions, π^0s are the most suppressed meson, having a flat behavior in the measured kinematic range. Other mesons are suppressed similar to π^0 meson above $p_T = 5$ GeV/c. For $p_T < 5$ GeV/c, the suppression is different for different mesons. At low p_T (1–2 GeV/c), K^{*0} and ϕ are not suppressed, however, suppression increases with p_T. The suppression of these particles are compared to the charged kaons and protons in Au+Au collisions at the same energy for the similar N_{part} as shown in Fig. 7.2. In peripheral collisions the R_{AA} factors are consistent with unity for $p_T > 2\,\mathrm{GeV}/c$. However, an enhancement ($R_{\mathrm{AA}} \approx 1.3$) is observed for protons. In central collisions, at higher p_T, all hadrons suffer similar suppression, within uncertainties. In the intermediate p_T range ($p_T = 2$–5 GeV/c), hierarchy in the suppression of particles is observed where, the protons shows enhancement, π^0s are the most suppressed and K^{*0} and ϕ mesons show an intermediate behavior. The similar magnitude in suppression in central collisions at high p_T points to the fact that energy loss occurs at the parton level.

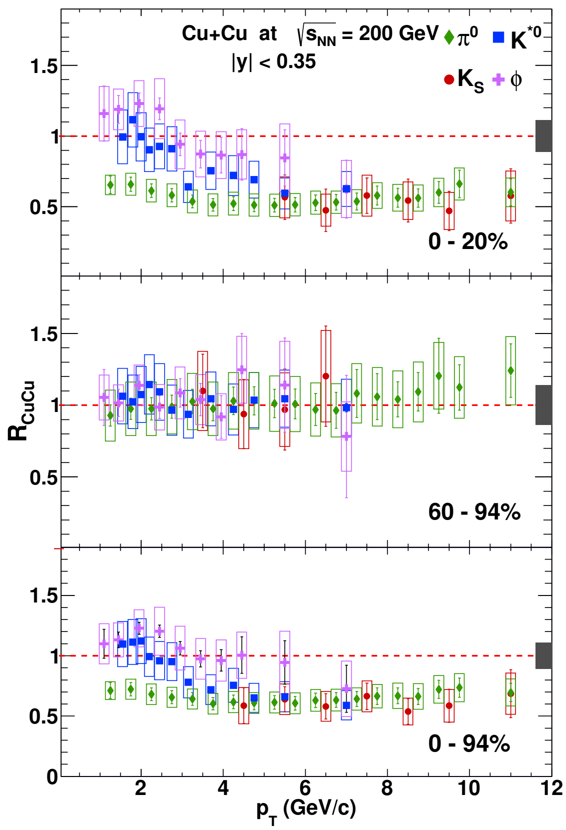

Figure 7.1: Nuclear modification factor as a function of p_T for K_S^0, K^{*0} for centralities (a) 0%–20%, (b) 0%–94% (MB) and (c) 60%–94% in Cu+Cu collisions at $\sqrt{s_{NN}} = 200\,\text{GeV}$. Results from π^0 [87] and ϕ [86] are also shown. The statistical errors are shown by vertical bars. The systematic uncertainties are shown by boxes. The global $p + p$ uncertainty of $\sim$ 10% is not shown.

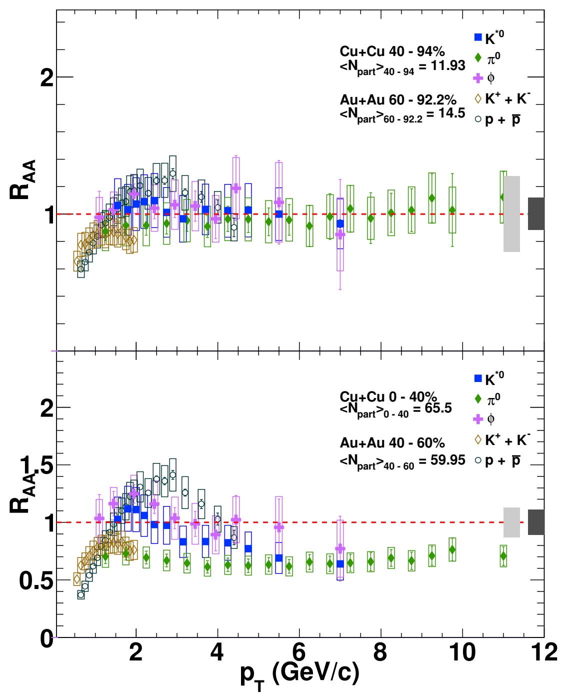

Figure 7.2: Comparison of the nuclear modification factor of π^0 [87], ϕ [86], and K^{*0} in Cu+Cu collisions and proton [35] and kaon [35] in Au+Au collisions at $\sqrt{s_{NN}} = 200\,\text{GeV}$. The comparisons are made for (a) 40%–60% and (b) 60%–92% in Au+Au system and 0%–40% and 40%–94% in the Cu+Cu system corresponding to similar N_{part} values in the two systems. The statistical errors are shown by vertical bars. The systematic uncertainties are shown by boxes. The global $p+p$ uncertainty of $\sim 10\%$ is not shown.

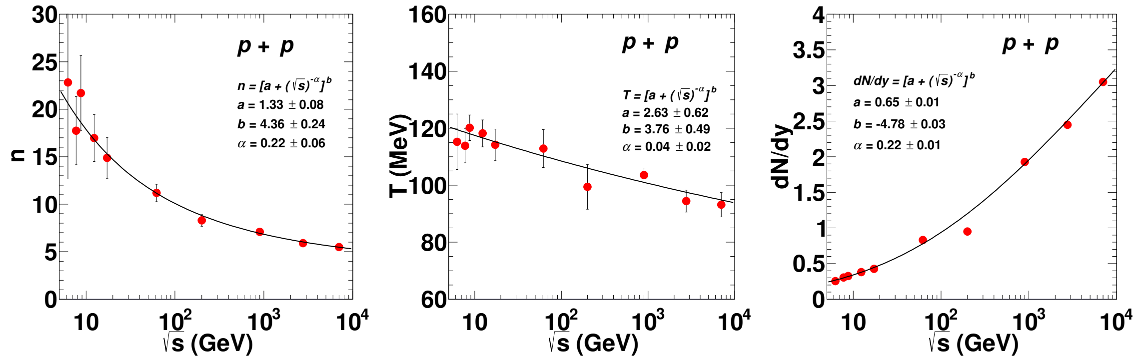

Figure 7.3: (Color online) The variation of the Tsallis parameter n, T and dN/dy for charged pions as a function of $\sqrt{s}$. The solid curve represents the parameterization $(a + (\sqrt{s})^{-\alpha})^b$.

7.2 Theoretical study

7.2.1 Charged pion spectra in $p + p$ collisions

Charged pion transverse momentum spectra for different collisional energies ($\sqrt{s}$) and also for different event multiplicity classes ($\langle N_{tracks} \rangle$) (only for LHC energies) are studied with the Tsallis distribution in $p + p$ collisions. The Tsallis distribution describes the particle spectra in terms of two parameters - the non-extensivity parameter q and temperature T. The parameter q in Tsallis statistics is related to the power n in the pQCD calculations for particle spectra, as $n = 1/(q$ - $1)$, which eventually describes the tail of the spectra coming from hard QCD scatterings. The Tsallis parameters T, n and dN/dy (integrated yield) are studied as a function of $\sqrt{s}$ and $\langle N_{tracks} \rangle$.

The Tsallis parameters as a function of $\sqrt{s}$ are shown in Fig. 7.3. It is seen that, the parameter n decreases with the increase in collision energies and starts saturating at LHC energies. The value of T decreases gradually from SPS energies to LHC energies. This means that the contribution from softer processes decreases with the increase in collision energies. The p_T integrated pion yield increases with increasing $\sqrt{s}$ and becomes 10 times while going from SPS to highest LHC energy. The Tsallis parameters are also obtained as a function of event multiplicity for all three LHC energies which can be described by the same curve, as

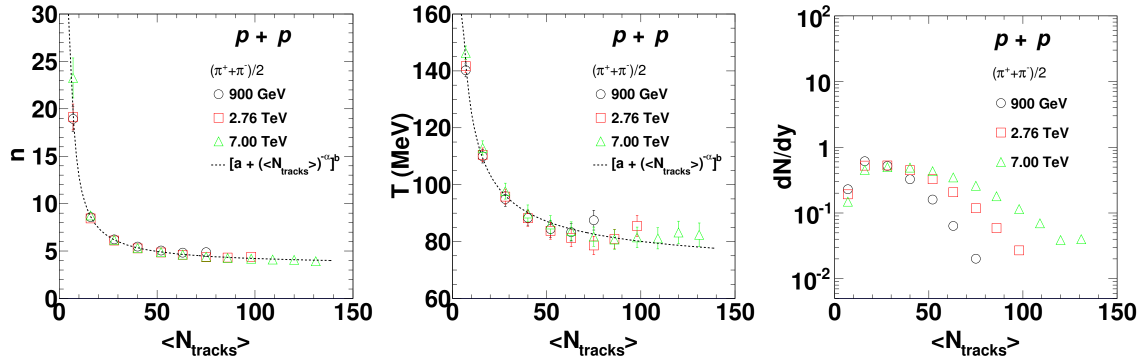

Figure 7.4: (Color online) The variation of the Tsallis parameter n, T and dN/dy for charged pions as a function of $\langle N_{tracks}\rangle$. The variation is shown for 900 GeV by black circles, 2.76 TeV by red squares and 7.00 TeV by green triangles. The dashed curve represents the parameterization $(a + (\langle N_{tracks}\rangle)^{-\alpha})^{b}$.

shown in Fig. 7.4. The variation of the parameters n and T as a function of $\langle N_{tracks}\rangle$ is very similar to the variation of these parameters as a function of $\sqrt{s}$. This behavior illustrates the fact that, events with higher multiplicity have larger contribution from hard processes. The value of n for high multiplicity events at 7 TeV is ~ 4 which is depictive of production from point quark-quark scattering. The p_T integrated pion yield distribution for the three LHC energies shows that as the energy increases, more and more high mutliplicity events are added in the sample with mean of the distribution shifting towards higher multiplicity.

7.2.2 Charged pion spectra in heavy-ion collisions

The transverse momentum spectra of charged pions measured in Au+Au collisions at $\sqrt{s_{NN}}$ = 200 GeV and Pb+Pb collisions at $\sqrt{s_{NN}}$ = 2.76 TeV are analyzed using the modified Tsallis distribution. All the spectra used in this analysis are well described by this distribution. The freeze-out temperature are also estimated from the measured particle multiplicity and the HBT volume of the system.

The parameter q of the modified Tsallis distribution suggests similar thermalization characteristics for systems at RHIC and LHC energies. The results for the kinetic freeze-out temperature (T) and the flow velocity (β) extracted from the pion spectra are shown

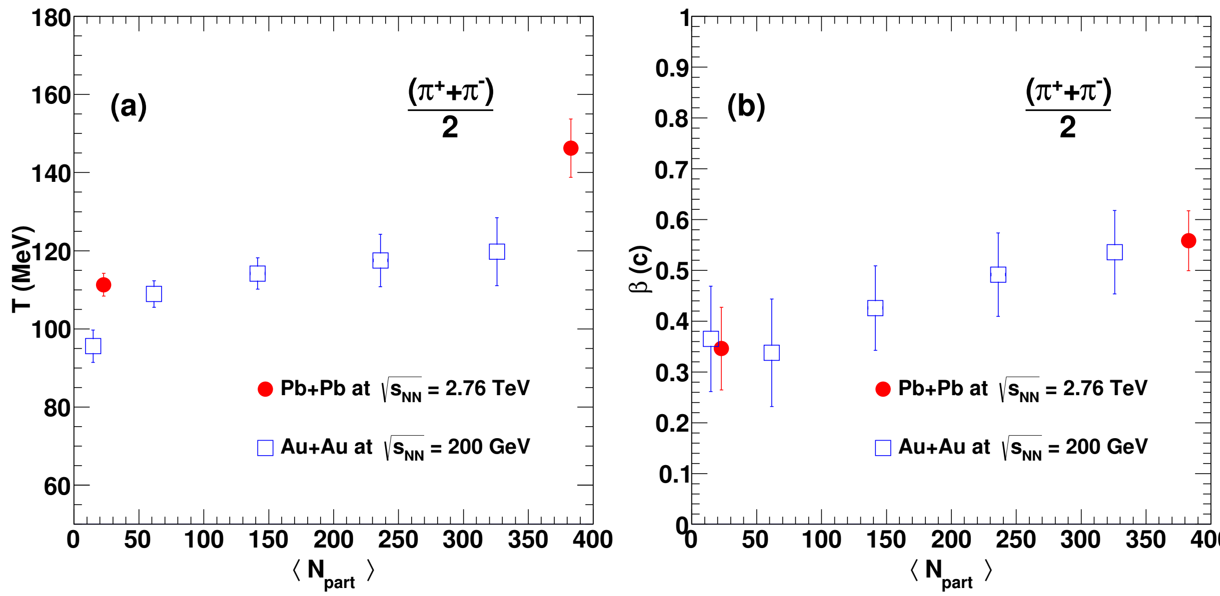

Figure 7.5: (Color online) Parameters (a) T and (b) β obtained for charged pions measured in Au+Au (open squares) collisions at $\sqrt{s_{NN}} = 200$ GeV and Pb+Pb (filled circles) collisions at $\sqrt{s_{NN}} = 2.76$ TeV as a function of $\langle N_{part} \rangle$.

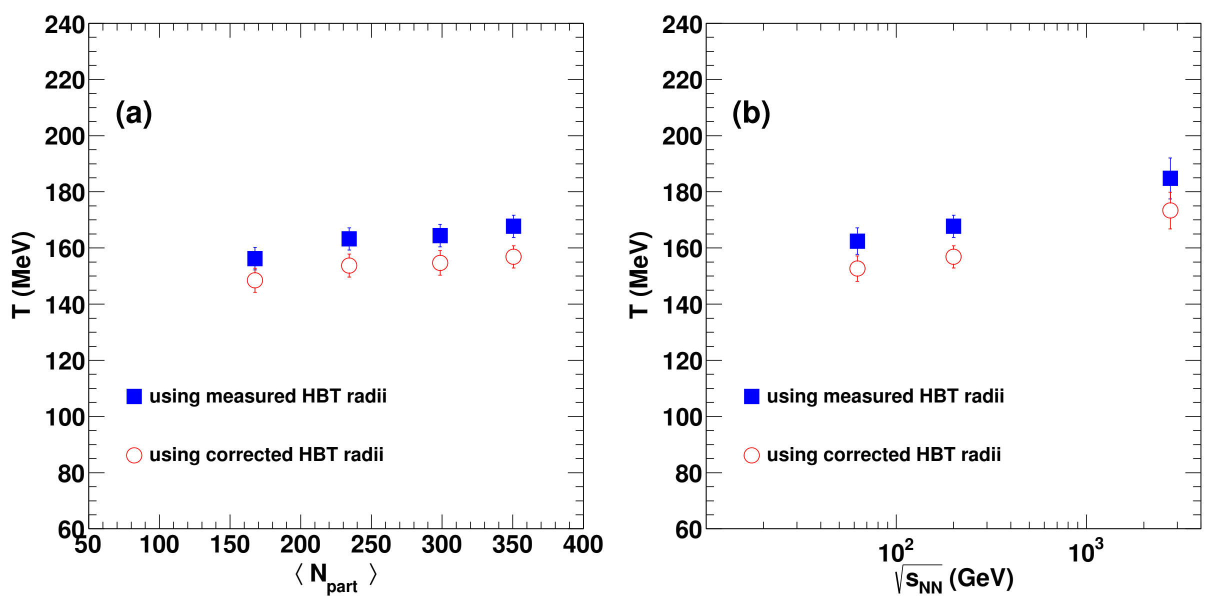

Figure 7.6: (Color online) Kinetic freeze-out temperature obtained (a) as a function of $\langle N_{part} \rangle$ and (b) as a function of $\sqrt{s_{NN}}$ (0-5% centrality) for RHIC and LHC energies.

in Fig 7.5. The parameter T remains flat for all centrality bins except for the peripheral bin at RHIC energy. The freeze-out temperature at LHC energy is higher than that of at RHIC energy. The parameter β increases with system size for both of these energies. The freeze-out temperature are also obtained from the measurements of HBT radii and particle multiplicity as a function of system size and collision energy. The measured HBT radii are extrapolated to $m_T = 0.140$ GeV/c^2 to correct for the effect of transverse flow in the system. Fig. 7.6 (a) shows the freeze-out temperature as a function of system size, obtained from this method. Fig. 7.6 (b) shows the same as a function of collision energies. The blue squares show the result obtained using the measured HBT radii and the open circles show the result obtained using the corrected HBT radii. The freeze-out temperature obtained from these two methods shows similar trend as a function of system size and as a function of collision energies.

BIBLIOGRAPHY

[1] J. D. Bjorken, Phys. Rev. D**27**, 140 (1983). 1, 14, 15, 131

[2] F. Karsch Lect. Notes Phys. **583**, 209 (2002), arXiv : - hep - lat/0106019. 1, 15

[3] E. V. Shuryak, Phys. Rept. **61**, 71 (1980). 1, 7

[4] E. Rutherford and H. Geiger, Proc. Roy. Soc. Lond. A, **81**, 162 (1908). 2

[5] J. Chadwick, Proc. Roy. Soc. Lond. A, **136**, 692 (1932). 2

[6] Cornell preprint CTSL-20, unpublished, (1961). 2

[7] M. Gell-Mann, Phys. Lett., **8** 214 (1964). 2

[8] G. Zweig, CERN preprint TH-412, unpublished (1964). 2

[9] J. Beringer *et al.* (Particle Data Group), Phys. Rev. D**86**, 010001 (2012). xxx, 3, 90

[10] J. Bjorken and S. Glashow, Phys. Lett., **11**, 255 (1970). 3

[11] J.E. Augustin *et al.*, Phys. Rev. Lett., **33**, 1406 (1974); J.J. Aubert *et al.*, Phys. Rev. Lett., **33**, 1404 (1974). 3

[12] S.E. Herb *et al.*, Phys. Rev. Lett., **39**, 252 (1977). 3

[13] F. Abe *et al.*, Phys. Rev. Lett., **74**, 2626 (1995); S. Abachi *et al.*, Phys. Rev. Lett., **74**, 2632 (1995); 3

[14] D. J. Ross and F. Wilczek, Phys. Rev. Lett., **30**, 26 (1973). xx, 6

[15] D. J. Gross and F. Wilczek, Phys. Rev. Lett., **30**, 1343 (1973). 6

[16] H. D. Ploitzer, Phys. Rev. Lett., **30**, 1346 (1973). 6

[17] J.C. Collins and M. J. Perry, Phys. Rev. Lett., **34**, 1353 (1975). 7

[18] N. Cabibo and G. Parisi, Phys. Lett. B**34**, 67 (1975). 7, 8

[19] E. V. Shuryak, Phys. Lett. B**78**, 150 (1978). 7

[20] F. Karsch, Lecture Notes of Physics, **583** (2002); arXiv:hep-lat/0106019. xx, 8

[21] R. S. Bhalerao, arXiv:1404:3294[nucl-th]. xx, 9

[22] Z. Fodor and S. D. Katz, Prog. Theor. Phys. Suppl., **153**, 86 (2004). 9

[23] S. Ejiri *et al.*, Prog. Theor. Phys. Suppl., **153**, 118 (2004). 9

[24] Z. Fodor, Nucl. Phys. A**715**, 329 (2003). 10

[25] A. Chodos *et al.*, Phys. Rev. D**9**, 3471 (1974). 10

[26] K. Yagi, T. Hatsuda and Y. Miake, Camb. Monogr. Part. Phys. Nucl. Phys. Cosmol., **23**, 1 (2005). xx, 13

[27] F. Karsch, Nucl. Phys. A **698**, 199 (2002). 15

[28] K. Adcox *et. al.* (PHENIX Collaboration), Phys. Rev. Lett **87**, 052301 (2001). 15

[29] S. S. Adler *et. al.* (PHENIX Collaboration), Phys. Rev. C**71**, 034908 (2005). 15

[30] K. Adcox *et. al.* (PHENIX Collaboration), Nucl. Phys. A**757**, 184 (2005). xx, 15, 16

[31] K. Aamodt *et. al.* (ALICE Collaboration), Phys. Rev. Lett. **105**, 252301 (2010). xx, 17

[32] K. Aamodt *et. al.* (ALICE Collaboration), Phys. Rev. Lett. **106**, 032301 (2011). xx, 17

[33] A. Adare *et. al.* (PHENIX Collaboration), Phys. Rev. Lett. **104**, 132301 (2010). xx, 18, 19

[34] N. Arbor for ALICE Collaboration, EPJ Web Conf. **60**, 13011 (2013). 19

[35] A. Adare *et al.* (PHENIX Collaboration), Phys. Rev. C **88**, 024906 (2013). xx, xxi, xxiv, xxv, xxvi, 20, 31, 104, 105, 132, 135, 136, 147

[36] B. Abelev *et al.* (ALICE Collaboration), Phys. Lett. B **736**, 196 (2014). xx, xxv, 20, 132, 135, 137

[37] A. Andronic, P. Braun-Munzinger, K. Redlich and J. Stachel, arXiv: 1210.7724. xx, 21, 22

[38] A. Andronic, P. Braun-Munzinger and J. Stachel, Nucl. Phys. A**772**, 167 (2006). 21, 115, 131

[39] B. Abelev *et. al.* (ALICE Collaboration), Phys. Lett. B**728**, 216 (2014). xxi, 23, 24

[40] J. Rafelski and B. Muller, Phys. Rev. Lett. **48**, 1066 (1982). 22

[41] E. Braaten and M. H. Thoma, Phys. Rev. D **44**, 2625 (1991). 24

[42] D. d'Enterria and B. Betz, Lect. Notes Phys. **785**, 285 (2010). 24

[43] X. N. Wang and M. Gyulassy, Phys. Rev. Lett. **68**, 1480 (1992). 24

[44] N. Armesto, J. Phys. G **32**, R367 (2006). 27

[45] J. W. Cronin *et al.*, Phys. Rev. D **11**, 3105 (1975). 27, 29, 30

[46] I. Tserruya, EPJ Web Conf. **70**, 00022 (2014). xxi, 25, 27

[47] Z. Yin (for ALICE Collaboration), Int. J. Mod. Phys. Conf. Ser. **29**, 1460228 (2014). xxi, 25, 27

[48] S. Chatrchyan *et al.* (CMS Collaboration), Eur. Phys. J. C **72**, 1945 (2012). xxi, 26, 28

[49] J. Aubert, Phys. Lett. B**123**, 275 (1983). 28

[50] T. Sakaguchi, J. Phys. Conf. Ser. **458**, 012022 (2013). xxi, 29

[51] CMS Collaboration, CMS PAS HIN-12-004. xxi, 32

[52] S. Chatrchyan *et. al.* (CMS Collaboration), Phys. Rev. C**84**, 024906 (2011). xxi, 32, 33

[53] M. Harrison, T. Ludlam and S. Ozaki. RHIC project overview, Nucl. Instr. and Meth., A**499**, 235 - 244 (2003). 37

[54] "RHIC Manual", `http://www.bnl.gov/cad/accelerator/docs/pdf/RHICConfManual.pdf`. 37

[55] M. Adamczyk *et. al.* The BRAHMS experiment at RHIC, Nucl. Instr. and Meth., A**499**, 437 - 468 (2003). 39

[56] B.B. Back *et. al.* The PHOBOS dectector at RHIC, Nucl. Instr. and Meth., A**499**, 603 - 623 (2003). 39

[57] K.H. Ackerman *et. al.* STAR detector overview, Nucl. Instr. and Meth., A**499**, 624 - 632 (2003). 39

[58] K. Adcox *et. al.* PHENIX detector overview, Nucl. Instr. and Meth., A**499**, 469 - 479 (2003). 39, 40

[59] H. Akikawa *et. al.* PHENIX Muon Arms, Nucl. Instr. and Meth., A**499**, 537 - 548 (2003). 42

[60] M. Allen *et. al.* PHENIX inner detectors, Nucl. Instr. and Meth., A**499**, 549 - 559 (2003). 45

[61] K. Ikematsu *et. al.* A start timing detector for the collider experiment PHENIX at RHIC -BNL., Nucl. Instr. and Meth., A**411**, 238 - 559 (1998). 45

[62] T. Ludlam *et. al.* Overview of experiments and detectors at rhic, Nucl. Instr. and Meth., A**499**, 428 - 432 (2003). 46

[63] C. Adler *et. al.* The RHIC zero degree calorimeters, Nucl. Instr. and Meth., A**470**, 488 - 499 (2001). 46

[64] S.H. Aronson *et. al.* PHENIX magnet system, Nucl. Instr. and Meth., A**499**, 480 - 488 (2003). 48

[65] K. Adcox *et. al.* PHENIX central arm tracking detectors, Nucl. Instr. and Meth., A**499**, 489 - 507 (2003). 49

[66] K. Adcox *et. al.* Construction and performance of the PHENIX pad chambers, Nucl. Instr. and Meth., A**497**, 263 - 293 (2003). 51

[67] Y. Akiba Aronson *et. al.* Ring imaging cherenkov detector of PHENIX experiment at RHIC , Nucl. Instr. and Meth., A**453**, 279 - 283 (2000). 53

[68] T. Sakaguchi *et. al.* Development of front end electronics for PHENIX RHIC, Nucl. Instr. and Meth., A**453**, 382 - 385 (2000). 53

[69] M. Aizawa *et. al.* PHENIX central arm and particle I.D. detectors, Nucl. Instr. and Meth., A**499**, 508 - 520 (2003). 54

[70] A Adare *et al.* (PHENIX Collaboration), Phys. Rev. C**83**, 064903 (2011). xxiv, 54, 116, 119, 120, 133

[71] B. Love *et. al.* The implementation and performance of the phenix time of flight west detector subsystem. 54

[72] L. Aphhecetche *et. al.* PHENIX calorimeter, Nucl. Instr. and Meth., A**499**, 521 - 536 (2003). 56

[73] S. C. Johnson, Three dimensional track finding in the phenix drift chamber by a combinatorial hough transform method, In Proc. of Intl. Conf. on Computing in High Energy Physics (CHEP), Chicago IL, (1998). 57

[74] J. T. Mitchell *et. al.*, Phenix central arm particle ID detectors, Nucl. Instr. and Meth., A**482**, 491 - 512 (2002). 58, 81

[75] A. Chikanian *et. al.*, A momentum reconstruction algorithm for PHENIX spectrometer at Brookhaven, Nucl. Instr. and Meth., A**371**, 480 - 488 (1996). 60

[76] A. Drees and X. Zhangbu, Results from Luminosity Scans during the RHIC 2000, Proceedings of the 2001 Particle Accelerator Conference, Chicago IL, 60 (2003). 61

[77] M.L. Miller, K. Reygers, S.J. Sanders and P. Steinberg Glauber Modelling in high energy nuclear collisions, Ann. Rev. Nucl. Part. Sci. **57**, 205 (2007). 64

[78] S.S. Adler *et. al.* PHENIX online systems, Nucl. Instr. and Meth., A**499**, 560 - 592 (2003). 64

[79] J. Adams *et al.* (STAR Collaboration), Phys. Rev. C**71**, 064902 (2005). 77

[80] G. I. Kopylov, Phys. Lett. B**50**, 472 (1974). 77

[81] D. Drijard, H. G. Fisher and T. Nakada, Nucl. Instr. Meth. A**225**, 367 (1984). 77

[82] D. L'Hote, Nucl. Instr. Meth. A**337**, 544 (1994). 77

[83] CERN program Library W5013, GEANT Manual, *v.3.2.1* (1994). 80

[84] T. Awes *et al.* PHENIX analysis note AN73 93

[85] A. Adare et al. (PHENIX), Phys. Rev. D**83**, 052004 (2011). 98, 116, 118, 119, 133

[86] A. Adare *et al.* (PHENIX Collaboration), Phys. Rev. C **83**, 024909 (2011). xxiv, xxv, xxvi, 101, 103, 104, 146, 147

[87] A. Adare *et al.* (PHENIX Collaboration), Phys. Rev. Lett. **101**, 162301 (2008). xxiv, xxv, xxvi, 101, 103, 104, 146, 147

[88] A. Adare *et al.* (PHENIX Collaboration), Phys. Rev. C **84**, 044905 (2011). 105

[89] G. Sterman *et al.* (CTEQ Collaboration), Rev. Mod. Phys. **67**, 157 (1995); J.F. Owens *et al.*, Phys. Rev. D**18**, 1501 (1978). 115

[90] R. Blankenbecler, S.J. Brodsky and J.F. Gunion, Phys. Lett. B**42**, 461 (1972). 115

[91] E. Fermi, Progress Theor. Phys., **5**, 570 (1950). 115

[92] C. Tsallis, J. Stat. Phys. **52**, 479 (1988). 115, 116, 118, 132

[93] T.S. Biro, G. Purcsel and K. Urmossy, Eur. Phys. J. A**40**, 325 (2009). 115, 119, 132, 133

[94] W.M. Alberico and A. Lavagno, Eur. Phys. J. A**40**, 313 (2009). 115

[95] T.S. Biro and G. Purcsel, Phys. Rev. Lett. **95**, 162302 (2005). 115

[96] K. Urmossy, arXiv:1212.0260[hep-ph]. 115, 124

[97] P.K. Khandai, P. Sett, P. Shukla and V. Singh, Int. J. Mod. Phys. **28**, 1350066 (2013). 116, 121, 132

[98] M. Rybczynski and Z. Wlodarczyk, Eur. Phys. J. C**74**, 2785 (2014). 116, 121

[99] M. D. Azmi and J. Cleymans, J. Phys. G**41**, 065001 (2014). 116

[100] J. Cleymans *et al.*, Phys. Lett. B**723**, 351 (2013). 116

[101] C.Y. Wong and G. Wilk, Phys. Rev. D**87**, 114007 (2013). 116, 132, 133

[102] R. Hagedorn, Riv. del Nuovo Cim. **6N 10**, 1 (1984). 116, 117, 132

[103] R. Blankenbecler and S. J. Brodsky, Phys. Rev. D**10**, 2973 (1974). 116, 118, 132

[104] N. Abgrall *et al.* Eur. Phys. C**74**, 2794 (2014). xxiv, 116, 119, 120

[105] S. Chatrchyan *et al.* (CMS Collaboration), Eur. Phys. J. C**72**, 2164 (2012). xxiv, 116, 119, 120, 124, 125

[106] R. Hagedorn, Nuovo Cim. Suppl. **3**, 147 (1965). 117

[107] D. B. Walton and J. Rafelski, Phys. Rev. Lett. **84**, 31 (2000). 117

[108] G. Wilk and Z Wlodarczyk, Phys. Rev. Lett. **84**, 2770 (2000). 118, 133

[109] A. Adare *et al.* (PHENIX Collaboration), Phys. Rev. C**83**, 064903 (2011). 119

[110] B. I. Abelev *et al.* (STAR Collaboration), Phys. Rev. C**75**, 64901 (2007). 119, 133

[111] J. Cleymans and D. Worku, Eur. Phys. J. A**48**, 160 (2012). 119, 133

[112] R. Blankenbecler, S.J. Brodsky and J. Gunion, Phys. Rev. **D 12**, 3469 (1975) . 119, 133

[113] S.J. Brodsky, H. J. Pirner and J. Raufeisen, Phys. Lett. **B 637**, 58 (2006). 119, 133

[114] T.S. Biro, K. Urmossy and G.G. Barnafoldi, J. Phys. G**35**, 044012 (2008). 119

[115] K. Aamodt *et al.* (ALICE Collaboration), Eur. Phys. J. C**71**, 1655 (2011). 119

[116] B. I. Abelev *et al.* (STAR Collaboration), Phys. Rev. C**75**, 64901 (2007). 119

[117] J. Adams *et al.* (STAR Collaboration), Phys. Lett. B**637**, 161 (2006), Phys. Rev. **C 75**, 064901 (2007). 119

[118] A. Adare *et al.* (PHENIX Collaboration), Phys. Rev. C**83**, 064903 (2011). 119

[119] See e.g the Proceedings of the Quark Matter Conference 2012, Nucl. Phys. A**904 - 905**, (2012). 131

[120] M. Gyulassy and L. McLerran, Nucl. Phys. A**750**, 30 (2005). 131

[121] T. Hirano and Y. Nara, Phys. Rev. C**69**, 34908 (2004). 132

[122] R. Fries, V. Greco and P. Sorensen, Ann. Rev. Nucl. Part. Sci. **58**, 177 (2008). 132

[123] R. Hagedorn, Rev. del Nuovo Cim. **6N 10**, 1 (1984).

[124] P. Sett and P. Shukla, Adv. High Energy Phys. **2014**, 896037 (2014). 132

[125] Z. Tang *et al.*, Phys. Rev. C **79**, 051901 (2009). 132

[126] P. K. Khandai, P. Sett, P. Shukla and V. Singh, J. Phys. G**41**, 025105 (2014). 132, 133

[127] B. De, Eur. Phys. J. A**50**, 138 (2014). 132

[128] J. Cleymans, G. Hamar, P. Levai, S. Wheaton, J. Phys. G**36**, 064018 (2009). 133

[129] B. I. Abelev *et al.* (STAR Collaboration), Phys. Rev. C**80**, 024905 (2009). xxv, 135, 136

[130] K. Aamodt *et al.* (ALICE Collaboration), Phys. Lett. B**696**, 328 (2014). 135

Appendices

APPENDIX A

RELATIVISTIC KINEMATICS AND THERMODYNAMICS

A.1 Relativistic kinematics

In high energy nuclear collisions, the nuclie travel nearly with the speed of light (c). Hence, it is convenient to use the kinematics in relativistic limits. In this field, the special theory of relativity is used for describing the events and results.

Here some of the important and widely used mathematical relations and parameters are discussed :

- In Special theory of relativity, any event in an interial refernce frame can be described in 4 - D as : $x^\mu = (t, x, y, z) \equiv (x^0, x^1, x^2, x^3)$, known as 4-vector. Covariant vectors are denoted as x^μ and Contravariant vectors are denoted as x_μ. These two are related as : $x_\mu = g_{\mu\nu}\, x^\nu$, $g_{\mu\nu}$ is known as metric tensor. It has only diagonal elements, the off-diagonal elements are zero, $g_{\mu\nu} = \mathrm{diag}(1, -1, -1, -1)$. Also, x^μ is denoted by (t, $\vec{x}$) and x_μ is denoted by (t, -$\vec{x}$). The scalar product of two 4-vectors is given as,

$$x^\mu x_\nu = x^0.x_0 - x^1.x_1 - x^2.x_2 - x^3.x_3 = x^2 \tag{A.1}$$
$$x^\mu y_\nu = x^0.y_0 - x^1.y_1 - x^2.y_2 - x^3.y_3 = x.y \tag{A.2}$$

  These scalar products are invariant quantities and often reffered as *Lorentz invariant*.

- Lorentz transformation: Let an event in an interial reference frame is at $x = (t, x, y, z) \equiv (x^0, x^1, x^2, x^3)$. Let x' be a 4-vector in another frame, which is moving with a velocity v along the X direction with respect to the initial frame. Let $x' = (t', x', y', z') \equiv (x^{0\prime}, x^{1\prime}, x^{2\prime}, x^{3\prime})$ be the co-ordinates in the other interial frame. In that case, these two frames are related as,

$$x^{0\prime} = \gamma(x^0 - \beta x^1) \tag{A.3}$$
$$x^{1\prime} = \gamma(x^1 - \beta x^0) \tag{A.4}$$
$$x^{2\prime} = x^2 \tag{A.5}$$
$$x^{3\prime} = x^3 \tag{A.6}$$

where, $\beta = v/c$ and $\gamma = 1/\sqrt{1-\beta^2}$, known as Lorentz factor.

- 4-velocity and 4-momentum: To obtain the 4-velocity and hence 4-momentum, proper time, which is a Lorentz invriant quantity, is defined as,

$$\tau^2 = t^2 - x^2 \tag{A.7}$$

The 4-velocity is given as,

$$u^\mu = \frac{dx^\mu}{d\tau} = \frac{dx^\mu}{dt}\frac{dt}{d\tau} = \gamma(1, \vec{v}) \tag{A.8}$$

The 4-momentum is defined as,

$$p^\mu = mu^\mu = m\gamma(1, \vec{v}) \tag{A.9}$$

Energy-Momentum four vector is also represented as : $p^\mu = (E,\, p_x,\, p_y,\, p_z) \equiv (p^0,\, p^1,\, p^2,\, p^3) \equiv (p^0,\, \vec{p})$. The invariant mass formula :

$$|p^2| = p^\mu p_\mu = E^2 - \vec{p}^2 = m^2. \tag{A.10}$$

In high energy nuclear collisions, the beams collide with each other along the beam direction. Generally, the beam direction is taken along Z direction of cartesian co-ordinates. The particles in beam travel with relativistic speed. Hence, the boost will be along Z direction with respect to the observers from rest frame. To make life simpler, some quantities are defined which are boost invariant or they transform in a simple manner with the boosted frame.

- Transverse momentum and mass : The components of energy-momentum four vector in a boosted frame (along Z axis) takes the form,

$$E^{0\prime} = \gamma(E^0 - \beta p_z) \tag{A.11}$$
$$p_x^\prime = p_x \tag{A.12}$$
$$p_y^\prime = p_y \tag{A.13}$$
$$p_z^\prime = \gamma(p_z - \beta E) \tag{A.14}$$

It is seen that, the transverse component of momentum $p_T = p_x^2 + p_y^2$, has not changed due to the Lorentz boost. Same is the case with transverse mass $m_T^2 = p_T^2 + m_0^2$, where m_0 is the rest mass. Hence, these two variables have utmost importance in relativistic high energy collision.

- Rapidity : This variable is defined as,

$$y = \frac{1}{2}\ln\left(\frac{E+p_z}{E-p_z}\right) = \ln\left(\frac{E+p_z}{m_T}\right) \tag{A.15}$$

This can be understood as a logarithmic measure of longitudinal momentum and total energy of particle. Using the relation $\beta_z = p_z/E$, y takes the form,

$$y = \frac{1}{2} \ln \left(\frac{1+\beta_z}{1-\beta_z} \right) \tag{A.16}$$

For low energy limit, it can be shown that $y \simeq \beta_z$. Under Lorentz boost, with a velocity β along Z direction, this variable transforms as,

$$y' = y + \ln \sqrt{\frac{1-\beta}{1+\beta}} \tag{A.17}$$

$$\implies y' = y - \tanh^{-1}\beta \tag{A.18}$$

The main advantage of using this variable is its additive property under boost along the beam direction. This variable is useful when comparing the rapidity distributions of particles in fixed target experiment and collider experiments (discussed later). The total energy E and momentum component p_z can be expressed interms of y, as,

$$E = m_T coshy, p_z = m_T sinhy \tag{A.19}$$

This leads to the relation, tanh$y = p_z/E$.

- Pseudo-Rapidity : Other than rapidity, another important variable in relativistic collision is pseudo-rapidity, denoted by η and defined as,

$$\eta = -\ln \left(\tan \frac{\theta}{2} \right) \tag{A.20}$$

  where, θ is the angle between the beam axis and the direction of emitted particle. For high energy limit $y \to \eta$. This variable is important as it involves single information. Further, in high energy collisions, it is difficult to obtain the information of total energy E and longitudinal momentum p_z. Hence, in those places, this variables become quite handy. It is seen that, for $\theta > 0$, η is also greater than zero. For $\theta = \pi/2$, $\eta = 0$. For $\theta > \pi/2$, η has negative values.

The particle multiplicity is expressed as a function of rapidity or pseudo-rapidity, dN/dy or $dN/d\eta$.

- Center of mass energy : The center of mass energy is defined as the energy in the center of momentum frame. The center of momentum frame of a system is the unique interial frame, in which the total momemtum of the system vanishes. Classically, the position ($\overrightarrow{r_{CM}}$), velocity ($\overrightarrow{v_{CM}}$) and acceleration ($\overrightarrow{a_{CM}}$) of center of mass is given as,

$$\overrightarrow{r_{CM}} = \frac{\sum_i m_i \overrightarrow{r_i}}{\sum_i m_i} \tag{A.21}$$

$$\overrightarrow{v_{CM}} = \frac{\sum_i m_i \overrightarrow{v_i}}{\sum_i m_i} \tag{A.22}$$

$$\overrightarrow{a_{CM}} = \frac{\sum_i m_i \overrightarrow{a_i}}{\sum_i m_i} \tag{A.23}$$

In case of center of momentum frame,

$$\overrightarrow{p_{CM}} = \sum_i \overrightarrow{p_i} = 0 \tag{A.24}$$

When an inelastic collision takes place in a small region and for a small duration of time, the energy dumped can be used in production of new particles. While working in high energy regime, it is important to estimate the amount of energy used and wasted in collision. This can be estimated by working in 'center of mass' frame. Let us consider inelastic collision of two particles A and B, giving rise to two particles C and D in final state.

$$\text{A} + \text{B} \rightarrow \text{C} + \text{D}$$

Let $p_A = (E_A, \vec{p_A})$, $p_B = (E_B, \vec{p_B})$ be the four-momentum of A and B, then, in center of mass frame, $\vec{p_A} + \vec{p_B} = 0$. From Mandelstam variable s, one can find the energy in center of mass frame for both fixed target experiment and collider experiments.

$$\begin{aligned} s^2 &= (p_A + p_B)^2 \\ &= p_A^2 + p_B^2 + 2.p_A.p_B \\ &= (E_A^2 - \vec{p_A}^2) + (E_B^2 - \vec{p_B}^2) + 2.(E_A.E_B - \vec{p_A}.\vec{p_B}) \\ &= m_A^2 + m_B^2 + 2.(E_A.E_B - \vec{p_A}.\vec{p_B}) \end{aligned} \tag{A.25}$$

- For *fixed target* experiment let B is at rest and $\vec{p_B} = 0$. Hence, $p_B = (m_B, 0)$,

$$s^2 = m_A^2 + m_B^2 + 2.(E_A.m_B) \tag{A.26}$$

- For *collider experiments*, none of $\vec{p_A}$ or $\vec{p_B}$ is zero. Hence,

$$\begin{aligned} s^2 &= m_A^2 + m_B^2 + 2.(E_A.E_B - \vec{p_A}.\vec{p_B}) \\ &= m_A^2 + m_B^2 + 2.(E_A.E_B - \vec{p_A}.-\vec{p}_A) \\ &= m_A^2 + m_B^2 + 2.(E_A.E_B + |\vec{p_A}|.|\vec{p_B}|) \end{aligned} \tag{A.27}$$

if $m_A << E_A$ and $m_B << E_B$, then,

$$\begin{aligned} s^2 &\sim 2.(E_A.E_B + E_A.E_B) \\ &\sim 4.E_A.E_B \end{aligned} \tag{A.28}$$

If the both the particles participating in the collisions are same i.e. $m_A = m_B = m_0$, $E_A = E_B = E$ and the rest masses are very small in comparison to the kinetic energy, then,

for *fixed target*, $\sqrt{s} = \sqrt{2mE}$
for *collider*, $\sqrt{s} = 2E$

- Luminosity : The rate of interaction R is proportional to the cross-section (σ). The constant of proportionality is known as Luminosity (L), which is defined as the number of particles in beam crossing in unit time through an unit area and has the unit of cm^{-2} s^{-1}.

  – Fixed target : In case of Fixed target, the reaction rate will depend on both the beam flux and the target centers. Let φ is the flux of the incoming beam i.e. number of particles (N_{beam}) per second. Now, let ρ be the density of the target and l be the target length. The density ρ can be percieved as, $\rho = N_{target}/V$, V is the volume. Then the reaction rate becomes,

$$\begin{aligned} R &= \varphi\,\rho\,l\,\sigma \\ &= N_{beam}\,\frac{N_{target}}{V}\,l\,\sigma \\ &= \frac{N_{beam}.N_{target}}{area} \end{aligned} \tag{A.29}$$

  Hence, the expression for L becomes, $L = \varphi\,\rho\,l = N_{beam}.N_{target}/area$

  – Collider : In case of colliding beams, the reaction depends on the bunches in the beam, beam cross-sectional area, number of particles in a bunch and number of bunch crossings per second. For Gaussian beam profile, reaction rate R is given by,

$$R = \frac{N_1\,.N_2.\,N_b.\,f}{4\pi\,\sigma_x\,\sigma_y}\,\sigma \tag{A.30}$$

  where N_1, N_2 are the number of particles in bunches in 1 and 2 respectively, f is the RF frequency which is the bunch crossings per second and N_b is the number of bunches. The transverse cross-sectional area of beam is given by $4\pi\sigma_x\sigma_y$. Hence, luminosity,

$$L = \frac{N_1.\,N_2.\,N_b.\,f}{4\pi\,\sigma_x\,\sigma_y} \tag{A.31}$$

- Integrated luminosity : Integrated Luminosity (L_{int}) is obtained by integrating the

Luminosity (L) over a certain time : $L_{int} = \int_0^T L(t)$dt This parameter relates the number of observed events as : $L_{int} = \sigma \; N_{events}$

A.2 Thermodynamics

The basic thermodynamical relations are :

- Density operator.

$$\hat{\rho} = \frac{1}{Z} e^{-(\hat{H}-\mu\hat{N})/T} \tag{A.32}$$

- Partition function.

$$Z(T,V,\mu) = Tre^{-(\hat{H}-\mu\hat{N})/T} \tag{A.33}$$

- Grand Potential

$$\Omega(T,V,\mu) = -TlnZ(T,V,\mu) = E - TS - \mu N = -pV \tag{A.34}$$

- Energy Density

$$\epsilon \;=\; \frac{E}{V} = -\frac{T^2}{V}\frac{\partial(\Omega/T)}{\partial T} - \frac{\mu}{T}\frac{\partial\Omega}{\partial\mu} \tag{A.35}$$

$$=\; \frac{T}{V}\frac{\partial(TlnZ)}{\partial T} + \mu n \tag{A.36}$$

- Particle Density

$$n = \frac{1}{V}\frac{\partial(TlnZ)}{\partial\mu} \tag{A.37}$$

- Pressure

$$P = \frac{\partial(TlnZ)}{\partial V} \tag{A.38}$$

- Entropy density

$$s = \frac{1}{V}\frac{\partial(TlnZ)}{\partial T} \tag{A.39}$$

- Pressure, energy density and number density for non-interacting relativistic bosonic gases

$$P_b = g\frac{4\pi}{3(2\pi)^3}\int_0^\infty \frac{p^3dp}{e^{p/T}-1} = g\frac{\pi^2}{90}T^4 \tag{A.40}$$

$$\epsilon_b = g\frac{4\pi}{(2\pi)^3}\int_0^\infty \frac{p^3dp}{e^{p/T}-1} = g\frac{\pi^2}{30}T^4 = 3P \tag{A.41}$$

$$n_b = g\int \frac{d^3p}{h^3}\frac{1}{e^{p/T}-1} = \frac{g}{(2\pi)^3}\int_0^\infty \frac{p^2dp}{e^{p/T}-1} = g\frac{\zeta(3)}{\pi^2}T^3, \zeta(3) = 1.202 \tag{A.42}$$

- Pressure, energy density and number density for non-interacting relativistic fermionic gases

$$P_f = g\frac{4\pi}{3(2\pi)^3}\int_0^\infty \frac{p^3dp}{e^{p/T}+1} = \frac{7}{8}P_b \tag{A.43}$$

$$\epsilon_f = \frac{7}{8}\epsilon_b \tag{A.44}$$

$$n_f = \frac{3}{4}n_b \tag{A.45}$$

This can be found in details in
http://web-docs.gsi.de/~andronic/intro_rhic2012/2012_04_phase_AA.pdf

APPENDIX B

TSALLIS FORMALISMS

In Botzmann-Gibbs statistics, the particle spectrum is given as,

$$E\frac{d^3N}{dp^3} = C_B e^{-E/T}, \tag{B.1}$$

where C_B is the normalization constant, E is the particle energy and T is the temperature of the system.

In non-extensive statistics (Tsallis), the Boltzmann-Gibbs distribution takes the form

$$E\,\frac{d^3N}{dp^3} = C_q \left(1 + (q-1)\frac{E}{T}\right)^{\frac{-1}{q-1}}, \tag{B.2}$$

where C_q is the normalization factor. One can use the relation $E = m_T$ at mid-rapidity and $n = 1/(q-1)$ in Eq. B.2 to obtain :

$$E\,\frac{d^3N}{dp^3} = C_n \left(1 + \frac{m_T}{nT}\right)^{-n}, \tag{B.3}$$

where, C_n is the normalization factor. Eq. B.3 can be re-written as :

$$\frac{1}{2\pi p_T}\frac{d^2N}{dp_T dy} = C_n \left(1 + \frac{m_T}{nT}\right)^{-n}, \tag{B.4}$$

The value of C_n can be obtained by integrating Eq. B.4 over momentum space :

$$C_n = \frac{dN/dy}{\int_0^{\infty} \left(1 + \frac{m_T}{nT}\right)^{-n} 2\pi p_T dp_T}, \tag{B.5}$$

The denominator of Eq.B.5 can be integrated by,

$$I = \int_0^{\infty} \left(1 + \frac{m_T}{nT}\right)^{-n} 2\pi p_T dp_T, \tag{B.6}$$

putting

$$m_T^2 = p_T^2 + m^2$$
$$2\ m_T\, dm_T = 2\ p_T\, dp_T$$

Hence Eq. B.6 becomes,

$$I = \int_m^\infty \left(1 + \frac{m_T}{nT}\right)^{-n} 2\pi m_T dm_T, \tag{B.7}$$

Substituting $1 + \frac{m_T}{nT} = x \implies dm_T = dx\ nT$

$$I = 2\,\pi\,n^2\,T^2 \int_{1+m_T/nT}^\infty x^{-n}\,(x-1)\,dx \tag{B.8}$$

Now,

$$\int_{1+m_T/nT}^\infty x^{-n}\,(x-1)\,dx = \frac{x^{2-n}}{(2-n)}\Big|_{1+\frac{m_T}{nT}}^\infty - \frac{x^(1-n)}{(1-n)}\Big|_{1+\frac{m_T}{nT}}^\infty \tag{B.9}$$

Putting the limits and doing some algebra,

$$\begin{aligned} I &= 2\,\pi\,n\,T\,\frac{(1+m_T/nT)^{-n+1}}{(n-1)\,(n-2)} \\ &.\quad [(n-1)\,(m+nT)\ -\ nT\,(n-2)] \end{aligned} \tag{B.10}$$

Hence,

$$C_n = \frac{dN/dy}{I} \tag{B.11}$$

$$= \frac{dN}{dy}\,\frac{1}{2\,\pi}.\frac{(n-1).\,(n-2)}{[nT+m(n-1)}.\left(\frac{nT}{nT+m}\right)^{-n} \tag{B.12}$$

Then,

$$\begin{aligned} E\frac{d^3N}{dp^3} &= C_n.\left(1+\frac{E}{nT}\right)^{-n} \\ &= \frac{dN}{dy}\,.\,\frac{1}{2\,\pi}.\frac{(n-1).\,(n-2)}{[nT+m(n-1)}\left(\frac{nT+m_T}{nT+m}\right)^{-n} \end{aligned} \tag{B.13}$$

APPENDIX C

ANALYSIS PLOTS

C.1 Calibration plots for "++" field configuration

C.1.1 Recalibration plots for $emcsdz$

The mean and sigma of the uncalibrated distributions of $emcsdz$ as a function of p_T are shown in Fig. C.1 for "++" field configuration. The calibrated distributions of the same are shown in Fig. C.2.

C.1.2 Recalibration plots for $pc3sd\phi$

The mean and sigma of the uncalibrated distributions of $pc3sd\phi$ as a function of p_T are shown in Fig. C.3 for "++" field configuration. The calibrated distributions of the same are shown in Fig. C.4.

C.1.3 Recalibration plots for $pc3sdz$

The mean and sigma of the uncalibrated distributions of $pc3sdz$ as a function of p_T are shown in Fig. C.5 for "++" field configuration. The calibrated distributions of the same are shown in Fig. C.6.

C.1.4 Recalibration plots for $tofsd\phi$

The mean and sigma of the uncalibrated distributions of $tofsd\phi$ as a function of p_T are shown in Fig. C.7 for "++" field configuration. The calibrated distributions of the same are shown in Fig. C.8.

C.1.5 Recalibration plots for $tofsdz$

The mean and sigma of the uncalibrated distributions of $tofsdz$ as a function of p_T are shown in Fig. C.9 for "++" field configuration. The calibrated distributions of the same

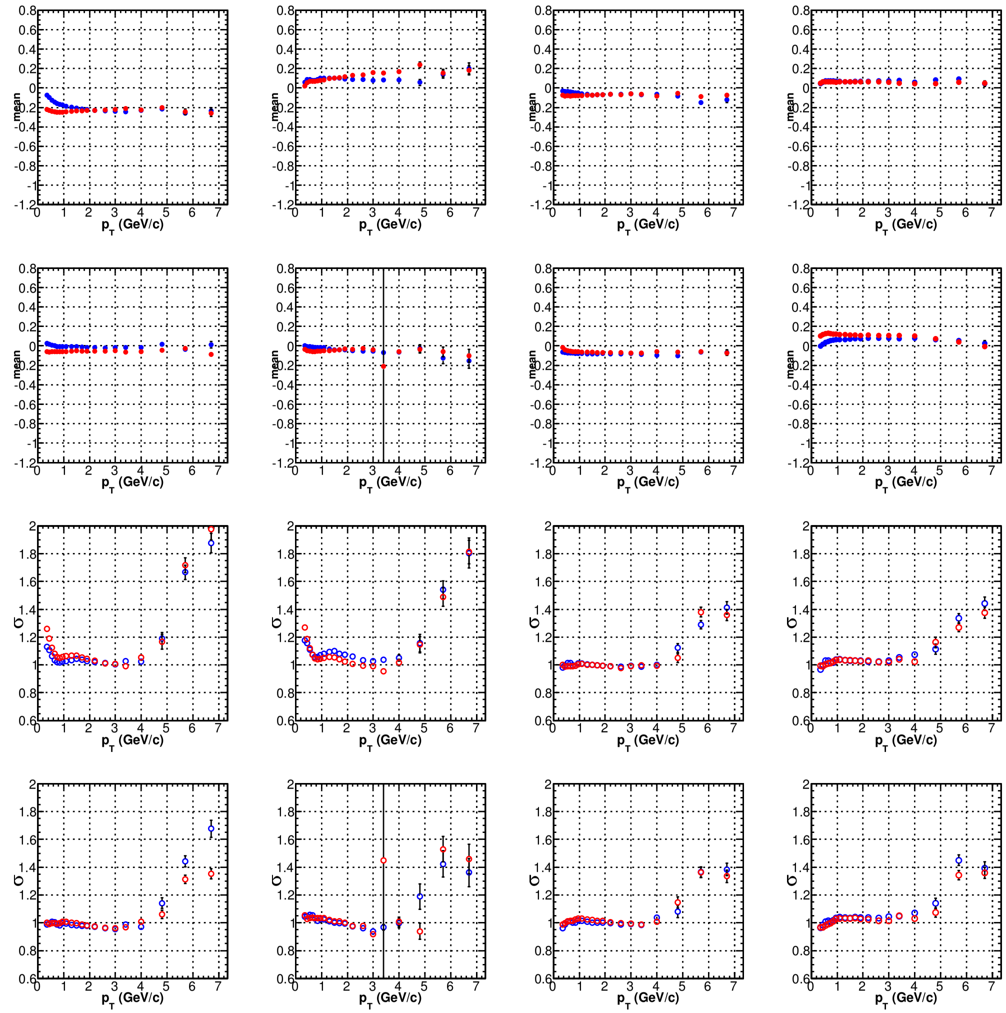

Figure C.1: The *emcsdz* distributions for "++" field as a function of p_T without any calibration. The upper 8 plots are for the mean of *emcsdz* and the lower 8 plots are the σ of *emcsdz*. The blue color markers are for the positive particle tracks and the red color markers are for the negative particle tracks.

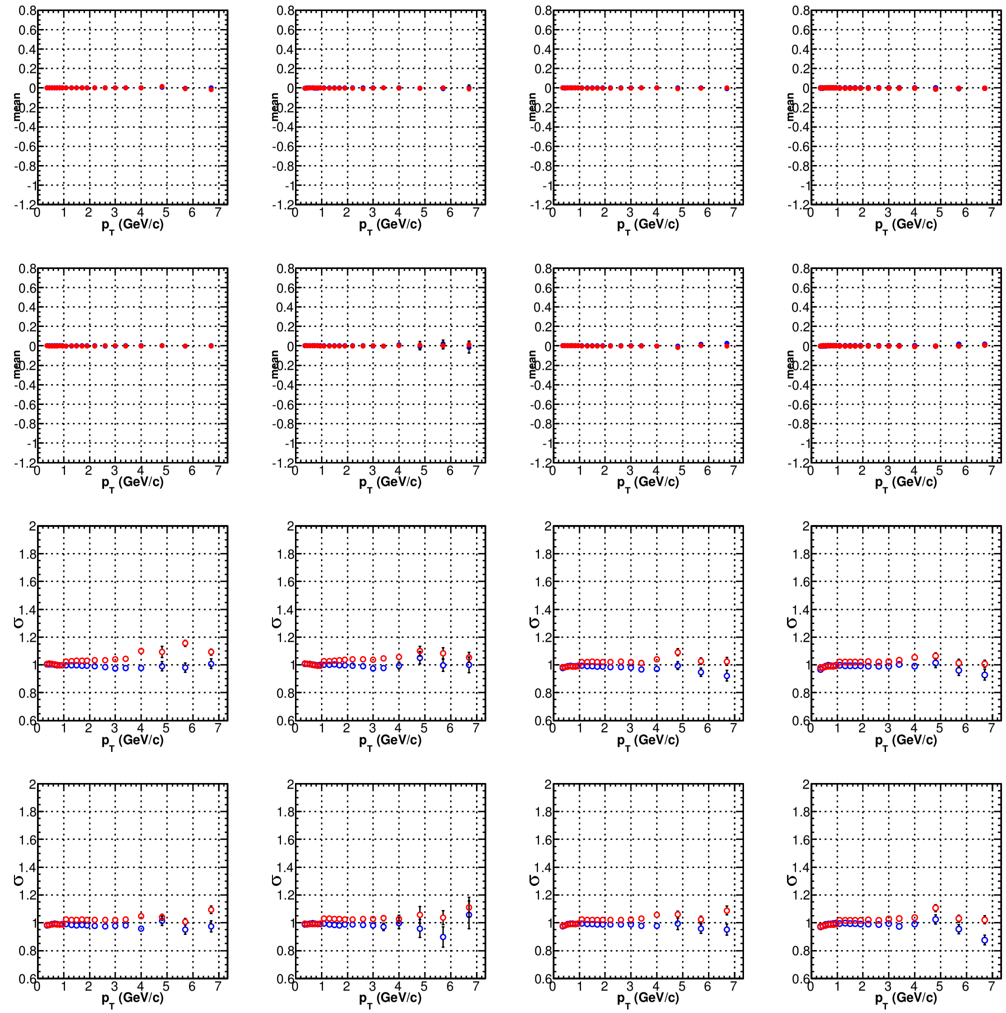

Figure C.2: The *emcsdz* distributions for "++" field as a function of p_T after calibration. The upper 8 plots are for the mean of *emcsdz* and the lower 8 plots are the σ of *emcsdz*. The blue color markers are for the positive particle tracks and the red color markers are for the negative particle tracks.

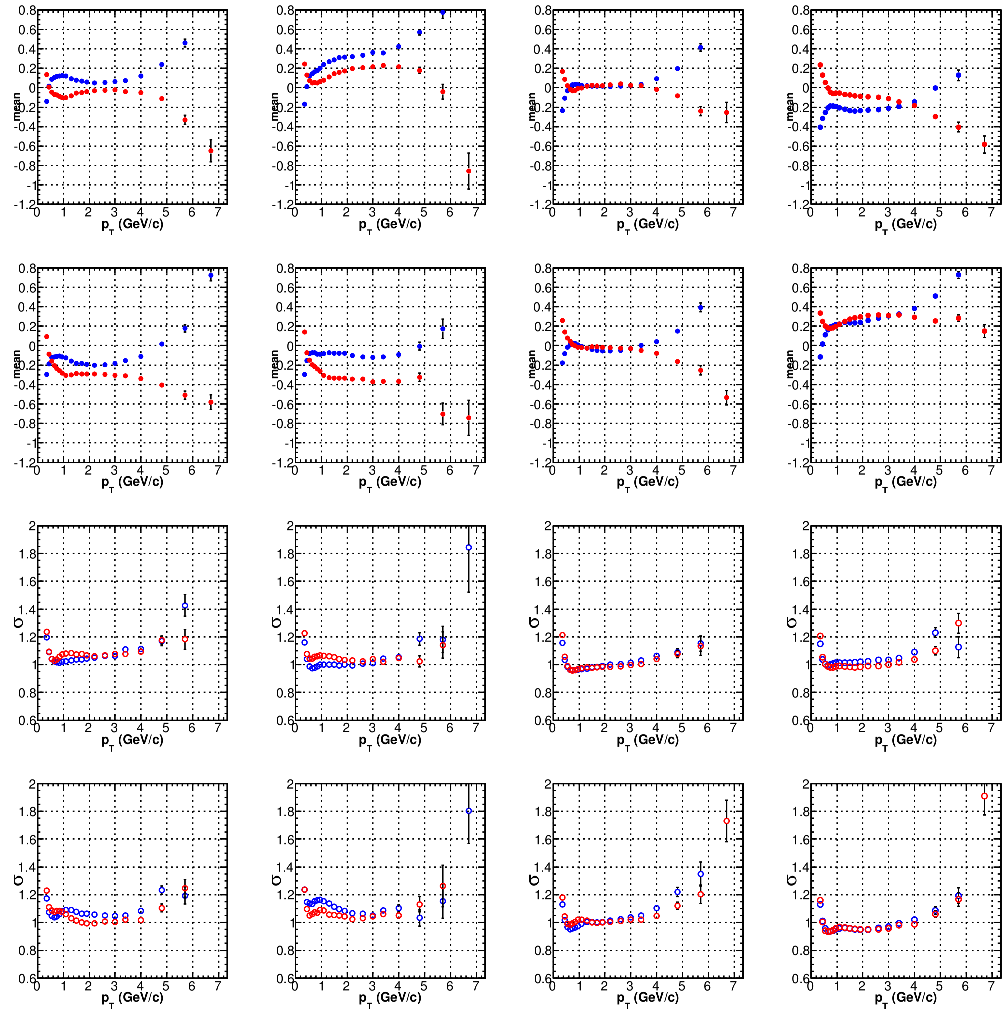

Figure C.3: The $pc3sd\phi$ distributions for "++" field as a function of p_T without any calibration. The upper 8 plots are for the mean of $pc3sd\phi$ and the lower 8 plots are the σ of $pc3sd\phi$. The blue color markers are for the positive particle tracks and the red color markers are for the negative particle tracks.

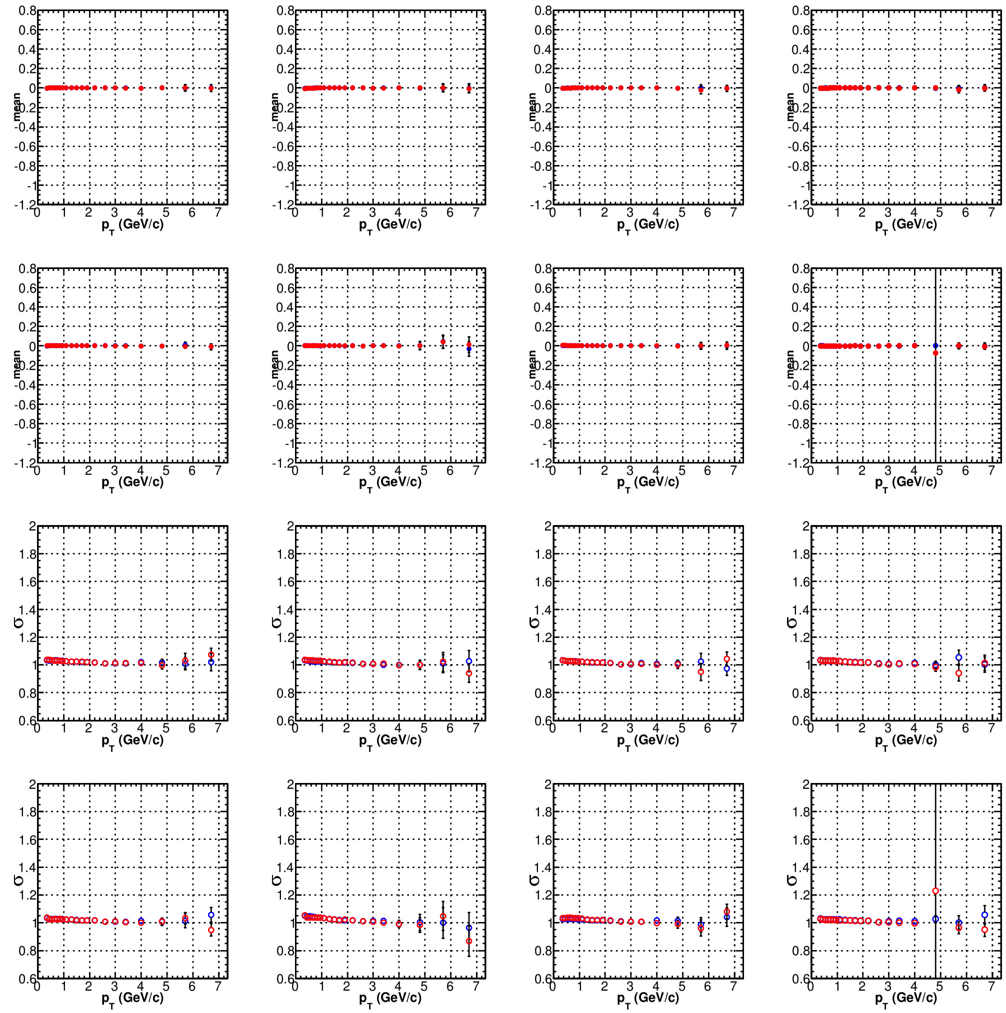

Figure C.4: The $pc3sd\phi$ distributions for "++" field as a function of p_T after calibration. The upper 8 plots are for the mean of $pc3sd\phi$ and the lower 8 plots are the σ of $pc3sd\phi$. The blue color markers are for the positive particle tracks and the red color markers are for the negative particle tracks.

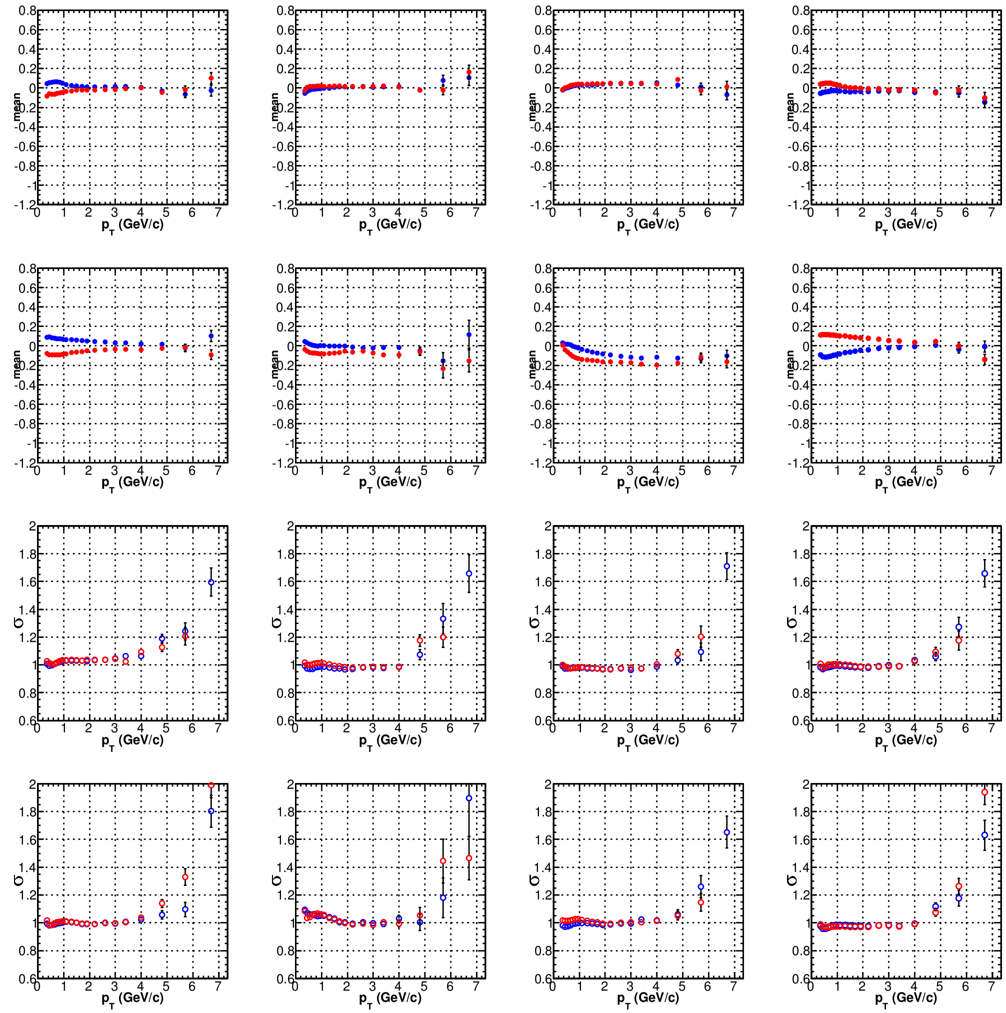

Figure C.5: The $pc3sdz$ distributions for "++" field as a function of p_T without any calibration. The upper 8 plots are for the mean of $pc3sdz$ and the lower 8 plots are the σ of $pc3sdz$. The blue color markers are for the positive particle tracks and the red color markers are for the negative particle tracks.

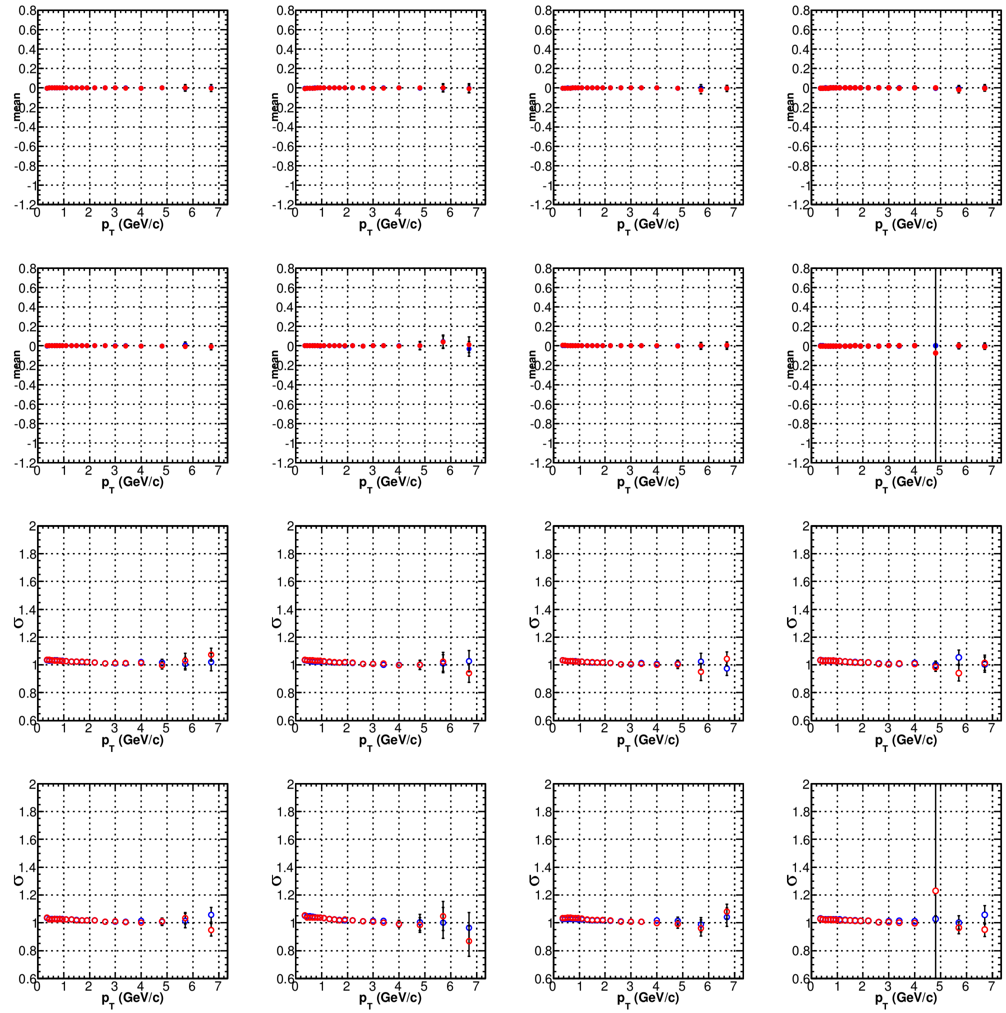

Figure C.6: The *pc3sdz* distributions for "++" field as a function of p_T after calibration. The upper 8 plots are for the mean of *pc3sdz* and the lower 8 plots are the σ of *pc3sdz*. The blue color markers are for the positive particle tracks and the red color markers are for the negative particle tracks.

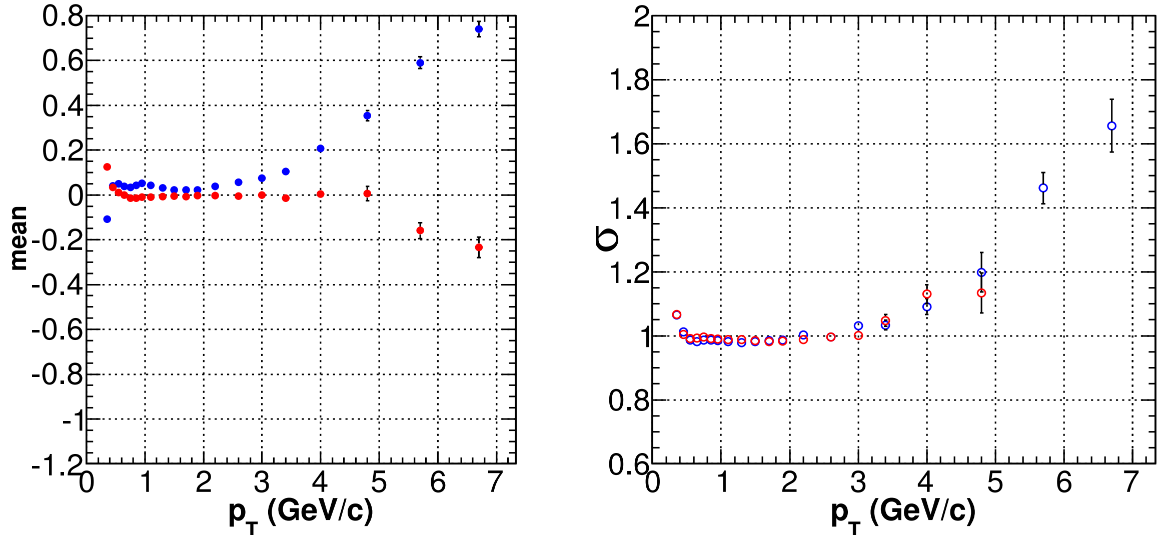

Figure C.7: The $tofsd\phi$ distributions for "++" field as a function of p_T without any calibration. The left and right plots correspond to the mean and σ of $tofsd\phi$ distribution, respectively. The blue color markers are for the positive particle tracks and the red color markers are for the negative particle tracks.

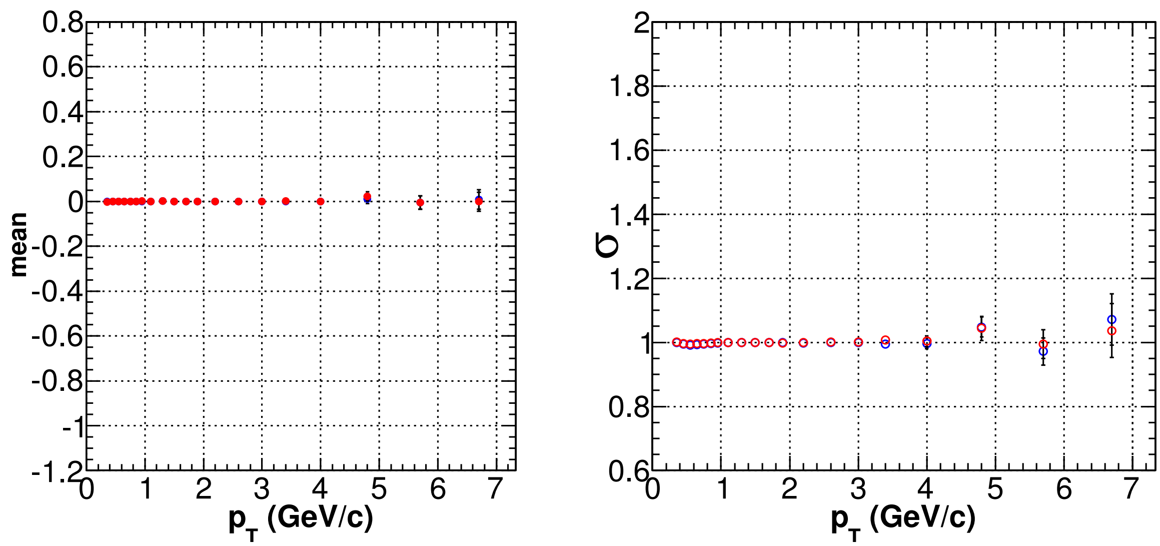

Figure C.8: The $tofsd\phi$ distributions for "++" field as a function of p_T after calibration. The left and right plots correspond to the mean and σ of $tofsd\phi$ distribution, respectively. The blue color markers are for the positive particle tracks and the red color markers are for the negative particle tracks.

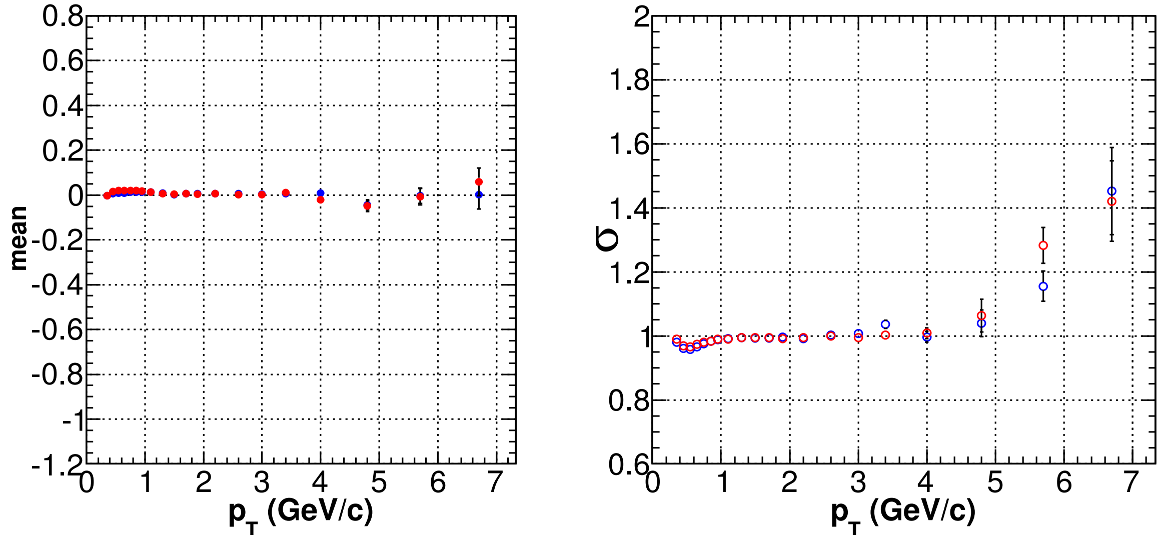

Figure C.9: The $tofsdz$ distributions for "++" field as a function of p_T without any calibration. The left and right plots correspond to the mean and σ of $tofsdz$ distribution, respectively. The blue color markers are for the positive particle tracks and the red color markers are for the negative particle tracks.

are shown in Fig. C.10.

C.1.6 Recalibration plots for isK

The mean and sigma of the uncalibrated distributions of isK as a function of p_T are shown in Fig. C.11 for "++" field configuration. The calibrated distributions of the same are shown in Fig. C.12.

C.2 Calibration plots for "- -" field configuration

C.2.1 Recalibration plots for $emcsd\phi$

The mean and sigma of the uncalibrated distributions of $emcsd\phi$ as a function of p_T are shown in Fig. C.13 for "- -" field configuration. The calibrated distributions of the same are shown in Fig. C.14.

C.2.2 Recalibration plots for $emcsdz$

The mean and sigma of the uncalibrated distributions of $emcsdz$ as a function of p_T are shown in Fig. C.15 for "- -" field configuration. The calibrated distributions of the same are shown in Fig. C.16.

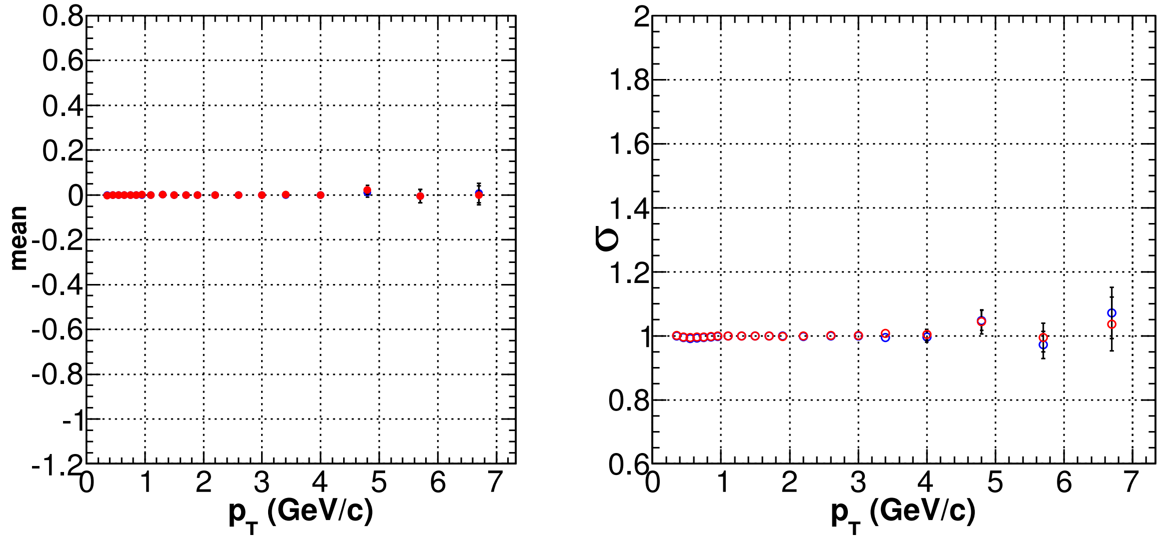

Figure C.10: The $tofsdz$ distributions for "++" field as a function of p_T after calibration. The left and right plots correspond to the mean and σ of $tofsdz$ distribution, respectively. The blue color markers are for the positive particle tracks and the red color markers are for the negative particle tracks.

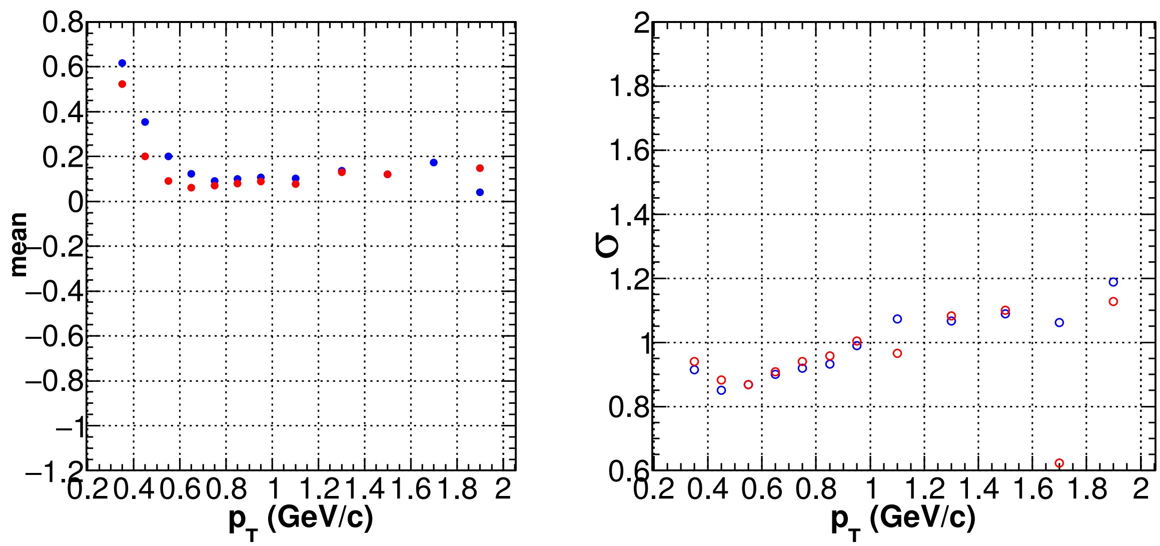

Figure C.11: The isK distributions for "++" field as a function of p_T without any calibration. The left and right plots correspond to the mean and σ of isK distribution, respectively. The blue color markers are for the positive particle tracks and the red color markers are for the negative particle tracks.

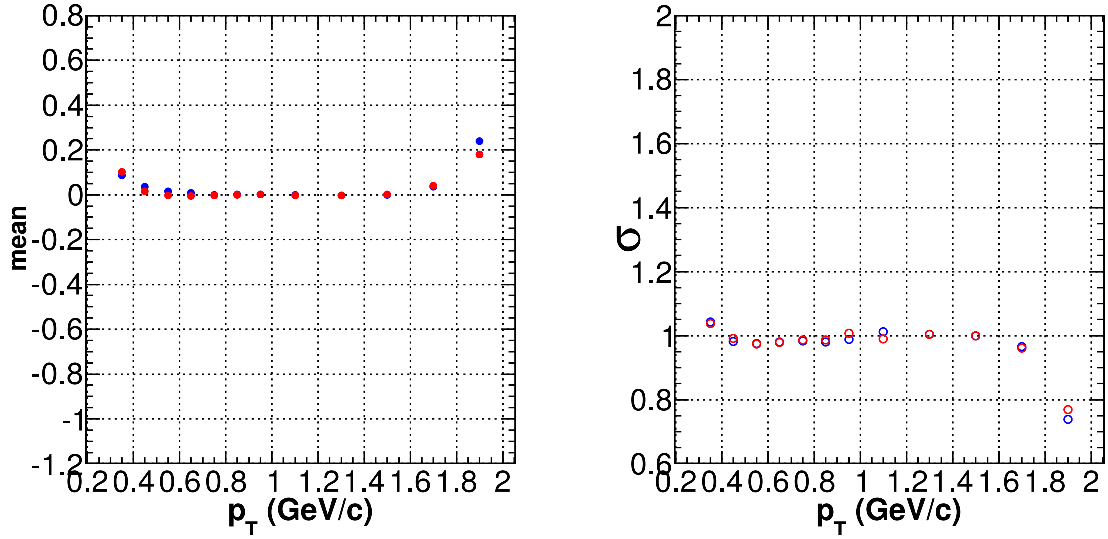

Figure C.12: The isK distributions for "++" field as a function of p_T after calibration. The left and right plots correspond to the mean and σ of isK distribution, respectively. The blue color markers are for the positive particle tracks and the red color markers are for the negative particle tracks.

C.2.3 Recalibration plots for $pc3sd\phi$

The mean and sigma of the uncalibrated distributions of $pc3sd\phi$ as a function of p_T are shown in Fig. C.17 for "- -" field configuration. The calibrated distributions of the same are shown in Fig. C.18.

C.2.4 Recalibration plots for $pc3sdz$

The mean and sigma of the uncalibrated distributions of $pc3sdz$ as a function of p_T are shown in Fig. C.19 for "- -" field configuration. The calibrated distributions of the same are shown in Fig. C.20.

C.2.5 Recalibration plots for $tofsd\phi$

The mean and sigma of the uncalibrated distributions of $tofsd\phi$ as a function of p_T are shown in Fig. C.21 for "- -" field configuration. The calibrated distributions of the same are shown in Fig. C.22.

C.2.6 Recalibration plots for $tofsdz$

The mean and sigma of the uncalibrated distributions of $tofsdz$ as a function of p_T are shown in Fig. C.23 for "- -" field configuration. The calibrated distributions of the same are shown in Fig. C.24.

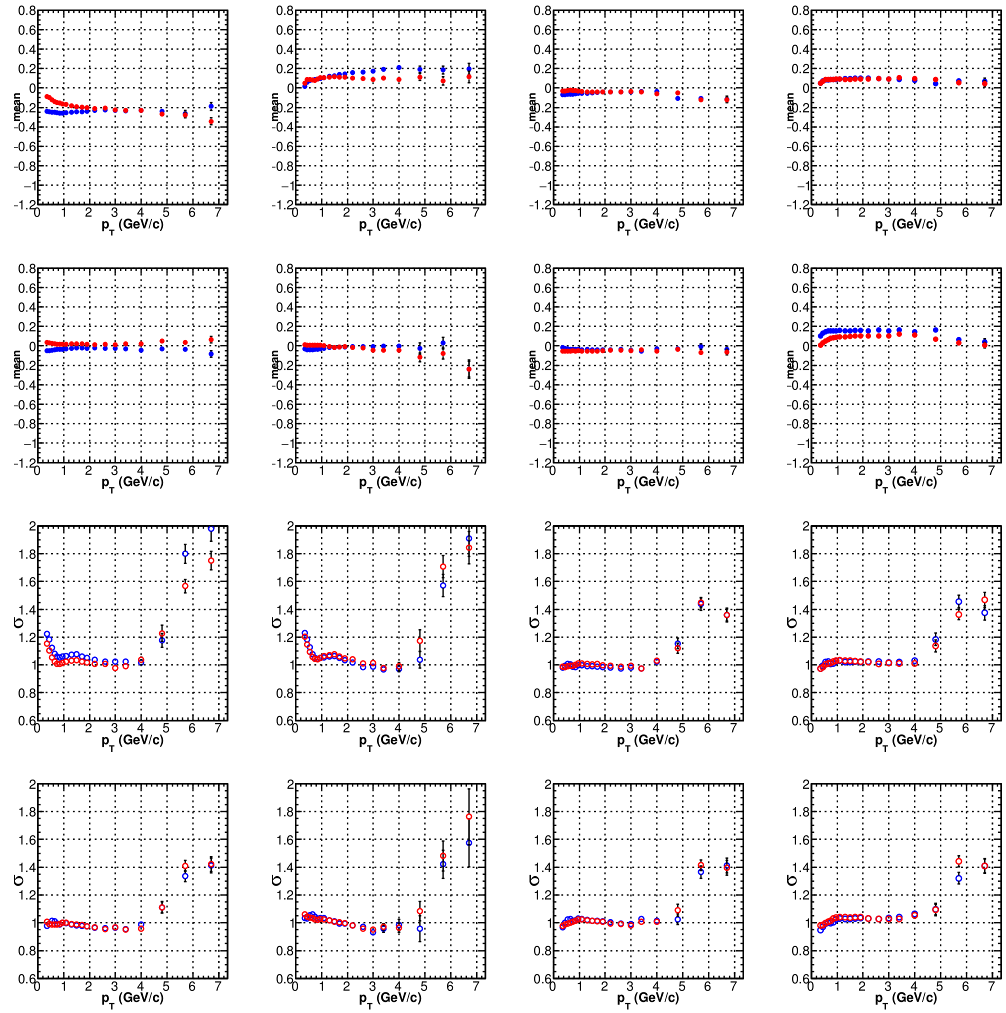

Figure C.13: The *emcsdz* distributions for "- -" field as a function of p_T without any calibration. The upper 8 plots are for the mean of *emcsdz* and the lower 8 plots are the σ of *emcsdz*. The blue color markers are for the positive particle tracks and the red color markers are for the negative particle tracks.

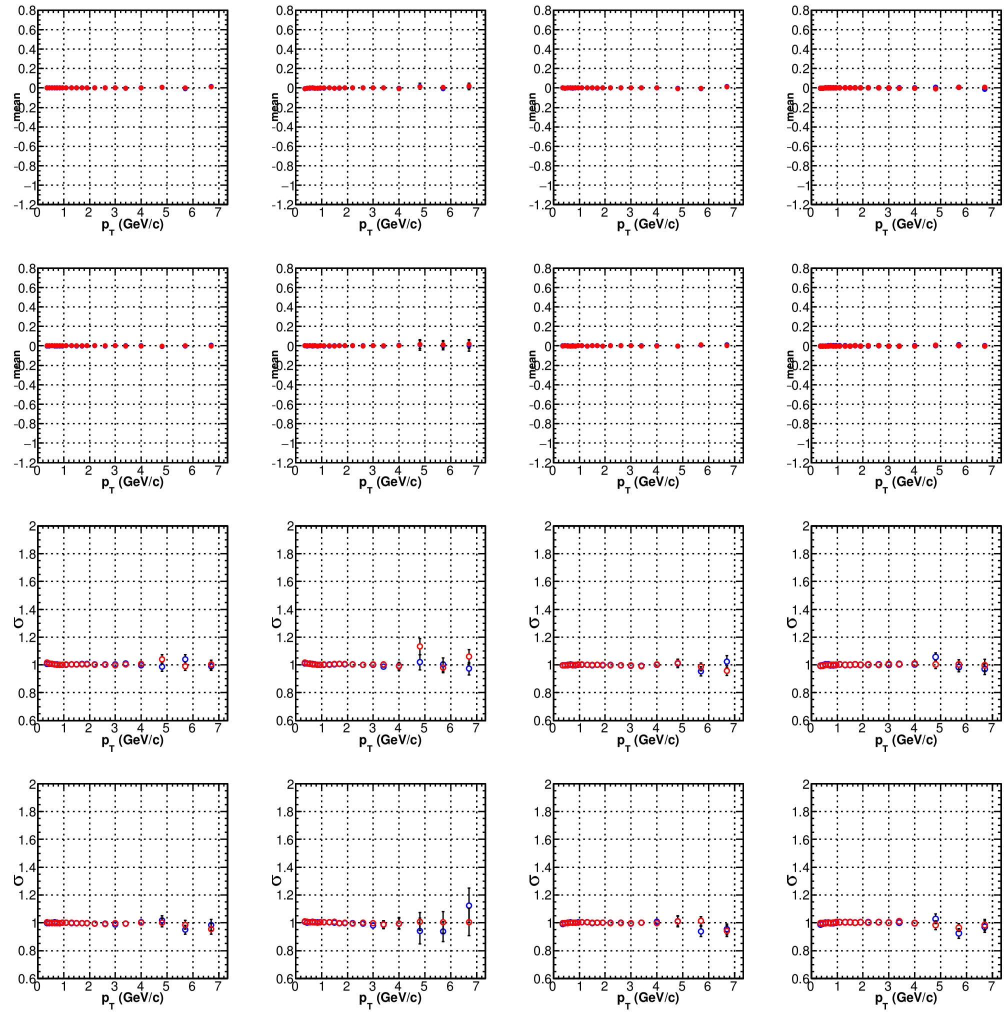

Figure C.14: The *emcsdz* distributions for "- -" field as a function of p_T after calibration. The upper 8 plots are for the mean of *emcsdz* and the lower 8 plots are the σ of *emcsdz*. The blue color markers are for the positive particle tracks and the red color markers are for the negative particle tracks.

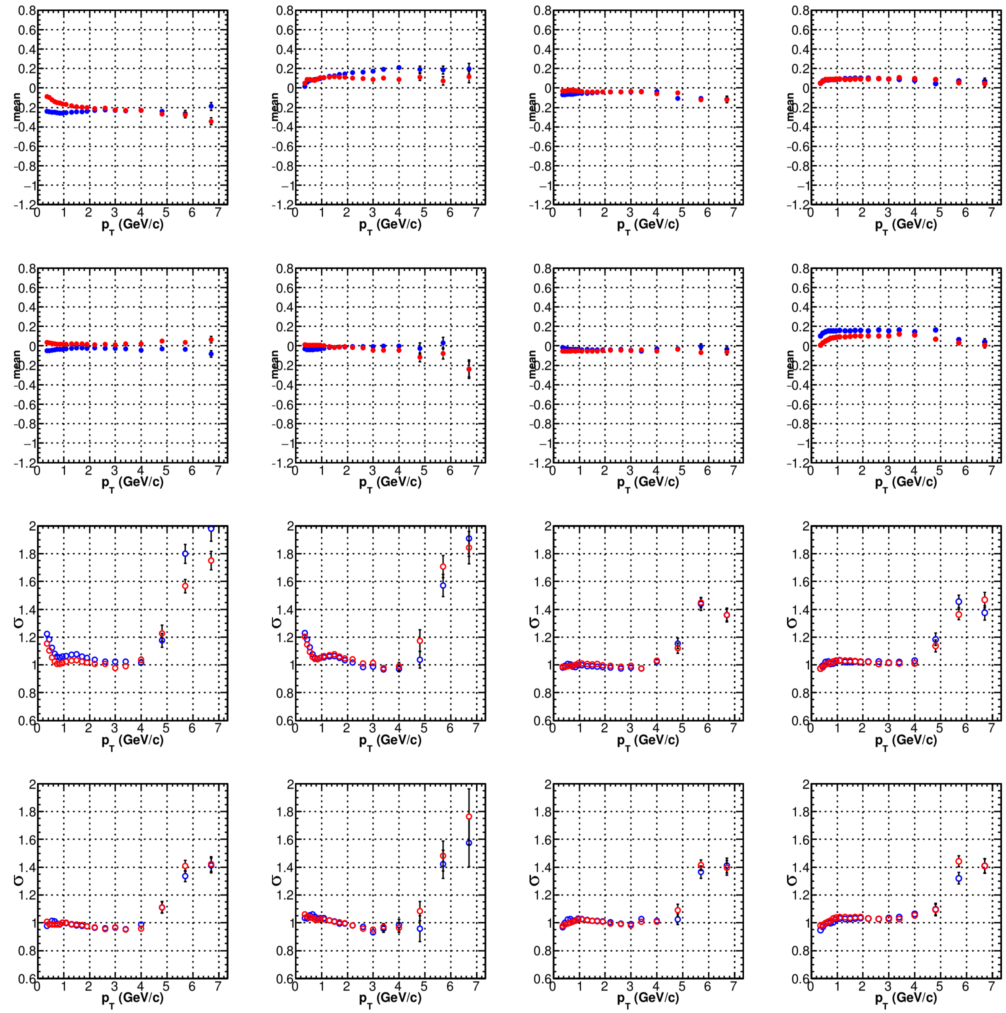

Figure C.15: The *emcsdz* distributions for "- -" field as a function of p_T without any calibration. The upper 8 plots are for the mean of *emcsdz* and the lower 8 plots are the σ of *emcsdz*. The blue color markers are for the positive particle tracks and the red color markers are for the negative particle tracks.

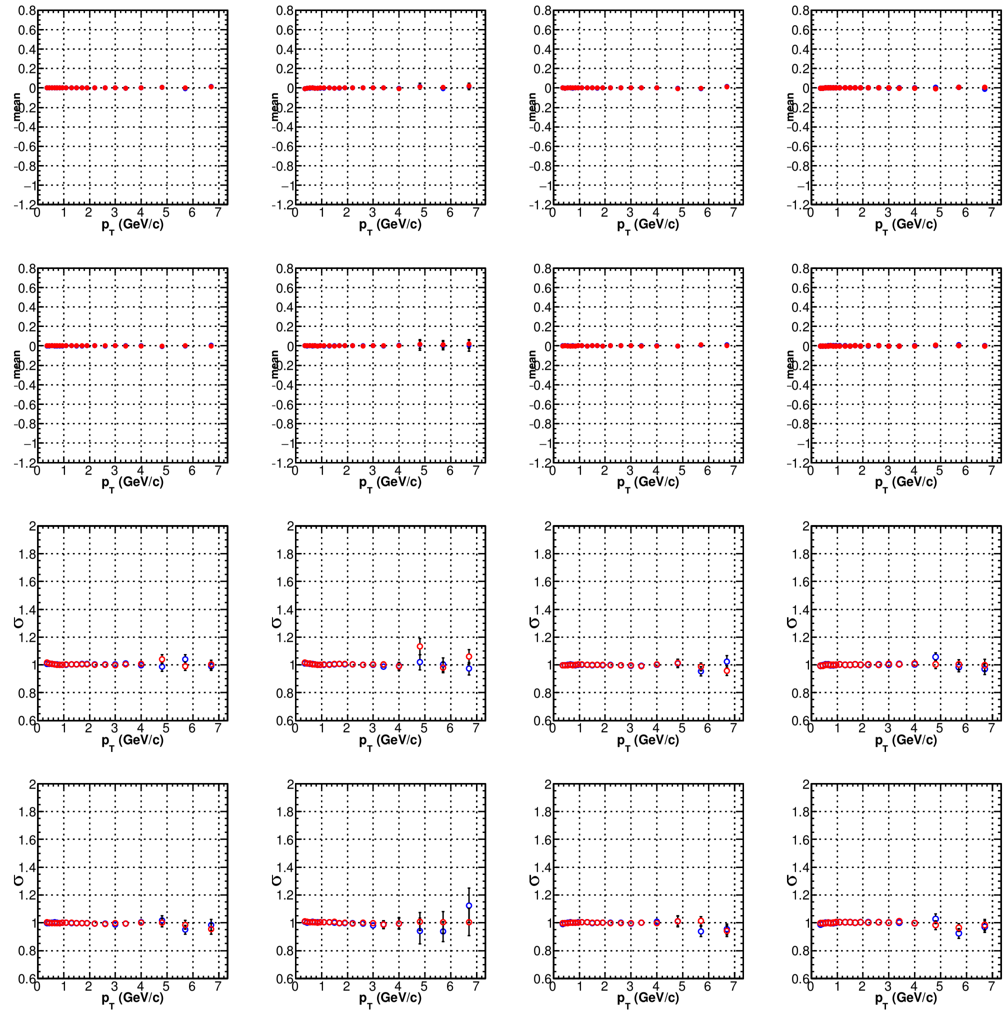

Figure C.16: The *emcsdz* distributions for "- -" field as a function of p_T after calibration. The upper 8 plots are for the mean of *emcsdz* and the lower 8 plots are the σ of *emcsdz*. The blue color markers are for the positive particle tracks and the red color markers are for the negative particle tracks.

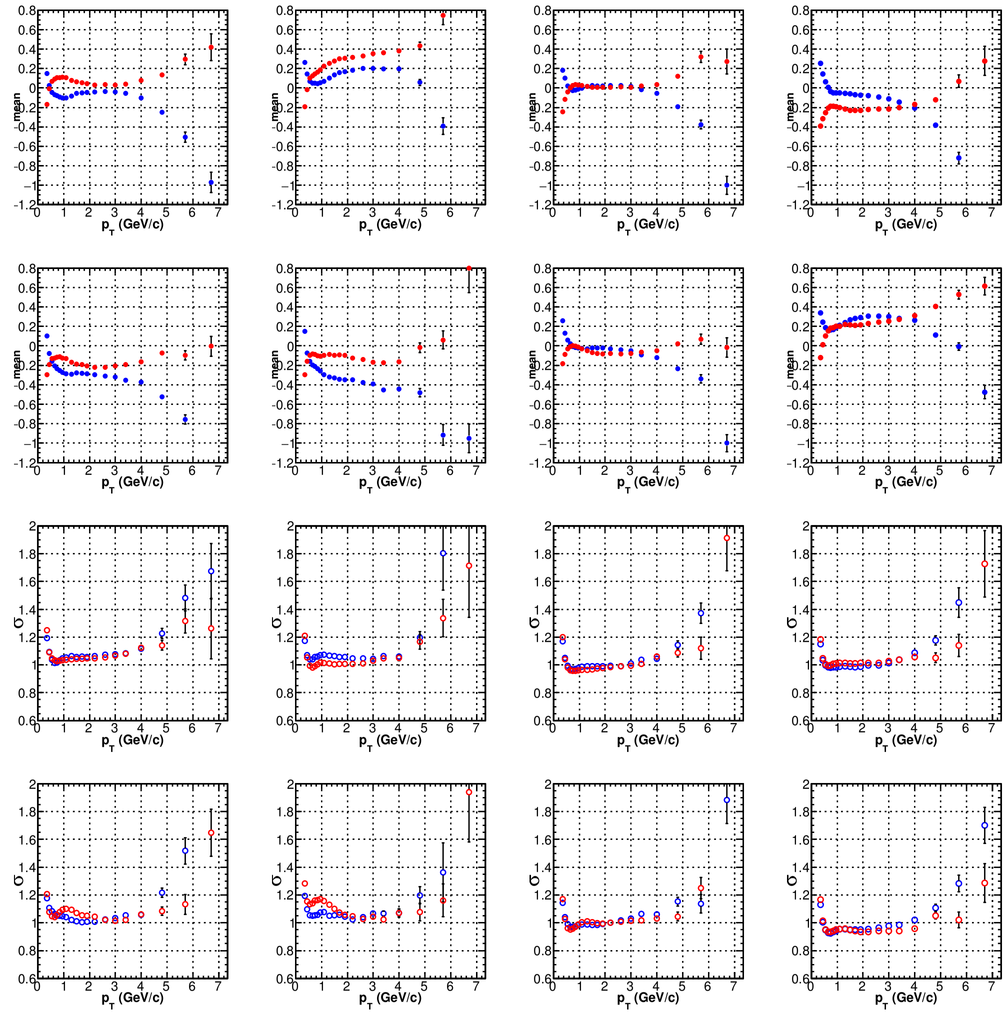

Figure C.17: The $pc3sd\phi$ distributions for "--" field as a function of p_T without any calibration. The upper 8 plots are for the mean of $pc3sd\phi$ and the lower 8 plots are the σ of $pc3sd\phi$. The blue color markers are for the positive particle tracks and the red color markers are for the negative particle tracks.

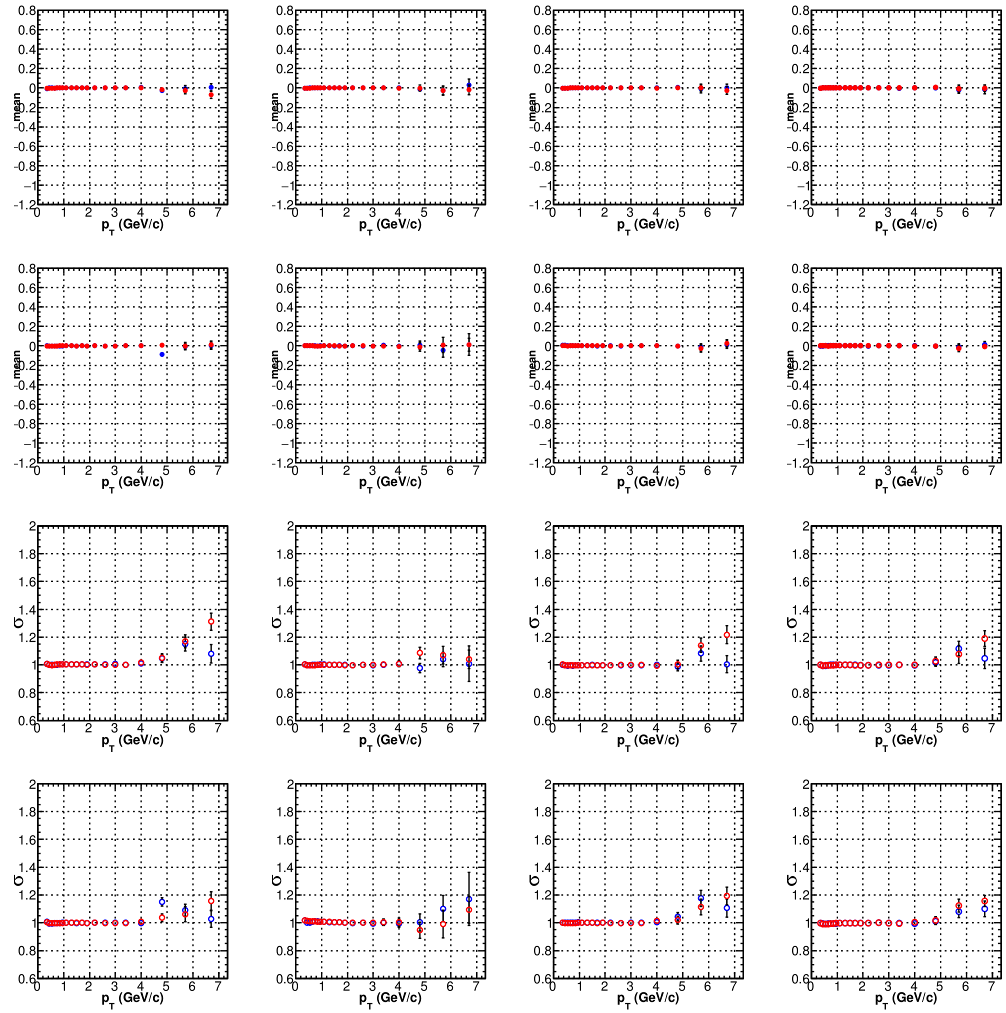

Figure C.18: The $pc3sd\phi$ distributions for "- -" field as a function of p_T after calibration. The upper 8 plots are for the mean of $pc3sd\phi$ and the lower 8 plots are the σ of $pc3sd\phi$. The blue color markers are for the positive particle tracks and the red color markers are for the negative particle tracks.

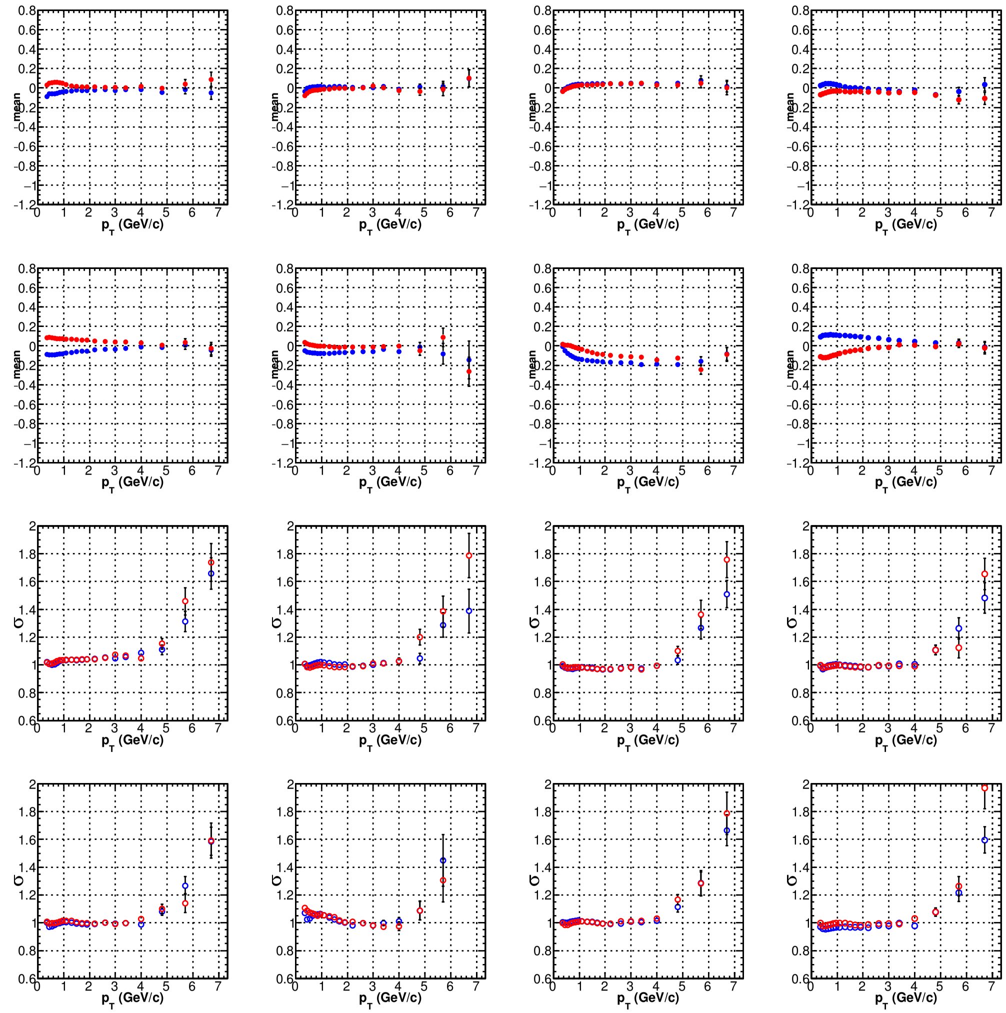

Figure C.19: The $pc3sdz$ distributions for "- -" field as a function of p_T without any calibration. The upper 8 plots are for the mean of $pc3sdz$ and the lower 8 plots are the σ of $pc3sdz$. The blue color markers are for the positive particle tracks and the red color markers are for the negative particle tracks.

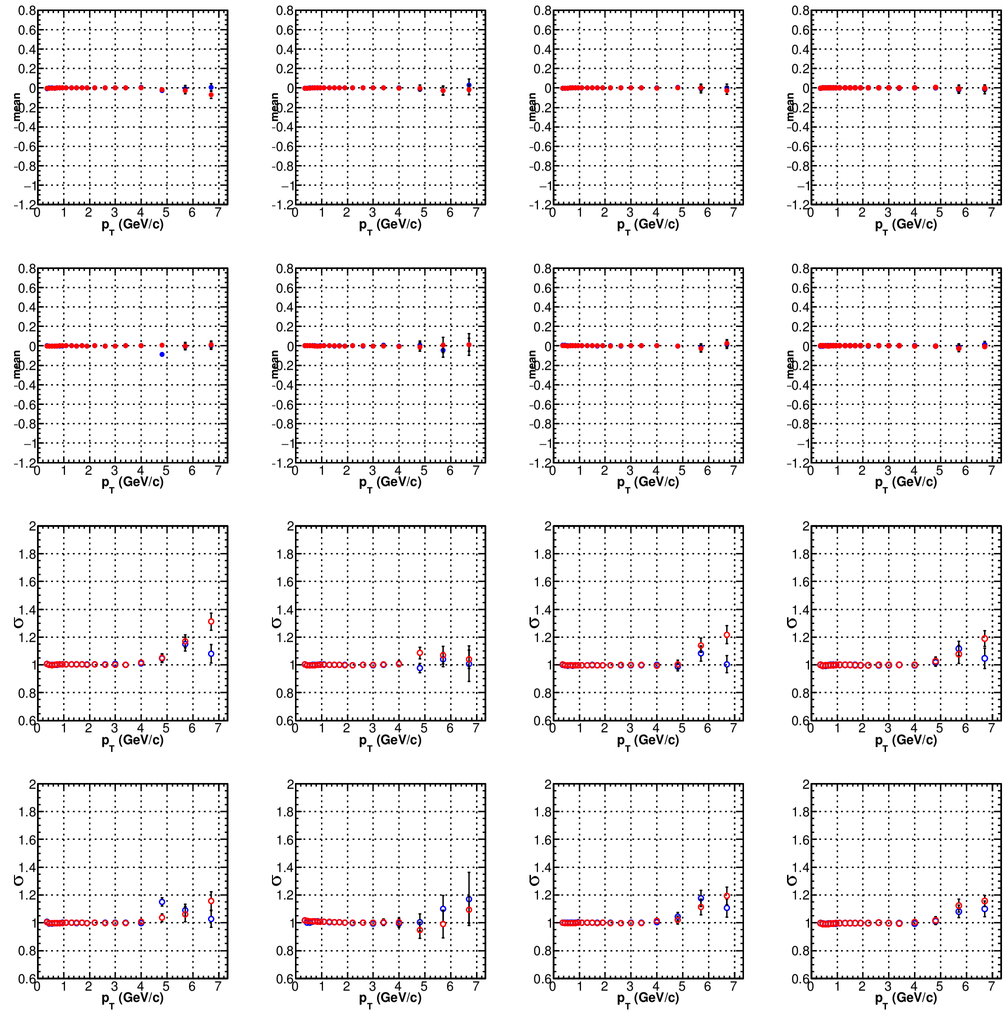

Figure C.20: The $pc3sdz$ distributions for "- -" field as a function of p_T after calibration. The upper 8 plots are for the mean of $pc3sdz$ and the lower 8 plots are the σ of $pc3sdz$. The blue color markers are for the positive particle tracks and the red color markers are for the negative particle tracks.

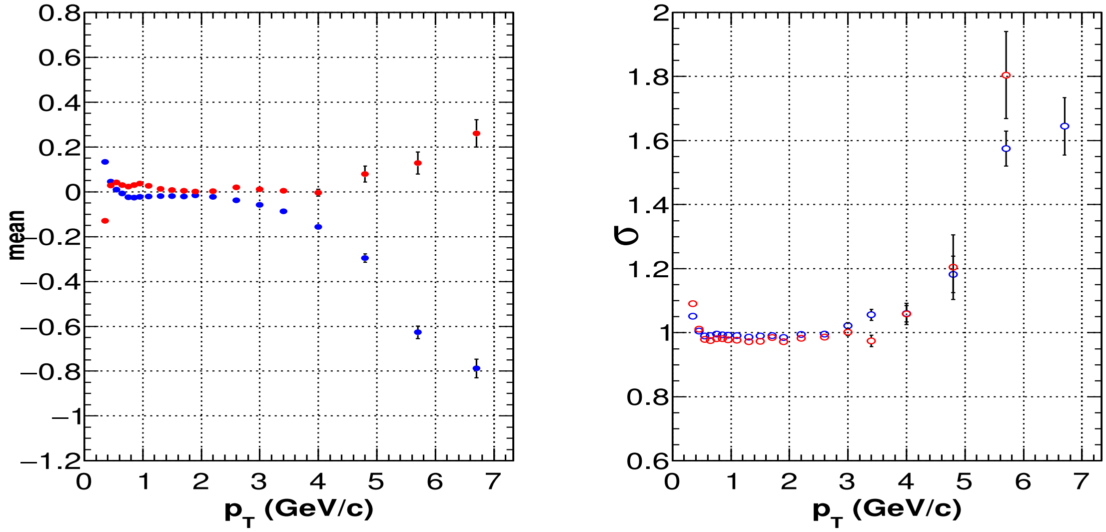

Figure C.21: The $tofsd\phi$ distributions for "- -" field as a function of p_T without any calibration. The left and right plots correspond to the mean and σ of $tofsd\phi$ distribution, respectively. The blue color markers are for the positive particle tracks and the red color markers are for the negative particle tracks.

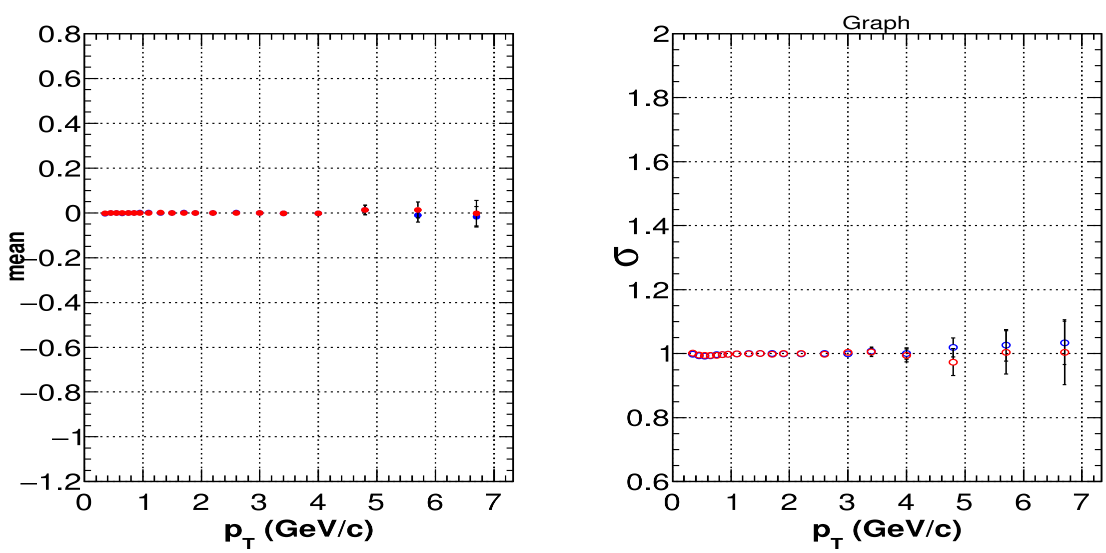

Figure C.22: The $tofsd\phi$ distributions for "- -" field as a function of p_T after calibration. The left and right plots correspond to the mean and σ of $tofsd\phi$ distribution, respectively. The blue color markers are for the positive particle tracks and the red color markers are for the negative particle tracks.

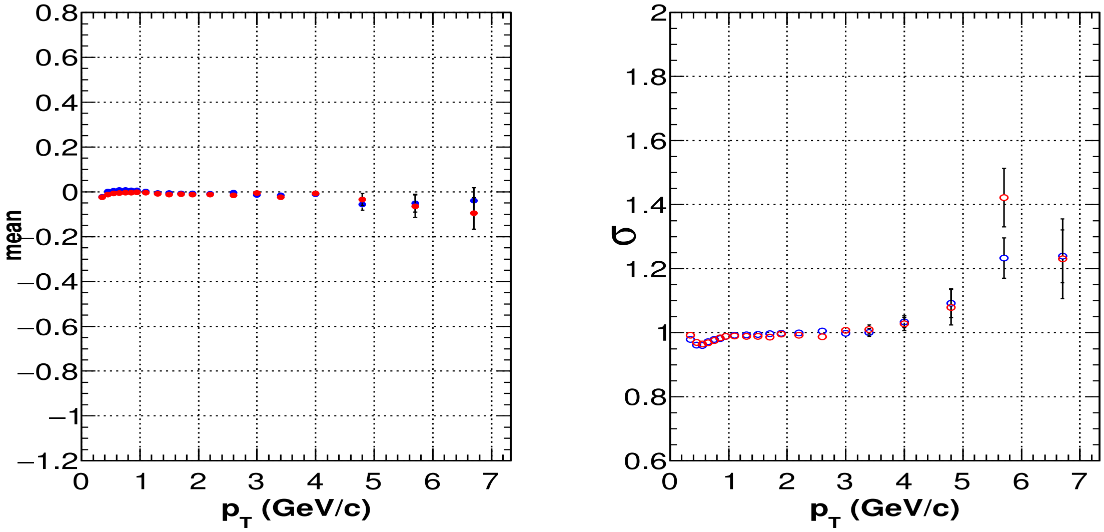

Figure C.23: The $tofsdz$ distributions for "- -" field as a function of p_T without any calibration. The left and right plots correspond to the mean and σ of $tofsdz$ distribution, respectively. The blue color markers are for the positive particle tracks and the red color markers are for the negative particle tracks.

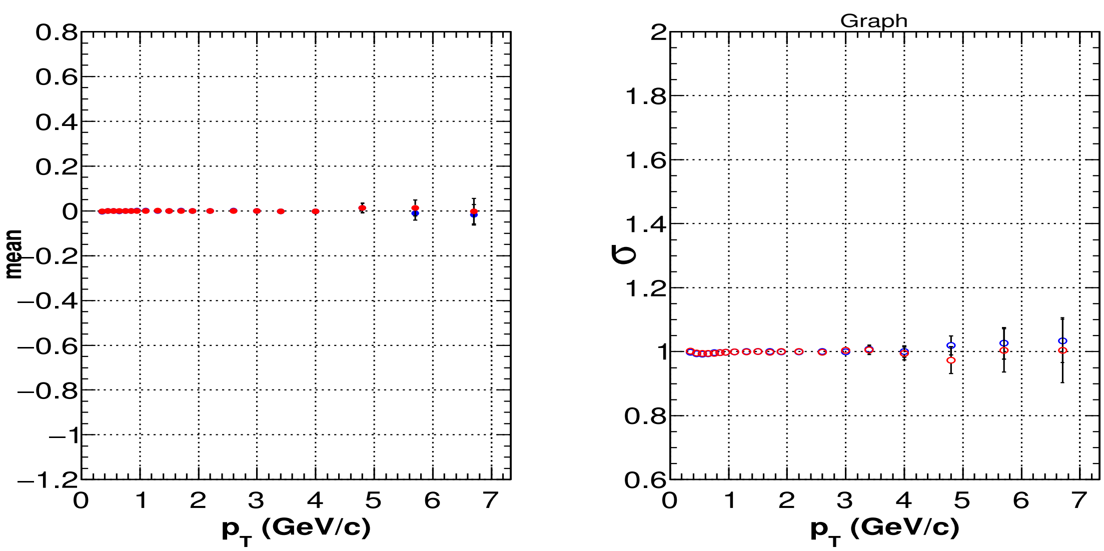

Figure C.24: The $tofsdz$ distributions for "- -" field as a function of p_T after calibration. The left and right plots correspond to the mean and σ of $tofsdz$ distribution, respectively. The blue color markers are for the positive particle tracks and the red color markers are for the negative particle tracks.

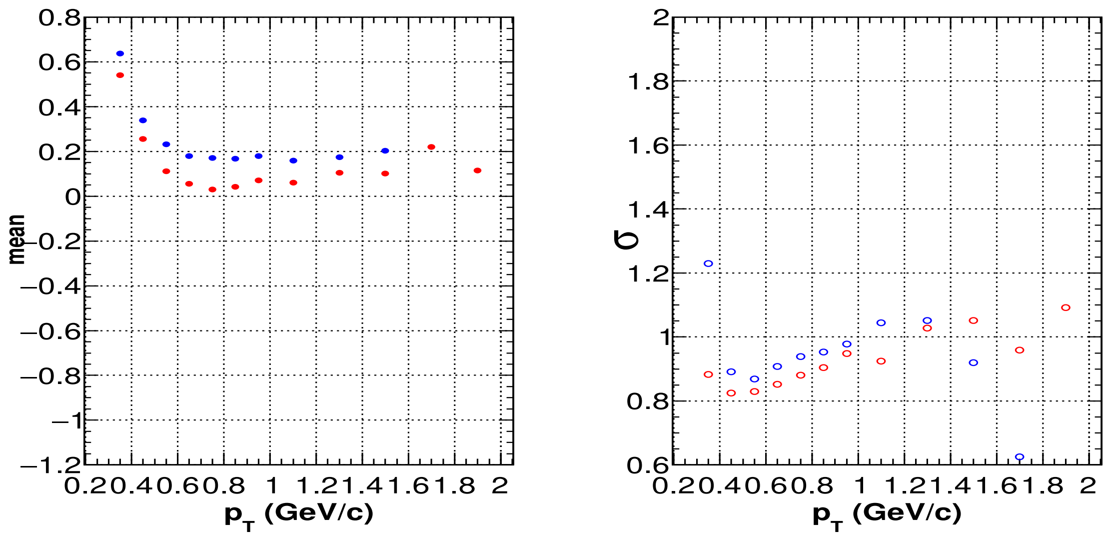

Figure C.25: The isK distributions for “- -” field as a function of p_T without any calibration. The left and right plots correspond to the mean and σ of isK distribution, respectively. The blue color markers are for the positive particle tracks and the red color markers are for the negative particle tracks.

C.2.7 Recalibration plots for isK

The mean and sigma of the uncalibrated distributions of isK as a function of p_T are shown in Fig. C.25 for “- -” field configuration. The calibrated distributions of the same are shown in Fig. C.26.

C.3 Invariant mass plots

C.3.1 Invariant mass plots before background subtraction

The K^{*0} meson invariant mass spectra with the correlated (K^0_S meson and ϕ meson) and uncorrelated background contributions for “Kaon Identified”, “Unidentified” and “Full Identified” techniques are shown in Fig. C.27, Fig. C.28 and Fig. C.29, respectively.

C.3.2 Invariant mass plots after background subtraction

The K^{*0} meson invariant mass spectra after the removal of uncorrelated background contributions for “Kaon Identified”, “Unidentified” and “Full Identified” techniques are shown in Fig. C.30, Fig. C.31 and Fig. C.32, respectively.

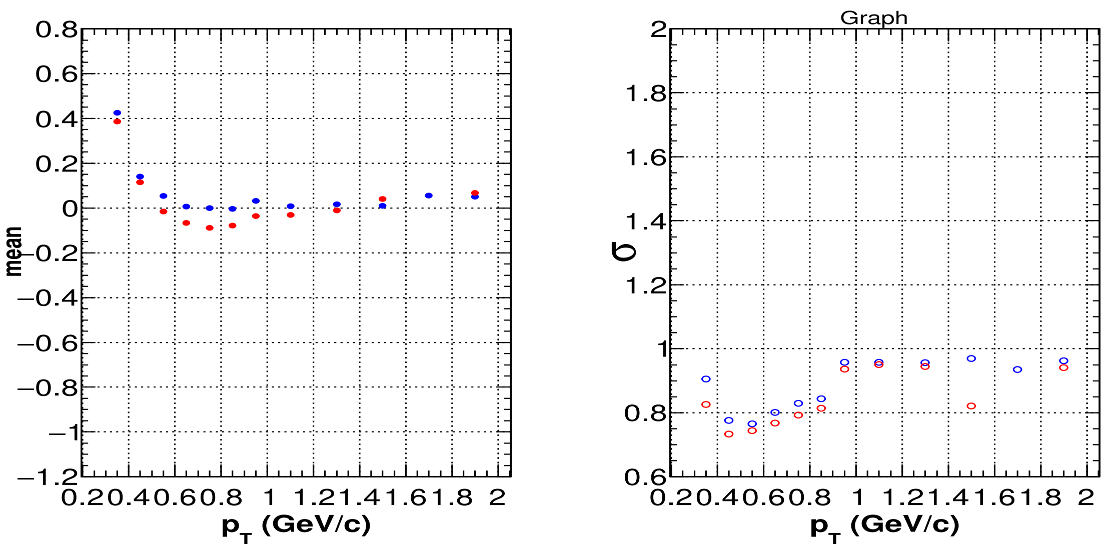

Figure C.26: The isK distributions for "- -" field as a function of p_T after calibration. The left and right plots correspond to the mean and σ of isK distribution, respectively. The blue color markers are for the positive particle tracks and the red color markers are for the negative particle tracks.

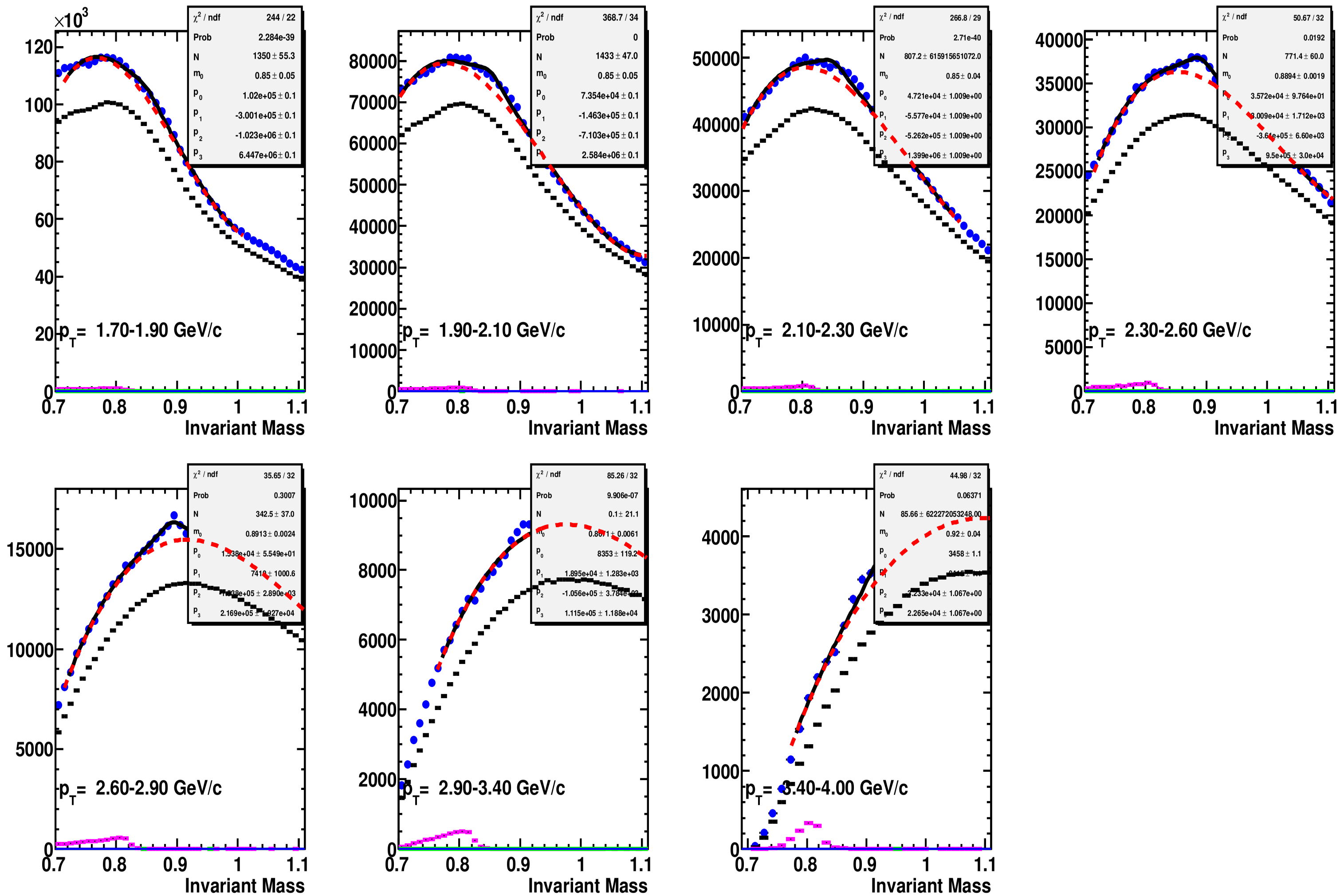

Figure C.27: Invariant mass plots for “Kaon Identified” technique in Cu+Cu collisions for MB data. Blue symbols are the data points, black line is RBW function plus third order polynomial fitted to the data points, red line is the third order polynomial as residual background, black histogram is the mixed event background. Magenta is the mis-identified pairs from ϕ and green one is the mis-identified pairs from K_S^0.

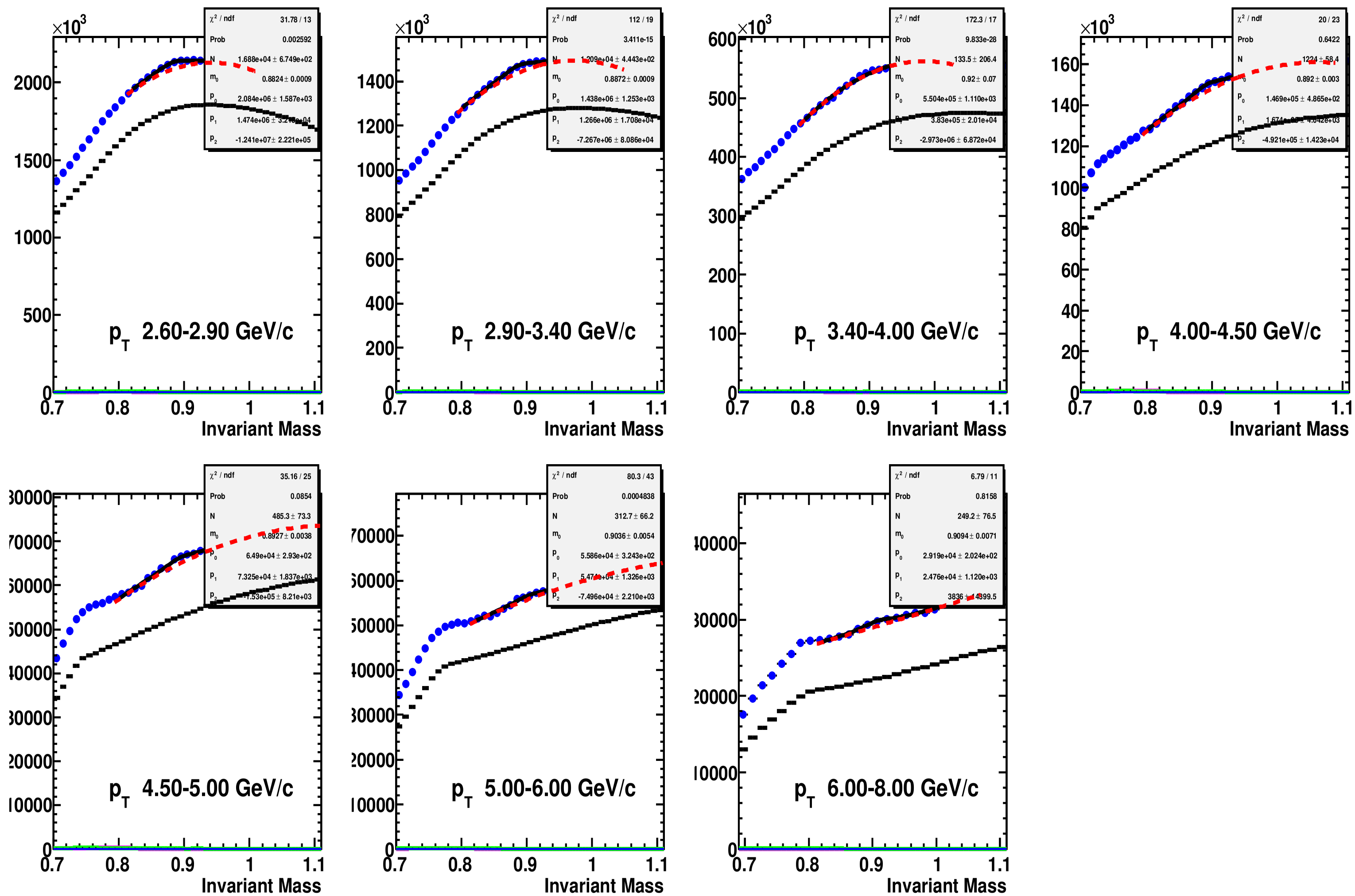

Figure C.28: Invariant mass plots for “Unidentified” technique in Cu+Cu collisions for MB data. Blue symbols are the data points, black line is RBW function plus third order polynomial fitted to the data points, red line is the third order polynomial as residual background, black histogram is the mixed event background. Magenta is the mis-identified pairs from ϕ and green one is the mis-identified pairs from K_S^0.

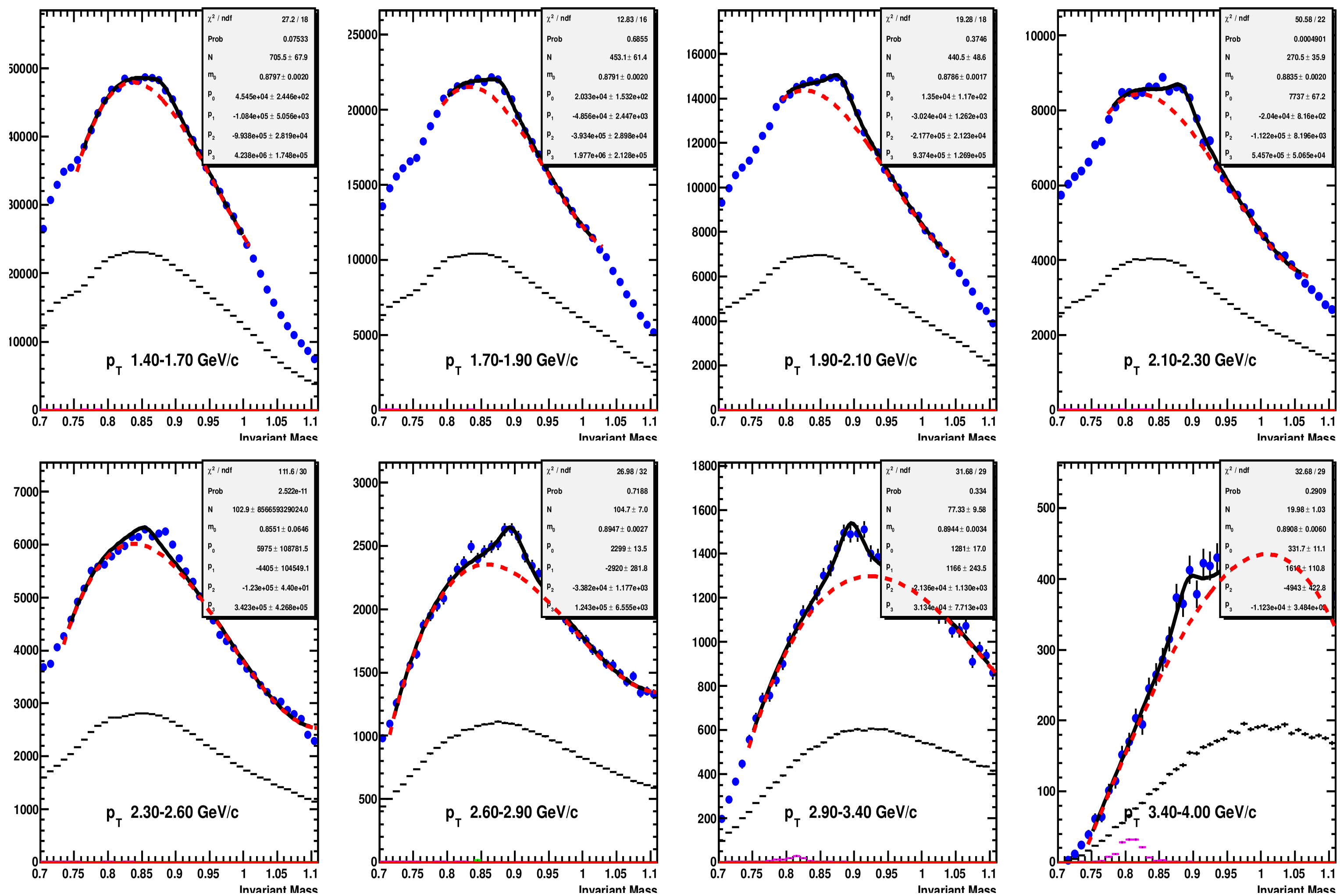

Figure C.29: Invariant mass plots for "Fully Identified" technique in Cu+Cu collisions for MB data. Blue symbols are the data points, black line is RBW function plus third order polynomial fitted to the data points, red line is the third order polynomial as residual background, black histogram is the mixed event background. Magenta is the mis-identified pairs from ϕ and green one is the mis-identified pairs from K_S^0.

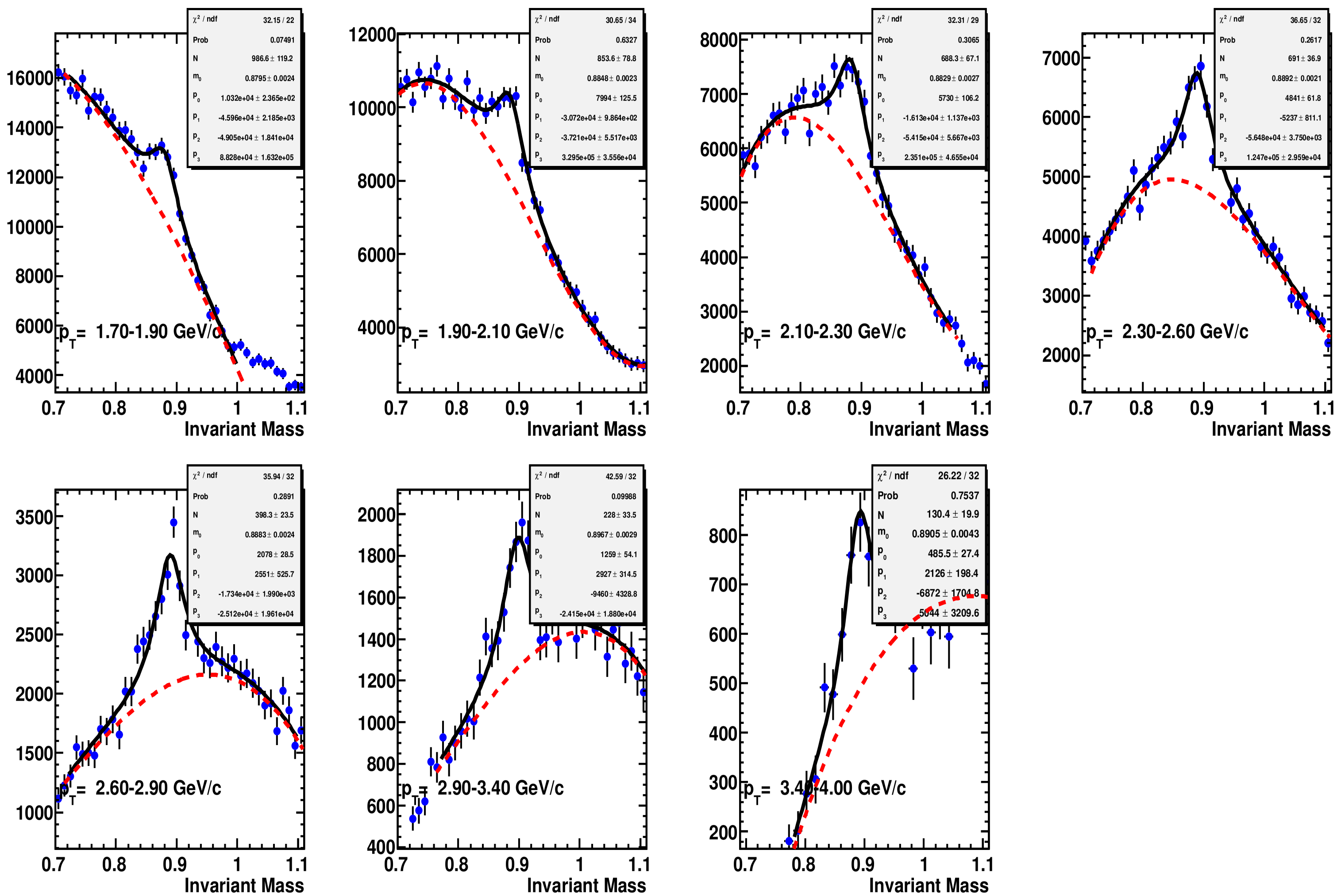

Figure C.30: Invariant mass plots for "Kaon Identified" technique in Cu+Cu collisions for MB data. Blue symbols are the data points, black line is RBW function plus third order polynomial fitted to the data points, red line is the third order polynomial as residual background.

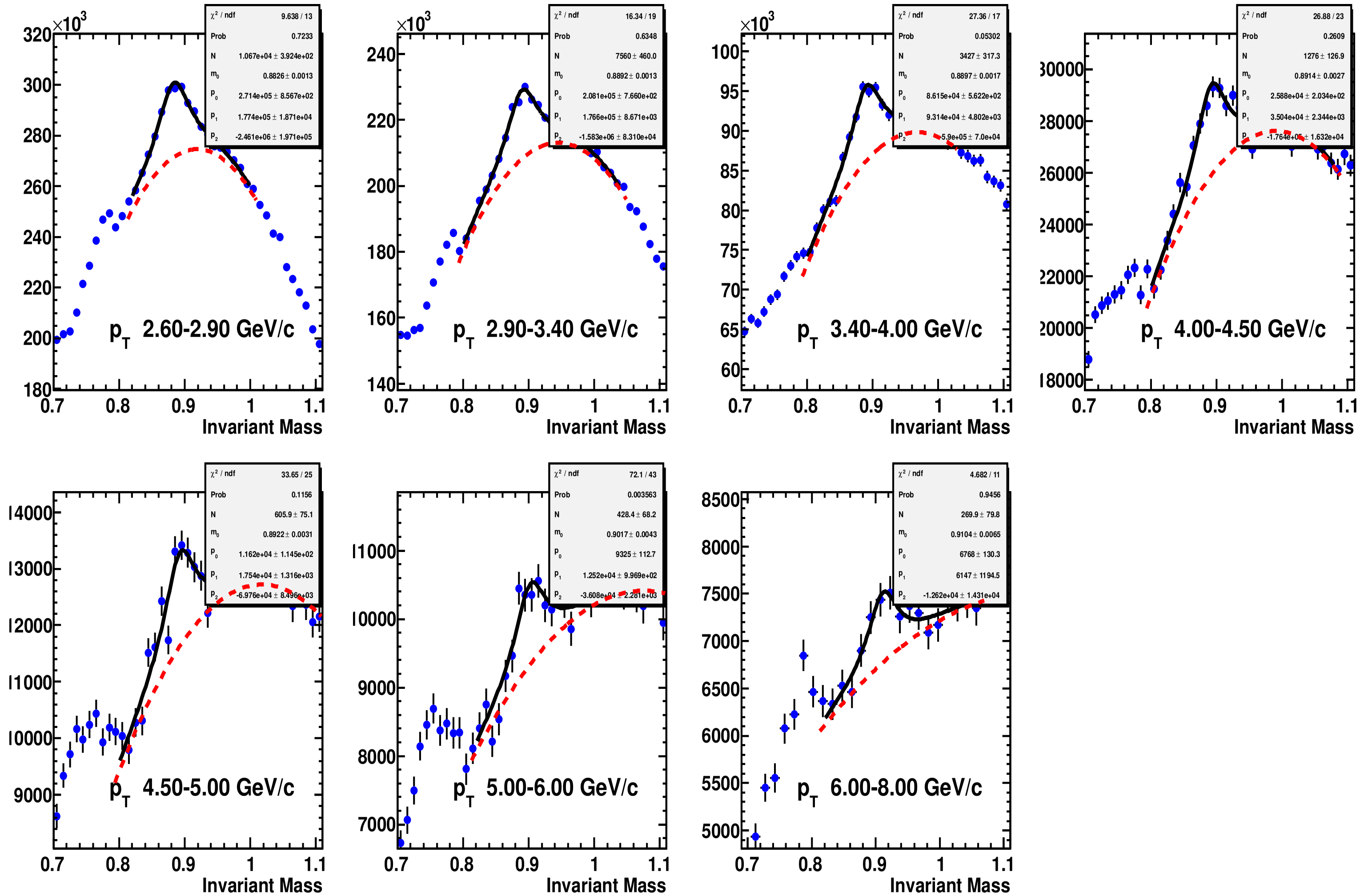

Figure C.31: Invariant mass plots for "Unidentified" technique in Cu+Cu collisions for MB data. Blue symbols are the data points, black line is RBW function plus third order polynomial fitted to the data points, red line is the third order polynomial as residual background.

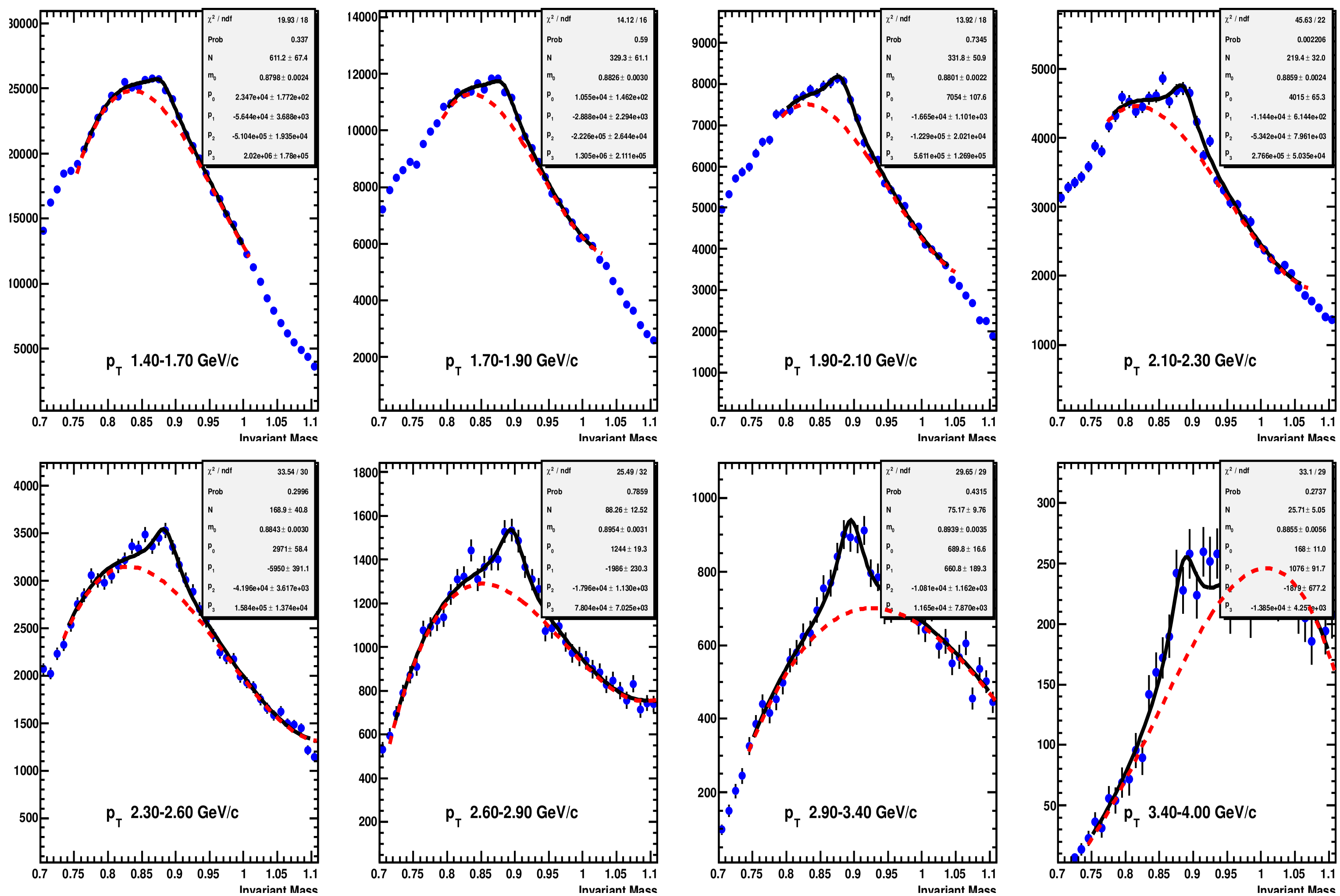

Figure C.32: Invariant mass plots for "Fully Identified" technique in Cu+Cu collisions for MB data. Blue symbols are the data points, black line is RBW function plus third order polynomial fitted to the data points, red line is the third order polynomial as residual background.